UNIVERSITY OF PARMA

DEPARTMENT OF CHEMICAL, LIFE AND ENVIRONMENTAL SUSTAINABILITY SCIENCES

Doctor of Philosophy in Materials Science and Technology

Cycle XXXVII

Electron Nanocrystallography of Metal-Organic Frameworks

Tutor:

Dr. Mauro Gemmi

Coordinator:

Prof. Mauro Riccò

Candidate:

Moussa Diame Faye Diouf

ANNI ACCADEMICI 2022 - 2025

Dedicated to ***my parents****,*
for their love, trust, and support,
and to ***Massimo Daouda Faye Fusco****,*
whom I'll always love, trust, and support.

Abstract

The rapid progress in the production and application of nanomaterials highlights the critical importance of advanced characterization techniques adapted to their nanoscale dimensions. This thesis focuses on method development and application of 3D Electron Diffraction (3D-ED) [1] as an effective alternative to traditional X-ray diffraction (XRD) for the analysis of submicron-sized crystals [2, 3].

We begin by exploring the foundational principles of 3D-ED and the specific requirements necessary for the accurate acquisition and analysis of electron diffraction data. Following this, we detail the development and implementation of automated data acquisition protocols, which significantly improve the efficiency, precision, and reproducibility of structural characterizations.

Expanding on these developments, the study focuses on the application of 3D-ED, to investigate a range of novel and unreported metal-organic frameworks (MOFs), demonstrating the versatility and robustness of 3D-ED techniques in resolving complex structural details, as validated by Rietveld refinements.

This thesis illustrates how 3D-ED can serve as an indispensable tool for the structural characterization of nanomaterials, demonstrating its potential to significantly contribute to advancements in materials science.

Glossary

3D-ED 3D Electron Diffraction.

ADP Atomic Displacement Parameter.

AI Artificial Intelligence.

AIS Automatic Illumination-aperture Selection.

CA Condenser Aperture.

CBED Convergent Beam Electron Diffraction.

cRED Continuous Rotation Electron Diffraction.

DIALS Diffraction Integration for Advanced Light Sources.

DMF N,N-Dimethylformamide.

ED Electron Diffraction.

EDT Electron Diffraction Tomography.

GUI Graphical User Interface.

IEDT Integrated Electron Diffraction Tomography.

LAG Liquid Assisted Grinding.

MicroED Microcrystal Electron Diffraction.

MOF Metal-Organic Framework.

NBED Nano-Beam Electron Diffraction.

ND Neutron Diffraction.

NPD Neutron Powder Diffraction.

OVF Overlapping Virtual Frame.

PEDT Precession-Assisted Electron Diffraction Tomography.

PETS2.0 Process Electron Tilt Series.

PXRD	Powder X-ray Diffraction.
RED	Rotation Electron Diffraction.
SAA	Selected Area Aperture.
SAED	Selected Area Electron Diffraction.
SCND	Single-Crystal Neutron Diffraction.
SCXRD	Single-Crystal X-ray Diffraction.
SEM	Scanning Electron Microscope.
SerialED	Serial Electron Diffraction.
SerialRED	Serial Rotation Electron Diffraction.
STEM	Scanning Transmission Electron Microscope.
SX	Serial Crystallography.
TEM	Transmission Electron Microscope.
XDS	X-ray Detector Software.
XFEL	X-ray Free-Electron Laser.
XRD	X-ray Diffraction.

Contents

List of Figures

Chapter 1

Introduction

1.1 Motivation

The determination of crystal structures is fundamental for understanding the properties and functionalities of materials. Metal-Organic Frameworks (MOFs), with their vast structural diversity, large unit cells, and potential for applications in catalysis, gas storage, and drug delivery, present unique challenges in crystallography. These materials frequently crystallize as micro or nanocrystals, making them unsuitable for traditional structural determination techniques. As a result, the development of new methodologies for solving the structures of nanocrystalline MOFs is essential for advancing this field.

Traditional diffraction techniques, while very powerful, face significant limitations when applied to nanocrystalline MOFs. Neutron Diffraction (ND), including both Single-Crystal Neutron Diffraction (SCND) and Neutron Powder Diffraction (NPD), excels at locating light atoms, such as hydrogen, and investigating magnetic structures [14, 15]. However, it requires large crystals or significant sample volumes, often exceeding several millimeters in size [16]. Similarly, Single-Crystal X-ray Diffraction (SCXRD), the most widely used technique for structural determination, requires high-quality single crystals ranging from 50 micrometers to several millimeters [17]. Although synchrotron radiation can extend the capability of SCXRD to smaller crystals, access to such facilities is limited.

Powder X-ray Diffraction (PXRD) offers an alternative for polycrystalline samples and thanks to the signal enhancement due to the simultaneous diffraction of thousands of crystals it can analyze smaller crystallites down to 50 nanometers [18]. However, the technique struggles with peak overlap and broadening, particularly for complex structures with large unit cells where smaller crystallites worsens these effects [18] and for multiphase samples. This issue complicates *ab-initio* structure solution [19], and even global optimization techniques [20], such as simulated annealing [21], commonly used to solve MOF structures from PXRD data [22], have seen limited success.

3D-ED [1] fills a critical gap in the characterization of nanocrystalline materials. With the ability to analyze crystals smaller than one micrometer, 3D-ED enables *ab-initio* structure determination of single crystals [19] that are too small for SCXRD [2, 3]. Additionally, 3D-ED is typically performed on widely available Transmission Electron Microscopes (TEMs), combining accessibility with rapid data collection. These advantages make 3D-ED an invaluable tool for characterizing MOFs and other complex materials.

Table 1.1: Diffraction techniques and their typical crystal size ranges.

Technique	**Crystal Size Range**	**Notes**
SCND	> 1 cm	Requires very large crystals due to low neutron flux.
NPD	> 0.5 mm^3 (sample volume)	Suitable for large amounts of polycrystalline samples.
SCXRD	50 µm – several mm	Can analyze down to a few µm at synchrotron facilities.
PXRD	50 nm – 10 µm	Limited by peak overlap in complex structures.
3D-ED	< 1 µm	Ideal for nanocrystalline materials.

1.2 Introduction to 3D Electron Diffraction

3D Electron Diffraction has emerged as a powerful technique in crystallography, particularly suited for analyzing nanocrystalline materials that are challenging to study using traditional methods [1]. This section introduces the fundamental principles of 3D-ED, starting with the wave nature of electrons and progressing to the geometric considerations essential for diffraction analysis, followed by an overview of data acquisition and analysis protocols specific to 3D-ED.

1.2.1 Wave Nature of Electrons

The wave-particle duality of electrons is a fundamental concept in quantum mechanics and is essential for understanding electron diffraction. As described by Louis de Broglie's hypothesis, all moving particles exhibit both wave-like and particle-like characteristics. The wavelength (λ) associated with a moving electron is inversely proportional to its momentum ((p)):

$$\lambda = \frac{h}{p} = \frac{h}{m_0 \gamma v}, \tag{1.1}$$

where:

- h is Planck's constant (6.626×10^{-34} J·s),
- m_0 is the rest mass of the electron (9.109×10^{-31} kg),
- $\gamma = \frac{1}{\sqrt{1-\frac{v^2}{c^2}}}$ is the relativistic correction to the rest mass which is not negligible in a TEM with accelerating voltages in the order of several hundreds of kV
- v is the velocity of the electron.

For electrons accelerated to high velocities in a TEM, the resulting de Broglie wavelengths are on the order of a few picometers (typically 2-3 pm), which, while two orders of magnitude smaller than typical interatomic distances (100-300 pm), is still crucial for facilitating diffraction by the periodic potential created by the atomic arrangement within a crystalline material. This diffraction produces interference patterns characteristic of the crystal structure.

1.2.2 Diffraction Geometry

Having established the wave nature of electrons and their associated wavelengths, it is now crucial to understand how these waves interact with the periodic structure of crystalline materials to produce observable diffraction patterns. This subsection will introduce the fundamental geometric principles governing diffraction, progressing from the simplified representation of Bragg's law to the more comprehensive Ewald sphere construction.

1.2.2.1 Bragg's Law

Consider a crystalline material with atoms arranged in parallel planes separated by a distance d, as illustrated in Figure 1.1. When a beam of electrons with wavelength λ interacts with these planes at an angle θ, scattering occurs at each atom. Constructive interference, and thus diffraction, will occur when the path difference between waves scattered by adjacent planes is an integer multiple of the electron wavelength.

The path difference between the wave scattered at atom O and the wave scattered at atom G can be calculated as follows: The wave scattered at G travels an extra distance FG + GH. From the geometry of Figure 1.1, we can see that:

$$\mathrm{FG} = d\sin\theta$$

$$\mathrm{GH} = d\sin\theta$$

$$\mathrm{FG} + \mathrm{GH} = 2d\sin\theta$$

Therefore, the total path difference is $2d\sin\theta$. For constructive interference, this path difference must be equal to an integer multiple of the wavelength λ. This condition is expressed by Bragg's law:

$$n\lambda = 2d\sin\theta, \tag{1.2}$$

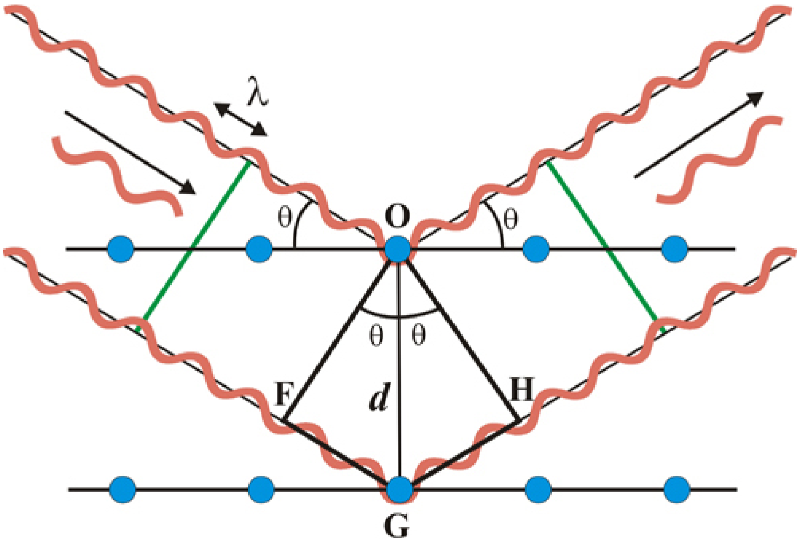

Figure 1.1: Illustration of Bragg's law. Incident waves are scattered by atoms in parallel planes separated by a distance d. Constructive interference occurs when the path difference between the scattered waves is an integer multiple of the wavelength λ.

where:

- n is an integer representing the order of diffraction,
- λ is the wavelength of the incident electrons,
- d is the inter-planar spacing between the diffracting planes, and
- θ is the Bragg angle, the angle between the incident beam and the diffracting planes.

Bragg's law provides a simple geometric relationship that predicts the angles at which diffraction maxima will be observed. However, it does not account for the intensities of the diffracted beams, which are influenced by the atomic scattering factors and other factors.

1.2.2.2 The Ewald Sphere Construction

For a better understanding of diffraction in reciprocal space and of its spatial geometry, it is helpful to consider a three-dimensional treatment. While Bragg's law provides the fundamental condition for diffraction in terms of real-space lattice planes, the Ewald sphere construction offers a geometric framework in reciprocal space, allowing for a comprehensive visualization of diffraction conditions in three dimensions.

In crystallography, reciprocal space is a mathematical construct where each point corresponds to a set of parallel lattice planes in real space. For a given set of lattice planes with Miller indices (hkl), the corresponding reciprocal lattice vector $\mathbf{g}_{hkl}$ is defined such that its direction is perpendicular to the (hkl) planes, and its magnitude is inversely proportional to the inter-planar spacing d_{hkl}:

$$|\mathbf{g}_{hkl}| = \frac{2\pi}{d_{hkl}}. \tag{1.3}$$

These reciprocal lattice vectors are derived from the real-space lattice vectors ($\mathbf{a}$, $\mathbf{b}$, $\mathbf{c}$) as follows:

$$\mathbf{g}_{100} = \frac{2\pi}{V}\mathbf{b} \times \mathbf{c}, \tag{1.4}$$

$$\mathbf{g}_{010} = \frac{2\pi}{V}\mathbf{c} \times \mathbf{a}, \tag{1.5}$$

$$\mathbf{g}_{001} = \frac{2\pi}{V}\mathbf{a} \times \mathbf{b}, \tag{1.6}$$

where V denotes the volume of the unit cell in real space. Consequently, any reciprocal lattice vector can be expressed as a linear combination of these basis vectors:

$$\mathbf{g}_{hkl} = h\mathbf{g}_{100} + k\mathbf{g}_{010} + l\mathbf{g}_{001}.$$

The Ewald sphere is often represented in two dimensions, which corresponds to a section of the sphere, as shown in Figure 1.2. In reciprocal space, an Ewald sphere is drawn with a radius of $2\pi/\lambda$, where λ is the wavelength of the incident radiation.

The origin of the reciprocal lattice (O) is placed on the surface of the Ewald sphere, representing the point where the incident beam exits the sphere. The incident beam direction is represented by the wave vector $\mathbf{K}_0$ pointing towards the origin of the reciprocal lattice. Diffraction occurs when a reciprocal lattice point lies on the surface of the Ewald sphere. The vector connecting the origin of the reciprocal lattice (O) to this intersecting point is the scattering vector $\mathbf{s}$. In Figure 1.2, the red dots represent reciprocal lattice points that satisfy the diffraction condition. The wave vector of the diffracted beam, $\mathbf{K}_2$, points from the center of the Ewald sphere to the intersecting reciprocal lattice point. The angle between $\mathbf{K}_0$ and $\mathbf{K}_2$ is 2θ, where θ is the Bragg angle.

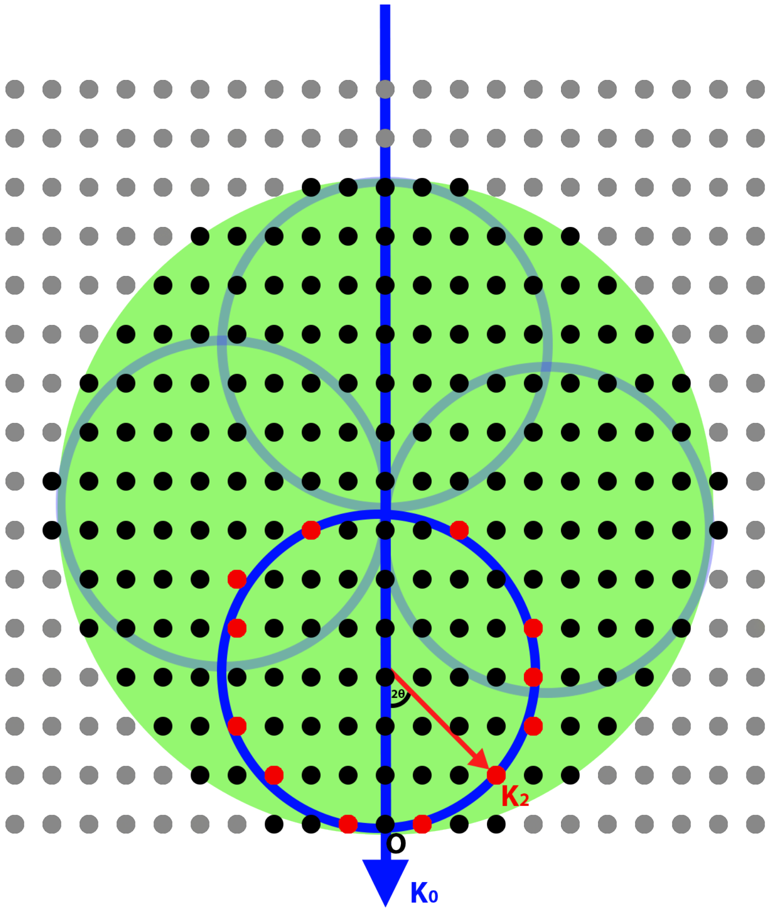

Figure 1.2: The Ewald sphere construction in reciprocal space. The blue circle represents the Ewald sphere, while the green circle is the limiting sphere (radius $2/\lambda$). Red dots indicate reciprocal lattice points satisfying the diffraction condition.

Typically, to observe more diffraction spots, the crystal is rotated. In reciprocal space, this is equivalent to rotating the Ewald sphere about the origin of the reciprocal lattice. This rotation is illustrated in Figure 1.2 by the partially transparent blue circles. It becomes apparent that not all reciprocal lattice points are accessible by rotating the Ewald sphere. The accessible region is defined by the limiting sphere (green circle), centered at the origin of the reciprocal lattice (O) with a radius of $2/\lambda$. Reciprocal lattice points falling outside this limiting sphere (represented in gray in Figure 1.2) cannot be brought onto the Ewald sphere by any rotation of the crystal. Therefore, to access higher scattering vectors, and thus obtain information from smaller inter-planar spacings in real space, shorter wavelengths (λ) are required.

1.2.3 Diffraction Intensities

In previous sections, we discussed Bragg's law and the Ewald sphere construction to explain the directions in which diffraction occurs, predicting the positions of reflections in a diffraction pattern. However, these considerations do not account for the intensities of the diffracted beams. The intensities of the reflections are crucial for determining the crystal structure and are governed by the structure factor, F_{hkl}.

1.2.3.1 The Structure Factor and Atomic Scattering Factors

Diffraction is fundamentally a quantum-mechanical phenomenon that arises from the interference of waves scattered by each atom in the structure. A complete theoretical description is beyond the scope of the present thesis, so we will focus on describing the main fundamental results without derivation. The interference of waves scattered by individual atoms leads, for each diffracted wave (reflection), to a complex amplitude proportional to the Fourier transform of the scattering quantity (electrostatic potential for electrons). This complex amplitude is known as the structure factor. Since the scattering quantity is periodic, with its fundamental periodicity defined by the unit cell, the structure factor can be expressed as:

$$F_{hkl} = \sum_{j=1}^{N} O_j f_j \exp\left[2\pi i \left(hx_j + ky_j + lz_j\right)\right] \exp\left[-B_j \left(\frac{\sin\theta}{\lambda}\right)^2\right], \tag{1.7}$$

where:

- O_j is the occupancy of the j-th atom.
- f_j is the atomic scattering factor of the j-th atom, related to the atom's scattering power. For X-rays, f_j depends on the electron density, while for electrons, it relates to the electrostatic potential. In all cases, f_j generally decreases with increasing scattering angle θ.
- x_j, y_j, z_j are the fractional coordinates of the j-th atom within the unit cell, each ranging from 0 to 1.
- N is the total number of atoms in the unit cell.
- h, k, l are the Miller indices of the reflecting planes, which define the reciprocal lattice vector $\mathbf{g}_{hkl}$.
- i is the imaginary unit, $\sqrt{-1}$.
- B_j is the isotropic thermal parameter for the j-th atom, representing the mean-square displacement due to thermal vibrations.
- θ is the Bragg angle corresponding to the (h, k, l) reflection.
- λ is the wavelength of the incident radiation.

The first exponential term in Equation 1.7 represents the phase difference between waves scattered by different atoms in the cell, the fundamental periodic unit of the structure. The second exponential term accounts for the thermal vibrations of atoms, where higher thermal parameters B_j indicate greater atomic displacement.

Under the hypothesis of single scattering (kinematical approximation), the intensity of a diffracted beam with Miller indices (hkl), denoted I_{hkl}, is proportional to the square of the magnitude of the structure factor $|F_{hkl}|^2$:

$$I_{hkl} \propto |F_{hkl}|^2 = F_{hkl} \times F^*_{hkl}, \tag{1.8}$$

where F^*_{hkl} is the complex conjugate of F_{hkl}. By taking the product $F_{hkl}F^*_{hkl}$, we ensure that the intensity is always a real, positive quantity.

We would like to point out that, although the diffracted intensities directly depend on the atomic positions, reconstructing the scattering quantity from the measured intensities is not a trivial problem because the phases of each diffracted wave are lost in the diffraction experiment. This is commonly referred to as the phase problem in crystallography. If the phases were measurable quantities, a simple inverse Fourier transform would reconstruct the scattering quantity, which is typically peaked at the atomic positions. The pioneering work of crystallographers on solving the phase problem in X-ray diffraction has established robust and reliable methods for determining the atomic structure of crystals. Examples of these methods include direct methods [19] and dual-space algorithms, such as charge flipping [23]. These approaches are also available for electron diffraction. However, they require more careful application compared to X-ray diffraction, as the kinematical approximation for electrons does not accurately represent the actual scattering process due to significant multiple scattering effects, resulting from the strong interaction of electrons with matter.

1.2.3.2 Symmetry in reciprocal space

The knowledge of crystal symmetry significantly simplifies the structure solution by reducing the number of unknown to be determined. From an extremely large number of atomic positions, the crystal structure can be completely determined by retrieving the atomic coordinates of the atoms of the asymmetric unit, a subset of the atoms belonging to the unit cell. All the atoms in the crystal can then be located by applying the symmetry elements to the asymmetric unit.

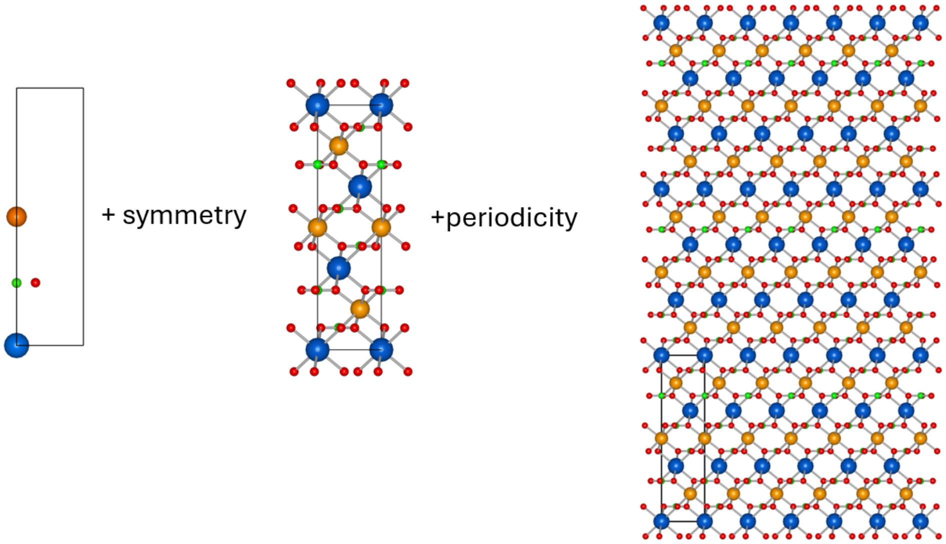

Figure 1.3: Visualization of crystal structure generation: Starting with the asymmetric unit (left), symmetry operations populate the unit cell (center). Repeating the unit cell through periodicity in three dimensions produces the complete crystal lattice (right).

Identifying the correct symmetry is therefore one of the main tasks in structure determination. The complete symmetry of a crystal is expressed by a mathematical group know as the space group. Unfortunately the space group cannot be completely determined from the diffracted intensities alone. In diffraction, the intensities inherently exhibit centrosymmetry, regardless of whether the crystal's space group is centrosymmetric or not. This property is expressed by Friedel's Law:

$$I_{hkl} = I_{\overline{hkl}} \tag{1.9}$$

Since symmetry in reciprocal space operates through the point group of the crystal, comparing the diffraction intensities of reflections related by point group symmetry operators allows determination of the centrosymmetric super-group of the crystal's point group, known as the Laue group. Crystals that share the same Laue group are classified as belonging to the same Laue class.

The last more subtle effect of the space group symmetry which can be determined with the inspection of diffraction intensities is the possible presence of translational symmetry elements like screw axis or glide planes or lattice centering. All these symmetry elements are signaled by systematic absences in the diffraction pattern, where certain reflections have zero intensity due to complete destructive interference.

The fundamental reason for systematic absences lies in the phase shifts introduced by these symmetry operations. For symmetry operations without a translational component, such as a simple rotation axis, the phases of symmetry-related reflections are always equal. However, symmetry operations with a translational component such as screw axes, glide planes or even centering introduce additional phase shifts.

1.2.3.2.1 Effect of a 2_1 Screw Axis

The 2_1 screw axis along the **b**-axis combines a 180° rotation with a fractional translation of $\frac{1}{2}$ along the **b**-axis. Consider two symmetry-related atoms: the first at (x, y, z), and the second transformed by the screw axis to $(-x, y + \frac{1}{2}, -z)$. The structure factor contributions from these two atoms are:

$$F(hkl) = f \exp\big[2\pi i(hx + ky + lz)\big] + f \exp\big[2\pi i(-hx + k(y + \tfrac{1}{2}) - lz)\big].$$

For $(0k0)$ reflections ($h = 0$, $l = 0$), this simplifies to:

$$F(0k0) = f \exp\big[2\pi i(ky)\big] + f \exp\big[2\pi i(ky + \tfrac{k}{2})\big].$$

Factoring out the common exponential term $\exp\big[2\pi i(ky)\big]$, we get:

$$F(0k0) = f \exp\big[2\pi i(ky)\big] \big[1 + \exp\big(i\pi k\big)\big].$$

Since $\exp(i\pi k) = (-1)^k$:

$$1 + (-1)^k = \begin{cases} 2, & k = 2\text{n}, \\ 0, & k = 2\text{n} + 1. \end{cases}$$

Thus, the structure factor $F(0k0)$ is zero when k is odd, leading to systematic absences for $(0k0)$ reflections with $k = 2n + 1$.

1.2.3.2.2 Effect of a Glide Plane

A glide plane involves a reflection across a plane followed by a fractional translation parallel to that plane. Consider an a-glide plane perpendicular to the b axis. This transforms coordinates (x, y, z) to $(x + \frac{1}{2}, -y, z + \frac{1}{2})$. The structure factor contribution for two atoms related by this glide plane would be:

$$F(hkl) = f \exp\big[2\pi i(hx + ky + lz)\big] + f \exp\big[2\pi i(h(x + \tfrac{1}{2}) - ky + l(z + \frac{1}{2}))\big].$$

For $h0l$ reflections $(k = 0)$, this simplifies to:

$$\begin{aligned} F(h0l) &= f \exp\big[2\pi i(hx + lz)\big] + f \exp\big[2\pi ih(x + \tfrac{1}{2}) + l(z + \frac{1}{2})\big] && (1.10)\\ &= f \exp\big[2\pi i(hx + lz)\big]\big[1 + \exp(\pi i(h + l))\big]. && (1.11)\end{aligned}$$

Since $\exp(\pi i(h + l)) = (-1)^{h+l}$:

$$1 + (-1)^{h+l} = \begin{cases} 2, & h + l = \text{2n}, \\ 0, & h + l = \text{2n+1}. \end{cases}$$

Therefore, the structure factor $F(h0l)$ is zero when $h{+}l$ is odd, leading to a systematic absence for $(h0l)$ reflections with $h + l = 2n + 1$.

1.2.3.2.3 Effect of Centering

Centered lattices, such as body-centered, face-centered, and base-centered structures, incorporate additional translational symmetry elements within the unit cell. These centering translations impose specific conditions that lead to systematic absences in the diffraction pattern. The criteria for these absences based on different centering types are summarized in Table 1.2.

Table 1.2: Systematic Absences Induced by Different Centering Types

Centered Lattice	**Systematic Absence Condition**
A-Centered	$k + l = 2n + 1$
B-Centered	$h + l = 2n + 1$
C-Centered	$h + k = 2n + 1$
Body-Centered (I)	$h + k + l = 2n + 1$
Face-Centered (F)	Mixed parity of h, k, l

By combining the information derived from the observed extinction conditions with the Laue class determined through the symmetry of the intensities, we can extract the maximum symmetry information that diffraction can reveal, summarized by the extinction symbol. Typically, more than one space group is compatible with a given extinction symbol, and determining the correct space group is resolved during the structure solution step. If the chosen space group is incorrect, the resulting solution will not be chemically plausible. However, in some cases, the differences between two possible space groups can be subtle (e.g., due to small distortions), and both structure solutions may appear plausible. In such instances, only a detailed refinement can distinguish the correct solution. The discussion so far assumes the ideal case of kinematical diffraction. In the case of electron diffraction, however, symmetry determination is complicated by dynamical scattering, which can activate reflections that would otherwise be extinct. This effect makes identifying extinction conditions and determining the correct Laue class more challenging.

1.2.4 Differences between Electron Diffraction and X-Ray Diffraction

Electron diffraction and X-ray diffraction are both powerful techniques for determining crystal structures, yet they differ significantly in their principles and applications. While dedicated electron diffractometers exist [24], electron diffraction is predominantly performed using a TEM as of the time of writing.

In a TEM, the electron beam is shaped and focused due to the ability of charged particles to be deflected by magnetic fields while in motion. This property enables the creation of magnetic fields that focus electrons in much the same way a lens focuses light rays. In contrast, this effect is extremely challenging to achieve for X-rays, another type of radiation widely used in crystallography, because X-rays are not easily deflected.

Thanks to that, in a TEM, an objective lens can focus the scattered and diffracted electrons from the sample, into a diffraction pattern in its back focal plane and into an intermediate image in its image plane, exactly as it happens in any optical system for light. This means that both the diffraction pattern and the image are present simultaneously within the TEM and can be captured by a lens system below the objective lens, such as the intermediate lens, which is specifically designed for this purpose. Its focus determines whether the diffraction pattern or the image is projected onto the second intermediate image plane. This projection is then magnified by the projective lens system and displayed on the fluorescent screen or detector. Switching between real space (image) and reciprocal space (diffraction) is therefore very fast and easy (Figure 1.4).

An important difference between ED and XRD is in the wavelengths between electrons and X-rays. As discussed previously, the radius of the Ewald sphere is inversely proportional to the wavelength of the incident radiation ($1/\lambda$). Electrons, with their much shorter wavelengths, result in Ewald spheres with significantly larger radii compared to those in XRD. This vast difference in radii leads to the "flat Ewald sphere" approximation in ED (Figure 1.5).

This flat Ewald sphere intersects with many more reciprocal lattice points simultaneously, resulting in diffraction patterns with a much higher density of reflections compared to XRD patterns acquired at the same orientation (Figure 1.5). As a consequence, a single ED pattern effectively represents a two-dimensional section through the three-dimensional reciprocal lattice, therefore, only two unit cell vec-

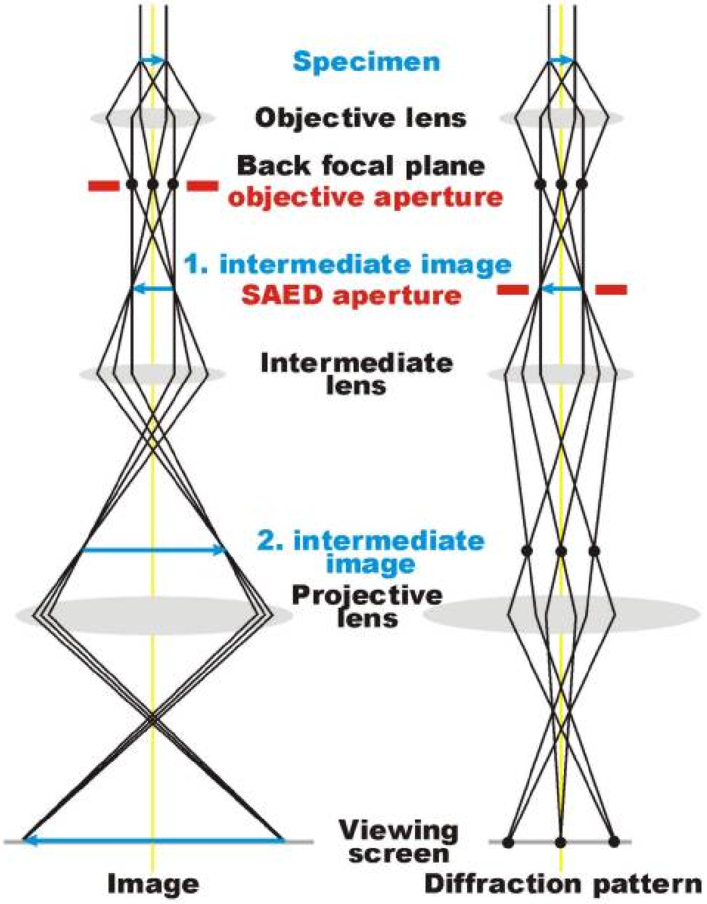

Figure 1.4: Schematic diagram of a TEM illustrating the formation of the diffraction pattern and intermediate image.

tors can be directly deduced from a single ED pattern. To fully reconstruct the three-dimensional reciprocal lattice and determine all three unit cell vectors, data from different orientations are required.

Another important difference, is the nature of the radiation source. Electrons are charged particles, while X-rays are electromagnetic radiation (photons), resulting in a significant difference in how they interact with matter. The electrons, thanks to their charge, interact strongly with the electrostatic potential of atoms, including both the positively charged nucleus and the negatively charged electron cloud via Coulomb forces [25, 26]. In contrast, X-rays interact primarily with the electron cloud, leading to weaker interactions. The stronger scattering of electrons, from 3

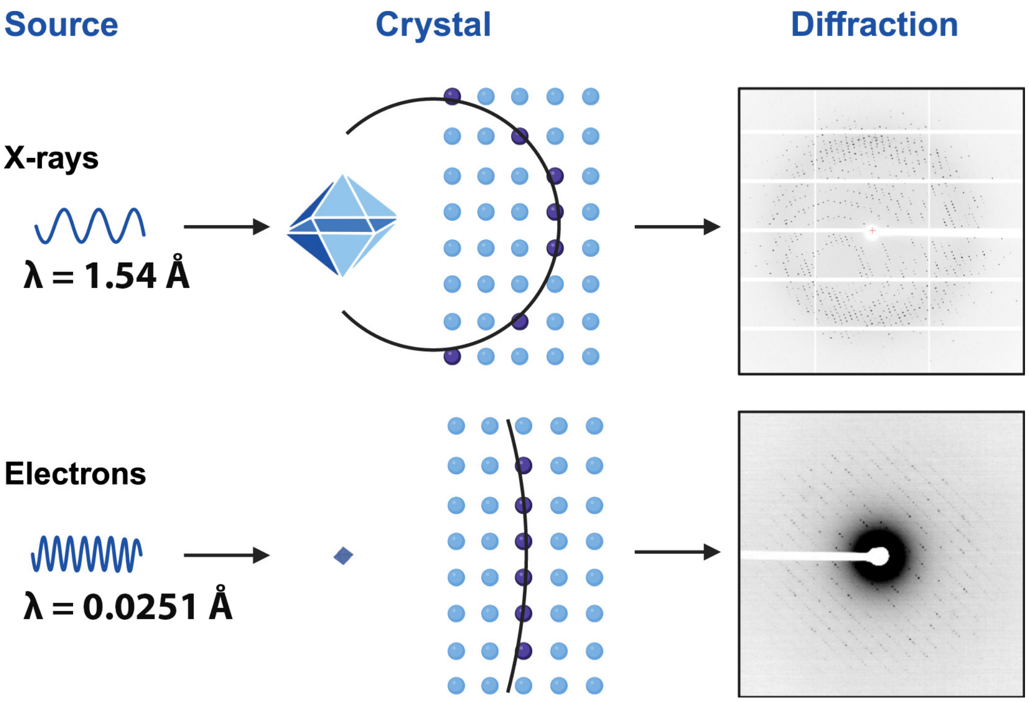

Figure 1.5: Differences between an XRD and ED pattern (adapted from [4]). The ED pattern contains more observed reflections due to the flat Ewald sphere.

to 4 orders of magnitude more than X-rays in amplitude, provides a much higher signal-to-noise ratio, enabling the study of very small crystals (nanocrystals) that would produce weak or undetectable diffraction signals with X-rays. Additionally, these accelerated electrons can be manipulated by electromagnetic lenses to produce small parallel beam with a size of few nanometers, allowing for diffraction analysis from very small areas. This level of spatial resolution can only be achieved with XRD in the last generation of synchrotron.

However, the strong scattering of electrons was a primary reason why Electron Diffraction (ED) was historically disregarded for structure analysis. This strong interaction leads to multiple scattering events, known as dynamical scattering, as electrons pass through the sample. Dynamical effects significantly impact the intensities of Bragg reflections (Figure 1.6), which are crucial for accurate structure determination. While dynamical diffraction is present in both X-ray Diffraction (XRD) and ED, it manifests differently. In XRD, dynamical effects are mainly significant in perfect large crystals, while for electrons, dynamical scattering is always present due to their inherently strong interaction with matter.

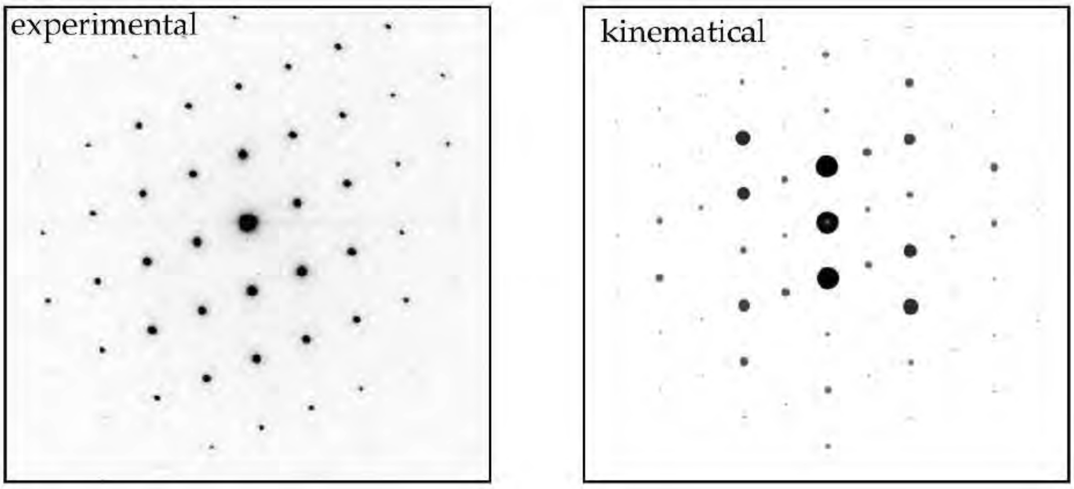

Figure 1.6: Experimental vs Kinematical Simulation of an ED pattern.

The kinematical theory of diffraction (Equation 1.8), which assumes single scattering events, provides a good approximation for many XRD experiments and is often sufficient for electron diffraction if the intensities are collected in a 3D-ED experiment. However, achieving refinement accuracy comparable to X-ray diffraction requires the implementation of a full dynamical model of electron scattering. Remarkably, while dynamical scattering has long been considered a significant limitation of electron diffraction, its correct modeling transforms it into a powerful advantage. Dynamical scattering enhances the sensitivity of electron diffraction to light atoms, such as hydrogen, and provides unique sensitivity to the absolute structure determination of enantiomeric crystals [6, 27]. In a later section (1.2.7.2.3), we will explore the method to incorporate dynamical scattering effects into structure determination.

1.2.5 Illumination and Data Acquisition Modes

A TEM is a versatile instrument, functioning as a microscope, spectrometer, and diffractometer. While primarily designed and optimized for imaging, its diffraction capabilities offer several advantages. These include the flexibility to precisely control the electron beam size and the unique ability for simultaneous observation in both real and reciprocal space. In the following sections, we will explore its functionalities from the perspective of a crystallographer, considering the TEM as a specialized single-crystal diffractometer for nanocrystals.

1.2.5.1 Parallel Illumination in Electron Diffraction

Sharp and well-defined diffraction spots, or reflections, are important for accurate 3D-ED analysis. Achieving this precision requires the electron beam to be parallel or quasi-parallel as it interacts with the sample. In a TEM, this is accomplished by ensuring that a proper de-magnified image of the electron source, known as the electron beam crossover, occurs at the front focal plane of the objective pre-field lens, also referred to as the upper objective lens.

This parallel illumination relies on the condenser lens system, which is responsible for the crossover formation. In a two-condenser lens configuration, the C1 lens adjusts the spot size, while the C2 lens is responsible for both controlling the beam intensity (brightness) and positioning the crossover at the front focal plane. As a consequence, for a given C1 lens current (defining the spot size), there is a corresponding C2 lens current that achieves parallel illumination. When a C2 condenser aperture is introduced, it further constrains the beam size, resulting in a single beam size capable of achieving parallel illumination, regardless of the C1 lens value.

In contrast, a three-condenser lens system introduces a C3 lens that automatically adjusts its current to maintain the beam crossover at the front focal plane of the objective pre-field lens. This adjustment allows the C2 lens to focus only on controlling the beam intensity (brightness). As a result, three-condenser lens systems offer a wide range of beam sizes that still produce parallel illumination.

The differences between the two systems for achieving parallel illumination are illustrated in Figure 1.7. In the two-condenser system (left), the dotted green lines show the beam path without the condenser aperture, while the continuous lines represent the effect of the C2 aperture in narrowing the beam. In the three-condenser system (right), two ray paths (green and orange) illustrate different C1 and C2 settings, with dotted lines showing the beam path without the condenser aperture and continuous lines showing the resulting beam with the aperture.

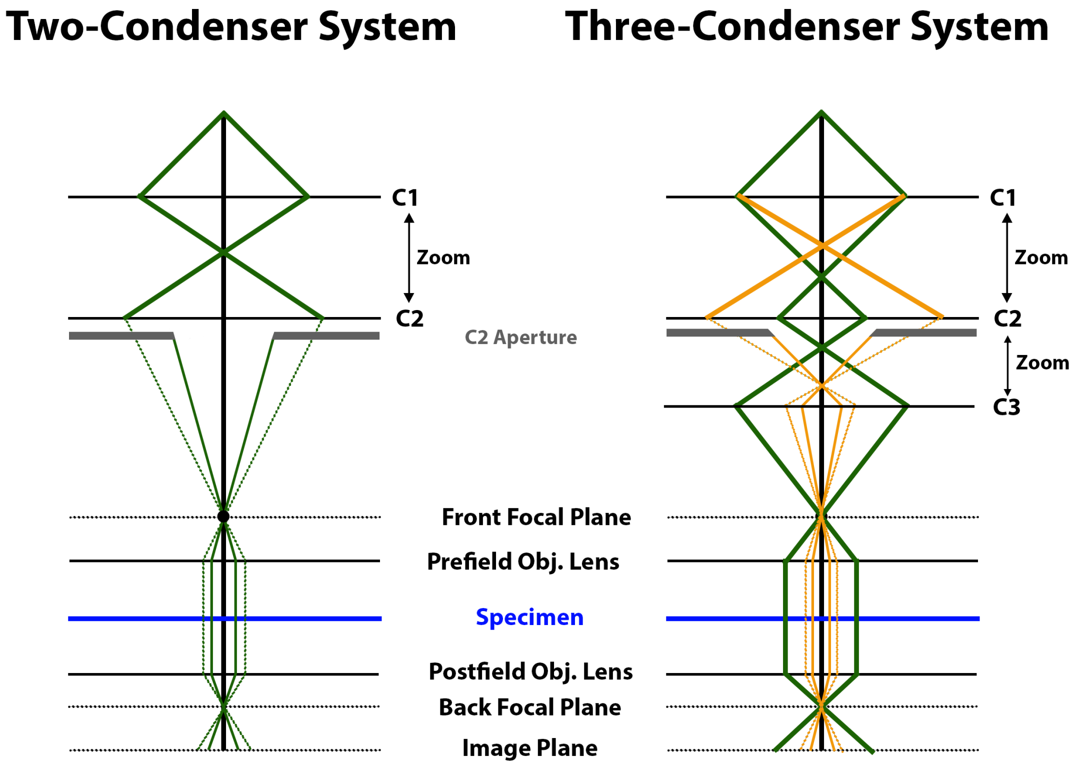

Figure 1.7: Beam paths in two- and three-condenser systems for parallel illumination.

1.2.5.2 Selected Area Electron Diffraction vs Nano-Beam Electron Diffraction

3D-ED data can be collected either in Selected Area Electron Diffraction (SAED) or Nano-Beam Electron Diffraction (NBED). In SAED, a relatively large area of the specimen is illuminated by the electron beam, and the Selected Area Aperture (SAA), located in the image plane, after the specimen, is used to define the region from which the diffraction pattern is collected. In this mode, the entire illuminated area is exposed to the electron beam, which can cause beam damage to sensitive crystals outside the selected area.

In NBED, the size of the illuminated region is controlled by the Condenser Aperture (CA), located in the condenser lens system, before the specimen. This produces a very small, nanometer-scale electron beam, ensuring that only the illuminated area contributes to the diffraction pattern.

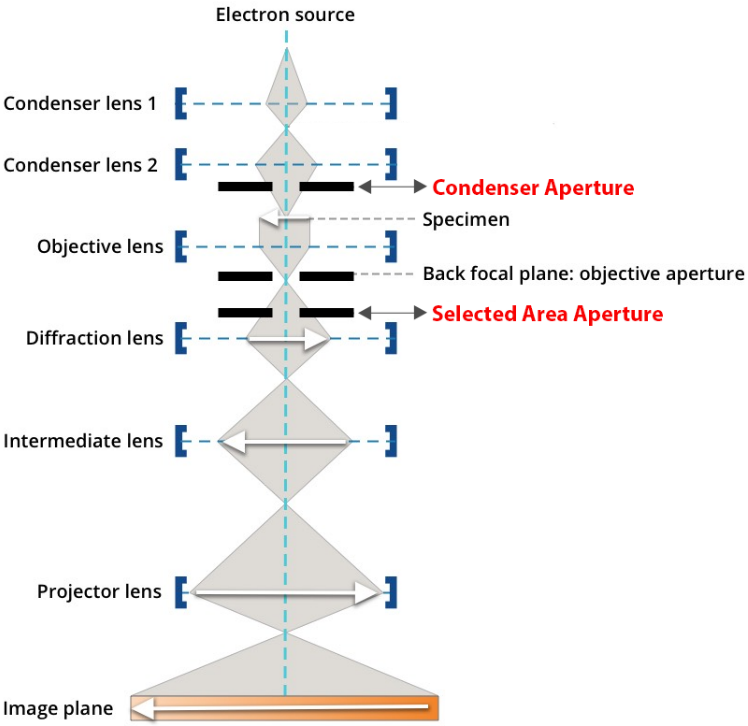

Figure 1.8: Illustration of the TEM optical system highlighting the locations of the CA, used in NBED and the SAA, used in SAED.

1.2.5.3 TEM vs Scanning Transmission Electron Microscope (STEM)

3D-ED can be performed while the TEM is collecting images either in standard TEM mode or in STEM mode instead.

In TEM mode, performing 3D-ED is much easier due to the naturally parallel electron beam. The choice of diffraction mode, such as SAED or NBED, depends on the specific requirements of the experiment and the capabilities of the TEM.

In a two-condenser lens system, where the beam sizes capable of achieving parallel illumination are limited, SAED is commonly used by selecting a condenser aperture that produces a beam size approximately matching the field of view, followed by the insertion of the SAA to isolate diffraction from a specific crystal.

NBED can also be employed in TEM systems with mechanisms that allow efficient switching between condenser apertures, such as motorized aperture systems or illumination systems capable of easily transitioning between different aperture sizes without altering the alignment of the TEM. A detailed explanation of such illumination systems, along with a visual illustration, will be provided in the next chapter (**Chapter 2.4.2.2**), as shown in Figure 2.5.

In STEM mode, the C3 (or C2 in a two condenser system) lens current is adjusted so that the beam crossover occurs at the sample, resulting in a highly focused, nanometer sized beam. A scanning system is employed to raster the beam over a defined region of the TEM grid, offering significant advantages, particularly in spatial resolution. While the focused, convergent beam is commonly used for techniques such as Convergent Beam Electron Diffraction (CBED), a parallel beam is instead necessary for 3D-ED experiments.

Many microscopes provide the capability to relax the strength of the C3 (or C2 in a two condenser system) lens, enabling the formation of a parallel beam while preserving the scanning functionality for locating regions of interest. Once the area of interest is identified, the beam is fixed on the crystal for data acquisition. Diffraction data in STEM mode are typically collected using the NBED approach.

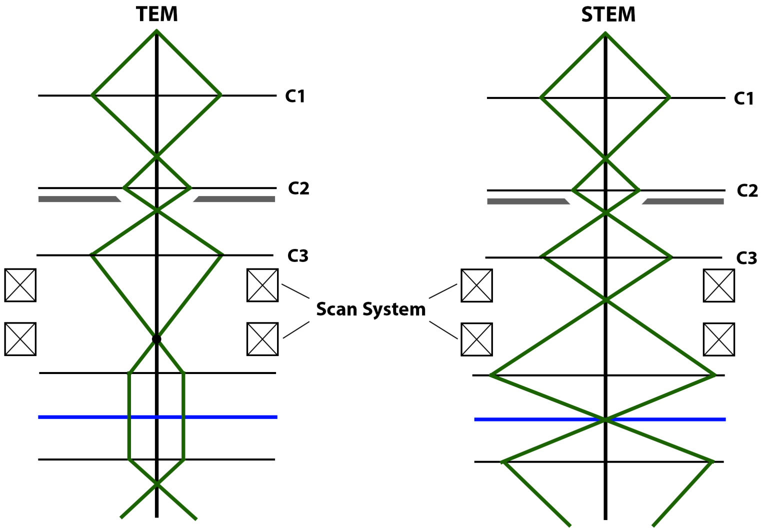

Figure 1.9: Comparison of beam paths in TEM and STEM modes.

1.2.6 Approaches to 3D Electron Diffraction Data Collection

In the early days of electron diffraction, data collection was often performed by recording oriented patterns along specific zone axes. While structure solution was possible with this approach, it was significantly limited. Modern electron diffraction methods have evolved to involve tilting the crystal through a range of angles [2], typically ±60°, depending on the TEM and the holder being used. Over the years, various methods have been developed for the acquisition of 3D-ED data. These methods can be implemented in both SAED and NBED modes, whether operating in TEM or STEM configurations. Despite their differences in implementation, the fundamental goal remains the same: to sample the reciprocal space as much as possible.

1.2.6.0.1 Stepwise Electron Diffraction Tomography (EDT)

Stepwise EDT was first introduced by Kolb et al [2]. In this approach, the crystal is tilted incrementally by fixed angles, typically between 1° and 2°, with a diffraction pattern recorded at each tilt step. This generates a series of discrete snapshots in reciprocal space, which can be combined to determine the unit cell and solve the crystal structure. However, because the data are collected at specific intervals, the recorded intensities are not fully integrated, which can affect their accuracy. Despite this limitation, stepwise EDT is a simple and systematic method that can be implemented in any TEM.

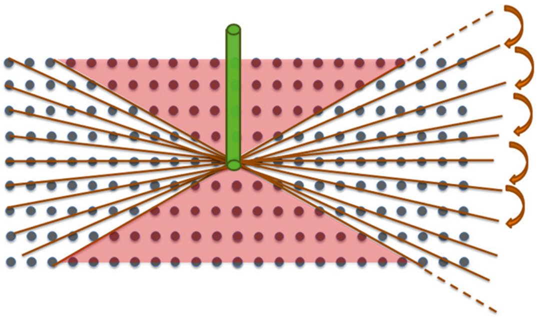

Figure 1.10: Sketch of reciprocal space sampling using Stepwise ADT. [1]

1.2.6.0.2 Stepwise Precession-Assisted Electron Diffraction Tomography (PEDT)

Precession Electron Diffraction Tomography (PEDT) builds on the stepwise approach by introducing a conical precession of the electron beam, originally invented by Vincent and Midgley in 1994 [28] for collecting quasi-kinematical zone axis patterns. Proposed for the first time by Mugnaioli et al. [29] as a way for integrating the reciprocal space in an EDT experiment, this method involves tilting the crystal incrementally, as in stepwise EDT, but at each tilt step, the beam is precessed conically around the crystal. This stepwise precession improves the sampling of reciprocal space and enables the integration of reflections during data collection, resulting in more reliable intensity measurements. The method requires a dedicated instrument capable of precessing the beam and this usually achieved with external devices such as the Spinningstar or the Digistar P1000 produced by Nanomegas which take control of some of the lens of the TEM.

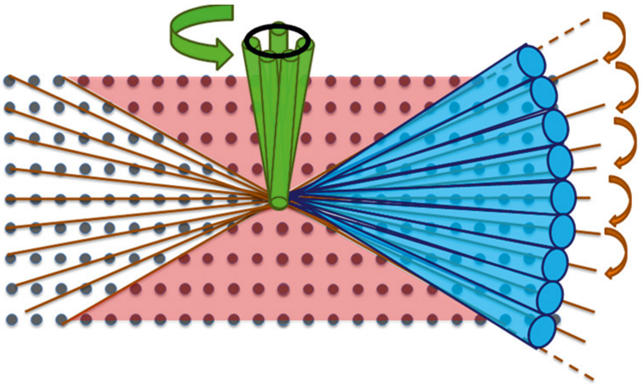

Figure 1.11: Sketch of reciprocal space sampling using PEDT. Blue regions show the sampled portion of reciprocal space. [1]

1.2.6.0.3 Stepwise Rotation Electron Diffraction (RED)

RED, proposed by Zhang et al. [30], is a stepwise approach that combines large mechanical tilts (typically 2–3°) with fine beam tilt steps controlled by the TEM's deflection coils. These fine tilts reduce the angular step size to less than 0.1°, enabling more uniform coverage of reciprocal space compared to the original stepwise method. RED was particularly valuable as an alternative for users who lacked access to instruments equipped for precession.

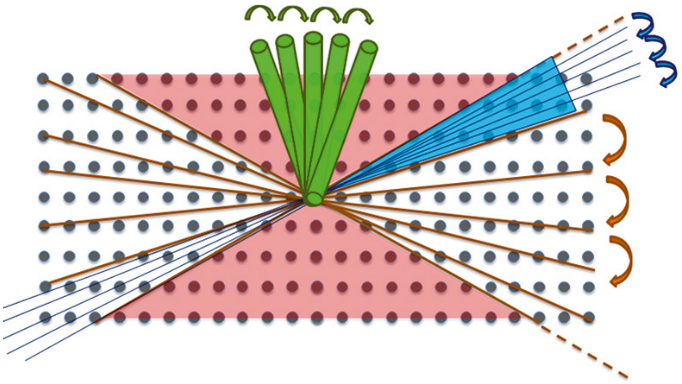

Figure 1.12: Sketch of reciprocal space sampling using RED. Blue regions show the sampled portion of reciprocal space. [1]

1.2.6.0.4 Continuous Rotation Electron Diffraction (cRED)

cRED, also known as Integrated Electron Diffraction Tomography (IEDT) [31] or Microcrystal Electron Diffraction (MicroED) [32], is the most widely utilized technique in 3D electron diffraction. This method involves continuous data acquisition while the goniometer rotates the sample without interruption. Unlike earlier approaches requiring discrete rotation steps, cRED adopts a continuous rotation strategy analogous to the oscillation method employed in single-crystal X-ray diffraction (SCXRD), allowing for a proper integration of the reciprocal space.

cRED relies heavily on the stability of the goniometer, ensuring that the crystal remains within the illuminated area throughout the rotation, and on the speed of the detector, which must be fast enough to keep up with the goniometer rotation speed and low readout time to minimize gaps (missing wedge) in reciprocal space. cRED can be performed in a very short amount of time, significantly reducing the exposure time of the sample to the beam. It is therefore advantageous for structural determination of beam-sensitive materials, such as small organic molecules and proteins.

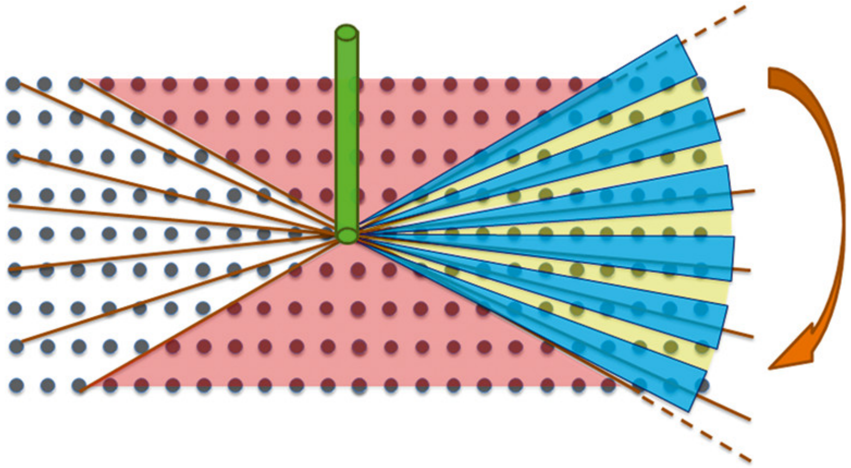

Figure 1.13: Sketch of reciprocal space sampling using cRED. Blue regions show the sampled portion of reciprocal space, while the light-green region represents the area that is unsampled due to the detector's dead time. [1]

1.2.6.0.5 Serial Electron Diffraction (SerialED)

SerialED is an emerging technique in 3D electron diffraction that incorporates principles of serial crystallography. This approach involves collecting single diffraction patterns from a large number of randomly oriented crystals. These patterns can be obtained either through single snapshots of reciprocal space or, preferably, in combination with precession to ensure that each diffraction frame contains integrated intensities.

SerialED is particularly advantageous for studying highly beam-sensitive samples [33, 34]. However, as of today, successful data analysis of SerialED datasets generally requires prior knowledge of the unit cell parameters to facilitate indexing and data merging.

An alternative to this approach is Serial Rotation Electron Diffraction (SerialRED) [35], which involves collecting multiple small-range datasets (5-10 degrees) from different crystals and merging them to achieve comprehensive reciprocal space coverage.

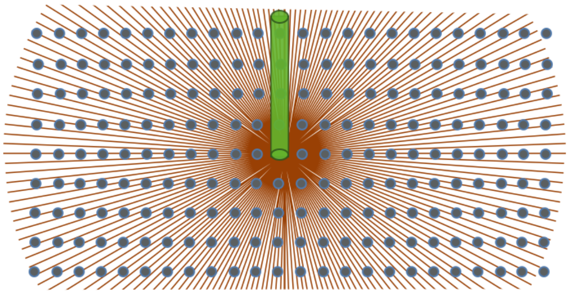

Figure 1.14: Sketch of reciprocal space sampling using SerialED. The brown lines represent the portions of reciprocal space sampled by a single randomly oriented crystal. By combining data from many such crystals, it is possible to sample the entire reciprocal space. If SerialED is performed with precession, each snapshot (brown line) sweeps through a larger area of reciprocal space, resulting in integrated intensities and reducing missing cone effects.

1.2.7 3D-ED Data Analysis: Processing and Refinement

Following the detailed discussion on the requirements and methodologies for collecting 3D-ED data, this subsection covers key aspects of processing such data. To enhance clarity and avoid repetitions throughout the thesis, this subsection will serve as a foundational reference for the data analysis procedures applied in subsequent chapters.

1.2.7.1 Data Processing of 3D-ED Data

Our datasets were primarily processed using `Process Electron Tilt Series (PETS2.0)` [36], `X-ray Detector Software (XDS)` [37, 5], and Diffraction Integration for Advanced Light Sources (DIALS) [38]. `PETS2.0` is specifically designed for 3D-ED data. On the other hand, `XDS`, originally developed for XRD data, can also process cRED data with some modifications within its input file. `DIALS`, an open-source and highly flexible software, was initially created for processing X-ray diffraction data and has since been adapted to handle 3D-ED datasets [39]. A recent publication by Xiaodong Zou's group from Stockholm University provides a detailed overview of using `DIALS` for 3D-ED data processing [40].

We will therefore focus on the workflows for processing 3D-ED data using `XDS` and `PETS2.0`.

1.2.7.1.1 Data Processing with `XDS`

`XDS` [37] handles diffraction data through a modular approach, dividing data reduction into several tasks specified in the `XDS.INP` file. The `XDS.INP` file is the only input file required to run `XDS` and contains all the necessary information to process a dataset. This includes details such as the image data and the format, the geometry, the calibrations and other experimental parameters. The JOB line within this file defines the sequence of tasks, such as *XYCORR*, *INIT*, *COLSPOT*, *IDXREF*, *DEFPIX*, *INTEGRATE*, and *CORRECT*. Each task produces an output file (<TASK>.LP), which serves as the input for the subsequent task.

In the datasets analyzed throughout this thesis, the `XDS.INP` files were automatically generated by the `LibraEDT` software, as detailed in chapter 2.

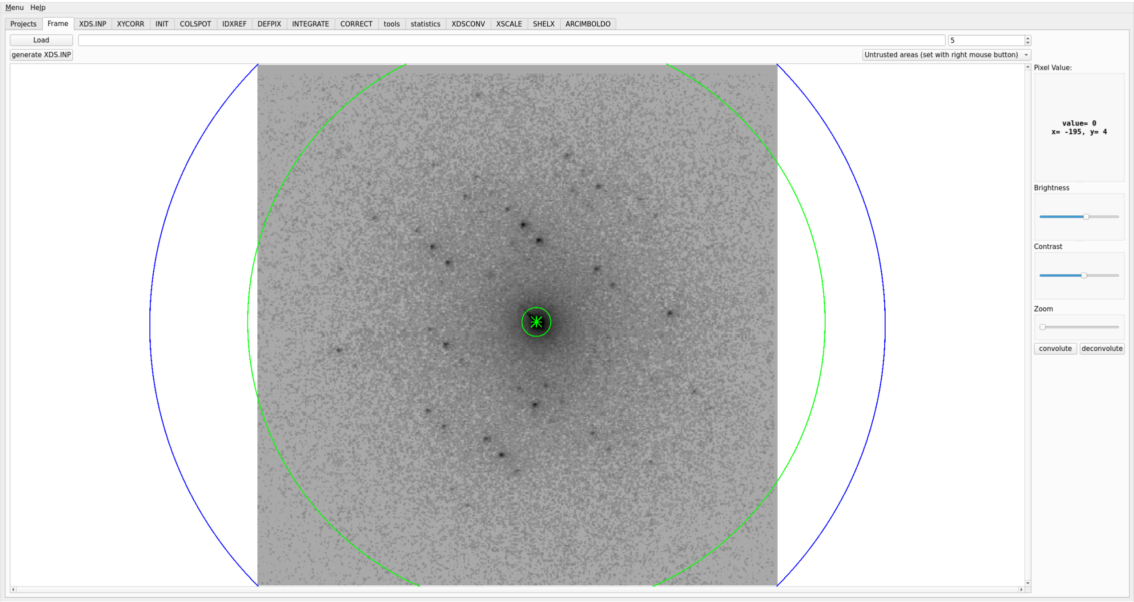

5

Untrusted areas (set with right mouse button)

```
value= 0
x= -195, y= 4
```

Figure 1.15: `XDSGUI` [5] Interface for processing of ED data using `XDS`.

The first tasks in `XDS` are *XYCORR* and *INIT*. The *XYCORR* task generates lookup tables that apply spatial corrections to detector pixel positions, ensuring their accurate mapping into the laboratory coordinate system. These corrections can be particularly relevant when distortions are present, especially in high-symmetry space groups. Meanwhile, the *INIT* task produces background noise and pixel gain maps, along with initial estimates of the background at each pixel, which are essential for distinguishing between background and signal pixels in subsequent steps.

The next steps include *COLSPOT* and *IDXREF*. The *COLSPOT* task identifies strong diffraction spots in the images and stores their centroids, which are then read by *IDXREF* to determine the crystal lattice parameters and orientation. While `XDS` can attempt to guess the symmetry, it is often necessary to manually select a unit cell from the proposed list and assign a space group, making sure that the Laue class is correct, before re-running the *IDXREF* task.

```
A lattice character is marked "*" to indicate a lattice consistent with the
observed locations of the diffraction spots. These marked lattices must have
low values for the QUALITY OF FIT and their implicated UNIT CELL CONSTANTS
should not violate the ideal values by more than
MAXIMUM_ALLOWED_CELL_AXIS_RELATIVE_ERROR=  0.03
MAXIMUM_ALLOWED_CELL_ANGLE_ERROR=           2.0 (Degrees)

 LATTICE-  BRAVAIS-   QUALITY  UNIT CELL CONSTANTS (ANGSTROEM & DEGREES)
CHARACTER  LATTICE     OF FIT      a      b      c   alpha  beta gamma

*  44        aP          0.0      15.2   15.5   24.7  90.2  90.8  90.1
*  31        aP          0.8      15.2   15.5   24.7  89.8  89.2  90.1
*  33        mP          4.1      15.2   15.5   24.7  90.2  90.8  90.1
*  35        mP         12.7      15.5   15.2   24.7  90.8  90.2  90.1
*  34        mP         15.2      15.2   24.7   15.5  90.2  90.1  90.8
*  32        oP         16.0      15.2   15.5   24.7  90.2  90.8  90.1
*  14        mC         25.8      21.7   21.7   24.7  89.6  90.8  89.0
*  10        mC         26.6      21.7   21.7   24.7  90.4  90.8  91.0
*  13        oC         32.3      21.7   21.7   24.7  89.6  90.8  89.0
*  11        tP         33.1      15.2   15.5   24.7  90.2  90.8  90.1
   37        mC        238.9      51.5   15.2   15.5  90.1  90.2  73.6
   36        oC        242.2      15.2   51.5   15.5  89.8  90.1 106.4
   28        mC        242.6      15.2   51.5   15.5  89.8  89.9  73.6
   29        mC        254.4      15.2   34.6   24.7  90.2  90.8  63.7
   41        mC        256.0      51.5   15.2   15.5  90.1  90.2  73.6
```

Figure 1.16: Output from the *IDXREF* task in `XDS` showing possible lattice solutions, their quality of fit, and corresponding unit cell parameters.

The final stages of data processing are handled by *DEFPIX*, *INTEGRATE* and *CORRECT*. *DEFPIX* is responsible for masking invalid regions of the detector, such as shadows or unexposed areas, making sure that only reliable data are included for the intensity extraction. The *INTEGRATE* task then calculates the intensities of the reflections and outputs them in the `INTEGRATE.HKL` file. Finally, the *CORRECT* task performs scaling of the integrated intensities, rejects outliers, computes statistical parameters, and produces the final reflection data file, `XDS_ASCII.HKL`. Among the statistics reported are the completeness of the data, the I/σ, and the $CC_{1/2}$ values for each resolution shell.

The $CC_{1/2}$, introduced by Andrew Karplus and Kay Diederichs [41], provides a reliable criterion for selecting a high-resolution cutoff. To compute this metric, the unmerged experimental data are split into two random halves, each containing independent measurements of the same reflections. The Pearson Correlation Coefficient (CC) is then calculated between the average intensities of the two subsets. At low resolution, the $CC_{1/2}$ value is typically close to 100% and gradually decreases, approaching 0% as the resolution limit of the data is reached [41, 42].

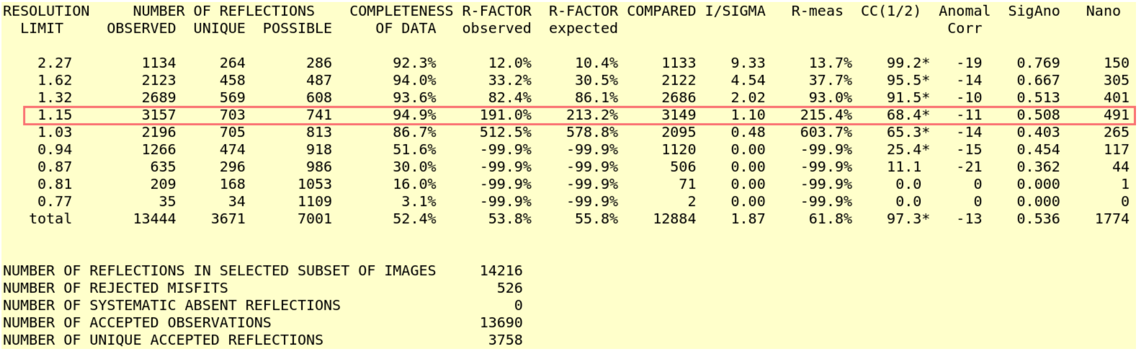

```
RESOLUTION     NUMBER OF REFLECTIONS    COMPLETENESS R-FACTOR  R-FACTOR COMPARED I/SIGMA   R-meas  CC(1/2)  Anomal  SigAno   Nano
  LIMIT     OBSERVED  UNIQUE  POSSIBLE     OF DATA   observed  expected                                      Corr

    2.27        1134     264       286       92.3%      12.0%     10.4%     1133    9.33     13.7%    99.2*   -19    0.769     150
    1.62        2123     458       487       94.0%      33.2%     30.5%     2122    4.54     37.7%    95.5*   -14    0.667     305
    1.32        2689     569       608       93.6%      82.4%     86.1%     2686    2.02     93.0%    91.5*   -10    0.513     401
    1.15        3157     703       741       94.9%     191.0%    213.2%     3149    1.10    215.4%    68.4*   -11    0.508     491
    1.03        2196     705       813       86.7%     512.5%    578.8%     2095    0.48    603.7%    65.3*   -14    0.403     265
    0.94        1266     474       918       51.6%     -99.9%    -99.9%     1120    0.00    -99.9%    25.4*   -15    0.454     117
    0.87         635     296       986       30.0%     -99.9%    -99.9%      506    0.00    -99.9%    11.1    -21    0.362      44
    0.81         209     168      1053       16.0%     -99.9%    -99.9%       71    0.00    -99.9%     0.0      0    0.000       1
    0.77          35      34      1109        3.1%     -99.9%    -99.9%        2    0.00    -99.9%     0.0      0    0.000       0
   total       13444    3671      7001       52.4%      53.8%     55.8%    12884    1.87     61.8%    97.3*   -13    0.536    1774


NUMBER OF REFLECTIONS IN SELECTED SUBSET OF IMAGES     14216
NUMBER OF REJECTED MISFITS                               526
NUMBER OF SYSTEMATIC ABSENT REFLECTIONS                    0
NUMBER OF ACCEPTED OBSERVATIONS                        13690
NUMBER OF UNIQUE ACCEPTED REFLECTIONS                   3758
```

Figure 1.17: Statistics from the *CORRECT* task in `XDS`, showing relevant metrics. The red box indicates the resolution shell where $CC_{1/2}$ falls below 70%.

`XDS` suggests resolution shells to retain based on $CC_{1/2}$ values. For the datasets processed in this thesis, resolution shells with $CC_{1/2}$ values of approximately 70% or higher were generally retained.

Once the resolution limit is determined, the `XDS.INP` file can be updated, and the *CORRECT* task re-run to finalize the data processing.

1.2.7.1.2 Data Processing with `PETS2.0`

PETS2.0 utilizes an input file with the extension `.pts2`, which contains critical information regarding image data location, calibration, experimental geometry, and detector parameters. These parameters include settings for noise estimation, which are used for calculating sigma values during processing.

However, most parameters can also be adjusted directly through the GUI. For example, users can specify the data collection method, such as cRED, PEDT, or stepwise EDT, and define the upper and lower resolution limits for peak search and integration. The detector parameters and calibration settings can also be refined within the GUI to optimize data processing.

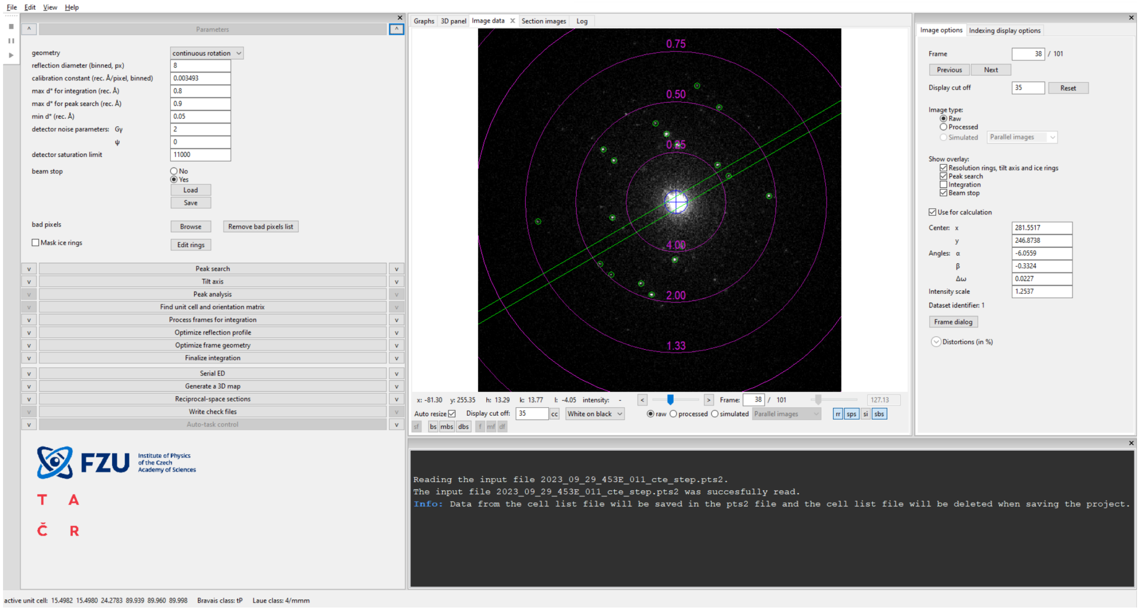

geometry: continuous rotation
reflection diameter (binned, px): 8
calibration constant (rec. Å/pixel, binned): 0.003493
max d* for integration (rec. Å): 0.8
max d* for peak search (rec. Å): 0.9
min d* (rec. Å): 0.05
detector noise parameters: Gγ 2
ψ 0
detector saturation limit: 11000
beam stop: ○ No ● Yes
bad pixels
☐ Mask ice rings

x: -81.30 y: 255.35 h: 13.29 k: 13.77 l: -4.05 intensity: -
Frame: 38 / 101 127.13
Auto resize ☑ Display cut off: 35 White on black
● raw ○ processed ○ simulated Parallel images

Frame 38 / 101
Display cut off 35
Image type:
● Raw
○ Processed
○ Simulated Parallel images
Show overlay:
☑ Resolution rings, tilt axis and ice rings
☑ Peak search
☐ Integration
☑ Beam stop
☑ Use for calculation
Center: x 281.5517
y 246.8738
Angles: α -6.0559
β -0.3324
Δω 0.0227
Intensity scale 1.2537
Dataset identifier: 1

```
Reading the input file 2023_09_29_453E_011_cte_step.pts2.
The input file 2023_09_29_453E_011_cte_step.pts2 was succesfully read.
Info: Data from the cell list file will be saved in the pts2 file and the cell list file will be deleted when saving the project.
```

active unit cell: 15.4982 15.4980 24.2783 89.939 89.960 89.998 Bravais class: tP Laue class: 4/mmm

Figure 1.18: `PETS2.0`'s Graphical User Interface

Once the parameters have been defined, the first step is typically the *Peak Search*, followed by *Tilt Axis Refinement*. The peak search identifies local maxima based on a specified I/σ threshold and determines the central beam position.

Subsequently, the ω angle, which represents the projection of the tilt axis on the diffraction images, is refined. This parameter is influenced by camera length and focusing conditions, and can slightly vary from one dataset to another.

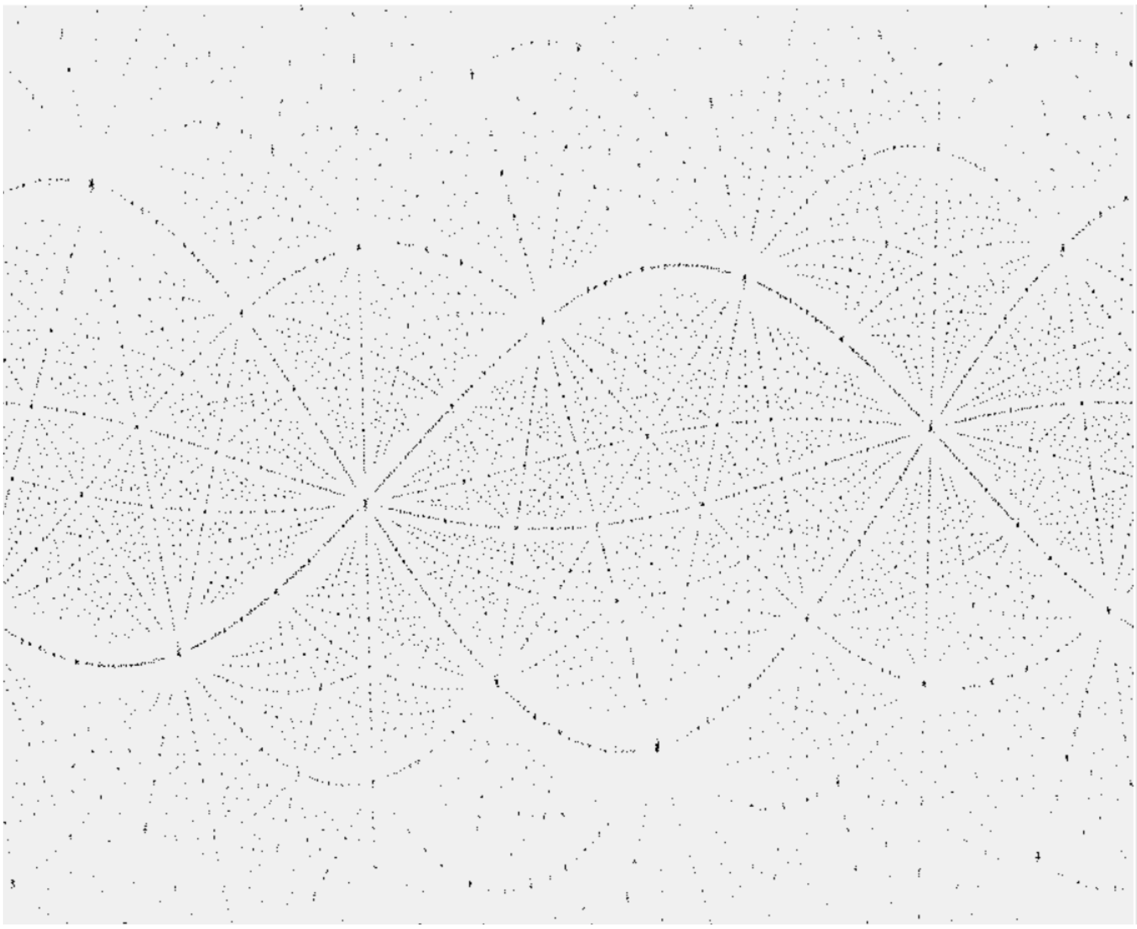

Figure 1.19: Cylindrical projection of all the detected peaks. If the ω angle is properly refined, the projection should look clear.

The *Peak Analysis* task in `PETS2.0` refines the reflections by clustering the peaks identified in the peak search step. It begins by analyzing the distance distribution between peaks in the image plane, followed by an auto-convolution of the diffraction pattern, where groups of peaks in the auto-convolution are replaced by their cluster centers. This process generates additional peak lists, including `xyz`, `clust`, and `diff` files, while the raw peak distribution remains in the `.cor` file.

These files are subsequently used in the next task, *Find Unit Cell and Orientation Matrix*, where the unit cell parameters and the orientation matrix can be determined and refined. During this step, the distortions present in the 3D-ED data can also be refined [43].

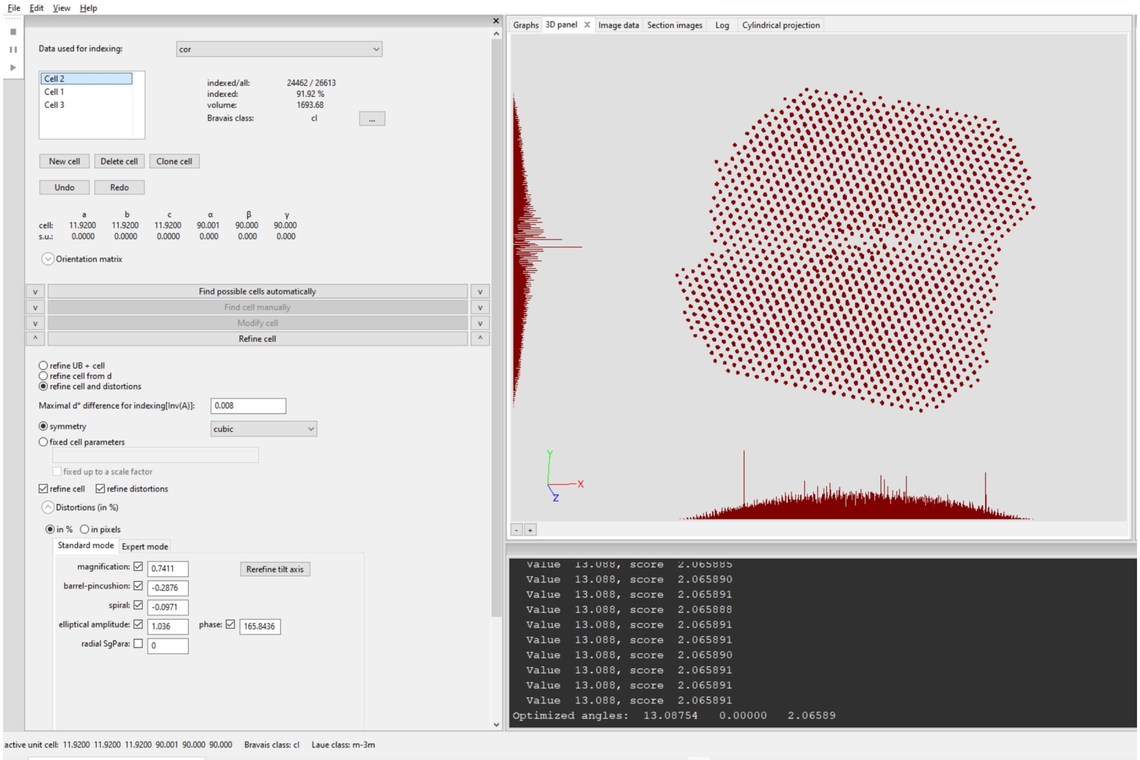

Data used for indexing: cor

Cell 2
Cell 1
Cell 3

indexed/all: 24462 / 26613
indexed: 91.92 %
volume: 1693.68
Bravais class: cI

	a	b	c	α	β	γ
cell:	11.9200	11.9200	11.9200	90.001	90.000	90.000
s.u.:	0.0000	0.0000	0.0000	0.000	0.000	0.000

Orientation matrix

○ refine UB + cell
○ refine cell from d
● refine cell and distortions

Maximal d* difference for indexing[Inv(A)]: 0.008

● symmetry cubic
○ fixed cell parameters

☐ fixed up to a scale factor

☑ refine cell ☑ refine distortions

Distortions (in %)

● in % ○ in pixels

magnification: ☑ 0.7411
barrel-pincushion: ☑ -0.2876
spiral: ☑ -0.0971
elliptical amplitude: ☑ 1.036 phase: ☑ 165.8436
radial SgPara: ☐ 0

```
  Value  13.088, score  2.065885
  Value  13.088, score  2.065890
  Value  13.088, score  2.065891
  Value  13.088, score  2.065888
  Value  13.088, score  2.065891
  Value  13.088, score  2.065891
  Value  13.088, score  2.065890
  Value  13.088, score  2.065891
  Value  13.088, score  2.065891
  Value  13.088, score  2.065891
Optimized angles:  13.08754   0.00000   2.06589
```

active unit cell: 11.9200 11.9200 11.9200 90.001 90.000 90.000 Bravais class: cI Laue class: m-3m

Figure 1.20: Unit Cell and Orientation Matrix determination in `PETS2.0`

Once the unit cell parameters and orientation matrix have been determined, the next step is the *Process Frames for Integration* for the integration of reflections, which can be performed using either sum counts or profile fitting. During this step, the position of each reflection is predicted based on the previously determined orientation matrix, the orientation of the collected diffraction patterns and a starting mosaicity value, which will be later refined. `PETS2.0` integrates all these reflections (see Figure 1.21) and generates the rocking curve, also known as camel plot, which represents the recorded intensity of the reflection as a function of the excitation error (S_g). It is important to note that the shape of the camel plot depends strongly on the geometry of the experiment. For instance, in the case of cRED data, the profile typically appears as a Gaussian-like curve, centered around $S_g = 0$. The intensity of the reflections increases as they approach the Bragg condition and decreases as they move away from it. In contrast, when collecting PEDT data, the rocking curve contains two maxima at nonzero S_g that are symmetric around $S_g = 0$, proportional to the precession angle. These maxima occur because, at those precession tilt angles, the reflections intersect the Ewald sphere for a longer period of time due to the precession geometry, leading to a higher intensity. The different type of camel plots are illustrated in Figure 1.22.

The rocking curve profile is subsequently used in the *Optimize Reflection Profile* step to refine the apparent mosaicity which describes the broadening of the rocking curve and the reflection width which characterizes the basic Lorentzian shape of the reflection [36]. Following this refinement, the *Process Frames for Integration* task is re-run to ensure improved accuracy in the integration of reflection intensities.

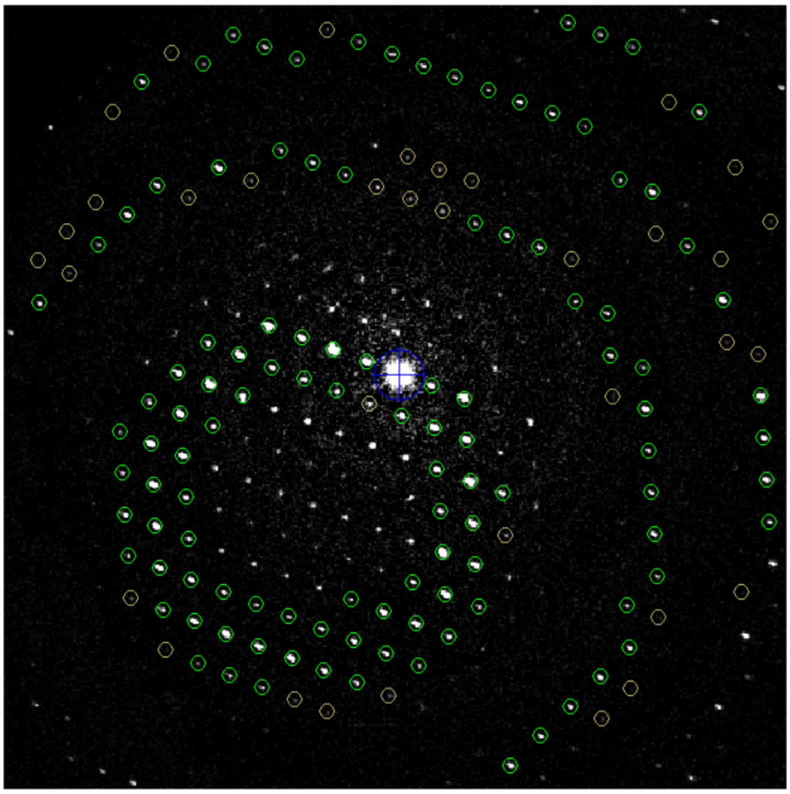

Figure 1.21: All the circles (color yellow by default) are predicted reflections positions based on orientation matrix, frame orientation and mosaicity. The color of these predicted reflections changes to green when $I/\sigma > 3$, often considered as observed reflections.

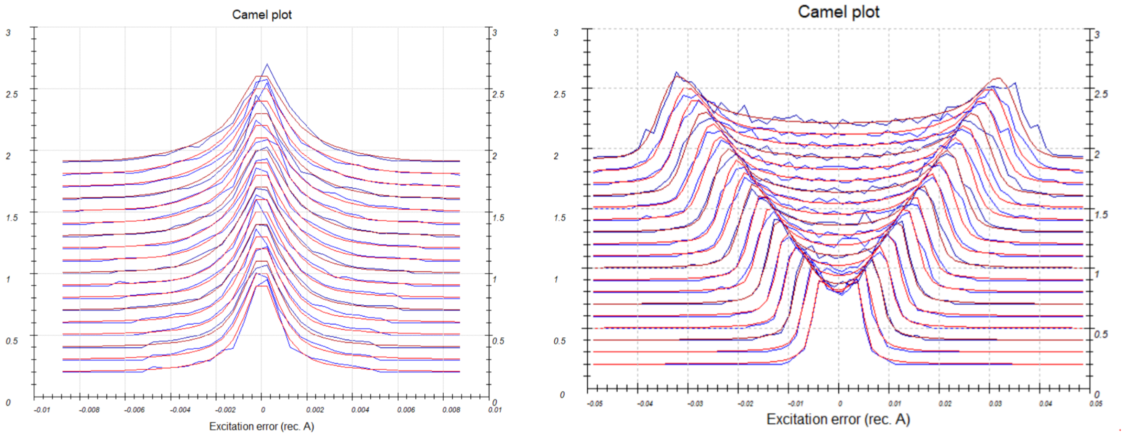

Figure 1.22: Rocking Curve or Camel Plot for cRED (left) and PEDT (right) data.

The final step in the `PETS2.0` workflow is the *Finalize Integration* task, which performs intensity estimation, frame scaling, outlier rejection, and error model refinement based on the specified Laue class [44]. This step generates an `.HKL` file that is used for structure solution and kinematical refinement.

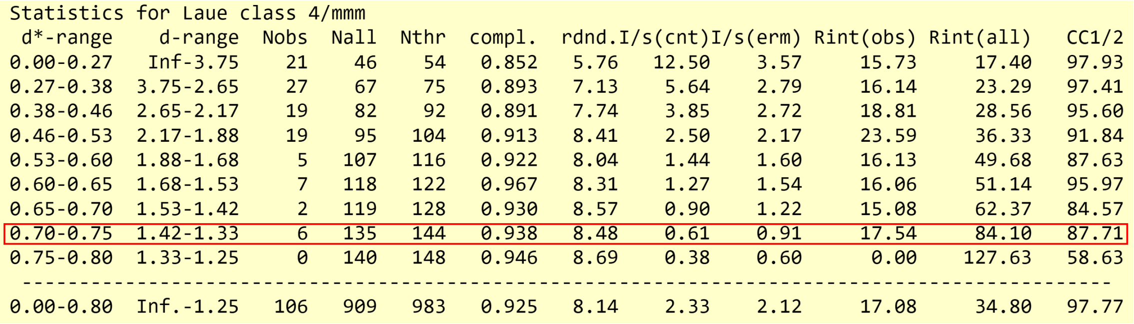

```
Statistics for Laue class 4/mmm
 d*-range    d-range  Nobs  Nall  Nthr  compl.  rdnd.I/s(cnt)I/s(erm) Rint(obs) Rint(all)   CC1/2
0.00-0.27   Inf-3.75    21    46    54   0.852   5.76   12.50    3.57     15.73     17.40   97.93
0.27-0.38  3.75-2.65    27    67    75   0.893   7.13    5.64    2.79     16.14     23.29   97.41
0.38-0.46  2.65-2.17    19    82    92   0.891   7.74    3.85    2.72     18.81     28.56   95.60
0.46-0.53  2.17-1.88    19    95   104   0.913   8.41    2.50    2.17     23.59     36.33   91.84
0.53-0.60  1.88-1.68     5   107   116   0.922   8.04    1.44    1.60     16.13     49.68   87.63
0.60-0.65  1.68-1.53     7   118   122   0.967   8.31    1.27    1.54     16.06     51.14   95.97
0.65-0.70  1.53-1.42     2   119   128   0.930   8.57    0.90    1.22     15.08     62.37   84.57
0.70-0.75  1.42-1.33     6   135   144   0.938   8.48    0.61    0.91     17.54     84.10   87.71
0.75-0.80  1.33-1.25     0   140   148   0.946   8.69    0.38    0.60      0.00    127.63   58.63
 ------------------------------------------------------------------------------------------------
0.00-0.80  Inf.-1.25   106   909   983   0.925   8.14    2.33    2.12     17.08     34.80   97.77
```

Figure 1.23: Statistics from the finalize integration task in `PETS2.0`, showing relevant metrics. The red box indicates the resolution shell where the $CC_{1/2}$ falls below 70%.

A recent version of `PETS2.0` introduced the implementation of the $CC_{1/2}$ metric, which is now included alongside other key statistics such as completeness and I/σ (Figure 1.23). Based on the $CC_{1/2}$ values, a high-resolution cut-off can be selected to ensure data quality. After determining the resolution limit, the *Finalize Integration* task is re-run to refine the results further.

Additionally, `PETS2.0` can produce a dedicated file for dynamical refinement. To achieve this, for cRED data, `PETS2.0` creates Overlapping Virtual Frames (OVFs) by grouping together multiple frames. The angular range covered by each virtual frame must be large enough to ensure all the reflections within the frame are fully integrated over the excitation error. Furthermore, sufficient overlap between consecutive virtual frames is essential to ensure that each measured reflection is fully integrated (Figure 1.24). `PETS2.0` can automatically set the number of frames and the number of overlapping frames based on the tilt semi-angle. In the case of PEDT data, where each frame already contains integrated intensities, single frames can be directly treated as virtual frames and used for refinement without additional grouping [36].

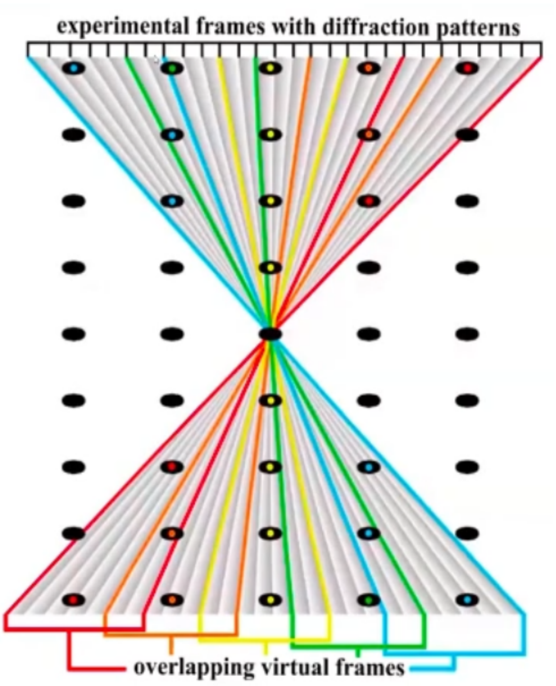

Figure 1.24: Illustration of the concept of OVFs [6]. Each Virtual Frame consists of seven frames, with the last two shared with the subsequent frame.

After completing the previous steps, the optional *Optimize Frame Geometry* task can be used to enhance data quality. This step refines some parameters such as apparent mosaicity, the center of diffraction patterns, distortions, and the angle orientation of frames (Figure 1.25). Refining frame orientation is especially important due to potential instabilities in TEM goniometers, which are not specifically designed for electron diffraction tomography. This task also compensates for issues like a non-flat sample grid or a crystal not laying perfectly flat on the grid.

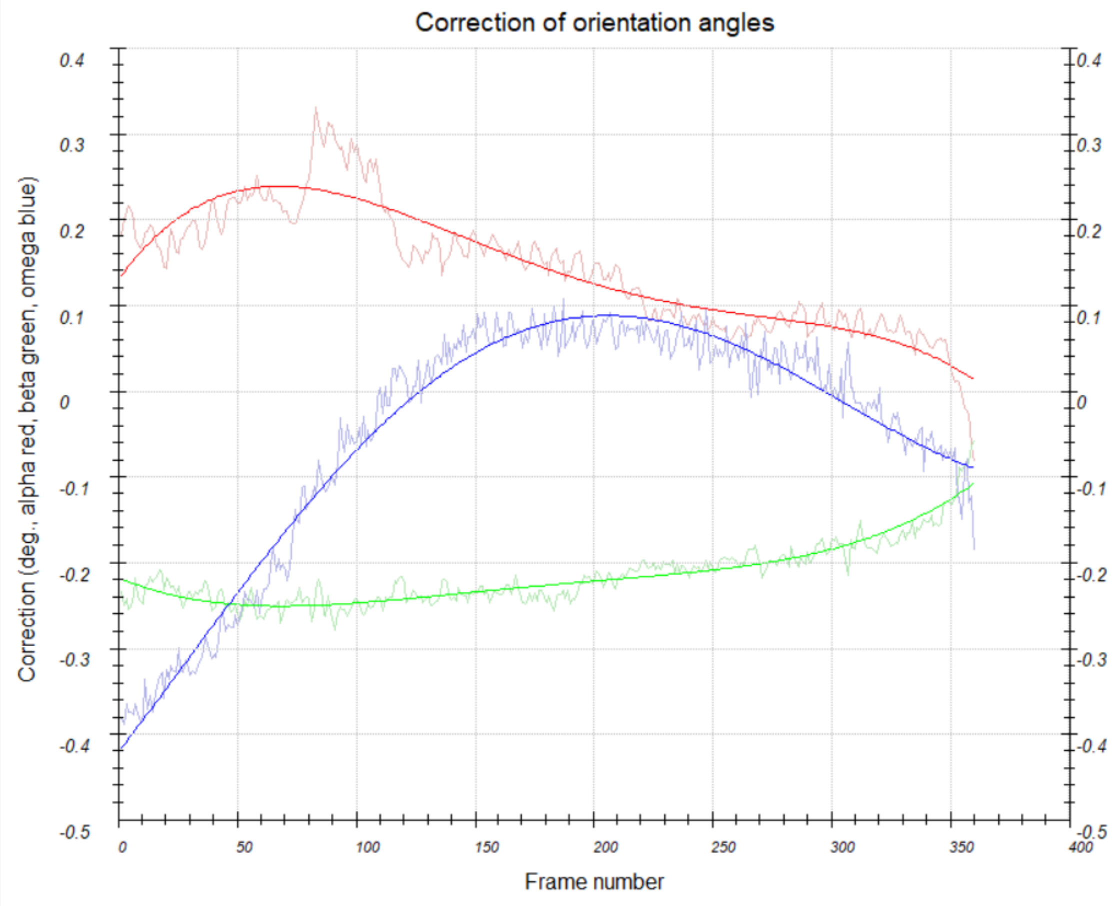

Figure 1.25: Correction of orientation angles across frames. The plot shows the refinement of alpha (α, red), beta (β, green), and omega (ω, blue) angles as a function of the frame number. Smoothed curves represent polynomial fits applied during the optimization process.

After this step, the *Peak Search* task is typically re-run with the updated optimizations, followed by all the subsequent tasks previously described [36].

1.2.7.2 Refinement of 3D-ED Data

Once the 3D-ED data has been processed, the next critical step is solving the crystal structure. The primary tools used for structure solution in this study were

`Superflip` [45] and `SHELXT` [46]. Both `Superflip` and `SHELXT` simplify the structure solution process by implementing algorithms capable of accurately guessing the space group, provided the correct Laue class is specified. A major advantage of these programs is that they do not require prior estimation of the cell content or density, as is common in traditional direct methods [19]. Instead, providing only the elemental composition is sufficient for these algorithms to proceed. This is particularly important for MOFs, whose densities can vary widely due to their high porosity and diverse chemical compositions, making reliable estimations challenging.

If structure solution is successful, the result is an initial model comprising atomic types and their coordinates within the unit cell. To ensure that this model accurately represents the crystal structure, it is essential to refine the parameters of the model by comparing the calculated and experimentally observed intensities.

Refinement is carried out using least squares fitting, which iteratively optimizes the agreement between observed and calculated data. With 3D-ED data, two types of refinement can be performed: kinematical refinement, which assumes single scattering events, and dynamical refinement, which accounts for multiple scattering effects. These methods differ in the objective functions used to minimize the residual sum of squares.

1.2.7.2.1 Least Squares Fitting

Least squares fitting is a fundamental method used to estimate the parameters of a model by minimizing the sum of the squared differences between observed experimental data and the model's predictions. Mathematically, given a set of n data points (x_i, y_i) and a model function $f(x, \mathbf{p})$ parameterized by a vector of parameters $\mathbf{p} = (A, B, C, D, E)$, the objective is to find the parameter values that minimize the residual sum of squares (RSS):

$$\mathrm{RSS}(\mathbf{p}) = \sum_{i=1}^{n} \left[y_i - f(x_i, \mathbf{p})\right]^2 \tag{1.12}$$

For example, consider a trigonometric-quadratic model defined by:

$$f(x,\mathbf{p}) = A\sin(k_1x) + B\cos(k_2x) + Cx^2 + Dx + E \tag{1.13}$$

where $\mathbf{p} = (A, B, C, D, E)$ are the parameters to be determined. Suppose the true parameters of the system are $A = 15.0$, $B = 20.0$, $C = 0.1$, $D = -0.5$, and $E = 1.0$. To simulate experimental measurements, random Gaussian noise is added to the true values, introducing systematic errors. The least squares fitting procedure then adjusts the parameters $\mathbf{p}$ to minimize the RSS, thereby recovering an estimate of the true model.

Table 1.3: Refined Parameters from Least Squares Fitting for Various Numbers of Data Points. The true parameter values are $A = 15.0$, $B = 20.0$, $C = 0.1$, $D = -0.5$, and $E = 1.0$.

Number of Data Points (n)	**Refined A**	**Refined B**	**Refined C**	**Refined D**	**Refined E**
5	-37.16	17.66	0.20	0.60	-48.18
10	7.44	16.37	0.10	-0.13	-0.56
20	15.48	18.48	0.10	-0.44	3.86
100	14.00	21.26	0.10	-0.52	1.43

Table 1.3 presents a comparison between the true parameters and the parameters refined through least squares fitting for datasets with varying numbers of data points. As the number of data points increases, the refined parameters (A, B, C, D, E) converge closer to their true values, as illustrated in Figure 1.26. Least squares fitting is very effective in accurately estimating model parameters, especially as the number of data points relative to the number of parameters increases. In the context of crystallographic refinement, maintaining a sufficient number of data points relative to the number of structural parameters is essential for achieving precise and accurate structural models. However, least squares fitting is highly sensitive to the starting model, making it crucial to have initial parameters that are as close as possible to the true values. The structure solution step aims to generate an initial model with

atomic parameters that closely approximate the true values.

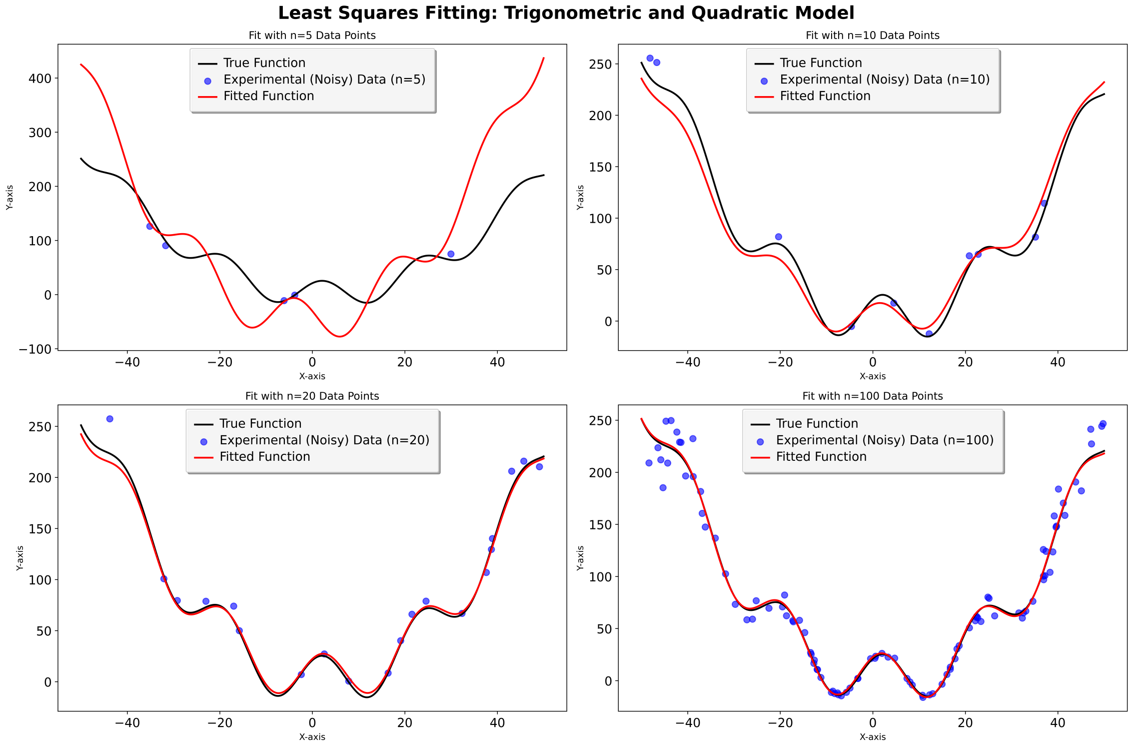

Figure 1.26: Least-Squares Fitting of a Trigonometric-Quadratic Model with Varying Numbers of Data Points. The plot illustrates the true trigonometric-quadratic function (black solid line), noisy experimental data (blue scatter points), and the fitted function (red solid line) for different dataset sizes (n=5,10,20,100).

1.2.7.2.2 Kinematical Refinement of 3D-ED Data

Under the kinematical approximation, it is assumed that each electron undergoes only a single scattering event within the crystal lattice. Consequently, the measured intensity I_{hkl} of a diffraction spot is directly proportional to the square of the structure factor F_{hkl}, as defined in Equation 1.8:

$$I_{hkl} \propto |F_{hkl}|^2 \tag{1.14}$$

The structure factor F_{hkl}, elaborated in Section 1.2.3.1, incorporates both the atomic positions and the thermal vibrations of atoms within the unit cell.

$$F_{hkl} = \sum_{j=1}^{N} O_j f_j \exp\left[2\pi i(hx_j + ky_j + lz_j)\right] \exp\left[-B_j\left(\frac{\sin\theta}{\lambda}\right)^2\right] \tag{1.15}$$

In kinematical refinement, the objective function is the minimization of the weighted RSS between the experimentally measured intensities and the calculated intensities derived from the structure factor equation. The RSS is defined as:

$$\mathrm{RSS}(\mathbf{p}) = wR = \left[\frac{\sum_{m=1}^{M} w_m\left(F_o^2 - F_c^2(\mathbf{p})\right)^2}{\sum_{m=1}^{M} w_m F_o^2}\right]^{1/2} \tag{1.16}$$

where:

- M is the total number of observed reflections.
- F_o^2 are the experimentally observed squared structure factors.
- $F_c^2(\mathbf{p})$ are the calculated squared structure factors based on the current model parameters.
- w_m are the weighting factors, typically derived from the standard uncertainties of the observed reflections, reflecting the confidence in each measurement.

The parameter vector $\mathbf{p}$, as can be seen in Equation 1.16, includes the atomic parameters of each atom in the unit cell, such as the fractional coordinates (x_j, y_j, z_j), the thermal parameter B_j, and the occupancy factor O_j of the j-th atom, as well as the overall scale factor (osf) of the structure. These parameters are adjusted to minimize the weighted RSS, refining the model to achieve the best possible agreement between the observed and calculated intensities.

To evaluate the quality of the refinement, the R_1 factor is commonly used. It quantifies the agreement between the observed and calculated structure factor amplitudes and is defined as:

$$R_1 = \frac{\sum_{j=1}^{N}\left||F_j^{\text{obs}}| - |F_j^{\text{calc}}|\right|}{\sum_{j=1}^{N}|F_j^{\text{obs}}|} \tag{1.17}$$

Kinematical refinement of the 3D-ED data shown in the following chapters was performed using `SHELXL` [47] interfaced in `OLEX2` [48] and `ShelXle` [49]. The process is identical to the refinement of XRD data, with the key difference being the inclusion of electron scattering factors (represented by f_j in the structure factor equation Equation 1.7) and the electron wavelength (λ) in the calculations.

To improve the refinement, restraints and constraints were applied when appropriate, including those for enforcing planarity (*FLAT*), constraining benzene rings to idealized geometry (*AFIX 66*), restraining bond distances (*DFIX*), and restraining Atomic Displacement Parameters (ADPs) of chemically equivalent atoms (*RIGU* and *SIMU*). This not only improves the quality of the refined model but also increases the data-to-parameter ratio by reducing the number of independent parameters to be refined, leading to more robust results.

In cases where it was not possible to model guest molecules in the channels, either due to low resolution of the data or highly disordered molecules, solvent masking within `OLEX2` was employed to exclude these regions from the refinement.

1.2.7.2.3 Dynamical Refinement of 3D-ED Data

Dynamical theory is necessary when multiple scattering events occur within the crystal, rendering the simple kinematical assumption $I_{hkl} \propto |F_{hkl}|^2$ incomplete. In the dynamical theory [50], the electron wavefunction inside the crystal is described by accounting for the fact that each diffracted beam, indexed by a reciprocal lattice vector $\mathbf{g}_i$, can interact and exchange amplitude with the other diffracted beams [36].

A practical way to handle these couplings is by constructing a structure matrix $\mathbf{A}$, with a finite set of reflections $\{\mathbf{g}_1, \dots, \mathbf{g}_N\}$ that contribute most strongly to the scattering. The diagonal elements a_{ii} often include the excitation error $S_{\mathbf{g}_i}$, which measures how close beam $\mathbf{g}_i$ is to satisfying the Bragg condition. The off-diagonal elements a_{ij} $(i \neq j)$ encode the coupling between beams $\mathbf{g}_i$ and $\mathbf{g}_j$ through the Fourier components of the crystal potential, which are proportional to the structure factors $F_{\mathbf{g}_i-\mathbf{g}_j}$. This can be represented as:

$$a_{ii} = 2K\, S_{\mathbf{g}_i}, \quad a_{ij} = U_{\mathbf{g}_i-\mathbf{g}_j},$$

where K is the wave-vector magnitude of the electrons in the crystal, and $U_{\mathbf{g}}$ is related to $F_{\mathbf{g}}$ through a multiplicative constant.

Once the structure matrix $\mathbf{A}$ is defined, the scattering matrix $\mathbf{S}$ is obtained by exponentiating $\mathbf{A}$ multiplied by the crystal thickness t, written as

$$\mathbf{S} \;=\; \exp\Big[\frac{2\pi i}{2K_n}\, t\, \mathbf{A}\Big],$$

where $\mathbf{K_n}$ is the component of the incoming wave vector along the crystal normal. The amplitude scattered into a particular beam $\mathbf{g}$ from the incident beam can be read from the corresponding element of the first column of $\mathbf{S}$. The intensity of that reflection, labeled $\mathbf{g}$, is given by

$$I_{\mathbf{g}}^{\mathrm{dyn}} = \big|\, S_{\mathbf{g}1}\big|^2.$$

Thus, each reflected beam's intensity emerges from the multiple-scattering coupling contained in $\mathbf{A}$ and the crystal thickness t.

The dynamical least-squares refinement is therefore performed by comparing the observed intensities $I_{\mathbf{g}}^{\mathrm{obs}}$ to the calculated intensities $I_{\mathbf{g}}^{\mathrm{dyn}}$. The structural parameters, including the fractional coordinates, thermal parameters, occupancies of each atom and the overall scale factor are still among the parameters to be refined. However, there are additional parameters must also be refined for each OVF created during the data processing step (described in 1.2.7.1.2):

- The *thickness* t of the crystal, which strongly influences $\mathbf{S}$.
- The *orientation* of each diffraction frame, which affects the excitation errors $S_{\mathbf{g}_i}$.

The weighted residual sum of squares (RSS) used to evaluate the agreement between the observed and calculated intensities is defined as:

$$\mathrm{RSS}(\mathbf{p}, t, \boldsymbol{\omega}) = wR = \sqrt{\frac{\sum_{\mathbf{g}} w_{\mathbf{g}} \big(I_{\mathbf{g}}^{\mathrm{obs}} - I_{\mathbf{g}}^{\mathrm{dyn}}(\mathbf{p}, t, \boldsymbol{\omega})\big)^2}{\sum_{\mathbf{g}} (w_{\mathbf{g}} I_{\mathbf{g}}^{\mathrm{obs}})^2}},$$

where $w_{\mathbf{g}}$ are weights related to the uncertainty of the experimental data, $\mathbf{p}$ represents the atomic parameters, t is the thickness of the crystal, and $\boldsymbol{\omega}$ corresponds to the orientation of the crystal during data collection.

At the time of writing, dynamical refinement can only be performed in `JANA2006` [51] and `JANA2020` [52]. There are some additional considerations for setting up a dynamical refinement in `JANA`.

The first one is the Number of Integration Steps (N_{int}), which determines the number of orientations at which the Block-wave calculations are performed for each virtual frame. It controls the sampling density of the calculated rocking curves, which are then integrated to produce the calculated intensities of the contributing reflections [6].

Another one is the resolution limit (g_{max}), which is the maximum reciprocal-space distance for the reflections included in the dynamical calculations. This parameter strongly impacts the computation time, as higher resolution limits increase the number of contributing reflections and the corresponding size of the scattering matrix which must be computed which actually scales with the square of number of reflections. For accurate refinement, $g_{\text{max}}^{\text{BW}}$, the resolution limit used for Bloch-wave calculations, must be equal to or greater than $g_{\text{max}}^{\text{ref}}$, the resolution of the observed reflections used in the refinement.

Finally, there are the reflection filtering options, which is used to exclude partially integrated reflections from the refinement. Only integrated intensities of reflections with a minimum distance D_{Sg} from the limiting Ewald Sphere and a small ratio

$$R_{Sg} = \frac{|Sg|}{D_{Sg} + |Sg|}$$

are considered for the refinement.

A useful consequence of dynamical effects in electron diffraction is the breaking of Friedel's law in case of non centrosymmetrical structures, which states that the intensities of reflections related by inversion in reciprocal space are equal, $I_{hkl} = I_{\overline{hkl}}$. Under kinematical scattering conditions, where only single scattering events are

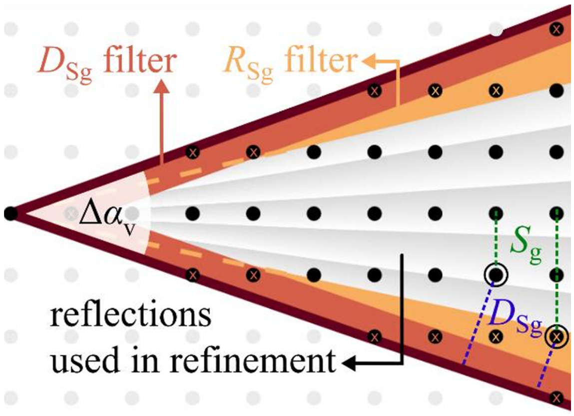

Figure 1.27: Effect of Dsg and Rsg filtering with the excluded reflections marked as x. Excitation error (Sg) and Dsg are shown for two (encircled) reflections. [6]

considered, Friedel's law holds true, making it impossible to distinguish between enantiomers or determine the absolute structure of chiral crystals.

In contrast, dynamical scattering introduces measurable differences between Friedel pairs due to multiple scattering events within the crystal [36, 27]. This asymmetry is directly influenced by the handedness of the crystal structure, allowing for the unambiguous determination of absolute configurations without the need for additional techniques, such as anomalous X-ray scattering [53, 54]. As such, dynamical refinement provides a critical advantage for the accurate characterization of chiral materials [6].

1.3 Conclusions

This chapter has introduced the fundamental principles and methodologies of 3D Electron Diffraction, emphasizing its potential for elucidating the structures of nanocrystalline materials. We have discussed the limitations of conventional diffraction techniques and highlighted how 3D-ED, with its modern approaches, overcomes these challenges. This foundation establishes the basis for the following chapters, which explore specific applications and advancements in 3D-ED to address a diverse range of crystallographic problems.

Chapter 2 presents a software tool to automate data acquisition, enabling the efficient use of the TEM as an electron diffractometer. By the end of this chapter, all the foundational concepts and methodologies required to begin acquiring data and solving crystal structures will have been comprehensively covered. Starting from **Chapter 3**, the focus shifts to the structural determination and dynamical refinement of a nanocrystalline MOF synthesized via mechanochemistry. In **Chapter 4**, we demonstrate the application of 3D-ED to determine the absolute structure of a nanocrystalline chiral MOF. **Chapter 5** investigates a family of heterometallic MOFs using 3D-ED.

Chapter 6 addresses the challenges of sample preparation and 3D-ED analysis of flexible and breathing MOFs, showing the adaptability of 3D-ED in studying dynamic materials. Finally, **Chapter 7** introduces SerialED, a comprehensive workflow from data acquisition to structure solution, demonstrating its effectiveness in handling beam-sensitive. All the crystal structures analyzed in this thesis are novel and previously unreported. Furthermore, all the structures solved by 3D-ED were later validated using PXRD, demonstrating the complementary nature of these techniques.

Chapter 2

`LibraEDT` Software for Electron Diffraction Data Acquisition

2.1 Introduction

The implementation of 3D-ED on TEMs has transformed nanoscale crystallography, enabling for the determination of atomic structures from extremely small crystals. However, exploiting the full potential of 3D-ED requires overcoming challenges inherent to the design of TEMs. Originally intended for imaging, TEMs lack the precision, stability, and automation needed for high-throughput diffraction experiments. As a result, using TEMs for 3D-ED is often limited to advanced users with specialized expertise, making the technique less accessible to the broader scientific community.

To overcome these challenges, this chapter introduces `LibraEDT`, a software designed to adapt the TEM into a fully functional platform for 3D-ED experiments. By addressing the technical demands of diffraction workflows, this software ensures precise beam control, stable sample positioning, and efficient data acquisition, all while minimizing manual intervention.

2.2 Motivation for Developing `LibraEDT`

2.2.1 Challenges in 3D Electron Diffraction

The development of `LibraEDT` was driven by the need to overcome specific difficulties associated with 3D electron diffraction, especially in the context of beam-sensitive nanocrystalline materials.

One of the primary concerns in 3D-ED is maintaining the crystal's position within the electron beam during continuous rotation. In electron microscopy, even slight instability in the goniometer or stage can lead to the crystal drifting out of the illuminated area, resulting in incomplete data collection and potential loss of critical structural information. This issue is particularly problematic for beam-sensitive materials, where prolonged exposure to the electron beam can cause significant radiation damage, compromising the quality of the data.

Additionally, 3D-ED experiments require careful tuning of the goniometer's rotation speed and the detector's exposure time to optimize data collections. Slow rotation speed can result in prolonged exposure to the electron beam, increasing the risk of radiation damage. Similarly, incorrect exposure time settings can either result in insufficient signal if too short or lead to overexposure and loss of detail if too long. This process is further complicated by the typical setup in which the detector is connected to a secondary computer that is isolated from the TEM's main control system. This means that adjusting exposure times or visualizing images from the detector must be done on this separate system, adding an extra layer of coordination and potential for error in the experimental workflow.

Moreover, working in low-dose mode requires precise adjustments to the microscope's lens configurations, which are crucial for minimizing radiation damage while still maintaining high-quality diffraction patterns. Frequent adjustments to the lenses, along with the need to maintain consistency across experiments, can be challenging and prone to errors, especially when these changes are made manually. Using the TEM's graphical user interface for these operations often requires significant expertise, making it difficult to get consistent and efficient results across multiple datasets. These difficulties highlight the need for a system that can simplify these processes and provide precise control over all experimental conditions.

Another major concern is the management and organization of the large volumes of data generated during 3D-ED experiments. These experiments can produce extensive datasets rapidly, particularly when analyzing multiple nanocrystals or low-symmetry systems that require merging data from various crystal orientations to achieve high completeness. Manually organizing these datasets and systematically tracking experimental conditions is both time-consuming and susceptible to errors, complicating efficient data processing and analysis.

2.2.2 The Need for Automation and Precision

Given the difficulties mentioned in the previous subsection, it became clear that an automated system was essential to achieve the accuracy, consistency and efficiency needed for high-quality 3D-ED data collection. Automation reduces the dependence on manual adjustments, which helps minimize the chance of human error and makes it easier to get consistent and reproducible results across multiple datasets. Moreover, automation allows for efficient handling of large amounts of data, ensuring that the files are organized and prepared for processing with the preferred data analysis tools.

In response to these needs, `LibraEDT` was developed and designed to automate the key aspects of 3D-ED experiments.

2.3 Design and Architecture of `LibraEDT`

2.3.1 Overview of Software Architecture

The design of `LibraEDT` is based on a modular architecture, which was necessary due to the separate installation of the TEM and the ASI Timepix Hybrid Pixel Detector. On one side, the TEM, equipped with an omega filter, is connected to and controlled by a main computer running Windows 7, which manages all microscope-related operations such as stage control, beam alignment, and lens configurations. On the other side, the ASI Timepix detector is connected to a secondary computer running Ubuntu Linux, responsible for data acquisition from the detector. This separation required the development of two different modules: the Server Module and the Client Module. Each module is designed to control and communicate with specific hardware components, ensuring efficient and reliable operation during 3D-ED experiments.

The Server Module, implemented in Python, operates on the secondary computer directly connected to the ASI Timepix Detector. Its primary function is to manage data acquisition by processing requests from the Client Module, such as adjusting exposure times and acquiring single or multiple frames. To execute these commands, the Server Module loads and uses a custom C++ library specifically designed to initialize and control the detector. Running these tasks on the secondary computer reduces drastically the load on the main TEM computer, improving therefore the system's responsiveness.

To the best of our knowledge, this implementation represents the first publicly available server specifically developed for the ASI Timepix1 detector. While newer versions of the detector, such as the Timepix3 and Medipix3, are equipped with built-in server capabilities and a toolkit known as `Serval`, which allows similar control and manipulation of the detector, the original Timepix1 lacked this functionality. `LibraEDT`'s Server Module addresses this gap by providing a robust solution for managing the Timepix detector, enabling it to perform functions typically available only in more recent hardware iterations.

The Client Module, entirely developed in C++, serves as the core component of `LibraEDT`, managing the interaction between the TEM and the ASI Timepix Detector. On one hand, it communicates directly with the TEM through its Application Programming Interface (API), facilitating comprehensive manipulation and control of the microscope's functionalities. This includes stage control, lens manipulation, and overall microscope configuration, allowing for detailed control over the experimental setup.

On the other hand, the Client Module interfaces with the Server Module via a TCP/IP connection, enabling remote control of the detector. This communication channel allows the Client Module to send commands such as adjusting exposure times and initiating image acquisition processes. Additionally, the Client Module receives image data from the Server Module, which is processed and displayed in real-time as a live visualization, providing the operator with immediate feedback on the specimen or diffraction patterns.

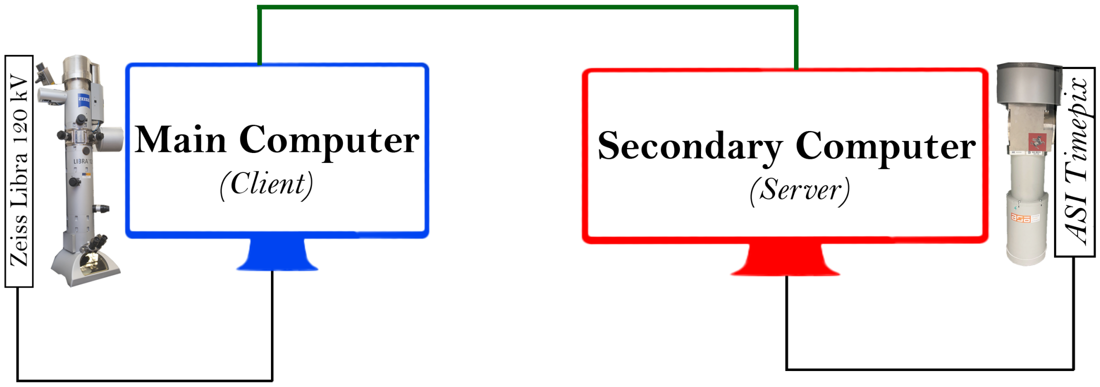

Figure 2.1: Schematic representation of the experimental setup. Main Computer (Client) controls the Zeiss Libra 120 kV TEM, while Secondary Computer (Server) handles data acquisition from the ASI Timepix detector. The two computers are networked to enable data transfer and synchronized control of the experiment.

All these functionalities are integrated into a user-friendly graphical user interface (GUI), as illustrated in Figure 2.2. The intuitive design of the GUI ensures that users can easily access and manage the complex control options without requiring extensive technical expertise. `LibraEDT` unifies the control of both the TEM and the detector into a single software platform, running on a single computer. This integration makes the experimental workflow much easier and straightforward, enhancing the overall efficiency and reliability of 3D Electron Diffraction experiments.

In the next section, we will provide a detailed explanation of the software's core functionalities, focusing on each of the different sections highlighted in the Figure 2.2.

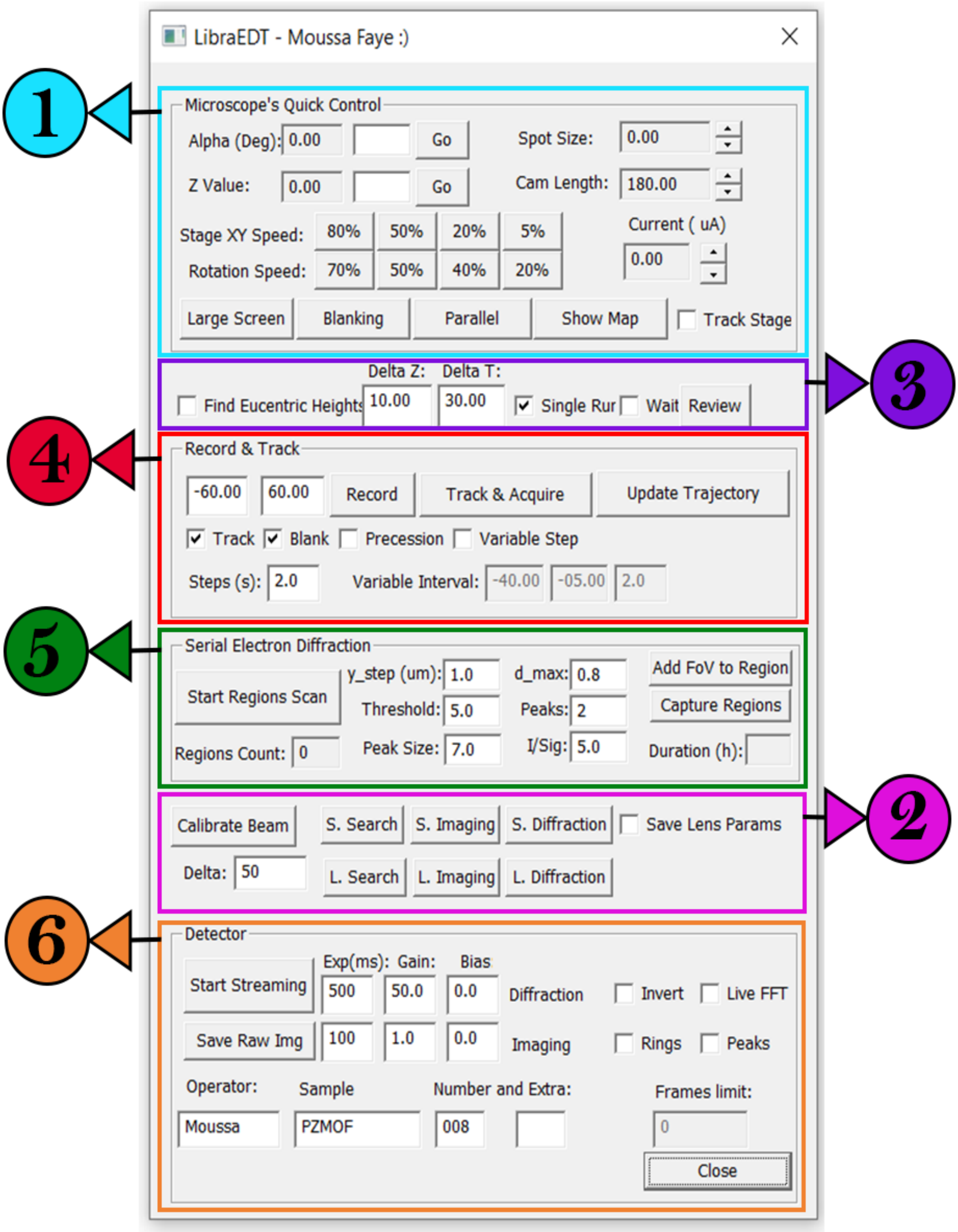

LibraEDT - Moussa Faye :)

Microscope's Quick Control

Alpha (Deg): 0.00

Z Value: 0.00

Spot Size: 0.00

Cam Length: 180.00

Current (uA) 0.00

☐ Track Stage

Delta Z: 10.00

Delta T: 30.00

☐ Find Eucentric Heights ☑ Single Rur ☐ Wait

Record & Track

-60.00 60.00

☑ Track ☑ Blank ☐ Precession ☐ Variable Step

Steps (s): 2.0

Variable Interval: -40.00 -05.00 2.0

Serial Electron Diffraction

y_step (um): 1.0

d_max: 0.8

Threshold: 5.0

Peaks: 2

Peak Size: 7.0

I/Sig: 5.0

Regions Count: 0

Duration (h):

☐ Save Lens Params

Delta: 50

Detector

	Exp(ms):	Gain:	Bias
Diffraction	500	50.0	0.0
Imaging	100	1.0	0.0

☐ Invert ☐ Live FFT

☐ Rings ☐ Peaks

Operator: Moussa

Sample: PZMOF

Number and Extra: 008

Frames limit: 0

Figure 2.2: GUI of the `LibraEDT` Client Module with highlighted sections, illustrating the main operational areas.

2.4 Core Functionalities

2.4.1 Microscope's Quick Control

The section **1** provides access to essential functionalities for 3D-ED experiments, with many controls useful for beam-sensitive samples. For example, tuning the rotation speed helps protect delicate materials by reducing their exposure time to the electron beam. Adjustments to the spot size and filament current allow precise control over the electron dose, while the beam blanking option turns off the beam during idle periods to minimize sample damage. Additional controls include the camera length adjustment for optimizing diffraction resolution and the ability to manage stage position and rotation. When operating `LibraEDT` in STEM mode, users can switch between parallel and convergent beam modes by relaxing and exciting the C3 lens respectively, as described in **Chapter 1.2.5.3**. Working in convergent beam mode can be particularly useful for crystal screening thanks to its higher image resolution, which simplifies identifying regions of interest.

Lastly, the *Show Map* button opens an interactive 2D live map of the stage's position (Figure 2.3), enabling the user to navigate intuitively by clicking on desired locations.

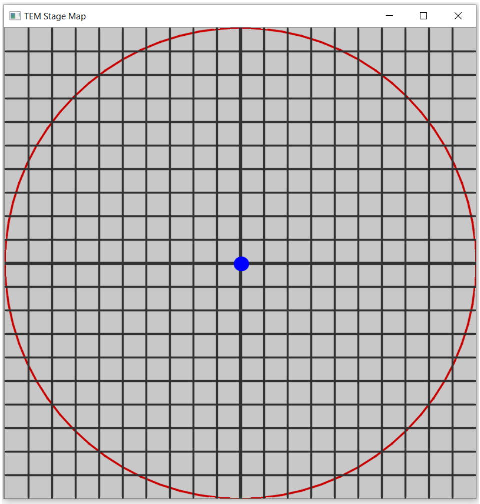

Figure 2.3: Interactive 2D stage map. Blue dot shows the current stage position.

2.4.2 Beam Calibration and Operational Settings

2.4.2.1 Beam Calibration

The *Calibrate Beam* button (Section **2**) is essential for precise control of the electron beam's position. This feature determines the amount of lens current adjustments needed to shift the electron beam by a specific number of pixels, effectively mapping the physical beam movements to the digital interface.

The calibration process involves capturing three beam images: one at the initial position as a reference, a second after shifting the beam along the X-axis, and a third after shifting it along the Y-axis. Afterward, the user selects the beam's size and position in the reference image, followed by the shifted positions in the subsequent images. These inputs are used to calculate the beam shift vectors in the X and Y directions, determining how much the beam moves per unit of current in the lenses. The current values for these shifts are defined in the GUI's *delta* textbox.

This calibration can also be automated in `LibraEDT`, and once complete, it allows users to direct the beam to any point on the screen by simply clicking on the desired location Figure 2.11.

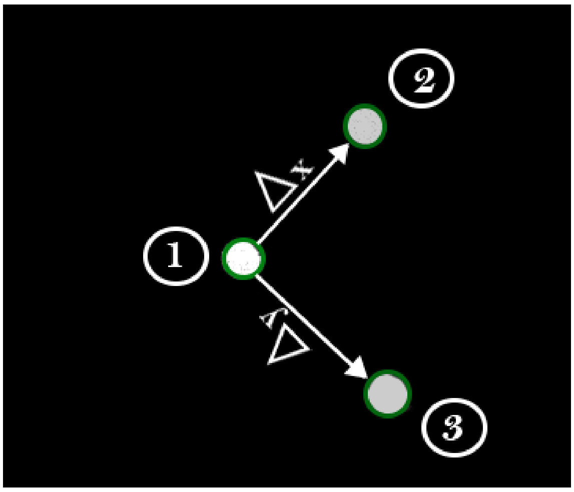

Figure 2.4: Superimposition of the three beam images captured during the calibration process. The reference position (1) and the shifted positions along the X-axis (2) and Y-axis (3).

2.4.2.2 Operational Settings

The *S.Search*, *S.Imaging*, and *S.Diffraction* buttons in section **2** allow the operator to store different condenser aperture and lens settings for various operational modes.

This functionality simplifies the process of maintaining different electron dosage levels for crystal searching, imaging, and diffraction data acquisition. For example, low electron doses can be used for searching and imaging to protect beam-sensitive samples, while higher doses can be applied during diffraction to achieve a better signal-to-noise ratio.

The corresponding settings can be loaded at any time using the *L.Search*, *L.Imaging*, and *L.Diffraction* buttons. However, `LibraEDT` will automatically load these settings when appropriate. For instance, diffraction settings are loaded during diffraction quality checks or data acquisition, while imaging settings are applied when capturing and saving images to disk.

In order to efficiently store and recall condenser aperture settings, we make use of the Automatic Illumination-aperture Selection (AIS) system in Zeiss Libra microscopes. This system allows us, on the one hand, to use a multi-hole condenser aperture (Figure 2.5A) with seven apertures for our setup. On the other hand, it incorporates a condenser deflecting system that electronically shifts the electron beam to any of the desired apertures (Figure 2.5A), and a scanning system, located below the condenser aperture, that compensates for this shift, returning the beam back to the optical axis (Figure 2.5B). This system eliminates the need for motorized apertures or microscope realignment.

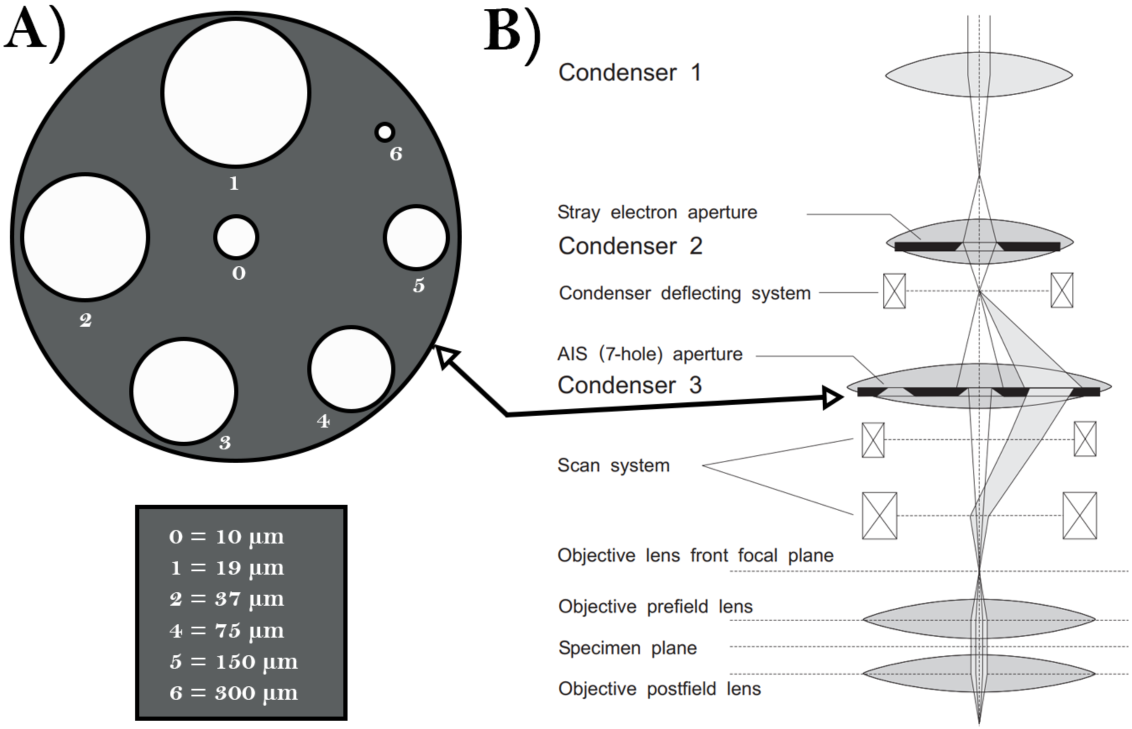

Figure 2.5: (A) Multi-hole condenser aperture with corresponding sizes, and (B) schematic representation of the AIS in Zeiss microscopes.

2.4.3 Automatic Eucentric Height Calculation

Adjusting the eucentric height is a critical step in 3D-ED experiments to ensure that the crystal remains within the illuminated area during stage tilting by minimizing lateral specimen movement. While several methods exist for estimating the eucentric height, a commonly used approach involves tilting the electron beam away from the optical axis and minimizing the observed shift of the crystal. This beam-tilt method is fast, but often imprecise.

In `LibraEDT`, the eucentric height is calculated using a more accurate automated method, closely mirroring the manual adjustment process [55, 56]. By acquiring images at two distinct tilt angles, α_1 and α_2, as well as at two different stage heights, z_1 and z_2, the displacement of the crystal, d, can be characterized as a function of both tilt and height. These measurements enable a linear regression approach that isolates the influence of height adjustments on the observed displacement.

At each tilt angle, the crystal displacement d is measured at both heights. From these data, the change in displacement at z_1 is Δd_{z_1}, and the change in displacement at z_2 is Δd_{z_2}. Their difference,

$$\Delta d = \Delta d_{z_2} - \Delta d_{z_1},$$

together with the known height difference $\Delta z = z_2 - z_1$, is used to calculate the slope (m) of the linear regression:

$$m = \frac{\Delta d}{\Delta z}.$$

The intercept (c) is determined from:

$$c = \Delta d_{z_1} - m \cdot z_1.$$

Finally, the optimal eucentric height z_{euc} is found by:

$$z_{\text{euc}} = -\frac{c}{m}.$$

This approach results in better eucentric height estimation. However, it is slower compared to the beam tilt approach and is therefore not commonly used in our routine workflows. Nevertheless, having this feature available in `LibraEDT` is advantageous, particularly for potential future applications such as unsupervised data acquisition.

2.4.4 Crystal Tracking

Crystal tracking is one of the most important functionalities offered by `LibraEDT`, and is implemented in Section **4** of the interface. Its primary objective is to record the crystal's trajectory during stage rotation and continuously adjust the beam position to ensure that the crystal remains within the beam throughout diffraction data collection. This approach was first proposed by Gemmi et al. [31] and later implemented by Plana-Ruiz [57].

The process begins by selecting the *Record* option, which loads previously defined imaging parameters (Section **2**, 2.4.2.2) and initiates stage rotation from the specified initial angle to the final angle. Images are acquired at user-defined time intervals and , when the recording is finished, they are displayed to the user, who marks the crystal's position in each frame. This step results in a trajectory map describing the crystal's positional changes over the course of the rotation. If the *Blank* checkbox is selected, the beam remains blanked at all times except for the brief moments when images are captured.

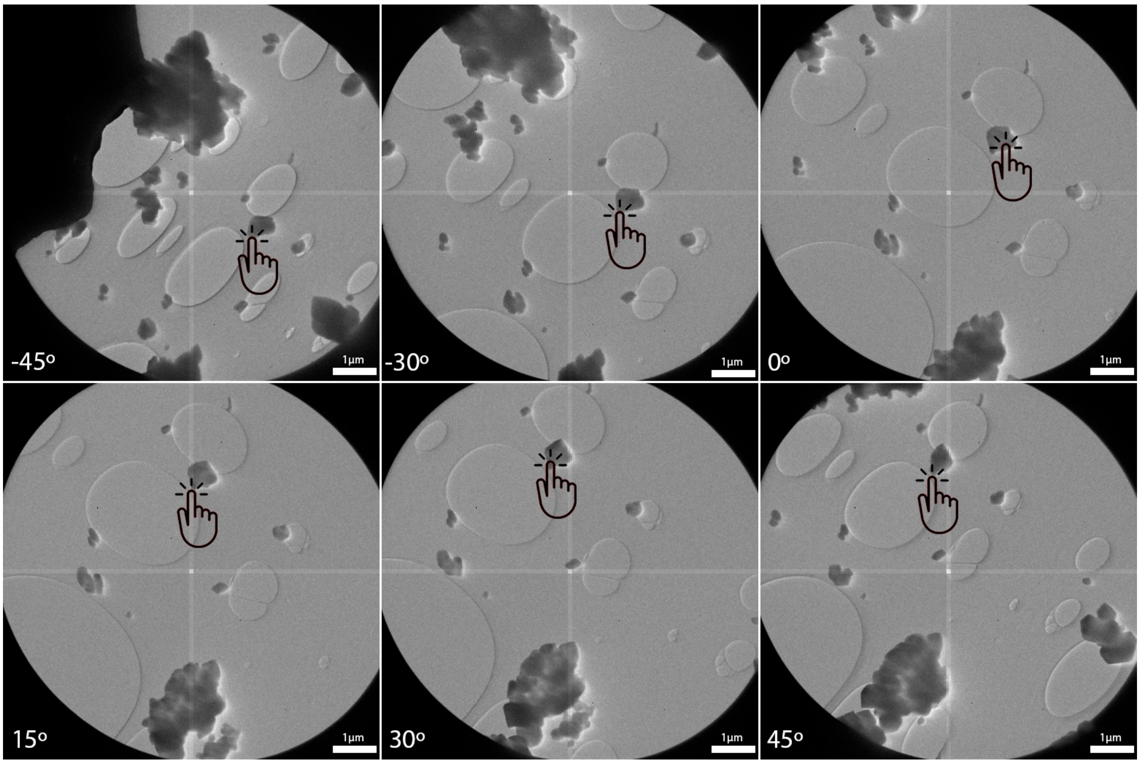

Figure 2.6: Illustration of how the crystal's position is marked (hand icon) in images acquired at different tilt angles to generate a trajectory.

Once this trajectory is established, the *Track & Acquire* option is selected, causing `LibraEDT` to switch into diffraction mode and load the previously configured diffraction settings (Section **2**, 2.4.2.2). The stage is then rotated through the same angular range, while the software continuously adjusts the electron beam position based on the determined trajectory to keep the crystal centered. To achieve this beam adjustment, the trajectory can be interpolated using either linear or spline methods. Although linear interpolation is simpler and often sufficient, spline interpolation is generally preferred as it provides a smoother path. In most cases, the difference between the two approaches is negligible. However, spline interpolation becomes particularly beneficial if the crystal undergoes abrupt changes in direction (Figure 2.7). These precise adjustments are further enabled by the prior beam calibration step (Section **2**, 2.4.2.1), which correlates lens currents with the corresponding screen coordinates.

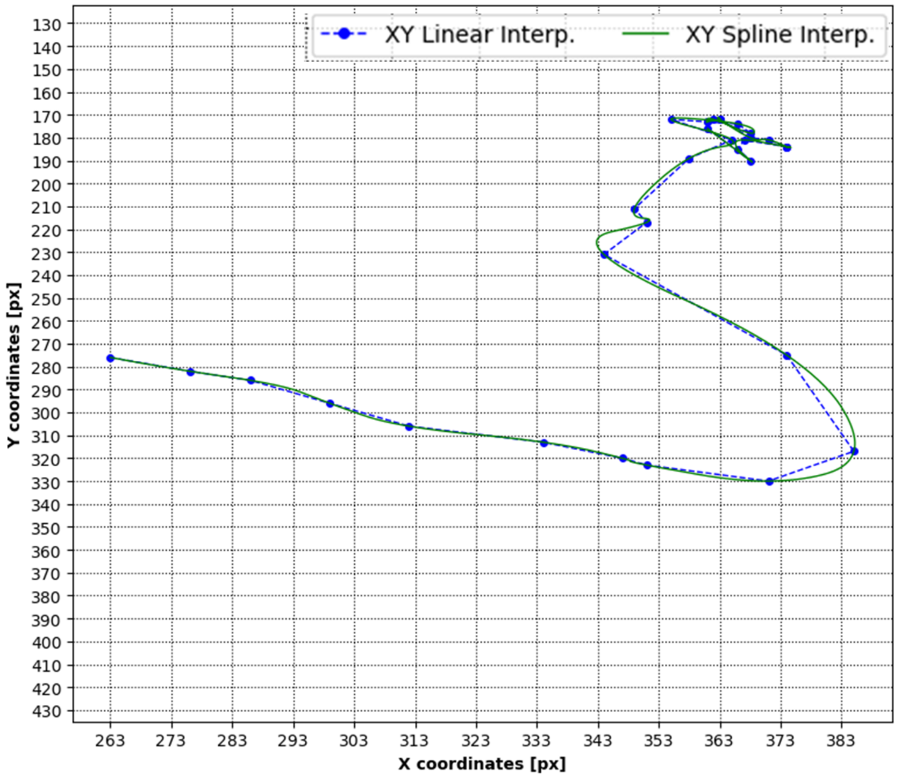

Figure 2.7: Comparison of linear and spline interpolation methods for crystal tracking. The largest difference between the two methods is observed along the rightmost portion of the trajectory.

`LibraEDT` also provides real-time visual feedback by superimposing the crystal's trajectory and a virtual beam indicator on the live display. As illustrated in Figure 2.8, this overlay allows the user to verify that the beam consistently follows the crystal's path, ensuring optimal alignment during diffraction data acquisition.

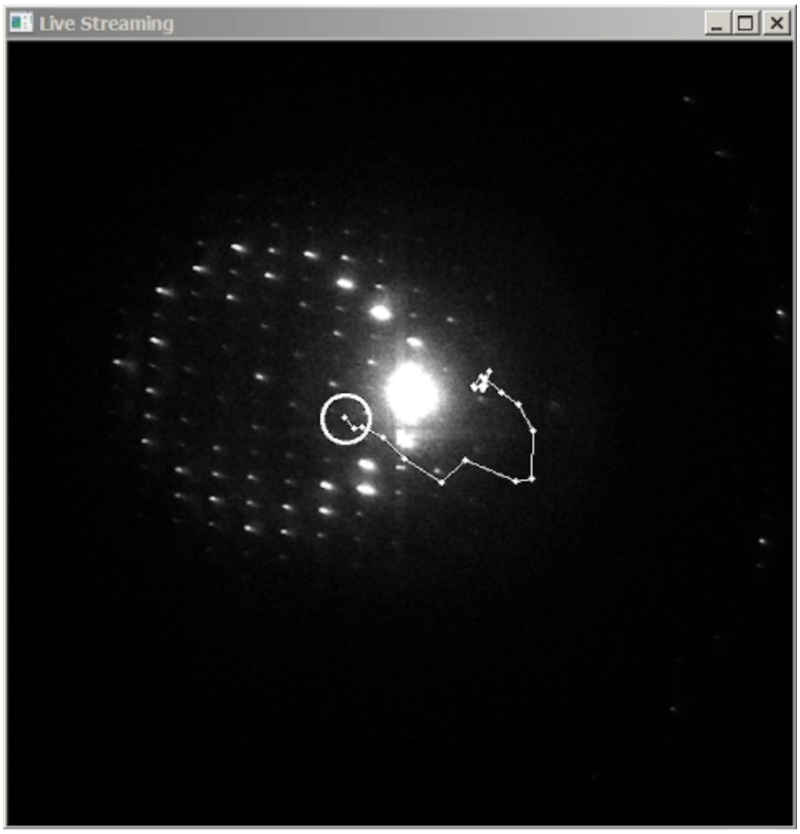

Figure 2.8: Example of the visual overlay of the crystal trajectory and a virtual beam marker during the *Track & Acquire* process.

The *Update Trajectory* button adds significant flexibility to the crystal tracking workflow. By re-displaying the previously acquired images from the *Record* step, this feature allows users to adjust the existing trajectory map for different regions of the same crystal or create new trajectory maps for other crystals that remained within the field of view during the angular range. For instance, in the images illustrated in Figure 2.6, more than six different crystals remained within the field of view for the given angular range. Using the *Update Trajectory* feature, data sets can be collected for all six crystals without needing to repeat the *Record* step. This not only significantly improves the efficiency of data acquisition but also minimizes additional beam exposure.

2.4.5 Serial Electron Diffraction

In Section **5**, `LibraEDT` introduces the capability to perform serial electron diffraction, employing an approach analogous to fixed-target serial crystallography. In traditional fixed-target serial crystallography, micro-crystals are mounted onto a support and systematically rastered through an X-ray beam [7, 58, 59] (Figure 2.9A). In our methodology, nanocrystals are deposited onto a TEM grid, after which `LibraEDT` is used to raster them through the electron beam. This methodology, originally proposed by Gerhard Hofer from Stockholm University, has been implemented and further refined in `LibraEDT`. The scanning process involves moving the TEM stage in a zig-zag pattern over a user-defined area, alternating between left-to-right and right-to-left motions while progressively shifting downward (Figure 2.9).

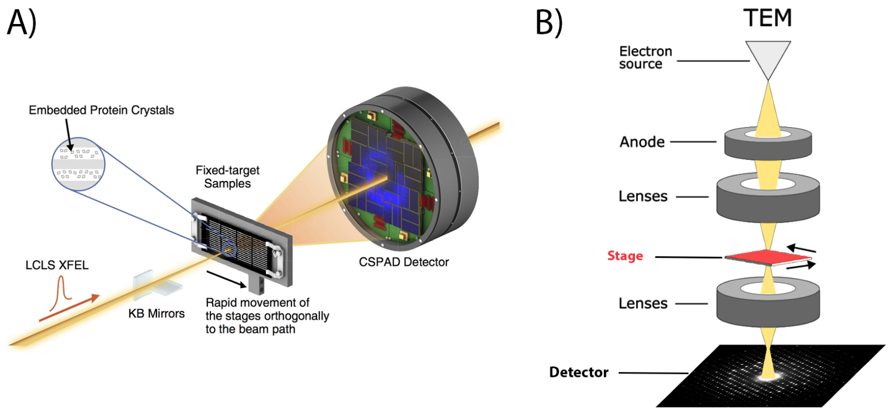

Figure 2.9: (A) Fixed-Target serial crystallography [7]. (B) Serial Electron Diffraction by stage movement.

`LibraEDT` offers multiple options for selecting regions on the grid to be rastered: users may choose to scan the entire grid, define regions interactively using the 2D map (Section **1**, 2.4.1), or add the current field of view as a target area. Additionally, users can acquire a low-magnification image, usually collected at much lower dose compared to standard TEM images, and manually specify regions of interest. These different approaches are particularly advantageous when dealing with non-uniform sample distributions, as they prevent the unnecessary collection of data from empty or irrelevant areas. Once the regions to be scanned are defined, users can configure parameters such as the stage's XY translation speed and the y-step size.

However, this methodology can rapidly generate an extensive volume of data, potentially producing tens of thousands of images per grid square depending on the selected exposure time. Efficient data management and filtration are therefore essential to make sure that only relevant data are saved. To address this challenge, `LibraEDT` employs the `peakfinder8` [60] algorithm, as implemented in `CrystFEL` [61], to perform peak detection. The algorithm rigorously evaluates each frame, retaining a frame only if it contains a minimum number of reflections (specified in the *peaks* text-box) that simultaneously meet both the intensity-to-noise ratio (I/σ) (specified in the *I/Sig* text-box) and resolution thresholds (specified in the *d_max* text-box) within the graphical user interface (GUI). Frames that do not satisfy these criteria are automatically discarded. An example of the serial electron diffraction workflow is shown in Figure 2.10. The TEM stage map displays the selected regions (highlighted in green) for scanning, while the blue dot indicates the current stage position. During data acquisition, the *Live Streaming* (Section **6**, 2.4.6) window provides a real-time view of diffraction patterns, with resolution rings and reflection peaks visualized for immediate quality assessment. The log window indicates the results of the filtering process, where only frames meeting the user-defined thresholds, such as a minimum of 5 detected peaks, a signal-to-noise ratio (I/σ) of at least 10.0, and a resolution better than 0.80 Å^{-1} (1.25 Å), are retained. For instance, the current frame visible in the live streaming window meets these criteria and would therefore be saved. In this particular dataset, at the moment of capturing this image, 4141 frames were identified as valid out of a total of 164080 frames.

In **Chapter 7**, we will analyze a data collected using this method.

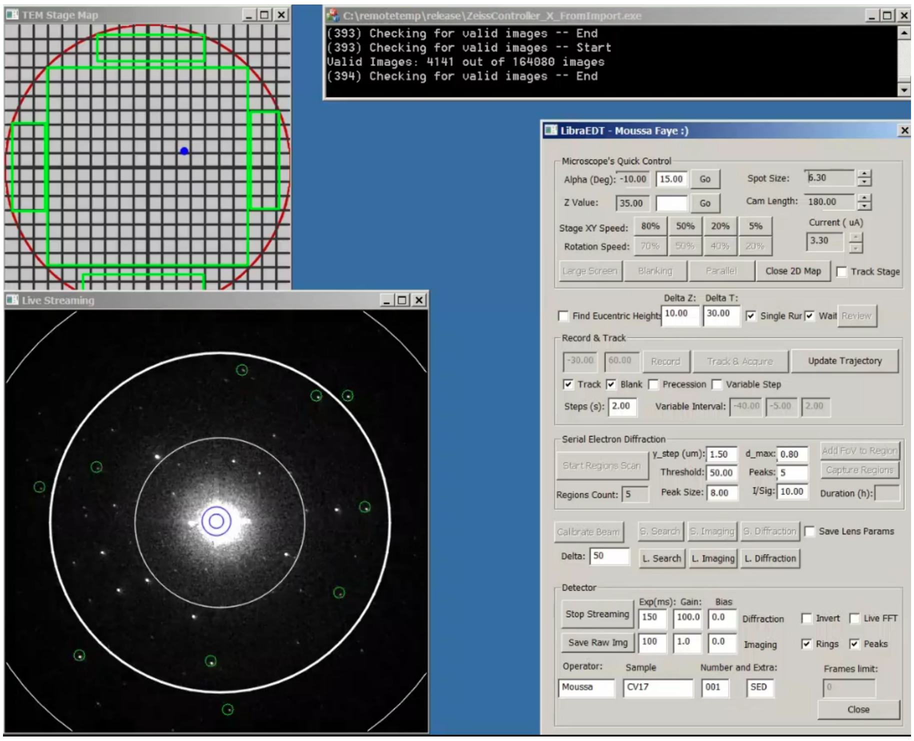

```
(393) Checking for valid images -- End
(393) Checking for valid images -- Start
Valid Images: 4141 out of 164080 images
(394) Checking for valid images -- End
```

Alpha (Deg): -10.00 15.00
Spot Size: 6.30
Z Value: 35.00
Cam Length: 180.00
Stage XY Speed: 80% 50% 20% 5%
Rotation Speed: 70% 50% 40% 20%
Current (uA) 3.30
☐ Track Stage
Delta Z: 10.00
Delta T: 30.00
☐ Find Eucentric Heights ☑ Single Rur ☑ Wait
-30.00 60.00
☑ Track ☑ Blank ☐ Precession ☐ Variable Step
Steps (s): 2.00
Variable Interval: -40.00 -5.00 2.00
y_step (um): 1.50
d_max: 0.80
Threshold: 50.00
Peaks: 5
Regions Count: 5
Peak Size: 8.00
I/Sig: 10.00
Duration (h):
☐ Save Lens Params
Delta: 50
Exp(ms): Gain: Bias
150 100.0 0.0 Diffraction
100 1.0 0.0 Imaging
☐ Invert ☐ Live FFT
☑ Rings ☑ Peaks
Operator: Moussa
Sample CV17
Number and Extra: 001 SED
Frames limit: 0

Figure 2.10: Serial Electron Diffraction workflow using `LibraEDT`, showing the interactive 2D map with selected regions, a console window displaying filtering process results, and a live streaming window with real-time diffraction patterns.

2.4.6 Detector Control

Section **6** is the Detector Control where `LibraEDT` manages data acquisition settings and serves as a bridge between the client and server modules.

One of the primary functions of this section is to send requests to the server, such as initiating image acquisition or adjusting the exposure time. For example, the *Save Raw Image* button sends a request to capture a single image from the detector and store it on disk. In contrast, the *Live Streaming* button requests the server to continuously acquire images from the detector and transmit them to the client. These images are displayed in real-time on an interactive window, providing a live view of the sample. This interactive window also allows the users to click on specific positions and automatically assess the diffraction pattern quality Figure 2.11. For that, `LibraEDT` automatically loads the diffraction settings (Section **2**, 2.4.2.2) and shift the beam to the selected positions (Section **2**, 2.4.2.1). When diffraction patterns are displayed, users can visualize resolution rings and reflection peaks, by enabling the *Rings* and *Peaks* check-boxes.

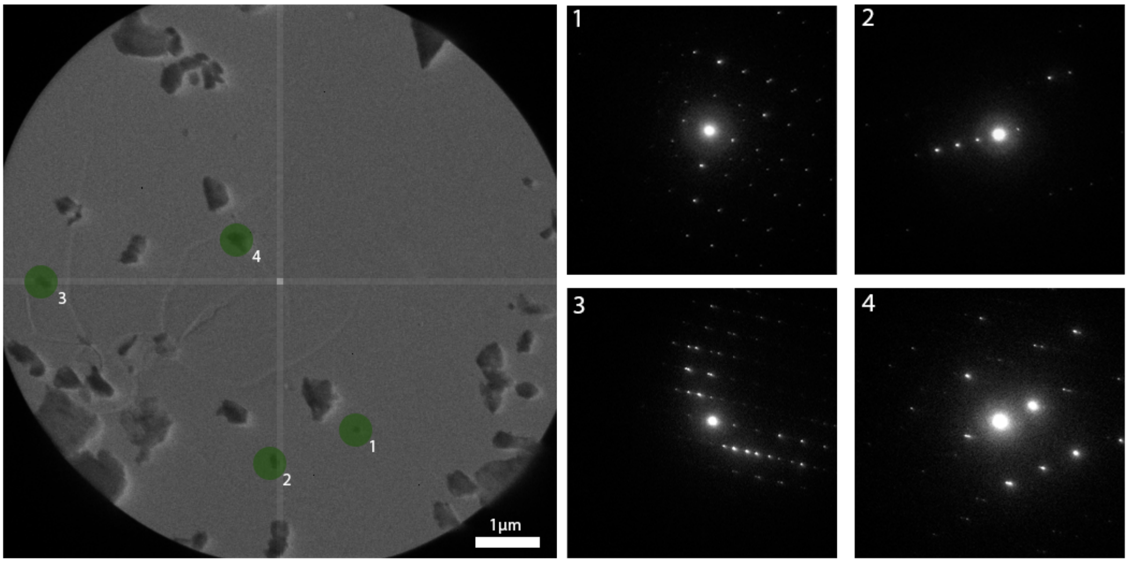

Figure 2.11: Interactive window in which the user can select several positions and automatically assess the diffraction quality.

Additionally, all image manipulation and post-processing, such as drawing resolution rings or highlighting peaks, gain and brightness adjustments are performed on the client side using the `OpenCV` library [62].

To ensure efficient data organization during diffraction data acquisition, each dataset is systematically stored within a hierarchical folder structure following the pattern `OperatorName/SampleName/Date/CrystalNumber`. When data is collected from additional crystals, the `CrystalNumber` automatically increments, ensuring that each new dataset is saved in the next sequential folder (`CrystalNumber+1`).

2.4.7 Corrections and Data Preparation in the Background

In addition to its user-controlled features, `LibraEDT` performs several processes in the background to enhance data quality. For instance, flat-field correction and dead-pixel correction are applied automatically to all acquired images, improving the accuracy of the diffraction patterns and reducing artifacts. The software also keeps track of metadata associated with each dataset, including acquisition parameters, timestamps, and beam settings. This metadata is embedded directly into the saved data files, ensuring reproducibility of the experimental conditions. Additionally, the crystal tracking trajectory is saved to disk, providing a record of the crystal's movement during the experiment.

Furthermore, `LibraEDT` automatically prepares input files compatible with widely used data processing software such as `PETS2` [36], `XDS` [37], and `DIALS` [38]. This enables automated processing of the collected data, giving users the possibility to solve the crystal structure within minutes of data acquisition.

All GUI-adjusted parameters are consistently saved to disk. When the software is reopened by the same user or another, `LibraEDT` automatically reloads these settings, provided they were saved on the same day.

2.5 Workflow for Data Acquisition Using `LibraEDT`

The overall workflow for data acquisition using `LibraEDT` is summarized in Figure 2.12. The process begins with *beam calibration* to ensure accurate beam positioning, followed by setting up the *searching, imaging, and diffraction settings.* Once configured, the operator proceeds to *crystal screening and eucentric height adjustments* to identify suitable crystals and align them for diffraction. If a suitable crystal is found, the next step is to *record the crystal trajectory map*, which defines the crystal's movement during stage rotation. The recorded trajectory is then used in the *Track and Acquire Diffraction Data* step, where diffraction patterns are collected while dynamically tracking the crystal's position. Once the data collection is complete, the corresponding dataset can be automatically processed, as the input files for software such as `PETS2` [36], `XDS` [37], and `DIALS` [38] are already prepared. On the other hand, the user may acquire additional data by reusing the recorded images to *update the trajectory map* for another crystal within the field of view, or they can move to a different stage position to restart the *crystal screening and eucentric height adjustment* steps.

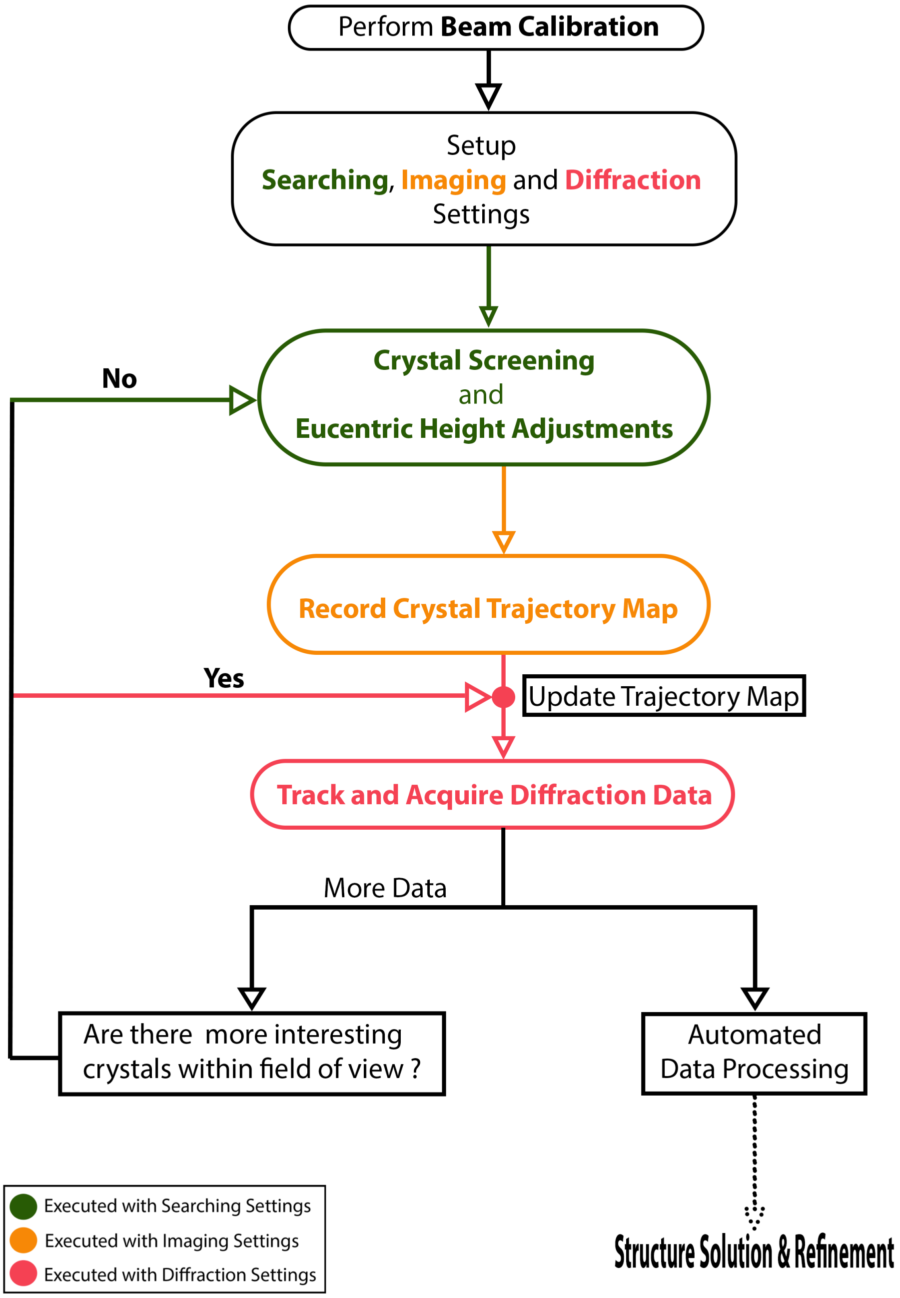

Figure 2.12: cRED/PEDT data acquisition using `LibraEDT`.

2.6 Conclusion

The development of `LibraEDT` addresses key challenges in 3D-ED by simplifying workflows, making experiments more accessible by integrating all essential functionalities into a unified software platform. With its ability to automate and optimize data acquisition, `LibraEDT` enables the collection of diffraction data from over 20 crystals in just half a TEM session. This efficiency not only allows for high-throughput experiments, but the analysis of multiple samples within a single day, enhancing productivity.

While not explicitly mentioned throughout the previous chapters, `LibraEDT` is highly versatile. All its features, including crystal tracking and serial electron diffraction, can be performed in both TEM and STEM. Additionally, the crystal tracking functionality supports cRED and stepwise modes (EDT), with or without precession (PEDT), providing flexibility for a wide range of experimental setups and requirements.

The modular design of `LibraEDT`, developed using object-oriented programming (OOP) principles, allows for the straightforward implementation of new features or adaptation to different microscope platforms. Adapting `LibraEDT` to a new instrument would primarily involve configuring a dedicated class to handle communication with the specific hardware, while the core functionalities and workflows remain largely unchanged.

The Python-based server module of `LibraEDT` provides a basis for future enhancements. For example, machine learning models for crystal recognition or diffraction quality assessment could be developed and integrated into the server module to analyze data in real time. These models could facilitate unsupervised data acquisition in both cRED and SerialED, reducing the need for manual intervention.

In summary, `LibraEDT` simplifies and automates 3D-ED experiments while providing a robust framework for future developments, including automation and machine learning applications. In the following chapters, we will present new crystal structures successfully solved using data acquired with `LibraEDT`, demonstrating its practical applications and potential.

The source code for the client module of `LibraEDT`, written in C++, is publicly available on LibraEDT Client Repository, while the server module, implemented in Python, can be accessed on its LibraEDT Server Repository.

Chapter 3

Structural Analysis of a Mechanochemically Synthesized Cu-Based Protocatechuate MOF

3.1 Introduction to Mechanochemical Synthesis and 3D Electron Diffraction

Mechanochemistry[63] involves chemical reactions that are initiated or accelerated by mechanical force, typically through grinding, milling, or shearing processes[64]. This method offers several advantages over traditional solution-based synthesis techniques. Firstly, it often requires minimal or no solvent, aligning with green chemistry principles by reducing waste and environmental impact[65, 66]. Secondly, mechanochemical reactions can proceed rapidly at ambient temperatures and pressures, enhancing safety and energy efficiency[67]. Additionally, mechanochemistry can facilitate the formation of novel compounds and materials that might be challenging to synthesize via conventional methods due to solubility limitations or kinetic barriers[68, 69].

In the context of MOFs, mechanochemical synthesis is particularly advantageous[70]. The coordination between metal ions and organic ligands can be effectively achieved under mechanical activation, leading to the rapid formation of glsplmof structures[71, 68]. However, the resulting materials often consist of nanometer-sized crystallites due to the high-energy milling process[71, 72]. While this small crystal size can hinder structural characterization using conventional SCXRD, it is ideally suited for gls3ded techniques. Electron diffraction is also highly sensitive to lighter elements, allowing for detailed structural analysis, including the localization of hydrogen atoms, which is often challenging with XRD. Therefore, the combination of mechanochemical synthesis and 3D-ED presents a powerful approach for the rapid and efficient synthesis and structural characterization of novel MOFs.

This chapter focuses on the mechanochemical synthesis of the Cu(II)-based MOF and its comprehensive structural characterization using 3D electron diffraction. We begin by detailing the liquid-assisted grinding (LAG)[68] method employed to synthesize the `PC-MOF`, highlighting its efficiency and environmental benefits compared to conventional aqueous solution reactions. The chapter then compares the yields and reaction kinetics of both synthetic methods, demonstrating the superior performance of mechanochemistry.

Subsequently, we explore the challenges associated with characterizing small-sized crystals produced via mechanochemistry and how 3D electron diffraction overcomes these obstacles. The structural analysis of the `PC-MOF` is presented, including dynamical refinement to accurately locate hydrogen atoms and guest molecules within the framework. The structure is then validated through a Rietveld refinement.

Finally, the chapter examines the thermal stability and phase transition behavior of the `PC-MOF`, including the formation of a new high-temperature phase upon heating.

3.2 Synthesis of the Cu(II)-Based PC-MOF

The synthesis of the Cu(II)-based protocatechuate metal-organic framework (`PC-MOF`) was carried out using a rapid, safe and environmentally friendly approach by conducting a Liquid Assisted Grinding (LAG) reaction, using water as a sole liquid additive (Figure 3.1), The reaction was completed within minutes of milling, facilitated by the minimal volume of liquid used in the LAG process, which enhances reagent diffusion and promotes efficient reaction kinetics.

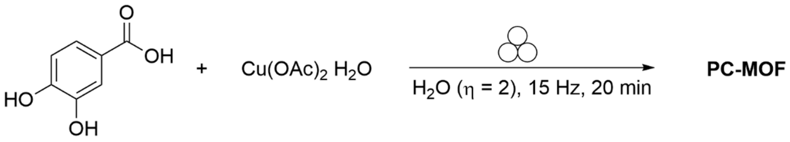

Figure 3.1: Reaction scheme of the `PC-MOF` in mechanochemical synthesis.

For comparison, the synthesis of `PC-MOF` was also performed using an aqueous solution reaction (Figure 3.2). While this conventional method successfully produced `PC-MOF`, the yield was significantly lower than that achieved through the mechanochemical approach. During the mechanochemical reaction, the acetic acid released from `PC-MOF` formation was not fully solubilized in the liquid additive. This resulted in the partial release of the byproduct into the surrounding atmosphere, thereby driving the mechanochemical reaction towards the formation of the desired framework within minutes (Figure 3.3). This mechanism significantly enhances both the reaction rate and total yield compared to the synthesis in solution.

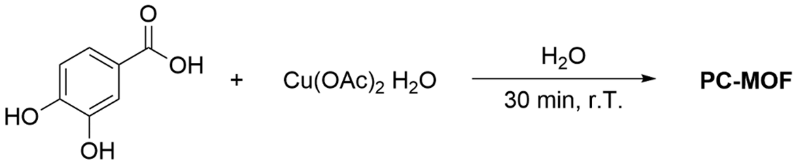

Figure 3.2: Reaction scheme of the `PC-MOF` in solution synthesis.

After 60 minutes of stirring, the aqueous solution reaction method yielded 45.4% `PC-MOF`, which increased to 46.1% after 90 minutes and reached 54.4% when the suspension was stirred overnight. In contrast, the mechanochemical (MC) method achieved a 49.9% yield in just 20 minutes of milling, which rose to 55.4% after 40 minutes and to 65.0% after 60 minutes (Figure 3.4).

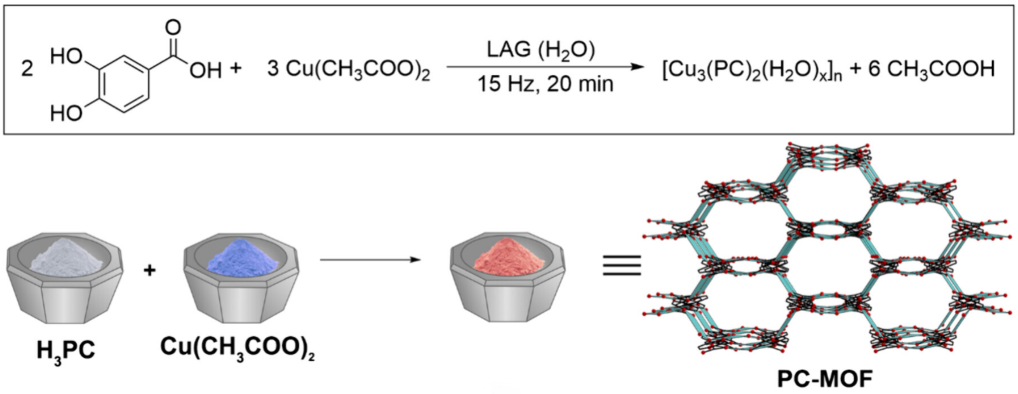

Figure 3.3: Schematic representation of the mechanochemical reaction followed for the `PC-MOF` synthesis.

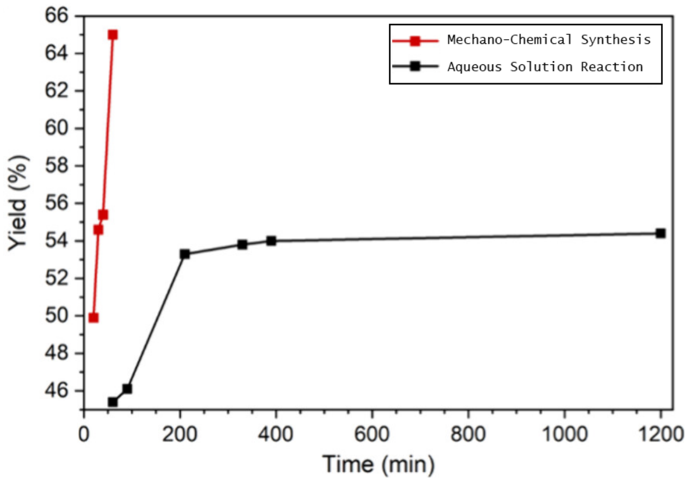

Figure 3.4: Comparison of the yield over time for the two synthetic methods, highlighting the better performance of mechanochemical synthesis over the aqueous solution reaction.

The successful formation of the new metal-organic framework was confirmed by diffraction techniques, which produced distinct diffraction patterns different from those of the precursor materials. The PXRD of the newly formed `PC-MOF` is illustrated in Figure 3.5.

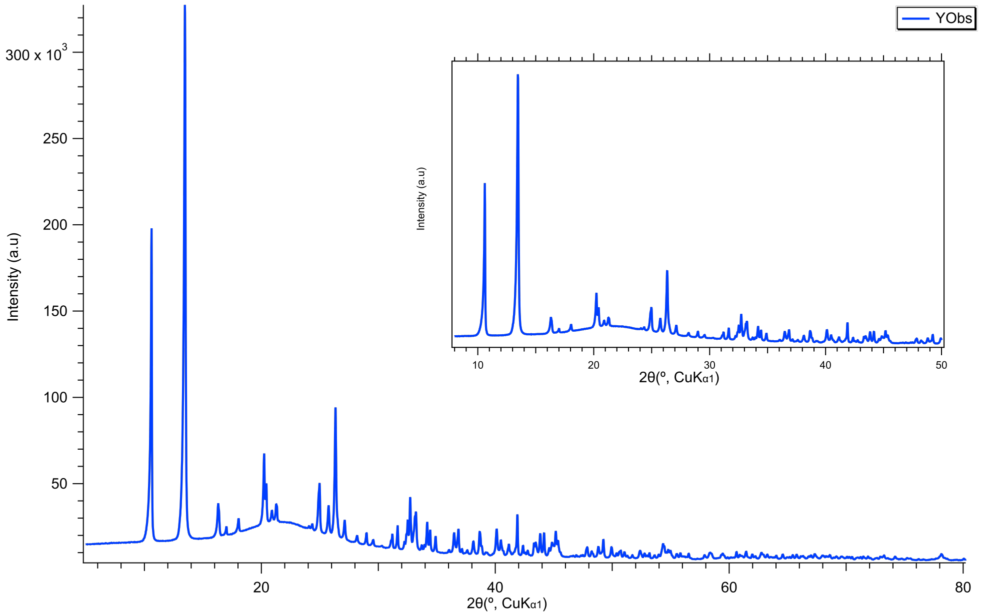

Figure 3.5: PXRD pattern of the mechanochemically synthesized `PC-MOF`.

The synthesized `PC-MOF` was then evaluated for stability in various solvents by dispersing separate batches of the powder in each solvent and monitoring them over three days. The `PC-MOF` demonstrated excellent stability across different solvent conditions, with a phase transition occurring only in the presence of N,N-Dimethylformamide (DMF) (Figure 3.6). This transition resulted in a PXRD pattern consistent with the reported $[Cu_3(PC)_2(DMF)_2]_n$ phase [73].

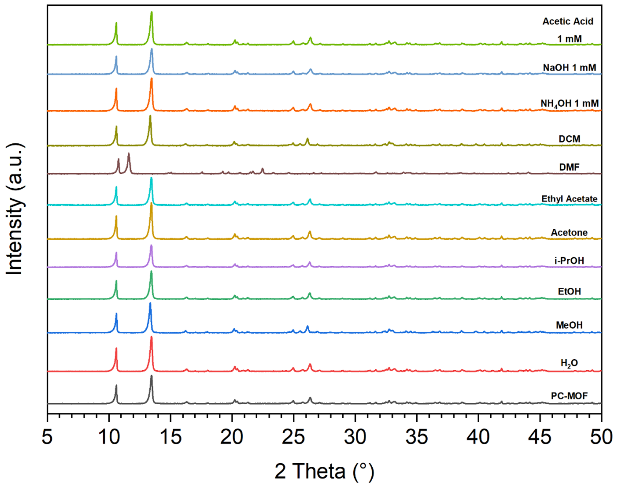

Figure 3.6: `PC-MOF` stability in different solvents.

3.3 Structural Characterization of `PC-MOF` using 3D-Electron Diffraction

As previously detailed in **Section** 3.1, mechanochemical synthesis, characterized by high-energy milling and solvent-free conditions, typically produces small crystals. In our case, the synthesized crystals ranged in size from 200-300 nm (Figure 3.7). Such small crystal sizes present considerable challenges for conventional crystallographic analysis. However, these limitations can be effectively overcome by performing electron diffraction. Because these crystals are beam-sensitive, rapid data acquisition was crucial to minimize exposure time and reduce the cumulative electron dose. Consequently, cRED, implemented with the `LibraEDT` software introduced in **Chapter** 2, was selected as the optimal method for acquiring diffraction data of the `PC-MOF`.

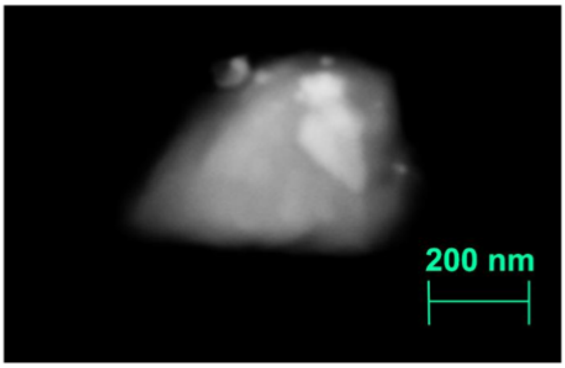

Figure 3.7: STEM-Image of the `PC-MOF` nanocrystal used for cRED.

The collected electron diffraction data were subsequently processed and indexed using `PETS2.0` [36]. All datasets were successfully indexed with a C-centered monoclinic cell, with the following refined lattice parameters: a = 21.171(7) Å, b = 7.005(3) Å, c = 16.903(6) Å, and β = 127.23(2). Symmetry analysis was performed by evaluating systematic absences in the two-dimensional sections of the reciprocal space (Figure 3.8). The reflection conditions for the *hkl* and *0kl* sections, specifically, h, $l = 2n$, and $h + k = 2n$ were consistent with the extinction symbol *C1c1*, indicating possible space groups of either *Cc* or *C2/c*. The structure was solved ab initio from a single cRED dataset (Table S3.1) in the space group C2/c using `SHELXT` [46], allowing for the localization of all non-hydrogen atoms within the MOF framework.

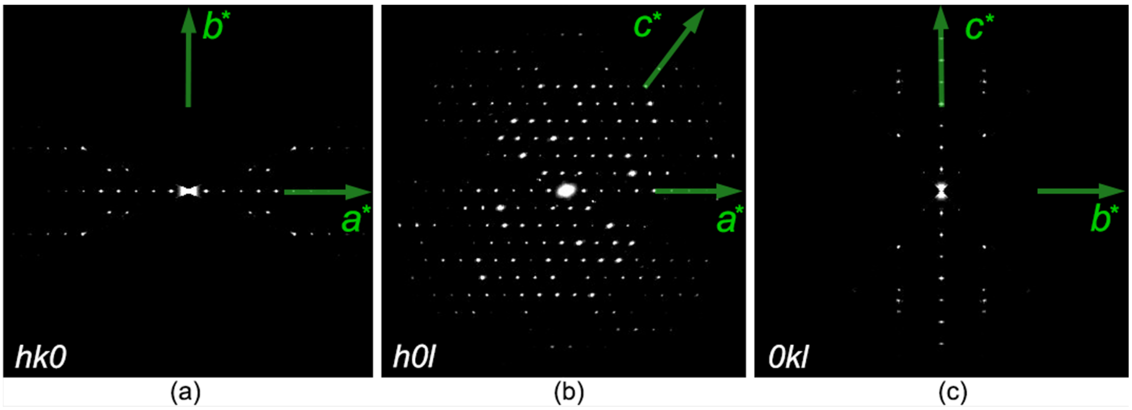

Figure 3.8: Reciprocal space sections for `PC-MOF` electron diffraction data, reconstructed using `PETS2.0` from the 3D-ED data. (a) *hk0* plane section highlighting the a* and b* axes; (b) *h0l* plane section highlighting the a* and c* axes; (c) *0kl* plane section highlighting the b* and c* axes. These sections aid in symmetry analysis and space group determination.

During the initial stages of model refinement, a *kinematical* approach was employed, resulting in an observed R-factor (R_{obs}) of **27.91%**. Analysis of the residual electrostatic potential maps within the channels of the crystal structure indicated the presence of trapped water molecules. However, the accurate location of these water molecules proved to be challenging within *kinematical* approximations.

3.3.1 Dynamical Refinement of `PC-MOF`

To address these challenges, a more sophisticated refinement strategy based on *dynamical diffraction theory* as detailed in Chapter 1.2.7.2.3 was implemented using the `JANA2020` software package [52, 51]. This approach significantly improved the refinement quality, reducing the R-factor from **27.91%** to **11.75%**.

Applying dynamical refinement not only reduced the R-factor but, more importantly, led to a more meaningful and sensible electrostatic potential map. This improvement enabled the unambiguous localization of all hydrogen atoms (Figure 3.15A), despite their low electrostatic potential and scattering power. Moreover, it facilitated the localization and stable refinement of disordered water molecules within the structure. A significant residual peak observed in the Fourier difference map (Figure 3.11B) was attributed to an oxygen atom likely originating from a water molecule. However, the initial refinement of this oxygen position and its thermal parameters was unstable, suggesting potential disorder or partial occupancy. To accurately model this uncertainty, the oxygen site was represented using two split positions, accounting in this way for its positional disorder. This dual-site model provides a more realistic representation of the water molecule's location and its interactions within the structure.

The asymmetric unit of the `PC-MOF` is composed of a single PC^{3-} molecule, two copper atoms, and a partially occupied water molecule (Figure 3.9A). This arrangement involves two distinct copper atoms, one in a general position `CU1` and the other in a special position (`CU2`), both displaying a square planar coordination geometry. The deprotonated carboxyl group establishes distinct coordination interactions with individual copper atoms, in which each oxygen acts as a monodentate ligand toward `CU1` or `CU2`. Furthermore, the catecholate group performs bidentate chelation on `CU1` while `O3` and `O4` are acting as bridging sites to `CU1`(1-x, y,3/2-z) and `CU2`, respectively (Figure 3.9B).

The connection of four molecules of H_3PC leads to a dimeric cluster, in which `CU1` and `CU1`(1-x, y, 3/2-z) atoms are involved in a distorted square planar coordination geometry, with their corresponding polyhedra sharing one edge (Figure 3.9B). This gives rise to a corrugated double chain that extends along the [101] direction (Figure 3.9B), with a corrugation angle of 149.8°. The `CU2` atom, located at a crystallographic special position, exhibits square planar coordination geometry. It shares one vertex with `CU1` and `CU1`(1-x, 1-y, 1-z), acting as a bridge between the corrugated double chains (Figure 3.10C). This connectivity results in the formation of a 3D framework with the formula $\{[Cu_3(PC)_2](H_2O)_0.75\}_n$ (Figure 3.10).

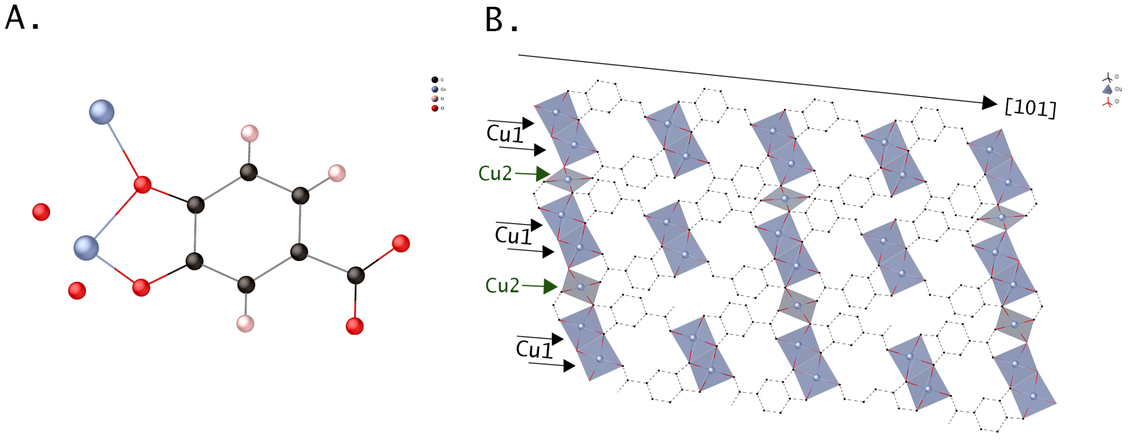

Figure 3.9: (A) Asymmetric unit of the PC-MOF structure, showing the coordination environment of the organic linker. (B) Representation of the layered structure of PC-MOF along the [101] direction. The figure highlights the dimeric CU1 clusters (blue polyhedra) and the bridging role of CU2 ions (green arrows) between different layers of the framework.

The framework features channels along the [101] direction. These channels are bordered by two opposite corrugated chains laterally connected by four CU2 square planar polyhedra, forming a distorted hexagonal cross-section (Figure 3.10). It displays a virtual void occupying 39.2% of the unit cell volume. Theoretical calculations, performed with Mercury [74], highlight the presence of pore diameters of around 4.33 Å and 3.90 Å (Figure 3.10B and Figure 3.10D respectively), with a total surface area of approximately 119.53 m^2g^{-1}.

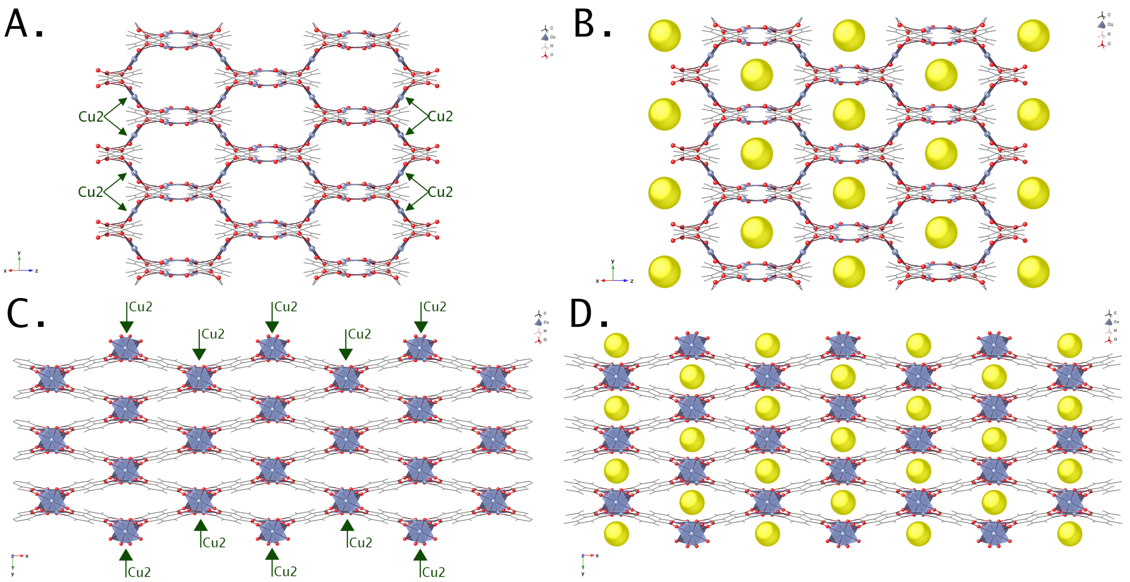

Figure 3.10: `PC-MOF` structure viewed along the crystallographic directions [101] in (A) and (B), and [001] in (C) and (D). In (A) and (C), the framework is shown without guest molecules, highlighting its porous nature. In (B) and (D), yellow spheres represent the pore diameters, emphasizing the available space within the structure.

3.3.2 Rietveld Refinement of `PC-MOF`

The structural model of `PC-MOF`, derived from 3D-ED analysis, was subsequently refined using the Rietveld [75] approach against PXRD data of the mechanochemically synthesized product. This refinement revealed slight variations in the lattice parameters, specifically a = 20.813(3) Å, b = 7.1431(5) Å, c = 16.9679(15) Å, and $\beta = 126.935(6)°$. While such changes could potentially result from distortions in the TEM data [43], they are most likely attributable to variations in solvent content. The high vacuum conditions inside the transmission electron microscope (approximately 10^{-9} bar) facilitate the desorption of guest molecules from the MOF cavities, leading to an almost empty `PC-MOF` structure in the 3D-ED analysis. In contrast, the PXRD data indicate that the channels are occupied with water molecules.

This discrepancy is further confirmed by the Rietveld refinement of the 3D-ED model, which significantly underestimates the intensity of the first peak at 10.61°. This peak is particularly sensitive to channel occupancy, as demonstrated by calculations using a completely empty model, where the peak intensity is markedly reduced (Figure 3.11A). Additionally, the Fourier difference map derived from the PXRD-refined model displays a broad electron density distribution within the channels (Figure 3.11C), confirming the presence of water. However, the inherent disorder of the water molecules within the channels complicates their precise positional refinement using the Rietveld method.

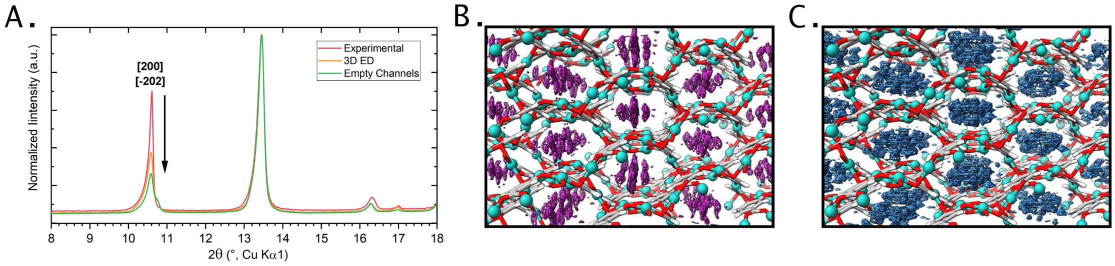

Figure 3.11: (A) Experimental PXRD profile compared with calculated patterns from the 3D-ED model, both with and without guest molecules in the framework channels. (B) and (C) Superposition of the structural model ([101] direction) with the Fourier difference maps from 3D-ED and PXRD analyses, respectively. The maps are displayed at isosurface levels of $2\sigma[\Delta V(r)]$ and $2\sigma[\Delta\rho(r)]$.

The Rietveld refinement [75] of `PC-MOF` was conducted using `TOPAS Academic software` [76], utilizing the atomic coordinates obtained from the 3D-ED model as the starting point. In this process, the ligand molecules were treated as semi-rigid bodies, allowing the torsion angles associated with single bonds to be freely refined. This semi-rigid body refinement approach accommodates the rotation of flexible parts of the ligands, enhancing the accuracy of the structural model. The refinement converged with an $R_{\text{wp}} = \mathbf{8.95\%}$. The final refined structural model maintains the same framework topology as determined by the 3D-ED analysis, confirming the reliability and consistency of the refinement process. Although the disorder of the water molecules prevents precise positional refinement through the Rietveld approach, the combined use of 3D-ED analysis and semi-rigid body refinement effectively models the solvent content.

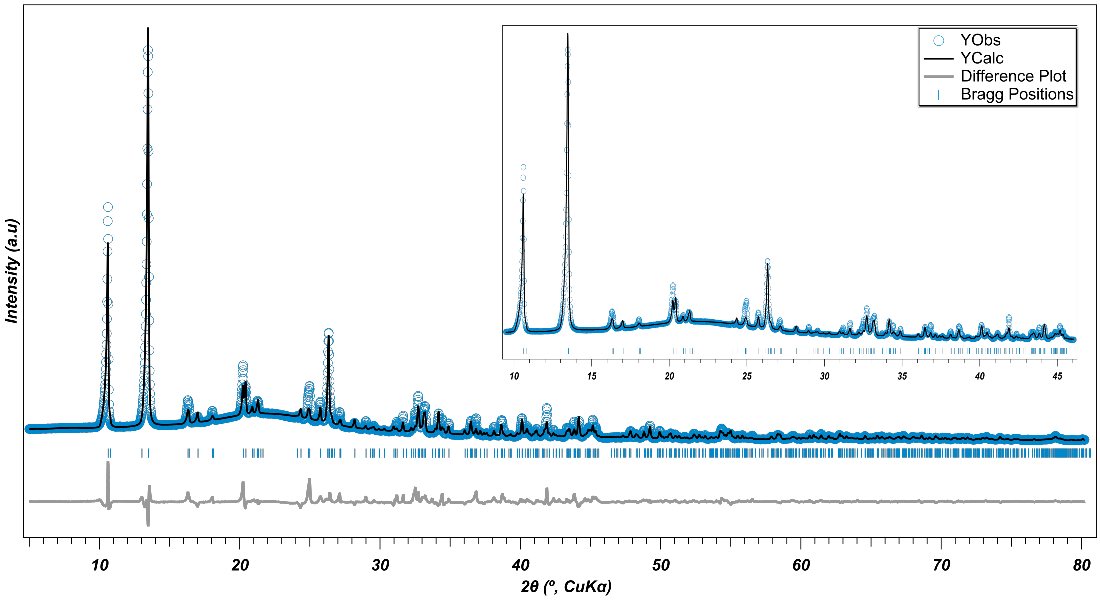

Figure 3.12: Profile fit from Rietveld refinement of the `PC-MOF` crystal structure, obtained after dynamical refinement of 3D-ED data, compared to the experimental PXRD pattern.

3.4 Thermal Stability and Phase Transition Analysis of `PC-MOF`

To assess the thermal stability of `PC-MOF`, in situ PXRD measurements were conducted by gradually increasing the temperature from room temperature to 155 °C. The PXRD patterns revealed significant structural changes as the temperature increased. Notably, around 100 °C, the data indicated the beginning of a phase transition, characterized by the appearance of new diffraction peaks and changes in existing ones. This transition suggests a structural rearrangement within the `PC-MOF` framework, potentially involving the removal or reorientation of guest molecules within the porous channels. As the temperature approached 155 °C, a noticeable loss in crystallinity was observed, evidenced by the broadening and decreasing intensity of diffraction peaks. This degradation signifies the breakdown of the ordered framework structure of `PC-MOF`, likely due to the thermal removal of guest molecules and the resulting destabilization of the MOF.

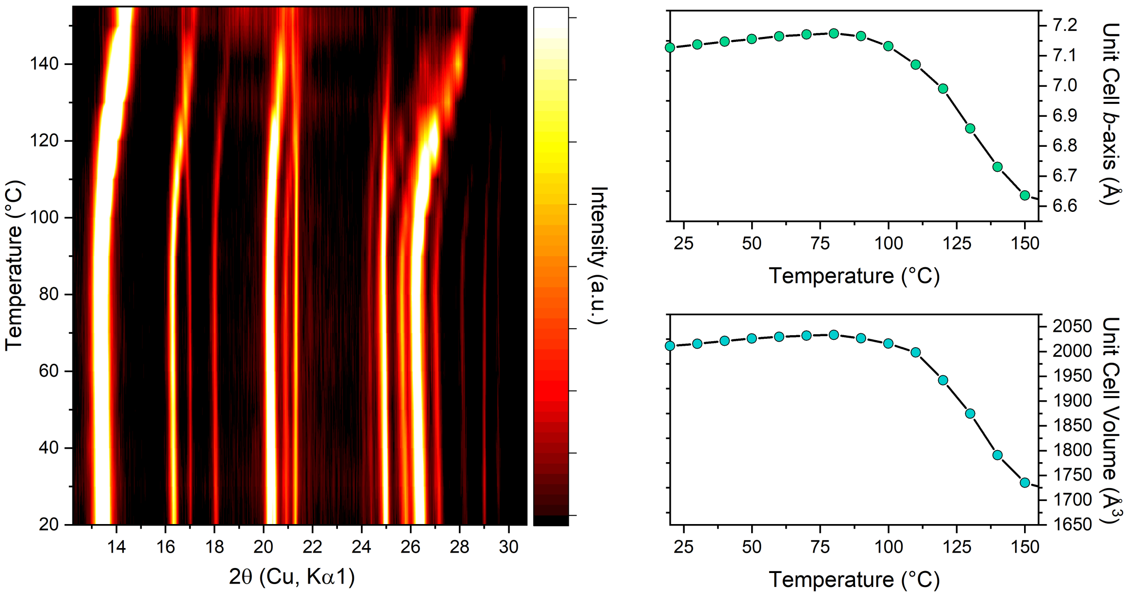

Figure 3.13: Temperature-dependent PXRD patterns and corresponding unit cell evolution. (Left) Contour plot showing intensity variations of diffraction peaks as a function of temperature from 20°C to 150°C. (Right) Graphs displaying the temperature-dependent behavior of the unit cell b-axis (top) and unit cell volume (bottom), indicating a structural phase transition or thermal expansion around 125°C.

3.4.1 Rapid Heating and Formation of a High-Temperature Phase

Following these observations, the `PC-MOF` sample was rapidly heated to 150 °C in a porcelain crucible at 150 °C for 60 minutes under open conditions. This fast heating induced an irreversible phase transition, resulting in the formation of a new crystalline phase. The resulting PXRD showed a sample with very low crystallinity, characterized by only a few identifiable peaks against a significant amorphous background (Figure 3.14). However, TEM analysis revealed the presence of a distinct high-temperature (HT) phase. This new phase was successfully solved using 3D-ED characterization performed under the same instrumental setup and conditions as those used for the original `PC-MOF`. Despite the presence of multiple reflections from different crystals due to the small size of the grains, data reduction was effectively carried out using `PETS2.0` software.

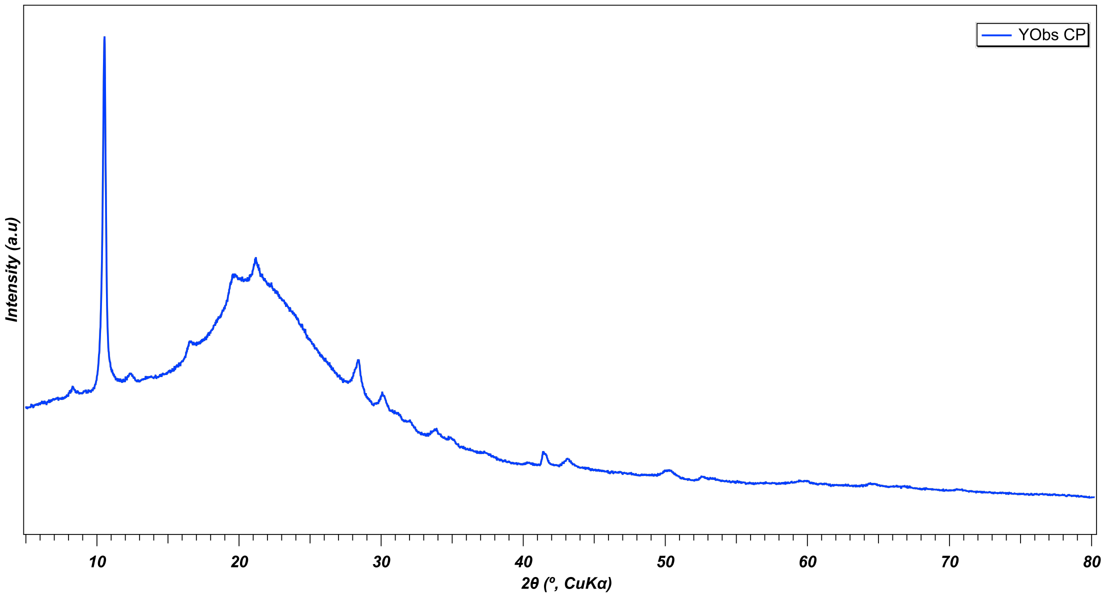

Figure 3.14: Experimental PXRD pattern of the new `CP` phase.

3.4.2 Structural Characterization of the High-Temperature Phase

The structural analysis of the HT phase showed a triclinic unit cell with parameters a = 5.4032(19) Å, b = 7.404(2) Å, c = 8.7168(15) Å, and angles α = 73.656(17)°, β = 88.24(2)°, and γ = 82.24(2)°. Ab initio structure solution identified the HT phase as a two-dimensional coordination polymer (`CP`) (Table S3.1). Dynamical refinement of the `CP` structure resulted in a significant reduction of the R-factor from **33.35%** in the kinematical refinement to **16.35%**. Additionally, hydrogen atom positions were all localized within the electrostatic potential map (Figure 3.15B).

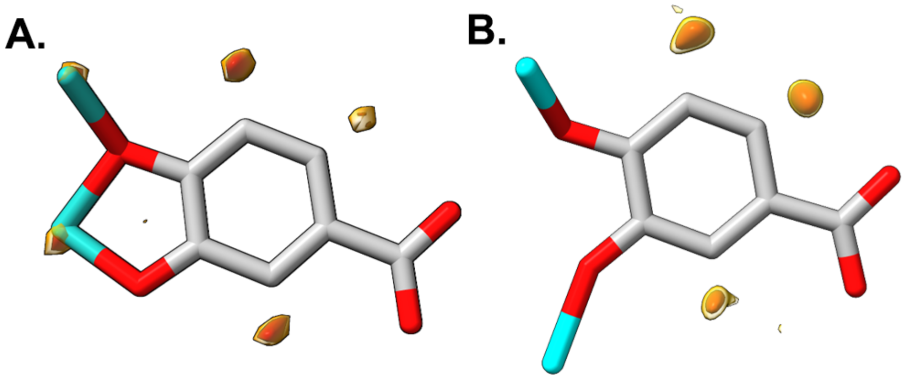

Figure 3.15: Fourier difference map calculated on the structural model without H atoms, respectively for: (B) `PC-MOF`; (C) `CP`. The resulting electrostatic potential map allows, in both cases, to identify the H atoms positions. Isosurface level: $2\sigma[\Delta V(r)]$ in yellow, $2.5\sigma[\Delta V(r)]$ in orange.

The asymmetric unit of the `CP` consists of a single PC_3^- unit and two copper atoms (Figure 3.16A). The overall unit cell contains two PC_3^- molecules and three copper atoms, with one of the copper atoms occupying a special position. The building units of the `CP` are identical to those in the original `PC-MOF`. In contrast to the `PC-MOF`, where the bonding of four H_3PC molecules results in a corrugated layer, the `CP` forms a double-chain structure with a flat geometry along the [001] direction due to bonding with a dimeric square planar cluster of `CU1` atoms (Figure 3.16B). This structure features slipped layers, where each layer is slightly offset relative to adjacent layers during stacking while maintaining a constant interlayer distance of 3.106 Å. The `CU2` atom occupies an inversion center, acting as a bridge between different layers. Both `CU1` and `CU2` atoms exhibit distorted square planar geometries. A key distinction lies in the coordination environment of `CU2`, which extends only along two dimensions, resulting in a distinctive layered staircase-like structure. In this arrangement, the layers are connected in a two-dimensional manner and exhibit stepwise growth along the [110] direction (Figure 3.17A and Figure 3.17B).

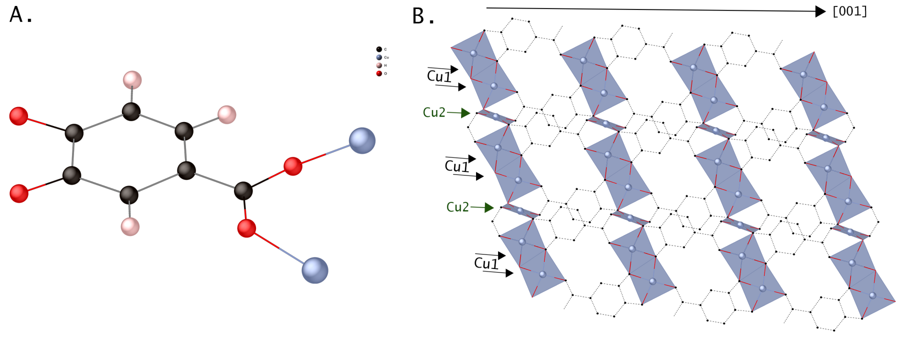

Figure 3.16: (A) Asymmetric unit of the `CP` structure, showing the coordination environment of the organic linker. (B) Representation of the layered structure of `CP` along the [001] direction. The figure highlights the dimeric `CU1` clusters (blue polyhedra) and the bridging role of `CU2` ions (green arrows) between different layers of the framework.

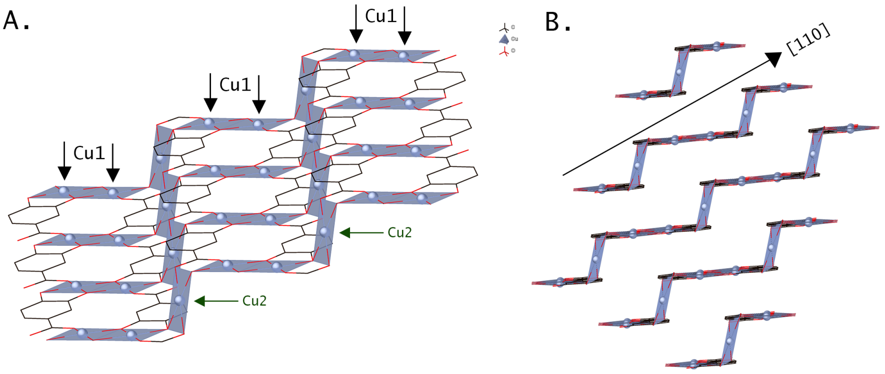

Figure 3.17: Two views of the crystal structure highlighting a unique stair-like motif. (A) The roles of different copper atoms (`CU1` and `CU2`) are illustrated, showing their positioning within the structure. (B) A packed view of the unit cell is displayed, emphasizing the growth direction of the stair-like feature along the [110] direction.

3.5 Conclusions

In this chapter, we successfully synthesized the `PC-MOF` using a rapid and environmentally friendly mechanochemical approach. By employing liquid-assisted grinding with just a drop of water, we achieved higher yields in shorter reaction times compared to the conventional aqueous solution reaction method. The mechanochemical synthesis not only enhanced the reaction kinetics but also demonstrated the advantages of solvent-free conditions and minimal byproduct formation, aligning with green chemistry principles. The small crystal size inherent to mechanochemically synthesized materials posed challenges for structural characterization using traditional XRD techniques. However, we overcame these obstacles by using 3D-ED, specifically cRED implemented with the `LibraEDT` software (**Chapter** 2). This allowed for the precise structural determination of the `PC-MOF` at the nanoscale, including the localization of hydrogen atoms and guest water molecules within the framework channels. Dynamical refinement of the 3D-ED data significantly improved the accuracy of the structural model, reducing the R-factor and providing a more reliable representation of the `PC-MOF` structure. The refined model was further validated through Rietveld refinement against PXRD, confirming the consistency and reliability of our findings. Thermal stability studies revealed that the `PC-MOF` undergoes a phase transition upon heating, leading to the formation of a new high-temperature phase (`CP`). This phase was characterized using 3D-ED, highlighting the method's capability to resolve structures even when traditional PXRD suggests poor crystallinity.

Overall, this work demonstrates the efficacy of mechanochemical synthesis combined with advanced electron diffraction techniques in the development and characterization of novel MOFs.

3.6 Supplementary Information

Table S3.1: Crystallographic data for PC-MOF and CP from 3D-ED analysis.

	PC-MOF	**CP**
Formula	$Cu_3C_{14}O_{8.75}H_6$	$Cu_3C_{14}O_8H_6$
Formula weight	524.84	331.55
Temperature/K	293	293
Crystal system	Monoclinic	Triclinic
Space group	C2/c	P-1
a/Å	21.171(7)	5.4032(19)
b/Å	7.005(3)	7.404(2)
c/Å	16.903(6)	8.7168(15)
$\alpha/°$	90.00	73.656(17)
$\beta/°$	127.23(2)	88.24(2)
$\gamma/°$	90.00	82.24(2)
Volume/Å^3	1995.92(14)	331.55(16)
Z	4	1
$\rho_{\mathbf{calc}}$**/g/cm^3**	1.680	2.468
F(000)	289.8	71.0
Crystal size/mm^3	0.004	0.02
Radiation	Electrons 120 kV ($\lambda = 0.0335$)	Electrons 120 kV ($\lambda = 0.0335$)
$2\Theta_{\mathbf{min,max}}/°$	0.11, 1.15	0.12, 1.05
Reflections collected/unique	*R(int) = 0.1953*	*R(int) = 0.1325*
R [>2σ(I)], wR	$R_1 = 0.1175, wR = 0.1315$	$R_1 = 0.1640, wR = 0.1643$

Listing S3.1: TOPAS Input File for PC-MOF Refinement

```
r_exp 0.8241775782 r_exp_dash 2.381867438 r_wp 8.250851878 r_wp_dash 23.84490423 r_p 5.428871087 r_p_dash
     24.40381218 weighted_Durbin_Watson 0.06471004022 gof 2.01101231
iters 100000
xdd "..\PC-MOF_Cu_03_s.xy"
    r_exp 0.8241775782 r_exp_dash 2.381867438 r_wp 8.250851878 r_wp_dash 23.84490423 r_p 5.428871087 r_p_dash
     24.40381218 weighted_Durbin_Watson 0.06471004022 gof 2.01101231
    bkg  11304.84721 -7210.180332 -221.5734406 3245.26905 -2383.149093 -361.0023369 1775.483834 -1359.284579
      -43.19925046 1088.555539 -1081.970547 88.04686003 609.7421722 -539.3681827 167.2331584 293.8954915
      -396.880857 170.3415251 234.6033242 -331.7371728 171.8699769 232.6986729 -231.0855467 86.96707724
     54.80195475
    LP_Factor( 27.3)
    Specimen_Displacement( 0.0138578699)
    Mixture_LAC_1_on_cm( 40.95188925)
    mixture_MAC 23.98816586
    mixture_density_g_on_cm3 1.707170506
    Rp 260
    Rs 260
    Simple_Axial_Model( 16.20136703)
    lam
        ymin_on_ymax  0.0001
        la  1 lo  1.540596 lh  0.07189831438 lg  1.384652476
    str

        ' ========= Parameters =========
        prm !bEqCu 0.954842034
        prm !bEqLig  0.205038462
        prm !bEqOs 4.57949644

        prm !occOs 0.188
        ' ========= Parameters =========

        ' ========= View Structure =========
        view_structure
        ' ========= View Structure =========

        ' ========= Fourier Difference =========
        'fourier_map 1
        'fourier_map_formula = 2Fobs - Fcalc;
        'fourier_map_formula = Fobs - Fcalc;
        ' ========= Fourier Difference =========


        site C2Z        x  0.75917` y  0.19080` z  0.85456` occ C   1.0      beq = bEqLig;
        site C1Z        x  0.84300` y  0.14649` z  0.94233` occ C   1.0      beq = bEqLig;
        site C3Z        x  0.70492` y  0.28407` z  0.86303` occ C   1.0      beq = bEqLig;
        site C7Z        x  0.73617` y  0.13554` z  0.76230` occ C   1.0      beq = bEqLig;
        site O1Z        x  0.85969` y  0.17522` z  1.02436` occ O   1.0      beq = bEqLig;
        site O2Z        x  0.89138` y  0.08375` z  0.92954` occ O   1.0      beq = bEqLig;
        site C4Z        x  0.62746` y  0.32230` z  0.77924` occ C   1.0      beq = bEqLig;
        site C6Z        x  0.65870` y  0.17356` z  0.67852` occ C   1.0      beq = bEqLig;
        site O3Z        x  0.56980` y  0.40955` z  0.77677` occ O   1.0      beq = bEqLig;
        site C5Z        x  0.60446` y  0.26703` z  0.68699` occ C   1.0      beq = bEqLig;
        site Cu1Z       x  0.46407` y  0.36035` z  0.64182` occ Cu  1.0      beq = bEqCu;
        site O4Z        x  0.52650` y  0.31022` z  0.60736` occ O   1.0      beq = bEqLig;

        site Os2        x  0.507    y  0.786    z  0.671    occ O    =1-occOs;   beq = bEqOs;
```

```
        site Os1        x  0.598    y  0.844    z  0.849    occ O    =occOs;   beq  = bEqOs;


        rigid
            z_matrix   C2Z
            z_matrix   C1Z    C2Z     1.4971633
            z_matrix   C3Z    C2Z     1.3910211     C1Z     122.081590
            z_matrix   C7Z    C2Z     1.3923071     C1Z     117.890536    C3Z         179.985890
            z_matrix   O1Z    C1Z     1.2338420     C2Z     117.281604    C3Z     @   8.64557`
            z_matrix   O2Z    C1Z     1.2348709     C2Z     119.165589    O1Z         179.907655
            z_matrix   C4Z    C3Z     1.3936339     C2Z     120.077977    C1Z         -179.984494
            z_matrix   C6Z    C7Z     1.3933911     C2Z     119.910370    C1Z         179.916288
            z_matrix   O3Z    C4Z     1.3304521     C3Z     126.320197    C2Z         179.825988
            z_matrix   C5Z    C4Z     1.3923218     C3Z     119.893024    O3Z         -179.851345
            z_matrix   Cu1Z   O3Z     @  2.03942`     C4Z    @  107.38465`   C3Z        @ -164.84100`
            z_matrix   O4Z    C5Z     1.3858826     C4Z     116.393651    C3Z         -179.980839

        Rotate_about_axies(@ -50.97981`,@  25.07839`,@ -67.19787`)
        Translate(@  0.75917`,@  0.19080`,@  0.85456`)


        Out_CIF_STR("PCMOF_Rietveld_Rigid.cif")
        Out_X_Yobs_Ycalc_Diff_csv(PCMOF_Rietveld_X_Yobs_Ycalc_Diff.xy)
        Out_Tick("PCMOF_Rietveld_Ticks.xy")

        LVol_FWHM_CS_G_L( 1, 120.1113001, 0.89, 167.9166462,,,@, 188.670389)
        TCHZ_Peak_Type(@, -0.008971194147,@, -0.01160573148,@, -0.0003922816385,, 0,@, 0.003871871028_LIMIT_MIN_0.0001,, 0)
        r_bragg  4.924856794
        phase_MAC 23.98816586
        phase_name "PCMOF_Rietveld_Rigid"
        MVW( 2075.1272, 2018.446385, 100)
        space_group C2/c
        scale @ 0.0006927507246
        Phase_LAC_1_on_cm( 40.95188925)
        Phase_Density_g_on_cm3( 1.707170506)
        a @ 20.81364179
        b @ 7.142483548
        c @ 16.98328694
        be @ 126.921186
        site Cu2 num_posns 4 x  0.5 y  0.5 z  0.5 occ Cu  1 beq =bEqCu; :  0.954842034
        PO_Spherical_Harmonics(sh_671377d2_1a8, 4 load sh_Cij_prm { y00 !sh_671377d2_1a8_c00 1 y20 sh_671377d2_1a8_c20 -0.2764975888 y22m sh_671377d2_1a8_c22p 0.09652935826 y22p sh_671377d2_1a8_c22m 0.1293664322 y40 sh_671377d2_1a8_c40 -0.1301012407 y42m sh_671377d2_1a8_c42p -0.02625562882 y42p sh_671377d2_1a8_c42m 0.005546554056 y44m sh_671377d2_1a8_c44p 0.01963150391 y44p sh_671377d2_1a8_c44m -0.05679835871 } )
```

Listing S3.2: PCMOF Crystallographic Information Framework file

```

#======================================================================
# CRYSTAL DATA
#----------------------------------------------------------------------
data_PCMOF

_chemical_name_common                  'C14 H6 Cu3 O8, 0.754(O1)'
_cell_length_a                         21.171(7)
_cell_length_b                         7.005(3)
_cell_length_c                         16.903(6)
_cell_angle_alpha                      90.000000
_cell_angle_beta                       127.23(2)
_cell_angle_gamma                      90.000000
_cell_volume                           1995.917904
_space_group_name_H-M_alt              'C 2/c'
_space_group_IT_number                 15

loop_
_space_group_symop_operation_xyz
   'x, y, z'
   '-x, -y, -z'
   '-x, y, -z+1/2'
   'x, -y, z+1/2'
   'x+1/2, y+1/2, z'
   '-x+1/2, -y+1/2, -z'
   '-x+1/2, y+1/2, -z+1/2'
   'x+1/2, -y+1/2, z+1/2'

loop_
   _atom_site_label
   _atom_site_occupancy
   _atom_site_fract_x
   _atom_site_fract_y
   _atom_site_fract_z
   _atom_site_adp_type
   _atom_site_U_iso_or_equiv
   _atom_site_type_symbol
   Cu1        1.0     0.46633(16)  0.3257(8)    0.64345(18)  Uiso   0.021300 Cu
   Cu2        1.0     0.500000     0.500000     0.500000     Uiso   0.021300 Cu
   O4         1.0     0.5304(4)    0.3016(14)   0.6002(5)    Uiso   0.032100 O
   C1         1.0     0.8478(4)    0.1651(11)   0.9354(5)    Uiso   0.020000 C
   C4         1.0     0.6290(2)    0.2956(11)   0.7741(4)    Uiso   0.020000 C
   O1         1.0     0.8644(4)    0.1849(18)   1.0186(5)    Uiso   0.032100 O
   C2         1.0     0.7637(2)    0.2018(8)    0.8476(4)    Uiso   0.020000 C
   O3         1.0     0.5688(4)    0.3538(16)   0.7733(5)    Uiso   0.032100 O
   C5         1.0     0.6087(4)    0.2663(11)   0.6798(4)    Uiso   0.020000 C
   O2         1.0     0.8965(4)    0.117(2)     0.9215(5)    Uiso   0.032100 O
   C6         1.0     0.6658(4)    0.2046(14)   0.6694(4)    Uiso   0.020000 C
   C3         1.0     0.7066(4)    0.2633(10)   0.8580(4)    Uiso   0.020000 C
   C7         1.0     0.7434(2)    0.1725(13)   0.7533(4)    Uiso   0.020000 C
   Os2        0.1889  0.507(3)     0.786(13)    0.671(3)     Uiso   0.058000 O
   Os1        0.1880  0.598(3)     0.844(14)    0.849(3)     Uiso   0.058000 O
   H6         1.0     0.651763     0.184130     0.604368     Uiso   0.024000 H
   H3         1.0     0.720599     0.283390     0.923062     Uiso   0.024000 H
   H7         1.0     0.782767     0.130155     0.746117     Uiso   0.024000 H
```

Listing S3.3: CP Crystallographic Information Framework file

```

#=======================================================================
# CRYSTAL DATA
#-----------------------------------------------------------------------
data_CP

_chemical_name_common                  'C14 H6 Cu3 O8'
_cell_length_a                         5.403(2)
_cell_length_b                         7.404(2)
_cell_length_c                         8.7168(15)
_cell_angle_alpha                      73.656(17)
_cell_angle_beta                       88.24(2)
_cell_angle_gamma                      82.24(2)
_cell_volume                           331.552119
_space_group_name_H-M_alt              'P -1'
_space_group_IT_number                 2

loop_
_space_group_symop_operation_xyz
   'x, y, z'
   '-x, -y, -z'

loop_
   _atom_site_label
   _atom_site_occupancy
   _atom_site_fract_x
   _atom_site_fract_y
   _atom_site_fract_z
   _atom_site_adp_type
   _atom_site_U_iso_or_equiv
   _atom_site_type_symbol
   Cu2        1.0     1.2005(13)  -0.1043(8)    0.9226(5)   Uiso  0.021600 Cu
   Cu1        1.0     0.500000     0.500000     1.000000    Uiso  0.022700 Cu
   O1         1.0     0.743(3)     0.1480(18)   0.2734(13)  Uiso  0.030000 O
   C1         1.0     0.5702(17)   0.2506(10)   0.3208(13)  Uiso  0.019300 C
   O2         1.0     0.411(3)     0.3614(18)   0.2242(13)  Uiso  0.028000 O
   O3         1.0     0.884(3)     0.056(2)     0.8677(10)  Uiso  0.030000 O
   C6         1.0     0.3097(17)   0.3417(14)   0.6938(8)   Uiso  0.019300 C
   C3         1.0     0.7379(16)   0.1436(13)   0.6015(7)   Uiso  0.019300 C
   C2         1.0     0.5549(13)   0.2425(8)    0.4882(7)   Uiso  0.019300 C
   C7         1.0     0.3399(17)   0.3402(13)   0.5346(7)   Uiso  0.019300 C
   C4         1.0     0.7060(16)   0.1428(13)   0.7611(7)   Uiso  0.019300 C
   O4         1.0     0.477(2)     0.2388(13)   0.9639(11)  Uiso  0.023000 O
   C5         1.0     0.4927(14)   0.2433(13)   0.8070(7)   Uiso  0.019300 C
   H6         1.0     0.162811     0.410542     0.725353    Uiso  0.023100 H
   H3         1.0     0.885713     0.076143     0.569678    Uiso  0.023100 H
   H7         1.0     0.212650     0.406395     0.456992    Uiso  0.023100 H
```

Chapter 4

Structure Determination of a Chiral MOF by 3D-Electron Diffraction

4.1 Introduction

Chirality, the geometric property where a structure cannot be superimposed on its mirror image (Figure 4.1), is fundamental in materials science and the basis of life, as all amino acids in living organisms are left-handed (L-enantiomers) while naturally occurring sugars are right-handed (D-enantiomers), a phenomenon that significantly influences biological processes and the development of functional materials. Chiral materials are crucial in applications such as asymmetric catalysis [77], enantioselective separations [78], and chiral sensing [79], where the distinct behaviors of enantiomers can profoundly influence performance and effectiveness. Therefore, accurate identification and control of chirality are critical in the design and synthesis of advanced materials.

Determining the correct enantiomorph in crystallography, particularly for materials crystallizing in chiral space groups, presents specific challenges. Conventional

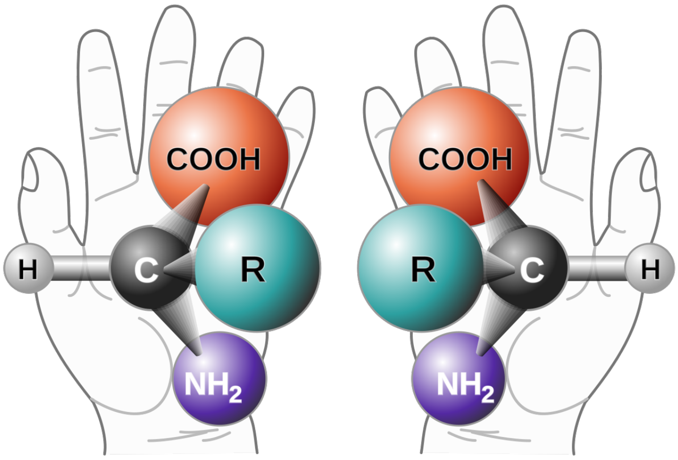

Figure 4.1: Representation of molecular chirality, showing non-superimposable mirror-image enantiomers with the central carbon (C) as the chiral center.

diffraction techniques, such as SCXRD, rely heavily on anomalous scattering effects to determine absolute structures, often necessitating the presence of heavier atoms to induce sufficient differences between enantiomers [53, 54]. However, for materials composed predominantly of lighter atoms, anomalous scattering is weak, making it difficult to distinguish between enantiomers using XRD alone.

Beam sensitivity further complicates absolute structure determination [80]. In XRD, enhancing anomalous scattering signals or achieving high-resolution data often requires increased exposure times or higher beam intensities. For beam-sensitive materials, such as MOFs, this prolonged exposure leads to significant radiation damage, resulting in the loss of crystallinity or alteration of the material's structure [80]. As a result, the quality of diffraction data is compromised, hindering accurate determination of the absolute structure. This challenge is particularly pronounced for small crystals, where the surface-to-volume ratio is high, and radiation effects are more destructive.

ED offers a promising alternative to XRD for absolute structure determination, particularly for beam-sensitive materials. As discussed in the **Chapter 1.2.4**, the stronger interaction of electrons with matter enables the analysis of smaller and more sensitive crystals while requiring significantly lower exposure times [1, 81].

Furthermore, as also discussed in the Chapter 1.2.7.2.3, dynamical scattering effects in ED break Friedel's law, allowing for the direct determination of absolute structure through measurable differences in intensities between Friedel-related reflections. By incorporating these dynamical effects into the refinement process, accurate determination of the absolute structure can be achieved, even for materials composed predominantly of lighter atoms [6].

In this chapter, we present the crystallographic analysis of a chiral MOF, `MUDEC4`, composed of Zinc and Pyridylcarbohydrazides, crystallizing in the enantiomorphic space group pair $P3_2$ and $P3_1$. We will go through the steps required to successfully identify the correct enantiomorph and its space group, demonstrating that it is possible to determine absolute structure configuration of individual crystals.

4.2 Synthetic Steps of the Chiral MOF MUDEC4

The precursors and the final chiral metal-organic framework were synthesized and provided by Dr. Claudio A. Jiménez from the University of Concepción, Chile (UdeC) and Dr. Jorge Pasán from the University of La Laguna (ULL), Spain.

As summarized in the following Table 4.1, each compound was sequentially synthesized to facilitate the preparation of the final chiral metal-organic framework, `MUDEC4`.

Table 4.1: List of Compounds and Their Assigned Numbers

Number	Compound Name
1	5-Methyl-2,4-dihydro-3H-pyrazol-3-one
2	2-Butyl-5-methyl-2,4-dihydro-3H-pyrazol-3-one
3	(1-Butyl-5-hydroxy-3-methyl-1H-pyrazol-4-yl)(phenyl)methanone
4	(E)-N'-((1-Butyl-5-hydroxy-3-methyl-1H-pyrazol-4-yl) (phenyl)methylene)isonicotinohydrazide (H_2L)

4.2.0.1 Synthesis of Compound 1

To a solution of ethyl acetoacetate (64 mL, 0.500 mol) in 100 mL ethanol, add dropwise hydrazine hydrate 80% v/v (30.7 mL, 0.626 mol) under vigorous stirring. Continue stirring until the reaction mixture reaches room temperature, then cool to 0°C for a couple of hours. Filter the mixture and wash with a small amount of cold ethanol to obtain white crystals. **Yield:** 95%.

4.2.0.2 Synthesis of Compound 2

In a capped flask, combine Compound 1 (40.0 g, 0.408 mol) and bromobutane (57.3 mL, 0.530 mol) in 50 mL of dioxane. Stir the mixture at 110°C for 2 days. After cooling to room temperature, evacuate the solvent under reduced pressure. Partially neutralize the reaction mixture (pH $\approx$ 6) with 10% w/v $NaHCO_3$ and extract with two 40 mL portions of dichloromethane. Combine the organic layers, dry with Na_2SO_4, and evaporate under reduced pressure to obtain a crude oil. Suspend the crude oil in 150 mL of boiling hexane for a few minutes, allow it to cool to room temperature, and then to –18°C overnight. Filter the solid (if no solid appears, discard the hexane and boil the crude oil with fresh hexane. Repeat until crystals form) and recrystallize from ether/hexane (1:1) at 8°C to obtain colorless crystals. **Yield:** 40%.

4.2.0.3 Synthesis of Compound 3

In a 500 mL flask under vigorous stirring and a dry atmosphere, dissolve Compound 2 (5.36 g, 34.8 mmol) in a suspension of $Ca(OH)_2$ (4.88 g, 65.9 mmol) and 100 mL of anhydrous dioxane. Reflux the mixture for 1 hour and cool to room temperature. Add benzoyl chloride (5.3 mL, 44.7 mmol) dropwise and resume refluxing overnight. Once cooled to room temperature, evacuate the solvent under reduced pressure. Partially neutralize the reaction mixture (pH $\approx$ 6) with 10% w/v HCl and extract with three 70 mL portions of dichloromethane. Combine the organic layers, dry with

Na_2SO_4, and evaporate under reduced pressure. Dissolve the obtained solid in 50 mL of hot ethanol and slowly add 50 mL of hot water containing $Cu(CH_3COO)_2{\cdot}H_2O$ (3.48 g, 17.4 mmol). Boil and vigorously stir the mixture for 30 minutes, then cool to room temperature and subsequently to 5°C overnight. Filter and wash with cold ethanol-water (1:1). Extract the green-brown solid with HCl 10% w/v and three 70 mL portions of dichloromethane. Combine the organic layers, dry with Na_2SO_4, and evaporate under reduced pressure. Recrystallize from ethanol-water (1:1) to obtain light yellow to colorless crystals. **Yield:** 64%.

4.2.0.4 Synthesis of Compound 4 (H_2L)

In a 100 mL round-bottom flask, dissolve Compound 3 (1 g, 3.9 mmol) and pyridine-4-carbohydrazide (0.54 g, 3.9 mmol) in 40 mL of ethanol. Add 4 drops of glacial acetic acid and reflux the reaction mixture overnight. Without cooling, add 90 mL of boiling deionized water (if the solution turns turbid or precipitates appear, add additional ethanol) and allow to cool to room temperature, then maintain at 5°C overnight. Filter the yellow crystals and wash with cold ethanol-water (3:7). Recrystallize from ethanol-water (3:7) if necessary. **Yield:** 67%.

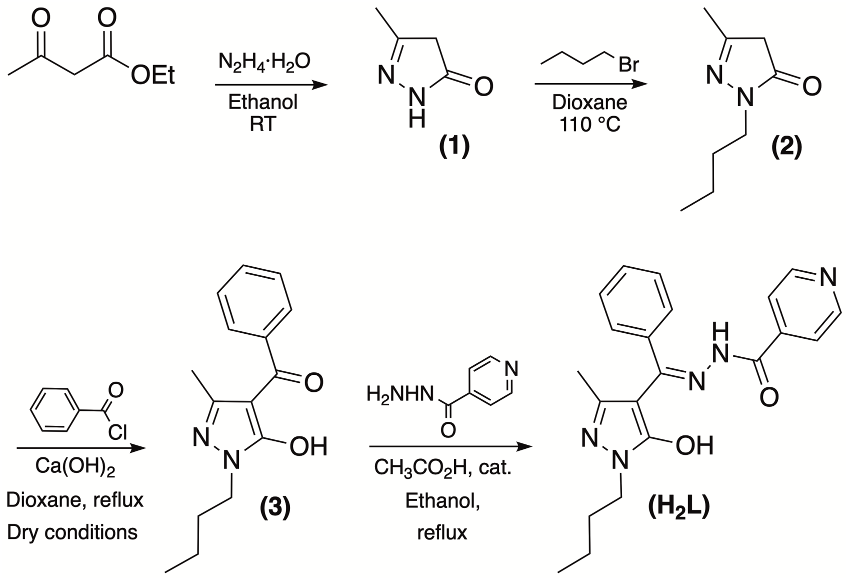

Figure 4.2: Schematic representation of the synthesis steps leading to H_2L.

4.2.0.5 Synthesis of MUDEC4 (ZnL)

The bulk synthesis of `MUDEC4` was carried out in a Teflon-lined stainless-steel autoclave (23 mL capacity). Dissolve Compound 4 (H_2L, 100 mg, 0.265 mmol) and 4,4'-bipyridine (41.4 mg, 0.265 mmol) in 18 mL of dimethylacetamide/methanol (4:1). Add $Zn(CH_3COO)_2 \cdot 2H_2O$ (58.2 mg, 0.265 mmol) and stir until obtaining a homogeneous solution. Seal the autoclave and heat overnight in a preheated oven at 100°C. Upon cooling, collect the tiny yellow crystals by filtration and wash with ethanol until the ethanol remains uncolored. Transfer the solid to a flask, add 60 mL of acetone, stir for one hour, and filter; repeat the acetone wash thrice. Finally, dry the solid under vacuum at 60°C to obtain the final product. **Yield:** 85%.

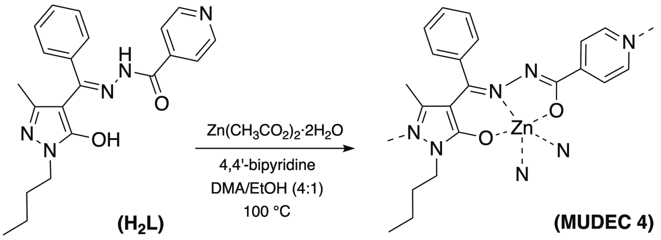

Figure 4.3: Schematic representation of the synthesis steps leading to `MUDEC4` (ZnL).

Scanning Electron Microscope (SEM) images of the crystals with sizes ranging from approximately 100 to 300 nm are shown in Figure 4.4.

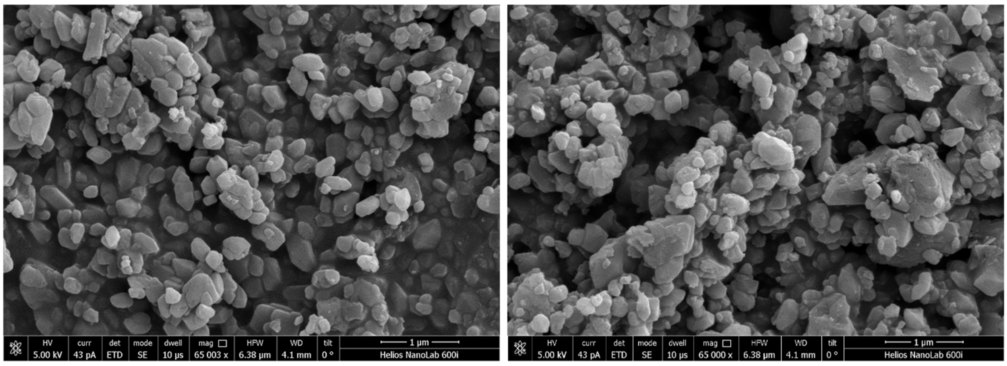

Figure 4.4: SEM images of `MUDEC4` showing the crystal morphology and size distribution, with individual crystals ranging from approximately 100 to 300 nm.

4.3 Structural Characterization of `MUDEC4` Using 3D Electron Diffraction

Crystallographic analysis of the synthesized `MUDEC4` was conducted using 3D-ED. A small quantity of the yellow nanocrystalline powder was carefully transferred into an Eppendorf tube and mixed with isopropanol. The mixture was subjected to sonication for 5 minutes to ensure uniform dispersion before depositing a droplet of the resulting solution onto a holey TEM grid.

High-throughput data acquisition was performed using the `LibraEDT` software (see chapter 2). Due to the beam sensitivity of the crystals (Figure 4.5), cRED was carried out at a rotation speed of 2°/s to ensure rapid data acquisition and minimize crystal exposure to the electron beam. The experimental parameters are detailed in Table 4.2. Multiple datasets were acquired and processed using the `PETS2.0` software [36] following the steps detailed in **Chapter** 1.2.7.1.2. The optimal dataset, based on criteria such as resolution, completeness, and internal R-values, was selected for structure solution and refinement.

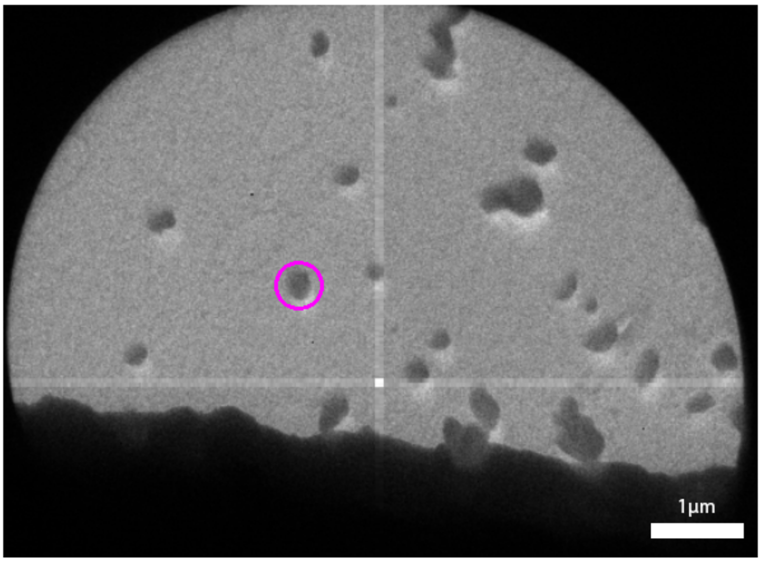

Figure 4.5: MOF crystal used for cRED with the pink circle representing the size of the beam used during data acquisition.

Table 4.2: Experimental Parameters for 3D-ED Data Acquisition of `MUDEC4`

Parameter	**MUDEC4**
Emission Current (μA)	1.20
TEM Mode: Illumination Angle (μrad)	2.00
Beam diameter size (nm)	550
Temperature (K)	298
Exposure Time (ms)	500
Data Collection Duration (s)	60.04
Rotation Speed (Deg/s)	2.00
Oscillation Range (Deg)	1.04
Starting Angle (Deg)	-60.00
Ending Angle (Deg)	60.50

The indexing step during data processing revealed a primitive trigonal setting with lattice parameters $a = b = 12.572(7)$ Å, $c = 14.781(5)$ Å, and angles $\alpha = \beta = 90.00°$, $\gamma = 120.00°$. Identification of the space group was carried out by carefully inspecting the two-dimensional reciprocal sections derived from the three-dimensional reciprocal space. The reflection conditions for the $h0l$ and $0kl$ planes were established as $l = 3n$, consistent with the $P3_1$ extinction symbol (see Figure 4.6).

This extinction symbol is compatible only with three pairs of enantiomorphic space groups:

- $P3_112$ and $P3_212$ (Nos. 151 and 153) within the Laue class $\bar{3}1m$,
- $P3_121$ and $P3_221$ (Nos. 152 and 154) within the Laue class $\bar{3}m$, and
- $P3_1$ and $P3_2$ (Nos. 144 and 145) within the Laue class $\bar{3}$.

Structure solution attempts were performed using these potential space groups. Successful ab-initio [19] structure determination was achieved only in the $P3_1$ and

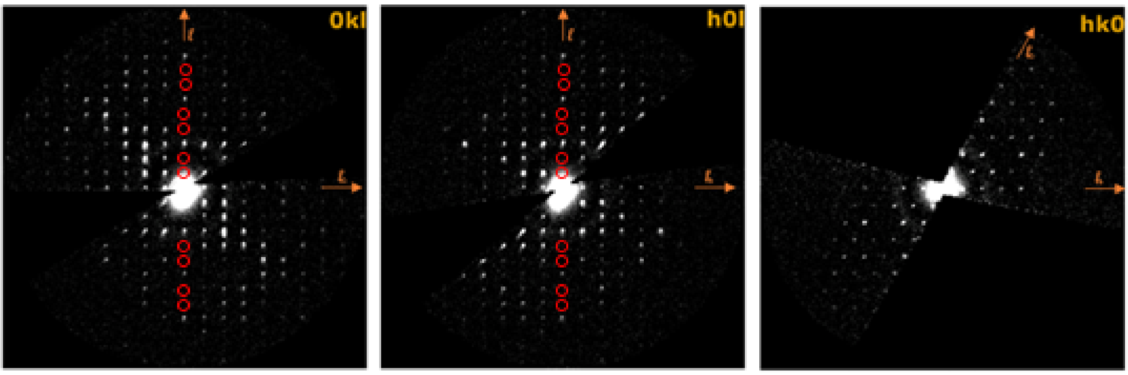

Figure 4.6: Reciprocal lattice sections (0kl, h0l, hk0) used to derive the correct symmetry of `MUDEC4`. Red circles show the missing reflections, confirming the $l = 3n$ condition, corresponding to a 3_1 screw axis.

$P3_2$ space groups using `SHELXT` [46], with all non-hydrogen atoms successfully localized, as illustrated in Figure 4.7.

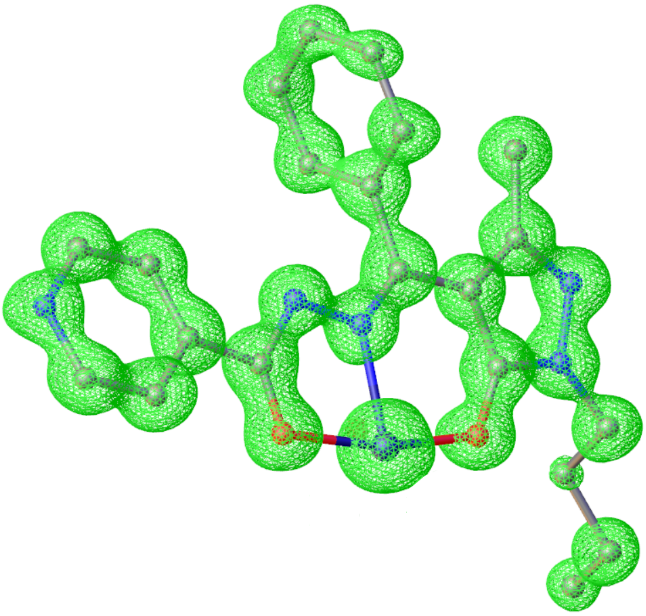

Figure 4.7: Initial model of `MUDEC4` obtained from direct methods using `SHELXT`. The green mesh represents the F_{obs} map contoured at 1σ.

4.3.1 Kinematical Refinement of `MUDEC4`

The obtained model was first refined using kinematical approximations with `JANA2020` [52]. The kinematical refinement employed the traditional least squares method to minimize the differences between the observed and calculated intensities by adjusting the atomic positions and ADPs, as detailed in **Chapter 1.2.7.2.1** and **Chapter 1.2.7.2.2**. During this process, the ADPs were refined isotropically, ensuring that all parameters remained positive to maintain physical plausibility. The kinematical refinement converged with an R_{obs} of **23%**, indicating a reasonable fit between the observed and calculated data.

4.3.2 Dynamical Refinement of `MUDEC4`

As discussed in **Chapter 1.2.7.1.2**, dynamical refinement requires a dedicated `.HKL` file containing OVFs, where every reflection within the frame is fully integrated. For this dataset, the OVFs were created by combining three individual frames with a two-frame overlap.

Dynamical refinements were then carried out using `JANA2020` in combination with `DYNGO` [36] by adjusting not only the atomic parameters such as atomic positions and ADPs, but also the the OVFs's thickness and orientation, as discussed in **Chapter 1.2.7.2.3**.

4.3.3 Absolute Structure Determination of `MUDEC4`

The absolute structure of `MUDEC4` was determined through multiple stages of the refinement process to ensure accuracy and reliability. Initially, the structure was refined in the space group $P3_1$. To assess the absolute configuration, the structure was inverted, transitioning from space group $P3_1$ to its enantiomorphic counterpart $P3_2$, and dynamical refinement was then performed to evaluate differences in refinement statistics. It was crucial to maintain an identical number of refined parameters for both enantiomorphs to ensure a fair comparison between the two refinements.

Under kinematical approximations, we confirm, as expected, that both enantiomorphic space groups $P3_1$ and $P3_2$ refine identically, converging to the same R_{obs} due to the absence of any modeling of the multiple scattering effects that could differentiate their structural parameters.

However, during the early stages of dynamical refinement, where only the scale factors and thickness of each OVF were refined, the R_{obs} for the $P3_1$ space group refinement was observed to be approximately **2.0%** higher than that of the $P3_2$ refinement (see Table 4.3). This discrepancy indicates a subtle preference for the $P3_2$ enantiomorph over $P3_1$ when multiple scattering effects are considered, thereby providing a first evidence for the true absolute configuration of the analyzed `MUDEC4` crystal.

Table 4.3: Comparison of dynamical refinement statistics for the two enantiomorphs. **59** parameters were refined during this first step, corresponding to only scale factors and thickness of each OVF.

Parameter	$P3_1$	$P3_2$
R factors	[4088=1386+2702/**59**]	[4088=1386+2702/**59**]
Damping factor	1.0000	1.0000
GOF(*obs*)	3.35	3.10
GOF(*all*)	2.04	1.88
R(obs) (%)	18.22	16.31
wR(obs) (%)	17.83	16.50
R(all) (%)	28.98	25.67
wR(all) (%)	18.54	17.02

The next step involved the incorporation of additional parameters to enhance the structural model of `MUDEC4`. This involved optimizing the orientation of each overlapping virtual frame to better account for their individual contributions to the diffraction pattern, removing frames that contained many outlier reflections, and performing anisotropic refinement of the ADPs to accurately capture the directional thermal motion of the atoms. These refinements were carefully performed, ensuring that the number of refined parameters remained consistent for both enantiomorphs, allowing for a fair and unbiased comparison. Following these adjustments, the refinement statistics of each enantiomorph ($P3_1$ and $P3_2$), summarized in Table 4.4, were reassessed, with the R_{obs} value for the $P3_2$ enantiomorph found to be **3%** lower than that of the $P3_1$ enantiomorph, reinforcing the determination of the absolute configuration of `MUDEC4`.

Table 4.4: Comparison of dynamical refinement statistics for the two enantiomorphs. **162** parameters were refined during this first step, corresponding to scale factors and thickness of each OVF as well as the atomic positions of each atom and their respective ADP.

Parameter	$P3_1$	$P3_2$
R factors	[3234=1173+2061/**162**]	[3234=1173+2061/**162**]
Damping factor	1.0000	1.0000
GOF(*obs*)	2.42	1.88
GOF(*all*)	1.59	1.24
R(obs) (%)	13.28	10.24
wR(obs) (%)	12.13	8.94
R(all) (%)	24.63	21.04
wR(all) (%)	13.12	10.04

To further confirm the absolute structure determination, a statistical assessment method inspired by Klar et al.[6] and Le Page et al.[82] was employed . This approach involves evaluating whether the observed difference in R-factors between the two enantiomorphs is statistically significant or could have arisen by random chance during the refinement process. By calculating the probability that the lower R_{obs} value for the $P3_2$ enantiomorph is not merely a result of random variations, we ensure that the observed preference is meaningful. If the difference were due to random chance, the probability of correctly identifying the true enantiomorph would be **0.5**. This statistical assessment was performed using `JANA2020` [52], providing a rigorous and quantitative validation of the absolute configuration determination. The results, summarized in Table 4.5, indicate that the probability of identifying $P3_2$ as the correct space group for the analyzed crystal is effectively **1.0**, confirming the reliability of the absolute structure determination.

Table 4.5: Statistical assessment for absolute structure determination.

Method 1 (with correction for experimental noise)	
Total reflections	1936
Better for $P3_1$	735
Better for $P3_2$	1201
Prob(wrong)	1298
z-score	10.591
Prob($P3_2$)	1.000000
Method 2 (without noise correction)	
Total reflections	3234
Better for $P3_1$	1384
Better for $P3_2$	1850
Prob(wrong)	0
z-score	8.194
Prob($P3_2$)	1.000000

The observed **3%** difference in R_{obs} between the two enantiomorphs underscores how multiple scattering effects can partially break Friedel's law, thus providing a mechanism to distinguish one enantiomorph from the other during refinement. In addition, the high z-score from the statistical assessment indicates that random chance is highly unlikely, further supporting that `MUDEC4` crystallizes in the $P3_2$

space group. Although these results demonstrate the feasibility of using 3D-ED for absolute structure determination, it must be stressed that this work represents a proof of concept. Only a limited number of crystals have been analyzed, and further investigations involving multiple samples would be necessary for a more definitive chirality study of this or related materials.

4.3.4 Rietveld Refinement of `MUDEC4`

Rietveld refinement [75] was conducted using `TOPAS Academic` [76], utilizing the structural model obtained from the dynamical refinement of the 3D-ED data as the starting point. In the initial refinement step, the model was directly imported into the `TOPAS Academic` software without altering the atomic positions or ADPs. During this stage, the cell parameters were refined to $a = b = 12.373(4)$ Å, $c = 15.330(5)$ Å, and angles $\alpha = \beta = 90.00°$, $\gamma = 120.00°$. This approach resulted in a low weighted profile R-factor (R_{wp}) of **3.253%**, highlighting the high accuracy and reliability of the dynamical refinement process.

Subsequently, a soft-rigid body refinement was performed to further optimize the structural model of `MUDEC4`. This involved allowing the rotation of the flexible segments of the ligand while simultaneously refining the atomic position of the zinc (Zn) center. Additionally, the ADPs of the phenyl moiety, the butyl chain, the remaining ligand framework, and the Zn atom were individually refined. By enabling these adjustments, the refinement included the flexibility within the ligand and the precise positioning of the Zn centers, leading to an improved fit between the calculated and experimental PXRD patterns (see Figure 4.8). This second refinement stage converged to a reduced R_{wp} of **2.495%**. The `.INP` file prepared to perform Rietveld refinement of `MUDEC4` using `TOPAS Academic` is listed in Listing S1.

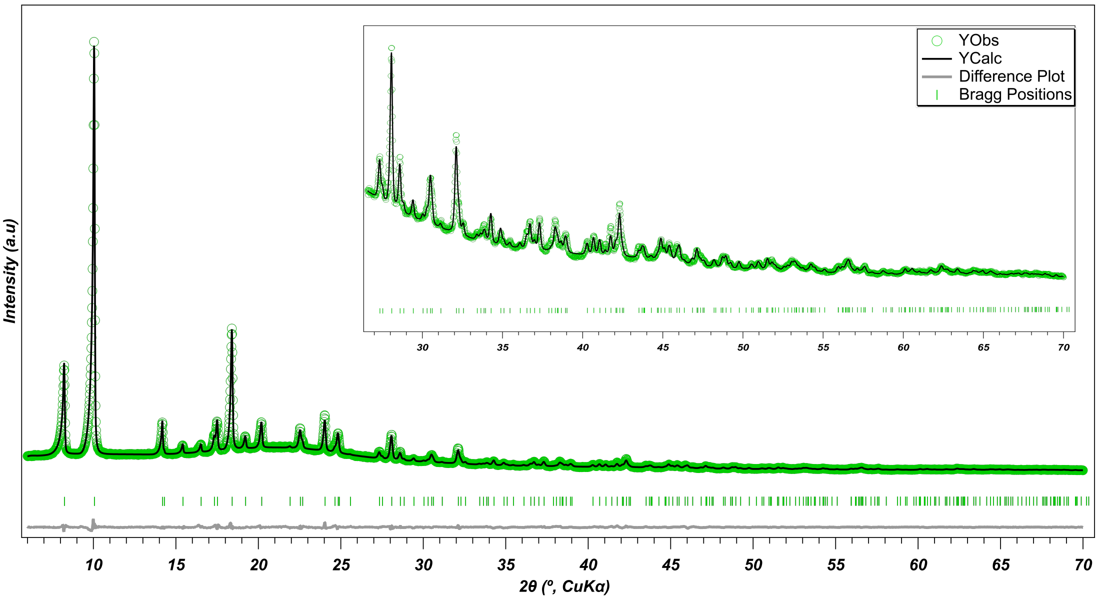

Figure 4.8: Profile fit from Rietveld refinement of `MUDEC4`, obtained after dynamical refinement of 3D-ED data, compared to the experimental PXRD pattern.

4.3.5 Crystal structure description of `MUDEC4`

The crystal structure of the MOF features a zinc (Zn^{2+}) cation in a distorted trigonal bipyramidal coordination geometry. The Zn^{2+} ion is chelated by a tridentate H_2L ligand, which forms both five-membered and six-membered chelate rings through coordinated nitrogen (N) and oxygen (O) donor atoms (Figure 4.9A). This tridentate coordination stabilizes the Zn^{2+} center and contributes to the rigidity of the framework. The Zn^{2+} ion's coordination sphere is further completed by two additional nitrogen atoms from symmetry-related H_2L ligands, with one nitrogen atom originating from the pyrazole moiety and the other from the isonicotinohydrazide moiety of the ligand (Figure 4.9B). This arrangement results in a robust three-dimensional network that supports the MOF's extended structure and porosity.

The crystal structure of the MOF exhibits a relatively low density of 1.088 g/cm^3, which reflects the significant void space within the framework. This porosity is further quantified [74] by a void volume that occupies approximately 35% of the unit cell. The pore limiting diameter of 4.15 Å and the maximum pore diameter of

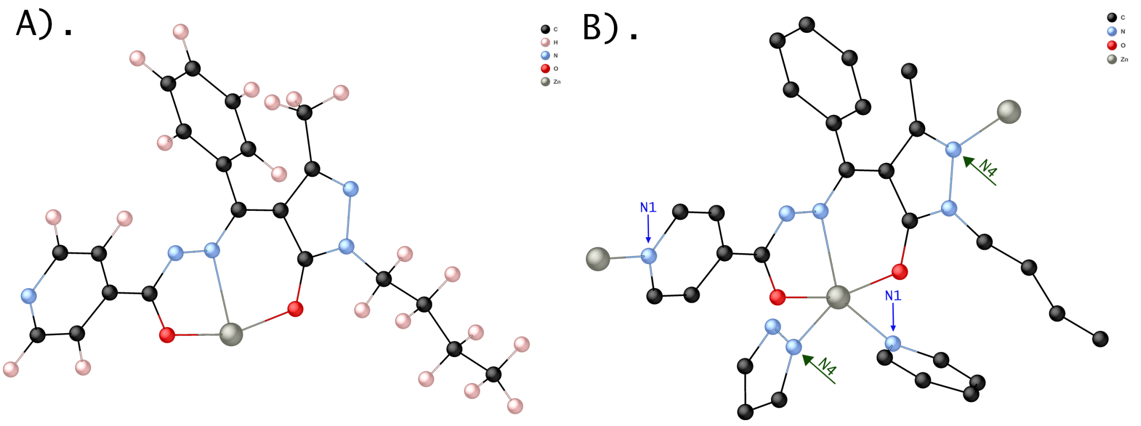

Figure 4.9: The asymmetric unit (A) shows the chelation of the Zn^{2+} ion by the tridentate H_2L ligand. The extended coordination sphere (B) reveals the complete coordination environment of the Zn^{2+} ion, including additional nitrogen atoms from pyrazole and isonicotinohydrazide moieties of neighboring ligands.

5.24 Å suggest that the channels are sufficiently wide to accommodate small guest molecules, making the `MUDEC4` a promising candidate for applications in gas adsorption or molecular separation. A detailed summary of the MOF's pore characteristics can be found in Table S3.

The chirality in this `MUDEC4` arises from the asymmetric coordination environment around the Zn^{2+} ion. The Zn^{2+} is coordinated to five atoms, including the tridentate H_2L ligand and additional nitrogen atoms from neighboring ligands, in a spatially asymmetric geometry. This specific arrangement of ligands creates a chiral coordination sphere around the Zn^{2+} ion, forcing the ligand into a non-planar conformation. Although the H_2L ligand itself is achiral, its coordination to the Zn^{2+} ion induces conformational asymmetry that propagates through the framework. The result is a chiral crystal lattice, which crystallizes in the $P3_2$ space group, with the chirality originating from both the coordination-induced asymmetry and the spatial arrangement of the ligands around the Zn^{2+} ion.

`MUDEC4` exhibits porosity through channels oriented along the c-axis in a zigzag configuration. This zigzag architecture significantly enhances the internal surface area, providing numerous interaction sites for guest molecules. While the zigzag pathway results in a longer diffusion route compared to straight channels, its uninterrupted continuity allows for efficient and free molecular transport along the c-axis.

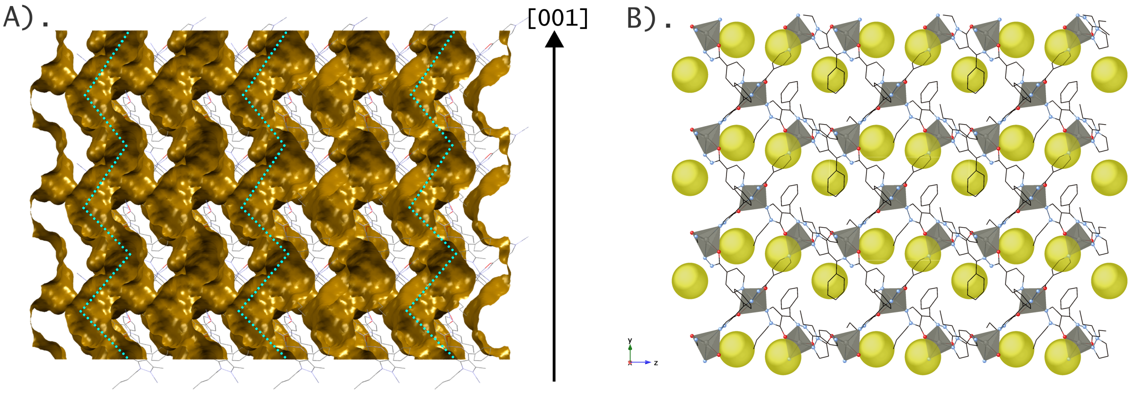

Figure 4.10: Structural visualization of `MUDEC4`'s pore channels and cavities. (A) View along the [110] direction showing zigzag channels along [001] with blue dotted lines tracing the pathway for guest diffusion. (B) Crystal packing with accessible cavities (yellow spheres) and coordination polyhedra illustrating the framework's connectivity.

4.4 Conclusions

In this chapter, we aimed to systematically demonstrate the methodological steps required to determine the chirality of a metal-organic framework. We successfully conducted a comprehensive crystallographic analysis of the chiral MOF `MUDEC4` by using 3D-ED combined with dynamical refinement.

While multiple datasets were collected to ensure the reliability of our findings, we performed dynamical refinement on a limited number of datasets due to time constraints, as this process is notably time-consuming. Our analysis confirmed that

`MUDEC4` crystallizes in the $P3_2$ space group, distinguishing it from its enantiomorphic counterpart $P3_1$. This precise identification is critical for understanding the material's chiral properties, which are essential for applications in asymmetric catalysis, enantioselective separations, and chiral sensing.

However, relying on crystallographic data from few crystal limits the generalizability of our findings. Potential variations among different crystals within the sample batch could influence the enantiomeric composition and structural integrity of `MUDEC4`, rendering our conclusions about its absolute structure and chiral properties preliminary. Future studies should analyze multiple crystals to ensure reproducibility and to identify any enantiomorphs that may exist. Additionally, the absence of complementary characterization techniques, such as circular dichroism (CD) spectroscopy and chiral chromatography, limits our ability to fully assess the enantiopurity of `MUDEC4`. Incorporating these techniques in future research will provide a more comprehensive understanding of the material's enantiomeric purity and its implications for potential applications.

Despite these limitations, our findings provide valuable insights into the structure of `MUDEC4` and lay the groundwork for future investigations. The methodologies developed in this study demonstrate the effective use of 3D-ED combined with dynamical refinement in overcoming challenges associated with absolute structure determination of beam-sensitive materials.

4.5 Supplementary Information

Table S1: Software and Tools Utilized in Crystallographic Analysis of `MUDEC4`

Software	**Purpose**
`LibraEDT`	Data Acquisition
`PETS2.0`	Data Processing
`SHELXT`	Structure Solution
`JANA2020`	Structure Refinement
`DYNGO`	Dynamical Refinement
`TOPAS Academic`	Rietveld Refinement

Table S2: Comparison of Unit Cell Parameters Obtained from PXRD and 3D-ED for `MUDEC4`

Parameter	**PXRD**	**3DED**	**Difference (%)**
a, b (Å)	12.373	12.572	1.96%
c (Å)	15.330	14.781	3.45%
α, β (°)	90.00	90.00	0.00%
γ (°)	120.00	120.00	0.00%

Note: The percentage difference is calculated using the formula:

$$\text{Difference (\%)} = \left(\frac{|\text{PXRD} - \text{3DED}|}{\text{PXRD}}\right) \times 100\%$$

Table S3: Summary of structural and surface properties of `MUDEC4`, as obtained from the pore analyzer in Mercury.

Parameter	**Result**	**Unit**
System Volume	2023.220	Å^3
System Mass	1325.519	g/mol
System Density	1.088	g/cm^3
Total surface area	87.82	Å^2
Total surface area per volume	434.04	m^2/cm^3
Total surface area per mass	398.97	m^2/g
Network-accessible surface area	87.82	Å^2
Network-accessible surface area per volume	434.04	m^2/cm^3
Network-accessible surface area per mass	398.97	m^2/g
Total helium volume	743.770	Å^3
Total helium volume	0.338	cm^3/g
Total geometric volume	955.806	Å^3
Total geometric volume	0.434	cm^3/g
Network-accessible helium volume	743.770	Å^3
Network-accessible helium volume	0.338	cm^3/g
Network-accessible geometric volume	955.454	Å^3
Network-accessible geometric volume	0.434	cm^3/g
Pore limiting diameter	4.15	Å
Maximum pore diameter	5.24	Å
Number of percolated dimensions	1	Dimension

Listing S1: TOPAS Input File for MUDEC4 Rietveld Refinement

```
r_exp 1.762538954 r_exp_dash 5.303337964
r_wp 2.495231319 r_wp_dash 7.507950365
r_p 1.88165449 r_p_dash 9.319253964
weighted_Durbin_Watson 0.4283612153
gof 1.415702793
iters 100000

xdd "MUDEC4_slow.xy"
    r_exp 1.762538954 r_exp_dash 5.303337964 r_wp 2.495231319 r_wp_dash 7.507950365 r_p 1.88165449 r_p_dash
     9.319253964 weighted_Durbin_Watson 0.4283612153 gof 1.415702793
    bkg @ 2551.36566 -1914.569017 124.0511297 631.4018646 -411.0277116 -81.51846912 290.521759 -173.1522464
     -109.6772892 241.3702307 -124.7137917 -44.94742473 105.4980256 -56.39842758 -15.13620563 51.10331524
     -34.3617281 -10.83655926 46.60877496 -19.98925496 -3.888889286 13.51509991 -8.533766903 0.3631206395
     -3.791090091 11.87484696 -23.18966977 19.76423974 -0.9487705533 -0.1303125778 -4.099601246
    start_X  6
    LP_Factor( 27.3)
    Mixture_LAC_1_on_cm( 14.21494618)
    mixture_MAC 13.81999413
    mixture_density_g_on_cm3 1.028578308
    Rp 260
    Rs 260
    axial_conv
        filament_length  10.3272402
        sample_length  9.137152078
        receiving_slit_length  10.17575788
        axial_n_beta  30
    lam
        ymin_on_ymax  0.0001
        la  1 lo  1.540596 lh  0.07189831438 lg  1.384652476
    str

        ' ################################ View Structure   ################################
          view_structure
        ' ################################ View Structure   ################################

        ' ################################ Fourier Map      ################################
         fourier_map 1
         fourier_map_formula = Fobs - Fcalc;
        ' ################################ Fourier Map      ################################

        ' ################################ Parameters       ################################
         prm bEqLig  1.92426228`
         prm bEqPh   22.3248512`
         prm bEqBut  14.5670294`
        ' ################################ Parameters       ################################



        site C8Z         x  0.56134` y  0.46535` z  0.33521` occ C   1.0      beq = bEqLig;
        site C9Z         x  0.67006` y  0.45504` z  0.32132` occ C   1.0      beq = bEqLig;
        site C7Z         x  0.56076` y  0.55071` z  0.38985` occ C   1.0      beq = bEqLig;
        site C10Z        x  0.47405` y  0.39220` z  0.27469` occ C   1.0      beq = bEqLig;
        site N5Z         x  0.64358` y  0.36989` z  0.26136` occ N   1.0      beq = bEqLig;
        site O1Z         x  0.77632` y  0.49177` z  0.35633` occ O   1.0      beq = bEqLig;
        site C1phZ       x  0.48822` y  0.60146` z  0.37349` occ C   1.0      beq = bEqPh;
        site N3Z         x  0.62565` y  0.58699` z  0.45673` occ N   1.0      beq = bEqLig;
```

```
         site N4Z         x  0.51733` y  0.32618` z  0.23231` occ N   1.0      beq = bEqLig;
         site C11Z        x  0.34552` y  0.35442` z  0.26455` occ C   1.0      beq = bEqLig;
         site C1butZ      x  0.71504` y  0.31695` z  0.22504` occ C   1.0      beq = bEqBut;
         site C6phZ       x  0.53014` y  0.70406` z  0.31570` occ C   1.0      beq = bEqPh;
         site C2phZ       x  0.37034` y  0.55238` z  0.41404` occ C   1.0      beq = bEqPh;
         site N2Z         x  0.64153` y  0.68293` z  0.50527` occ N   1.0      beq = bEqBut;
         site C2butZ      x  0.79812` y  0.40051` z  0.15117` occ C   1.0      beq = bEqBut;
         site C5phZ       x  0.45425` y  0.75700` z  0.29860` occ C   1.0      beq = bEqPh;
         site C3phZ       x  0.29437` y  0.60534` z  0.39692` occ C   1.0      beq = bEqPh;
         site C6Z         x  0.72790` y  0.74750` z  0.55967` occ C   1.0      beq = bEqLig;
         site C3butZ      x  0.90363` y  0.37218` z  0.13403` occ C   1.0      beq = bEqBut;
         site C4phZ       x  0.33636` y  0.70781` z  0.33914` occ C   1.0      beq = bEqPh;
         site C3Z         x  0.73607` y  0.84244` z  0.60804` occ C   1.0      beq = bEqLig;
         site O2Z         x  0.80471` y  0.70785` z  0.56101` occ O   1.0      beq = bEqLig;
         site C4butZ      x  0.99083` y  0.46171` z  0.06692` occ C   1.0      beq = bEqBut;
         site C4Z         x  0.65129` y  0.87627` z  0.61509` occ C   1.0      beq = bEqLig;
         site C2Z         x  0.83674` y  0.91200` z  0.65438` occ C   1.0      beq = bEqLig;
         site C5Z         x  0.65964` y  0.96871` z  0.66222` occ C   1.0      beq = bEqLig;
         site C1Z         x  0.85123` y  1.00574` z  0.70285` occ C   1.0      beq = bEqLig;
         site N1Z         x  0.77669` y  1.05058` z  0.70991` occ N   1.0      beq = bEqLig;

         rigid
             z_matrix   C8Z
             z_matrix   C9Z    C8Z      1.4292638
             z_matrix   C7Z    C8Z      1.3508268     C9Z     122.372056
             z_matrix   C10Z   C8Z      1.3671672     C9Z     107.876443    C7Z         169.976812
             z_matrix   N5Z    C9Z      1.3103028     C8Z     107.953322    C7Z         -176.136417
             z_matrix   O1Z    C9Z      1.2749814     C8Z     138.951796    N5Z         -168.945354
             z_matrix   C1phZ  C7Z      1.3514641     C8Z     120.830675    C9Z    @    147.66389`
             z_matrix   N3Z    C7Z      1.2396873     C8Z     122.703918    C1phZ       -179.813400
             z_matrix   N4Z    C10Z     1.3466893     C8Z     107.870158    C9Z         7.659701
             z_matrix   C11Z   C10Z     1.4241495     C8Z     132.395513    N4Z         163.114469
             z_matrix   C1butZ N5Z      1.4490886     C9Z     132.003425    C8Z         -176.428629
             z_matrix   C6phZ  C1phZ    1.4167706     C7Z     120.118757    C8Z    @    -83.26290`
             z_matrix   C2phZ  C1phZ    1.4130453     C7Z     120.081967    C6phZ       -179.951160
             z_matrix   N2Z    N3Z      1.3298591     C7Z     124.464813    C8Z         169.910747
             z_matrix   C2butZ C1butZ   1.5314637     N5Z     109.530391    C9Z    @    -84.98210`
             z_matrix   C5phZ  C6phZ    1.4121996     C1phZ   120.084289    C7Z         179.969279
             z_matrix   C3phZ  C2phZ    1.4133806     C1phZ   120.121496    C7Z         -179.958808
             z_matrix   C6Z    N2Z      1.2736366     N3Z     129.009728    C7Z    @    -159.70710`
             z_matrix   C3butZ C2butZ   1.5341261     C1butZ  109.455505    N5Z    @    160.73963`
             z_matrix   C4phZ  C5phZ    1.4130721     C6phZ   120.074281    C1phZ       0.046539
             z_matrix   C3Z    C6Z      1.3495714     N2Z     125.442127    N3Z    @    -178.54438`
             z_matrix   O2Z    C6Z      1.2689684     N2Z     108.896087    C3Z         179.908656
             z_matrix   C4butZ C3butZ   1.5015866     C2butZ  109.177582    C1butZ @    -175.24586`
             z_matrix   C4Z    C3Z      1.3138155     C6Z     126.748802    N2Z    @     8.00667`
             z_matrix   C2Z    C3Z      1.3133441     C6Z     120.086474    C4Z         -179.950255
             z_matrix   C5Z    C4Z      1.3125045     C3Z     126.540014    C6Z         -179.998523
             z_matrix   C1Z    C2Z      1.3120925     C3Z     123.453809    C6Z         179.988074
             z_matrix   N1Z    C5Z    @  1.48026`      C4Z     119.477554    C3Z          3.590689

         Rotate_about_axies(@  50.09315`,@  132.37679`,@  7.72172`)
         Translate(@  0.56134`,@  0.46535`,@  0.33521`)

         Out_X_Yobs_Ycalc_Diff_csv(MUDEC4_Rietveld_X_Yobs_Ycalc_Diff.xy)
         Out_Tick(MUDEC4_Ticks.xy)

```

```
        LVol_FWHM_CS_G_L( 1, 430.5059155, 0.89, 601.8510286,,,@, 676.2371107)
        TCHZ_Peak_Type(@, -0.125878574,@, 0.1111779911,@, -0.01113202541,, 0,@, 0.2234656445,, 0)
        r_bragg  0.6622634982
        phase_MAC 13.81999413
        phase_name "MUDEC4_Rietveld_Rigid"
        MVW( 1258.998, 2032.530508, 100)
        space_group P32
        scale @ 0.0002629467456
        Phase_LAC_1_on_cm( 14.21494618)
        Phase_Density_g_on_cm3( 1.028578308)
        Trigonal(@ 12.37270635,@ 15.3312311)
        site Zn1 num_posns 3 x @ 0.7999972409 y @ 0.60323071 z @ 0.4446275828 occ Zn  1 beq @ 4.575531167
        PO_Spherical_Harmonics(sh_671ca943_4e, 6 load sh_Cij_prm
                                { y00 !sh_671ca943_4e_c00 1 y20 sh_671ca943_4e_c20 0.4336552916
                                y40 sh_671ca943_4e_c40 -0.0006891116241 y43m sh_671ca943_4e_c43p 0.6281679316
                                y43p sh_671ca943_4e_c43m 0.583041525 y60 sh_671ca943_4e_c60 -0.09450412799
                                y63m sh_671ca943_4e_c63p 0.5158772527 y63p sh_671ca943_4e_c63m -0.1602635625
                                y66m sh_671ca943_4e_c66p 0.09475117049 y66p sh_671ca943_4e_c66m 0.0688277092})
```

Listing S2: MUDEC4 Crystallographic Information Framework file

```

#======================================================================
# CRYSTAL DATA
#----------------------------------------------------------------------
data_MUDEC4

_chemical_name_common                  'C21 H22 N5 O2 Zn1'
_cell_length_a                         12.572000(7)
_cell_length_b                         12.572000(7)
_cell_length_c                         14.780700(5)
_cell_angle_alpha                      90.000000
_cell_angle_beta                       90.000000
_cell_angle_gamma                      120.000000
_cell_volume                           2023.179145
_space_group_name_H-M_alt              'P 32'
_space_group_IT_number                 145

loop_
_space_group_symop_operation_xyz
   'x, y, z'
   '-y, x-y, z+2/3'
   '-x+y, -x, z+1/3'

loop_
   _atom_site_label
   _atom_site_occupancy
   _atom_site_fract_x
   _atom_site_fract_y
   _atom_site_fract_z
   _atom_site_adp_type
   _atom_site_U_iso_or_equiv
   _atom_site_type_symbol
   Zn1        1.0     0.8001(7)    0.5994(7)    0.4543(4)    Uani   0.052444 Zn
   C8         1.0     0.5388(18)   0.4681(15)   0.3284(9)    Uani   0.076333 C
   N5         1.0     0.6093(15)   0.3656(16)   0.2505(9)    Uani   0.081111 N
   N1         1.0     0.7682(17)   1.0427(18)   0.7137(10)   Uani   0.081111 N
   C5         1.0     0.6851(14)   0.9995(14)   0.6462(9)    Uani   0.076333 C
   N4         1.0     0.4879(17)   0.3330(16)   0.2192(8)    Uani   0.081111 N
   C1         1.0     0.8284(15)   0.9804(15)   0.7261(9)    Uani   0.076333 C
   C1ph       1.0     0.4591(11)   0.5891(9)    0.3842(5)    Uiso   0.205000 C
   C4         1.0     0.6776(13)   0.9118(13)   0.5937(9)    Uani   0.076333 C
   C9         1.0     0.6401(13)   0.4484(18)   0.3142(10)   Uani   0.076333 C
   C3         1.0     0.7403(10)   0.8544(14)   0.6020(8)    Uani   0.076333 C
   O1         1.0     0.7420(18)   0.4754(18)   0.3515(9)    Uani   0.081111 O
   C2         1.0     0.8163(13)   0.8932(13)   0.6710(8)    Uani   0.076333 C
   C7         1.0     0.5444(13)   0.5537(10)   0.3865(7)    Uani   0.076333 C
   C10        1.0     0.4521(15)   0.403(2)     0.2641(11)   Uani   0.076333 C
   N3         1.0     0.6266(17)   0.604(2)     0.4440(10)   Uani   0.081111 N
   O2         1.0     0.8114(17)   0.7290(15)   0.5440(10)   Uani   0.081111 O
   N2         1.0     0.6457(16)   0.7004(15)   0.4934(8)    Uani   0.081111 N
   C3ph       1.0     0.2656(14)   0.5684(17)   0.4386(10)   Uiso   0.205000 C
   C6         1.0     0.7329(16)   0.7642(14)   0.5482(9)    Uani   0.076333 C
   C1but      1.0     0.6725(13)   0.3063(11)   0.2122(10)   Uiso   0.115000 C
   C4ph       1.0     0.2805(16)   0.6633(18)   0.3793(11)   Uiso   0.205000 C
   C6ph       1.0     0.4739(15)   0.6841(13)   0.3249(7)    Uiso   0.205000 C
   C2ph       1.0     0.3549(11)   0.5315(13)   0.4410(7)    Uiso   0.205000 C
```

```
   C5ph       1.0     0.3847(17)   0.7210(17)   0.3225(10)   Uiso   0.205000 C
   C4but      1.0     0.959(3)     0.434(3)     0.063(2)     Uiso   0.370000 C
   C3but      1.0     0.860(2)     0.346(2)     0.1257(14)   Uiso   0.209000 C
   C11        1.0     0.3286(18)   0.376(2)     0.2525(15)   Uani   0.125222 C
   C2but      1.0     0.773(2)     0.395(2)     0.1475(16)   Uiso   0.340000 C
   H1c5       1.0     0.626303     1.036134     0.635540     Uiso   0.091700 H
   H1c1       1.0     0.887967     1.002754     0.782530     Uiso   0.091700 H
   H1c4       1.0     0.614525     0.884459     0.539174     Uiso   0.091700 H
   H1c2       1.0     0.870575     0.851741     0.682881     Uiso   0.091700 H
   H1n2       1.0     0.582352     0.726781     0.486234     Uiso   0.097400 H
   H1c3ph     1.0     0.187488     0.524935     0.481229     Uiso   0.246200 H
   H1c1but    1.0     0.608900     0.226576     0.176279     Uiso   0.137800 H
   H2c1but    1.0     0.712791     0.281144     0.264901     Uiso   0.137800 H
   H1c4ph     1.0     0.213571     0.691067     0.377509     Uiso   0.246200 H
   H1c6ph     1.0     0.551984     0.727485     0.282206     Uiso   0.246200 H
   H1c2ph     1.0     0.343628     0.460411     0.485432     Uiso   0.246200 H
   H1c5ph     1.0     0.395923     0.792035     0.278098     Uiso   0.246200 H
   H1c4but    1.0     0.999803     0.388480     0.030040     Uiso   0.442900 H
   H2c4but    1.0     0.921155     0.467379     0.014320     Uiso   0.442900 H
   H3c4but    1.0     1.027251     0.509119     0.101007     Uiso   0.442900 H
   H1c3but    1.0     0.899602     0.337498     0.186386     Uiso   0.251200 H
   H2c3but    1.0     0.809751     0.259262     0.094019     Uiso   0.251200 H
   H1c11      1.0     0.324677     0.458006     0.259816     Uiso   0.144400 H
   H2c11      1.0     0.297441     0.339100     0.187067     Uiso   0.144400 H
   H3c11      1.0     0.271932     0.311576     0.301975     Uiso   0.144400 H
   H1c2but    1.0     0.732069     0.402629     0.086920     Uiso   0.408400 H
   H2c2but    1.0     0.823068     0.482545     0.178379     Uiso   0.408400 H

loop_
   _atom_site_aniso_label
   _atom_site_aniso_U_11
   _atom_site_aniso_U_22
   _atom_site_aniso_U_33
   _atom_site_aniso_U_12
   _atom_site_aniso_U_13
   _atom_site_aniso_U_23
   Zn1    0.05700  0.07800  0.03600  0.04400  0.02200  0.00400
   C8     0.08100  0.11000  0.05700  0.06200 -0.00400 -0.03200
   N5     0.10800  0.10800  0.05800  0.07700 -0.00700 -0.01300
   N1     0.10800  0.10800  0.05800  0.07700 -0.00700 -0.01300
   C5     0.08100  0.11000  0.05700  0.06200 -0.00400 -0.03200
   N4     0.10800  0.10800  0.05800  0.07700 -0.00700 -0.01300
   C1     0.08100  0.11000  0.05700  0.06200 -0.00400 -0.03200
   C4     0.08100  0.11000  0.05700  0.06200 -0.00400 -0.03200
   C9     0.08100  0.11000  0.05700  0.06200 -0.00400 -0.03200
   C3     0.08100  0.11000  0.05700  0.06200 -0.00400 -0.03200
   O1     0.10800  0.10800  0.05800  0.07700 -0.00700 -0.01300
   C2     0.08100  0.11000  0.05700  0.06200 -0.00400 -0.03200
   C7     0.08100  0.11000  0.05700  0.06200 -0.00400 -0.03200
   C10    0.08100  0.11000  0.05700  0.06200 -0.00400 -0.03200
   N3     0.10800  0.10800  0.05800  0.07700 -0.00700 -0.01300
   O2     0.10800  0.10800  0.05800  0.07700 -0.00700 -0.01300
   N2     0.10800  0.10800  0.05800  0.07700 -0.00700 -0.01300
   C6     0.08100  0.11000  0.05700  0.06200 -0.00400 -0.03200
   C11    0.09000  0.17000  0.14900  0.09000 -0.03600 -0.02000


```

```
_atom_site_aniso_label , _atom_site_aniso_U_11 , _atom_site_aniso_U_12 , _atom_site_aniso_U_13 ,
     _atom_site_aniso_U_22 , _atom_site_aniso_U_23 , _atom_site_aniso_U_33
```

Chapter 5

Crystal Structure and Topology of Titanium-Based Heterometallic MOFs

5.1 Introduction

Designing MOFs with specific topologies is fundamental in reticular chemistry, enabling the development of materials with tailored properties for advanced applications [83]. The topology of a MOF, determined by the spatial arrangement of its metal nodes and organic linkers, critically influences its physical and chemical characteristics, such as pore size, shape, connectivity, and overall framework stability [84, 85].

While zirconium-based clusters, particularly the Zr_6 cluster, have been extensively explored due to their versatility and robustness [86, 87, 88], titanium-based MOFs remain less developed. Titanium's smaller ionic radius and high charge polarization capacity present significant challenges in forming stable metal-oxo clusters with defined geometries and connectivities. This limitation restricts the diversity of accessible framework topologies in titanium-based MOFs, despite titanium's inherent photoredox properties that make it highly attractive for photocatalytic applications like water splitting and CO_2 reduction [89].

In previous work, the Ti–Ca heterometallic cluster combined with tritopic linkers to form MUV-10 [90] and MUV-12 [8], exhibiting a **the** topology [85]. Building on this foundation, the present study investigates the combination of the Ti–Ca heterometallic cluster with tetratopic linkers to explore new MOFs with different network topologies. This approach aims to expand the structural diversity of titanium-based MOFs, emulating the versatility observed with Zr_6 clusters and overcoming current limitations in titanium MOF chemistry (Figure 5.1).

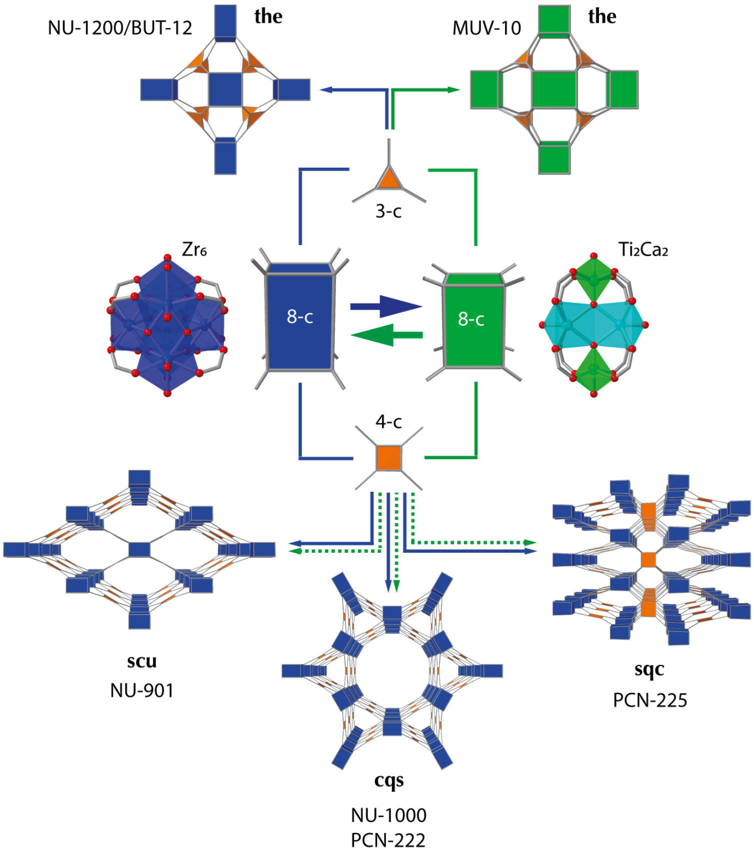

Figure 5.1: Comparison of the versatility between Zr_6 clusters and Ti–Ca heterometallic clusters in MOF synthesis.

A significant challenge in this exploration is the structural characterization of these new titanium-based MOFs. Factors such as small crystal sizes often render conventional X-ray diffraction techniques inadequate. To overcome these obstacles, we have employed 3D-ED, which allows for accurate structure determination of nano-sized crystals.

By successfully characterizing these complex materials, we not only expand the range of accessible network topologies but also open avenues for designing MOFs with enhanced or tailored functionalities.

Although a wide variety of tetratopic linkers were investigated during the course of this research, resulting in numerous successfully solved structures, this chapter narrows its focus to four specific ligands. These ligands, listed in Table 5.1 and shown in Figure 5.2, were selected to highlight the structural versatility achievable when tetratopic linkers are combined with the Ti–Ca heterometallic cluster.

Table 5.1: Tetratopic ligands investigated in this chapter

Ligand	**Full Name**
H_4TCPP	5,10,15,20-tetrakis(4-carboxyphenyl)porphyrin
H_4TBAPy	1,3,6,8-Tetrakis(4-carboxyphenyl)pyrene
H_4TCPB	1,2,4,5-Tetrakis(4-carboxyphenyl)benzene
H_4MTB	Methanetetrabenzoic acid

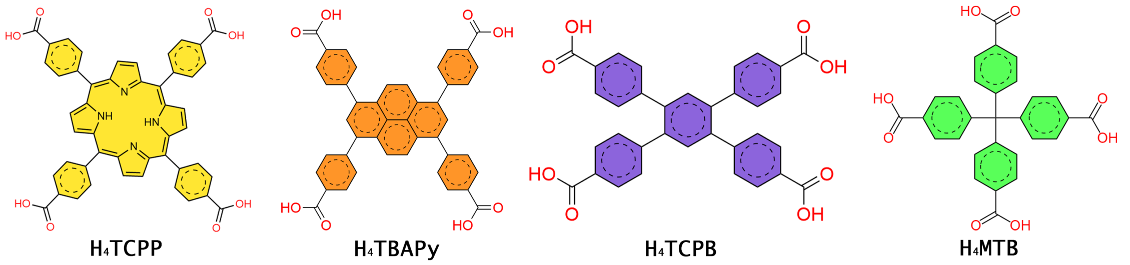

Figure 5.2: Structures of the tetratopic ligands investigated in this chapter.

The MOFs discussed in this chapter (Figure 5.3) were synthesized and provided by Natalia Muñoz Padial from Carlos Martí-Gastaldo's Functional Inorganic Materials Group at the Institute of Molecular Science of the University of Valencia.

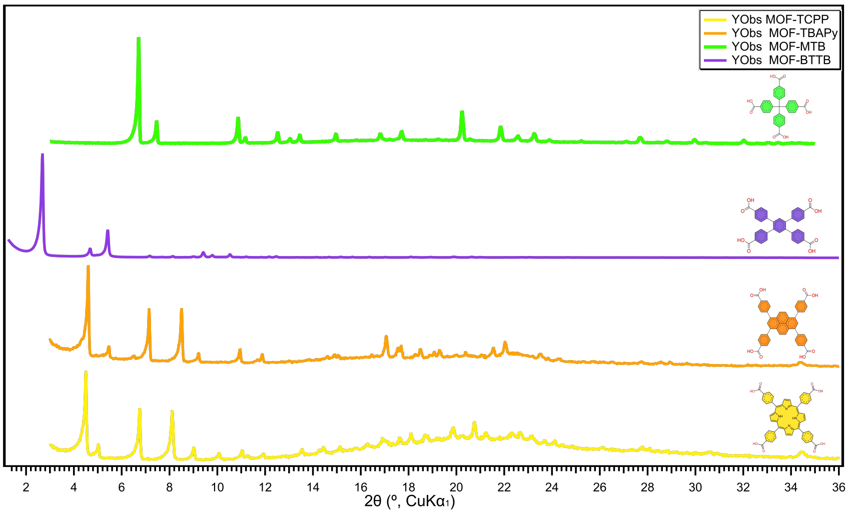

Figure 5.3: PXRD patterns of the studied MOFs. Each pattern is color-coded and includes the corresponding ligand molecule for clarity.

In Figure 5.4, SEM images of the different MOFs are shown, revealing the size, shape, and morphologies of the their crystals.

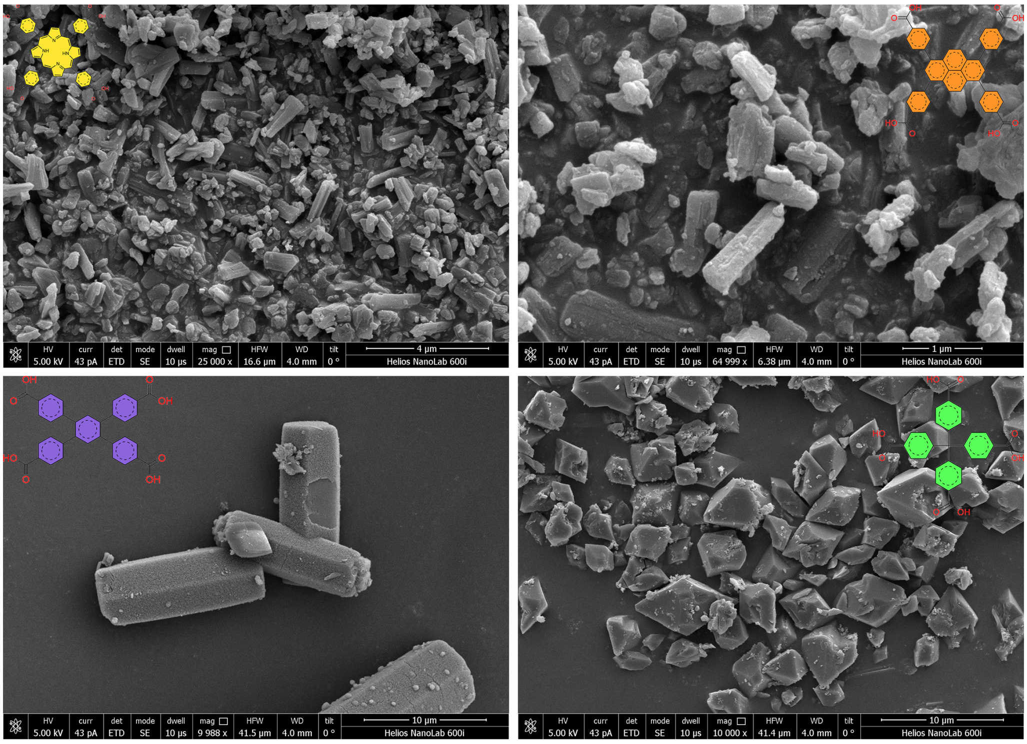

Figure 5.4: SEM images of the MOFs used in this study with their respective ligand structures overlaid.

5.2 3D-ED on Heterometallic Titanium MOFs

5.2.1 Sample Preparation Procedure

Accurate crystallographic characterization of the MOFs in this study required careful sample preparation due to their sensitivity to electron beam. To preserve the structural integrity of the nano-sized crystals during electron diffraction measurements, samples were prepared under cryogenic conditions utilizing a cryo-holder. The use of low temperatures was essential in minimizing beam-induced damage, reducing thermal vibrations, and enhancing the quality of the collected diffraction data.

The MOF samples were provided in DMF. For TEM analysis, a small aliquot of the MOF solution was carefully deposited onto a holey TEM grid, and excess solvent was removed by gentle bottom blotting with filter paper, ensuring a thin and uniform distribution of crystals across the grid. Prior to sample deposition, the cryo-holder was pre-cooled to facilitate rapid cooling of the TEM grid. Once the cryo-holder reached approximately 253 K (−20 °C), the prepared TEM grid was placed into the holder. The sample preparation steps are illustrated in Figure 5.5, providing a visual summary of the process.

To prevent ice formation during the TEM analysis, the grid was inserted into the microscope before the sample temperature reached 183 K. At this temperature, ice crystals begin to sublimate under the high vacuum conditions of the TEM, avoiding ice contamination. After insertion, the temperature of the sample was allowed to stabilize near 100 K. This low temperature effectively freezes the MOF crystals, stabilizing their structure for electron diffraction analysis.

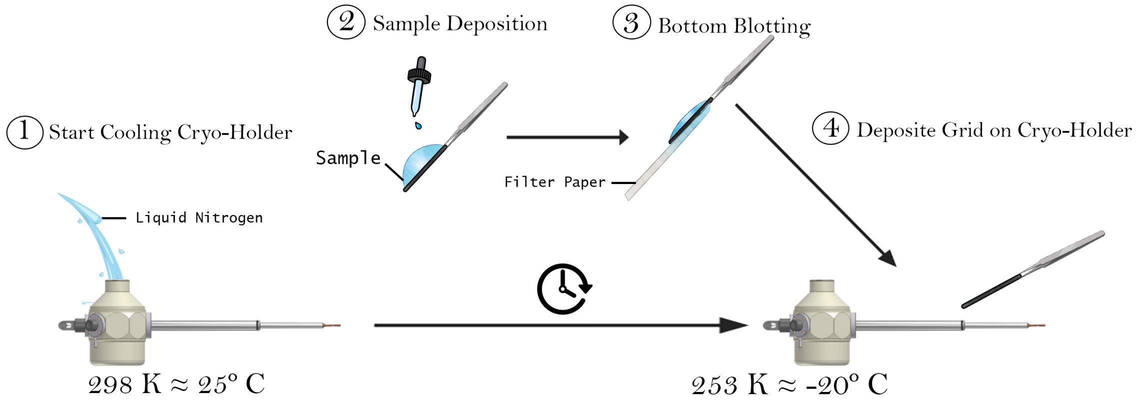

Figure 5.5: Illustration of the sample preparation steps of beam-sensitive MOFs for cryogenic 3D electron diffraction analysis.

5.2.2 Data Acquisition

The structural characterization of the MOFs was carried out using cRED, acquired using the `LibraEDT` software described in **chapter 2**, which is primarily developed for data acquisition of beam-sensitive samples. Detailed data acquisition parameters for each MOF are summarized in Table 5.2.

Table 5.2: Experimental Parameters for 3D-ED Data Acquisition

Parameter	**MOF-TCPP**	**MOF-TBAPy**	**MOF-TCPB**	**MOF-MTB**
Emission Current (μA)	0.75	0.75	0.40	1.66
STEM Mode: Spot Size (nm)	2.00	2.00	2.00	2.00
Beam diameter size (nm)	150	150	150	150
Temperature (K)	100	100	100	100
Exposure Time (ms)	500	500	500	500
Data Collection Duration (s)	60.04	60.04	60.04	60.04
Rotation Speed (Deg/s)	2.00	2.00	2.00	2.00
Oscillation Range (Deg)	1.04	1.04	1.04	1.04
Starting Angle (Deg)	-60.00	-60.00	-60.00	-60.00
Ending Angle (Deg)	60.50	60.50	60.50	60.50

Despite conducting experiments at low temperatures to minimize beam damage, the MOFs still exhibited beam sensitivity. As observed in the diffraction patterns shown in Figure 5.6, the MOFs display low resolution, with MOF-TCPP, MOF-TBAPy, and MOF-TCPB not diffracting beyond 1.4 Å, and MOF-MTB showing slightly improved resolution down to 1.1 Å. These results are consistent with the PXRD patterns presented in Figure 5.3, confirming that the low crystallinity of these materials is not attributable to the high vacuum conditions of the TEM but is an inherent property of the materials themselves.

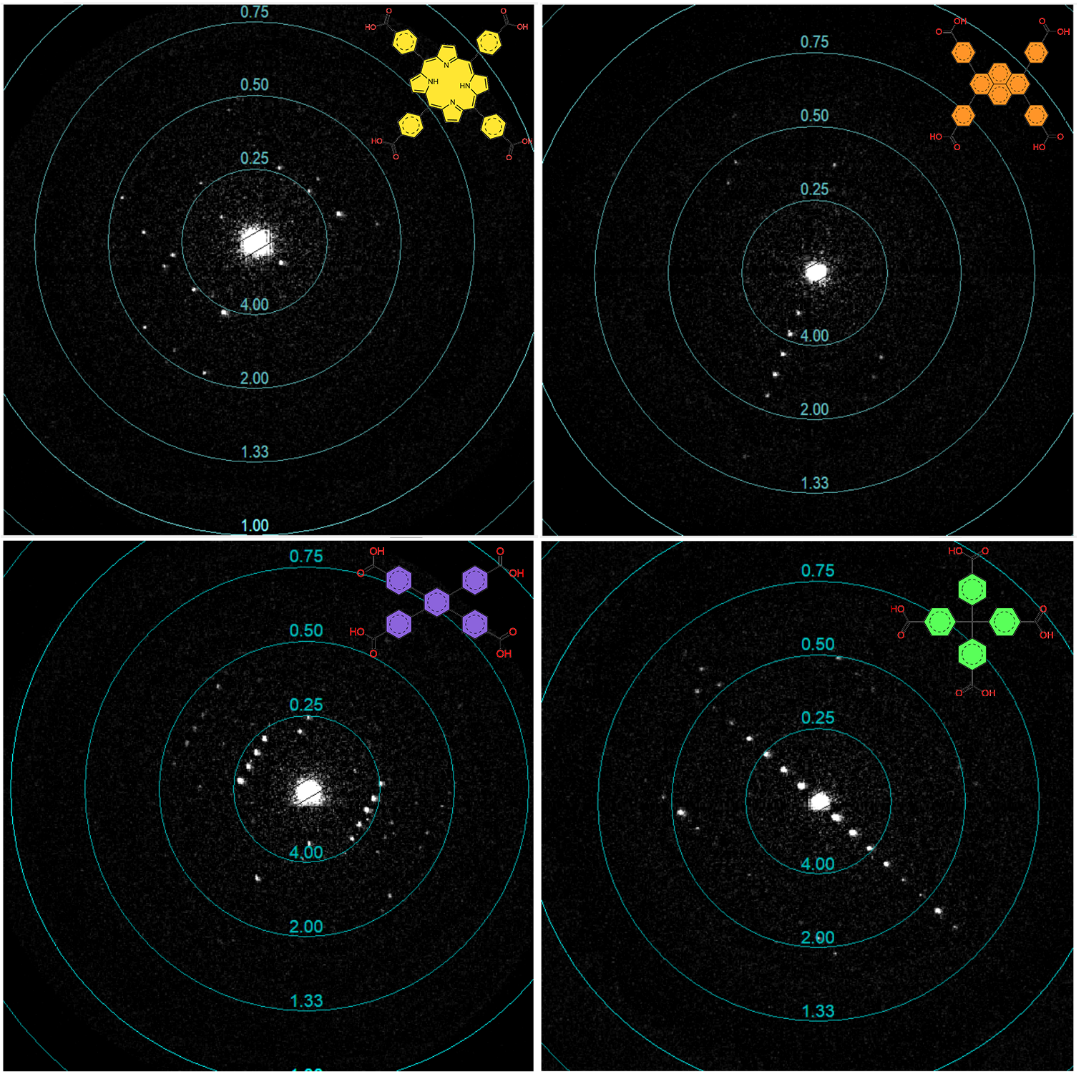

Figure 5.6: Snapshot of the diffraction patterns for each of the MOFs. Each resolution ring corresponds to steps of 0.25 (Å^{-1}).

5.2.3 Data Processing and Structure Solution

The acquired 3D-ED data were processed using the `XDS` package [37] following the steps outlined in **Chapter 1.2.7.1.1**, with the resolution cutoff established based on the correlation coefficient ($CC_{1/2}$) and the signal-to-noise ratio (I/σ) of each resolution shell. The `XDS_ASCII.HKL` files, generated after the scaling step in `XDS`, were imported into `XPREP` to merge symmetry-equivalent intensities and generate the necessary `.ins` and `.hkl` files for subsequent analysis.

Structure solution was performed using the `SHELXT` program [46]. Due to the relatively low resolution (approximately 1.4 Å) of the diffraction signal, the initial models contained numerous dummy or ghost atoms, with most of them incorrectly assigned as heavy atoms (Figure 5.7). This issue likely arose because the Fourier maps become less distinct as data completeness or resolution gets worse. In such instances, prior knowledge of the molecules involved was useful in identifying and removing these non-physical atoms.

All the structures were refined using the kinematical approximation using `SHELXL` [47] within `OLEX2` [48] and `ShelXle` [49], incorporating appropriate constraints and restraints, primarily `AFIX`, `FLAT`, and `SADI`, to achieve chemically reasonable and accurate models.

Due to the low resolution of the data, modeling the solvent molecules was not feasible, therefore, the solvent mask option in `OLEX2` was employed to eliminate residual electron density within the channels. The relevant crystallographic data of the structures, including the final refinement statistics are listed in Table 5.3.

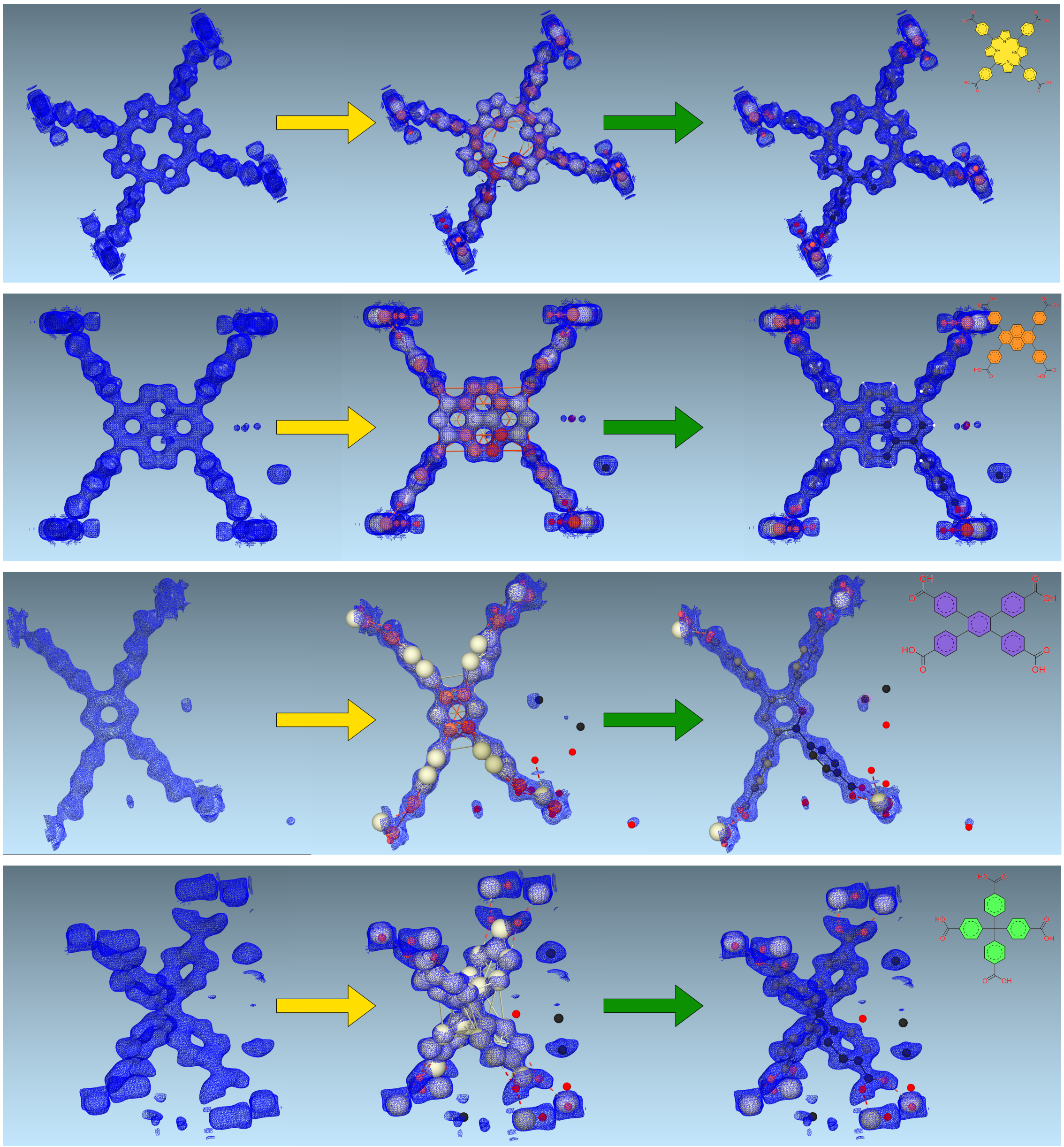

Figure 5.7: Left: Observed Fourier Map. Middle: Starting model obtained from SHELXT. Right: Properly adjusted model based on prior chemical knowledge.

Table 5.3: Crystallographic data for the studied MOFs.

Information	**MOF-TCPP**	**MOF-TBAPy**	**MOF-TCPB**	**MOF-MTB**
Empirical formula	$TiCaC_{48}N_4O_{11}H_{20}$	$TiCaC_{44}O_{10}H_{22}$	$TiCaC_{34}O_9H_{18}$	$TiCaC_{29}O_{11}H_{16}$
Formula weight	917.33	798.60	658.45	628.38
Temperature (K)	100	100	100	100
Crystal system	Tetragonal	Tetragonal	Hexagonal	Tetragonal
Space group	P4/*mmm*	P4/*mmm*	P6/*mmm*	I4/*mmm*
Topology	*scu*	*scu*	*csq*	*flu*
a (Å)	19.573(3)	19.160(3)	37.440(5)	15.811(2)
c (Å)	17.551(3)	16.140(3)	11.450(2)	23.639(5)
Volume (Å^3)	6724(2)	5925(2)	13900(5)	5909(2)
Z	2	2	6	4
ρ_{calc} (g/cm^3)	0.453	0.448	0.472	0.706
Resolution cut off (Å)	1.40	1.35	1.40	1.10
Reflections collected	6509	5267	8193	3352
Data	1052	954	1127	551
Restraints/parameters	68/47	218/44	277/40	31/33
Goodness-of-fit on F^2	1.404	1.625	1.244	1.770
Final R_{obs}	0.1976	0.2316	0.2464	0.2072

5.2.4 The Ti–Ca Heterometallic Cluster

The Ti-–Ca heterometallic cluster constitutes a fundamental structural motif within the studied MOFs, offering both robustness and versatility to the framework. This cluster comprises titanium (Ti^{4+}) and calcium (Ca^{2+}) ions, each adopting unique coordination geometries that are fundamental to the cluster's functionality and the overall architecture of the MOFs.

Calcium ions exhibit a pentagonal bipyramidal coordination environment, interacting with seven oxygen atoms while titanium ions are octahedrally coordinated by six oxygen atoms. A notable feature of the Ti-–Ca cluster is its capacity to generate open coordination vacancies. Under thermal treatment, the axial oxygen atoms coordinated to titanium can be removed, resulting in unsaturated metal centers. This effect is also observed in some of the electron diffraction models, with the axial oxygens being partially occupied or totally absent, likely due to the high vacuum within the TEM. This removal process has been proven to enhance the reactivity of the material [8].

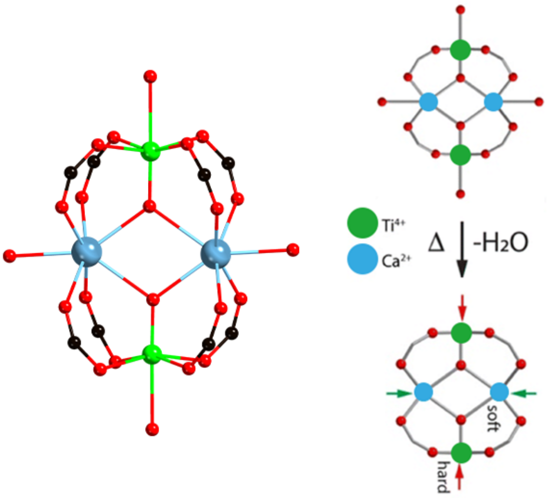

Figure 5.8: Heterometallic Ti–Ca cluster showing the formation of open coordination vacancies upon dehydration (-H_2O) [8]

The Ti–Ca heterometallic cluster exhibits significant structural disorder, often requiring complex modeling to capture its true nature. This disorder is due to the coexistence of multiple possible configurations within the same structure, which results in an averaged electron density in diffraction data. To address this complexity, the heterometallic cluster is often modeled as a superposition of two orientations, each representing a possible configuration of the cluster, as shown in Figure 5.9. This results in a model that better reflects the true nature of the system and a better fit to the experimental data. Interestingly, this modeling process leads to a representation of the cluster with higher symmetry than any of the individual configurations. The superposition results in an entirely symmetrical cluster, which contributes to a crystal structure of increased overall symmetry.

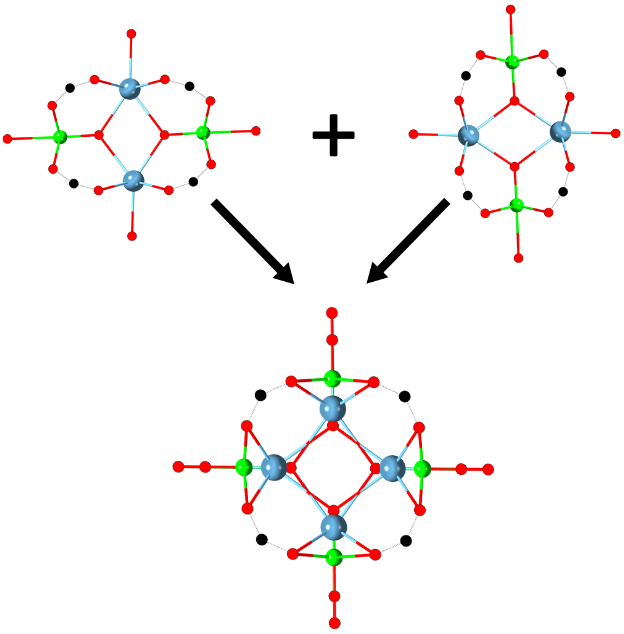

Figure 5.9: Modelling of the disordered heterometallic Ti–Ca cluster.

Structurally, the Ti—Ca heterometallic cluster can be conceptualized as an 8-connected node, effectively modeled as a cube with eight connections coming from eight different carboxylate groups of the organic ligands. This concept is illustrated in Figure 5.10. This 8-connected nature, with the right combination of organic linkers, enables the formation of diverse network topologies. Each connection can extend in different spatial directions, allowing the construction of complex and highly symmetric frameworks. The cube-like representation underscores the cluster's role as a highly symmetric and versatile building block, capable of supporting multiple organic linkers simultaneously.

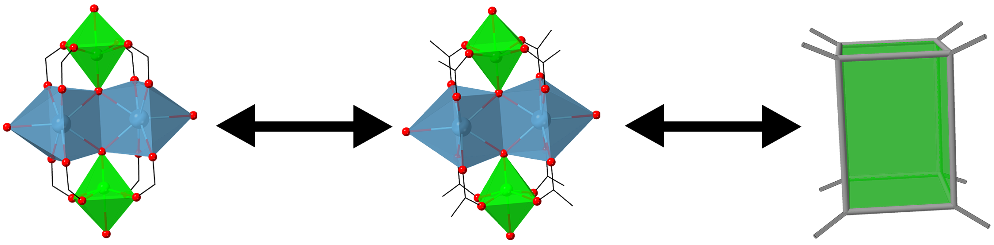

Figure 5.10: Representation of the 8-c Ti–Ca cluster with a cube-like topology.

5.2.5 Crystal Structures and Network Topologies

The structural characteristics of the MOFs investigated in this study are summarized in Table 5.3. Each MOF comprises an 8-coordinated (8-c) Ti–Ca heterometallic cluster combined with a tetratopic (4-c) linker. Among these linkers, three exhibit square planar geometries, while the fourth adopts a tetrahedral geometry. These variations in linker geometry introduce unique structural features and significantly influence the resulting network topology.

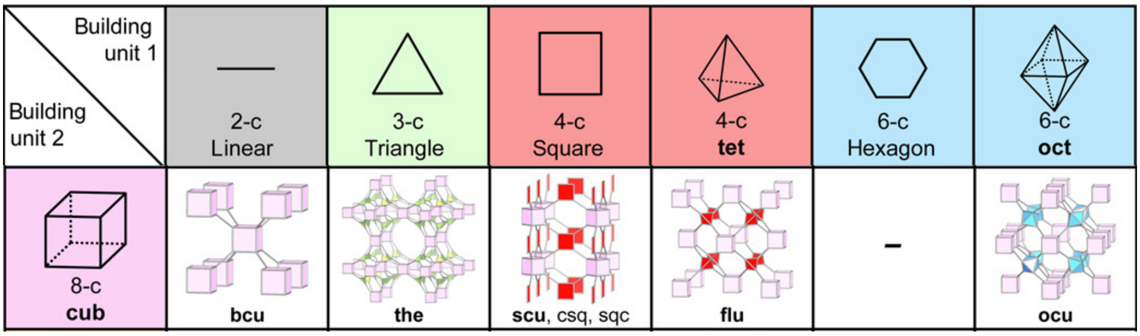

Figure 5.11: Schematic representation of possible network topologies formed by combining an 8-c node with 4-c linkers [9].

As illustrated in Figure 5.11 and stated in network topology theory [84, 9, 85], the combination of an 8-c cubic node with a 4-c square planar linker leads to the formation of **scu**, **csq**, and **sqc** topologies. Square planar linkers, such as those found in **scu**, **csq**, and **sqc** topologies, frequently result in frameworks characterized by straight channels and planar walls. These structures can exhibit high porosity and stability, making them suitable for applications like gas storage and separation. For instance, MOF-TCPP and MOF-TBAPy exhibit **scu** topologies, while MOF-TCPB adopts a **csq** topology. In contrast, tetrahedral linkers, as found in **flu** topologies, can result in more three-dimensional and interconnected frameworks. This structural arrangement leads to higher densities, which may offer advantages for applications that require enhanced structural stability and efficient material packing, such as catalysis, where robust frameworks can improve catalyst longevity and performance. MOF-MTB is a representative example of a flu topology MOF.

The geometry of the linker plays a pivotal role in determining the resulting network topology and, consequently, the material's physical properties. These structural determinations were achieved using electron diffraction and were subsequently validated through topological analysis using `TopCryst` [91] and `MOFid` [92].

5.2.5.0.1 MOF-TCPP and MOF-TBAPy

MOF-TCPP and MOF-TBAPy are isostructural MOFs that crystallize in a tetragonal cell with the space group $P4/mmm$, forming highly symmetric three-dimensional frameworks with a **scu** topology. Both structures incorporate linkers with orthogonally arranged carboxyphenyl functional groups, resulting in a square planar geometry. The 8-c heterometallic Ti–Ca clusters serve nodes, each coordinating with four linkers in the bc-plane and, by symmetry, another four in the ac-plane (Figure 5.12).

This coordination creates a robust 3D cubic network characterized by straight, one-dimensional channels aligned along the [001] direction. In this framework, the linkers form the edges of the cubic topology, while the nodes occupy the vertices. MOF-TCPP and MOF-TBAPy contain voids occupying 75% and 77% of their unit cell volume underscoring their high porosity.

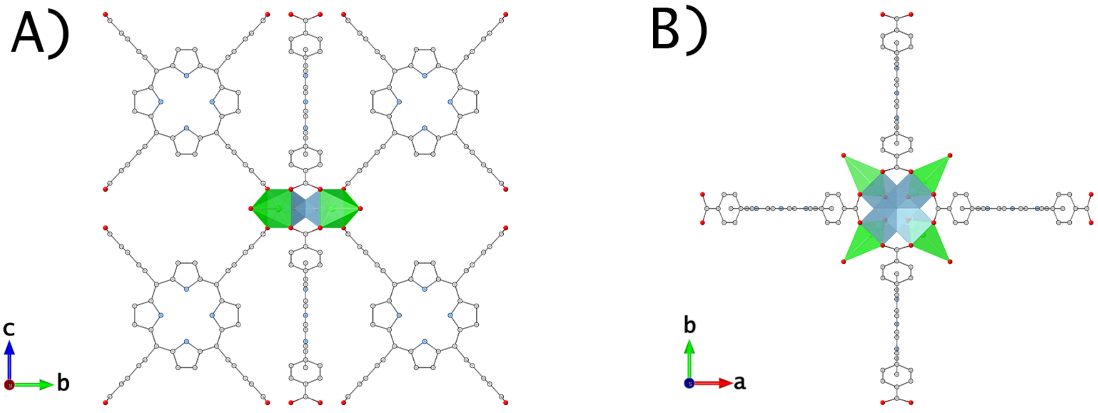

Figure 5.12: Top (A) and side (B) view of the Ti–Ca cluster in MOF-TCPP and MOF-TBAPy, illustrating its coordination environment.

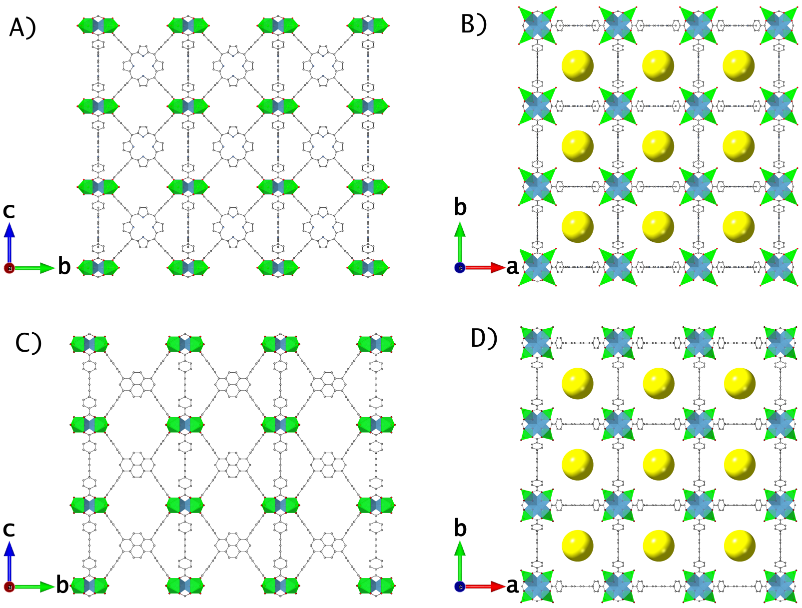

Figure 5.13: MOF-TCPP viewed along (A) a and (B) c axis. MOF-TBAPy viewed along (C) a and (D) c axis.

5.2.5.0.2 MOF-TCPB

MOF-TCPB crystallizes with a **csq** topology in the hexagonal space group *P6/mmm*. Similar to the previously discussed MOFs, each 8-c Ti–Ca node is bonded to eight linkers, four lying in the *ac*-plane and four in the *bc*-plane, as shown in Figure 5.14A and B.

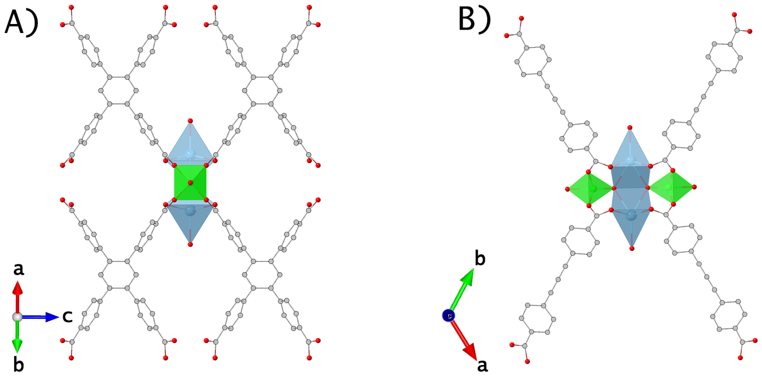

Figure 5.14: Top (A) and side (B) view of the Ti–Ca cluster in MOF-TCPB, illustrating its coordination environment.

This coordination leads to the formation of two different types of pores: smaller triangular pores that serve as the fundamental building blocks for the larger hexagonal pores, with their walls constructed from the orthogonally arranged organic linkers Figure 5.15B. MOF-TCPB has a cell volume of 14000 Å^3 with 76% of the volume consisting of voids.

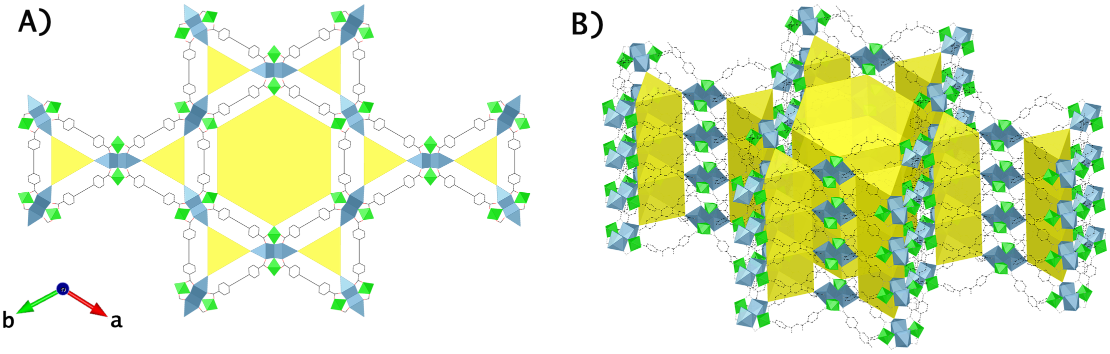

Figure 5.15: (A) View of MOF-TCPB along the c-axis, highlighting the triangular and hexagonal pores. (B) Side view showing the unobstructed channels formed by the pores running along the c-axis.

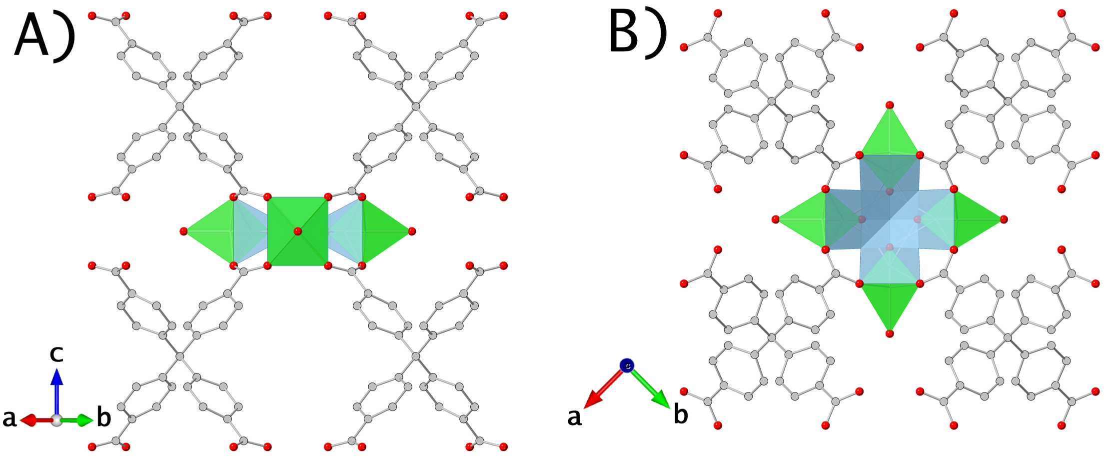

Figure 5.16: Top (A) and side (B) view of the Ti–Ca cluster in MOF-MTB, illustrating its coordination environment.

5.2.5.0.3 MOF-MTB

MOF-MTB crystallizes in a tetragonal structure with a space group of *I4/mmm*, distinguishing its overall architecture from the previously studied MOFs. Like its predecessors, MOF-MTB features the same Ti-–Ca cluster, whose coordination environment is illustrated in Figure 5.16. However, the primary differences between MOF-MTB and earlier MOFs lie in the geometry of the organic linkers and the resulting topology of the framework.

While the other frameworks used 4-connected square linkers to form **scu** and **csq** topologies with large, linear channels running along a principal axis, MOF-MTB employs 4-connected tetrahedral linkers. This change in linker geometry leads to the formation of a **flu** topology, which fundamentally alters the framework's connectivity and structural organization.

As a consequence of the **flu** topology, MOF-MTB is made of a network of smaller, interconnected octahedral cavities rather than the unobstructed, linear channels characteristic of **scu** and **csq** topologies (Figure 5.17).

MOF-MTB contains voids occupying 60% of its unit cell volume.

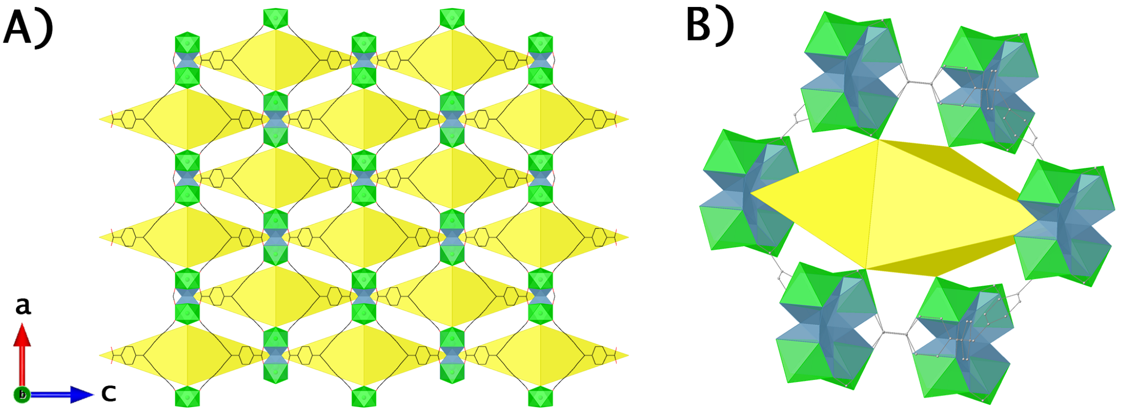

Figure 5.17: (A) View of MOF-MTB along the b-axis, showing the distribution of the pores. (B) Close-up of a single pore, highlighting its octahedral shape.

Le Bail profile fitting was performed for all structures using `TOPAS Academic` [76]. The corresponding plots are presented in Figure 5.18. Pore analysis was conducted using the pore analyzer tool in `MERCURY` [74], and the results are summarized in Table S5.1.

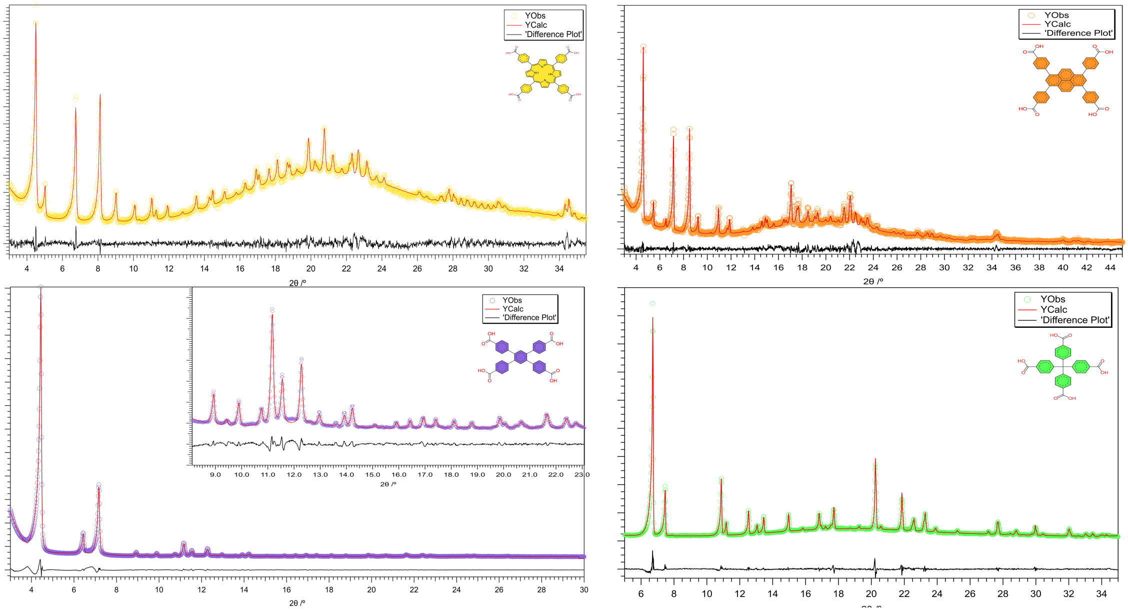

Figure 5.18: Le Bail fitting plots for MOFs in this chapter, showing observed (YObs), calculated (YCalc), and difference (Δ) plots with corresponding linker.

5.3 Conclusions

This chapter presented the structural characterization of a series of novel titanium MOFs featuring Ti–Ca heterometallic clusters and tetratopic organic linkers. The structural versatility of the Ti–Ca cluster facilitated the development of MOFs with diverse topologies, including **scu**, **csq**, and **flu**, demonstrating a degree of adaptability comparable to that of Zr_6 clusters, highlighting how linker geometry dictates the resulting framework architecture and properties.

The structural characterization of these nanoscale materials, which could not be achieved using conventional XRD, was successfully performed using 3D-ED. This method, operated under low-dose conditions and at cryogenic temperatures, minimized radiation damage and preserved structural integrity, enabling accurate and reliable crystallographic analysis.

Future research directions could include evaluating the performance of these materials in key applications, such as photocatalysis and water splitting, to evaluate their functional properties. Additionally, computational studies could provide a more detailed understanding of the factors determining the preference for specific topologies. Another promising area of exploration could involve broadening the scope of titanium MOFs even further by designing frameworks with the ocu topology using hexatopic linkers, diversifying their structural and functional potential.

Finally, the high porosity and structural diversity achieved in this study open the door for deploying titanium MOFs in many fields, such as bio-inspired materials and catalysis, broadening their potential applications.

5.4 Supplementary Information

Table S5.1: Pore Analysis Results for the Studied MOFs

Parameter	**MOF-TCPP**	**MOF-TBAPy**	**MOF-TCPB**	**MOF-MTB**
System Characteristics				
System Volume (Å^3)	6,723.829	5,925.084	13,899.776	5,909.460
System Mass (g/mol)	2,105.160	1,901.052	4,142.666	3,057.273
System Density (g/cm^3)	0.520	0.533	0.495	0.859
Surface Area				
Total Surface Area (Å^2)	1,754.90	1,090.10	2,398.32	1,128.42
Total Surface Area per Volume (m^2/cm^3)	2,609.96	1,839.80	1,725.44	1,909.52
Total Surface Area per Mass (m^2/g)	5,020.15	3,453.20	3,486.41	2,222.74
Network-Accessible Surface Area (Å^2)	1,754.90	1,090.10	2,398.32	1,128.42
Network-Accessible Surface Area per Volume (m^2/cm^3)	2,609.96	1,839.80	1,725.44	1,909.52
Network-Accessible Surface Area per Mass (m^2/g)	5,020.15	3,453.20	3,486.41	2,222.74
Volume Measurements				
Total Helium Volume (Å^3)	5,334.972	4,877.470	10,747.545	3,983.506
Total Helium Volume (cm^3/g)	1.526	1.545	1.562	0.785
Total Geometric Volume (Å^3)	5,209.752	4,665.737	10,771.372	3,948.785
Total Geometric Volume (cm^3/g)	1.490	1.478	1.566	0.778
Network-Accessible Helium Volume (Å^3)	5,334.972	4,877.470	10,747.545	3,983.506
Network-Accessible Helium Volume (cm^3/g)	1.526	1.545	1.562	0.785
Network-Accessible Geometric Volume (Å^3)	5,209.752	4,665.610	10,771.155	3,948.661
Network-Accessible Geometric Volume (cm^3/g)	1.490	1.478	1.566	0.778
Pore Dimensions				
Pore Limiting Diameter (Å)	11.56	13.33	23.28	4.51
Maximum Pore Diameter (Å)	15.88	15.18	24.05	9.63
Number of Percolated Dimensions	1	1	1	2

Listing S5.1: MOF-TCPP Crystallographic Information Framework file

```

#======================================================================
# CRYSTAL DATA
#----------------------------------------------------------------------
data_MOFTCPP

_chemical_name_common                  'C48 H20 Ca N4 O10 Ti, O'
_cell_length_a                         19.573(3)
_cell_length_b                         19.573(3)
_cell_length_c                         17.551(3)
_cell_angle_alpha                      90.000000
_cell_angle_beta                       90.000000
_cell_angle_gamma                      90.000000
_cell_volume                           6723.829173
_space_group_name_H-M_alt              'P 4/m m m'
_space_group_IT_number                 123

loop_
_space_group_symop_operation_xyz
   'x, y, z'
   '-x, -y, -z'
   '-x, -y, z'
   'x, y, -z'
   '-y, x, z'
   'y, -x, -z'
   'y, -x, z'
   '-y, x, -z'
   '-x, y, -z'
   'x, -y, z'
   'x, -y, -z'
   '-x, y, z'
   'y, x, -z'
   '-y, -x, z'
   '-y, -x, -z'
   'y, x, z'

loop_
   _atom_site_label
   _atom_site_occupancy
   _atom_site_fract_x
   _atom_site_fract_y
   _atom_site_fract_z
   _atom_site_adp_type
   _atom_site_U_iso_or_equiv
   _atom_site_type_symbol
   C5         1.0     0.3255(13)   1.000000     0.2910(13)  Uiso  0.128000 C
   C4         1.0     0.3002(8)    1.0606(4)    0.2642(8)   Uiso  0.128000 C
   C3         1.0     0.2528(8)    1.0606(4)    0.2053(8)   Uiso  0.128000 C
   C2         1.0     0.2273(11)   1.000000     0.1784(13)  Uiso  0.128000 C
   C1         1.0     0.1782(13)   1.000000     0.1188(13)  Uiso  0.128000 C
   C6         1.0     0.3738(10)   1.000000     0.3555(13)  Uiso  0.160000 C
   C7         1.0     0.3515(14)   1.000000     0.4325(16)  Uiso  0.117000 C
   N2         1.0     0.500000     1.000000     0.3774(13)  Uiso  0.128000 N
   C9         1.0     0.4425(4)    1.000000     0.3308(13)  Uiso  0.145000 C
   C8         1.0     0.2825(16)   1.000000     0.4563(13)  Uiso  0.132000 C
   N1         1.0     0.393(2)     1.000000     0.500000    Uiso  0.111000 N
```

```
O1     1.0     0.1597(10)  0.9386(9)   0.0904(10)  Uiso  0.141000 O
C10    1.0     0.4645(2)   1.000000    0.2551(13)  Uiso  0.180000 C
Ca1    0.5000  0.0748(13)  0.9252(13)  0.000000    Uiso  0.034000 Ca
Ti1    0.5000  0.1116(7)   0.8884(7)   0.000000    Uiso  0.015000 Ti
O2     0.5000  0.0499(9)   0.9501(9)   0.000000    Uiso  0.009000 O
O3     0.5000  0.189(5)    0.811(5)    0.000000    Uiso  0.210000 O
O4     0.5000  0.230(4)    0.770(4)    0.000000    Uiso  0.210000 O
H3     1.0     0.238392    1.101738    0.184071    Uiso  0.154000 H
H4     1.0     0.314710    1.101659    0.285434    Uiso  0.154000 H
H10    1.0     0.436512    1.000000    0.212245    Uiso  0.216000 H
```

Listing S5.2: MOF-TBAPy Crystallographic Information Framework file

```

#======================================================================
# CRYSTAL DATA
#----------------------------------------------------------------------
data_MOFTBAPy

_chemical_name_common                  'C44 H22 Ca O10 Ti'
_cell_length_a                         19.160(3)
_cell_length_b                         19.160(3)
_cell_length_c                         16.140(3)
_cell_angle_alpha                      90.000000
_cell_angle_beta                       90.000000
_cell_angle_gamma                      90.000000
_cell_volume                           5925.084066
_space_group_name_H-M_alt              'P 4/m m m'
_space_group_IT_number                 123

loop_
_space_group_symop_operation_xyz
   'x, y, z'
   '-x, -y, -z'
   '-x, -y, z'
   'x, y, -z'
   '-y, x, z'
   'y, -x, -z'
   'y, -x, z'
   '-y, x, -z'
   '-x, y, -z'
   'x, -y, z'
   'x, -y, -z'
   '-x, y, z'
   'y, x, -z'
   '-y, -x, z'
   '-y, -x, -z'
   'y, x, z'

loop_
   _atom_site_label
   _atom_site_occupancy
   _atom_site_fract_x
   _atom_site_fract_y
   _atom_site_fract_z
   _atom_site_adp_type
   _atom_site_U_iso_or_equiv
   _atom_site_type_symbol
   O1         0.5000  0.446(2)     0.554(2)     0.500000    Uani  0.018000 O
   Ti         0.5000  0.3867(10)   0.6133(10)   0.500000    Uani  0.054333 Ti
   C7         1.0     0.1813(7)    0.500000     0.000000    Uani  0.138000 C
   C8         1.0     0.0727(4)    0.500000     0.0751(4)   Uani  0.138000 C
   C5         1.0     0.1870(7)    0.500000     0.1535(7)   Uani  0.138000 C
   C9         1.0     0.0365(2)    0.500000     0.1505(5)   Uani  0.138000 C
   C4         1.0     0.2084(7)    0.4381(4)    0.1908(7)   Uani  0.138000 C
   C3         1.0     0.2491(7)    0.4379(4)    0.2619(7)   Uani  0.138000 C
   C2         1.0     0.2726(7)    0.500000     0.2963(7)   Uani  0.138000 C
   C1         1.0     0.3170(9)    0.500000     0.3711(9)   Uani  0.132333 C
   C10        1.0     0.0365(2)    0.500000     0.000000    Uani  0.138000 C
```

```
   C6         1.0     0.1456(4)    0.500000     0.0754(4)    Uani   0.138000 C
   Ca         0.5000  0.4249(13)   0.5751(13)   0.500000     Uani   0.054333 Ca
   O2         1.0     0.3383(9)    0.5570(5)    0.4056(8)    Uani   0.132333 O
   O4         0.2500  0.3034(13)   0.6966(13)   0.500000     Uiso   0.030000 O
   O3         0.2500  0.3375(14)   0.6625(14)   0.500000     Uiso   0.030000 O
   H3         1.0     0.260772     0.395652     0.286716     Uiso   0.166000 H
   H4         1.0     0.195051     0.395754     0.167405     Uiso   0.166000 H
   H7         1.0     0.229826     0.500000     0.000000     Uiso   0.166000 H
   H9         1.0     0.060890     0.500000     0.200354     Uiso   0.166000 H

loop_
   _atom_site_aniso_label
   _atom_site_aniso_U_11
   _atom_site_aniso_U_22
   _atom_site_aniso_U_33
   _atom_site_aniso_U_12
   _atom_site_aniso_U_13
   _atom_site_aniso_U_23
   O1    0.01700  0.01700  0.02000 -0.01000  0.00000  0.00000
   Ti    0.07700  0.07700  0.00900  0.05500  0.00000  0.00000
   C7    0.16800  0.18500  0.06100  0.00000  0.00000  0.00000
   C8    0.16800  0.18500  0.06100  0.00000  0.00000  0.00000
   C5    0.16800  0.18500  0.06100  0.00000  0.00000  0.00000
   C9    0.16800  0.18500  0.06100  0.00000  0.00000  0.00000
   C4    0.16800  0.18500  0.06100  0.00000  0.00000  0.00000
   C3    0.16800  0.18500  0.06100  0.00000  0.00000  0.00000
   C2    0.16800  0.18500  0.06100  0.00000  0.00000  0.00000
   C1    0.10600  0.24000  0.05100  0.00000 -0.01800  0.00000
   C10   0.16800  0.18500  0.06100  0.00000  0.00000  0.00000
   C6    0.16800  0.18500  0.06100  0.00000  0.00000  0.00000
   Ca    0.07700  0.07700  0.00900  0.05500  0.00000  0.00000
   O2    0.10600  0.24000  0.05100  0.00000 -0.01800  0.00000
```

Listing S5.3: MOF-TCPB Crystallographic Information Framework file

```

#=====================================================================
# CRYSTAL DATA
#---------------------------------------------------------------------
data_MOFTCPB

_cell_length_a                          37.440(5)
_cell_length_b                          37.440(5)
_cell_length_c                          11.450(2)
_cell_angle_alpha                       90.000000
_cell_angle_beta                        90.000000
_cell_angle_gamma                       120.000000
_cell_volume                            13899.774653
_space_group_name_H-M_alt               'P 6/m m m'
_space_group_IT_number                  191

loop_
_space_group_symop_operation_xyz
   'x, y, z'
   '-x, -y, -z'
   '-y, x-y, z'
   'y, -x+y, -z'
   '-x+y, -x, z'
   'x-y, x, -z'
   '-x, -y, z'
   'x, y, -z'
   'y, -x+y, z'
   '-y, x-y, -z'
   'x-y, x, z'
   '-x+y, -x, -z'
   'y, x, -z'
   '-y, -x, z'
   'x-y, -y, -z'
   '-x+y, y, z'
   '-x, -x+y, -z'
   'x, x-y, z'
   '-y, -x, -z'
   'y, x, z'
   '-x+y, y, -z'
   'x-y, -y, z'
   'x, x-y, -z'
   '-x, -x+y, z'

loop_
   _atom_site_label
   _atom_site_occupancy
   _atom_site_fract_x
   _atom_site_fract_y
   _atom_site_fract_z
   _atom_site_adp_type
   _atom_site_U_iso_or_equiv
   _atom_site_type_symbol
   Ti1        1.0     1.000000     0.5812(10)    0.000000    Uani  0.075333 Ti
   C1         1.0     0.7750(5)    0.5500(9)    -0.3779(13)  Uani  0.088889 C
   O1         1.0     1.000000     0.5363(11)    0.000000    Uani  0.078667 O
   C2         1.0     0.8077(5)    0.5501(7)    -0.4386(7)   Uani  0.088889 C
```

```
   C6          1.0      0.8983(7)     0.5429(7)     -0.2396(14)   Uani   0.088889 C
   C5          1.0      0.9036(5)     0.5816(7)     -0.2637(17)   Uani   0.088889 C
   C4          1.0      0.8744(7)     0.5852(5)     -0.3299(16)   Uani   0.088889 C
   C3          1.0      0.8399(5)     0.5501(7)     -0.3720(10)   Uani   0.088889 C
   C8          1.0      0.8346(5)     0.5113(7)     -0.3478(15)   Uani   0.088889 C
   C7          1.0      0.8638(7)     0.5077(7)     -0.2817(17)   Uani   0.088889 C
   O2          1.0      0.9552(13)    0.5699(10)    -0.114(3)     Uani   0.078667 O
   CaA         1.0      0.9298(13)    0.4649(7)      0.000000     Uani   0.096111 Ca
   C9          1.0      0.9305(7)     0.5391(9)     -0.179(2)     Uani   0.088889 C
   O3          1.0      0.9463(13)    0.5157(11)    -0.171(2)     Uani   0.078667 O
   O9          1.0      1.000000      0.6373(11)     0.000000     Uiso   1.600000 O
   O4          1.0      0.8467(14)    0.4233(7)      0.000000     Uiso   0.280000 O
   H1          1.0      0.774925      0.549850      -0.296727     Uiso   0.107000 H
   H4          1.0      0.877982      0.611178      -0.346036     Uiso   0.107000 H
   H5          1.0      0.926659      0.605160      -0.235578     Uiso   0.107000 H
   H7          1.0      0.860196      0.481804      -0.265533     Uiso   0.107000 H
   H8          1.0      0.811519      0.487823      -0.375992     Uiso   0.107000 H

loop_
   _atom_site_aniso_label
   _atom_site_aniso_U_11
   _atom_site_aniso_U_22
   _atom_site_aniso_U_33
   _atom_site_aniso_U_12
   _atom_site_aniso_U_13
   _atom_site_aniso_U_23
   Ti1    0.12900  0.10400  0.00200  0.06500  0.00000  0.00000
   C1     0.09300  0.09400  0.08000  0.04700 -0.00600 -0.01200
   O1     0.10300  0.09900  0.03600  0.05200  0.00000  0.00000
   C2     0.09300  0.09400  0.08000  0.04700 -0.00600 -0.01200
   C6     0.09300  0.09400  0.08000  0.04700 -0.00600 -0.01200
   C5     0.09300  0.09400  0.08000  0.04700 -0.00600 -0.01200
   C4     0.09300  0.09400  0.08000  0.04700 -0.00600 -0.01200
   C3     0.09300  0.09400  0.08000  0.04700 -0.00600 -0.01200
   C8     0.09300  0.09400  0.08000  0.04700 -0.00600 -0.01200
   C7     0.09300  0.09400  0.08000  0.04700 -0.00600 -0.01200
   O2     0.10300  0.09900  0.03600  0.05200  0.00000  0.00000
   CaA    0.12000  0.10600  0.06700  0.06000  0.00000  0.00000
   C9     0.09300  0.09400  0.08000  0.04700 -0.00600 -0.01200
   O3     0.10300  0.09900  0.03600  0.05200  0.00000  0.00000
```

Listing S5.4: MOF-MTB ystallographic Information Framework file

```

#======================================================================
# CRYSTAL DATA
#----------------------------------------------------------------------
data_MOFMTB
_chemical_name_common                   'C29 H16 Ca O11 Ti'
_cell_length_a                          15.811(2)
_cell_length_b                          15.811(2)
_cell_length_c                          23.639(5)
_cell_angle_alpha                       90.000000
_cell_angle_beta                        90.000000
_cell_angle_gamma                       90.000000
_cell_volume                            5909.459625
_space_group_name_H-M_alt               'I 4/m m m'
_space_group_IT_number                  139

loop_
_space_group_symop_operation_xyz
   'x, y, z'
   '-x, -y, -z'
   '-x, -y, z'
   'x, y, -z'
   '-y, x, z'
   'y, -x, -z'
   'y, -x, z'
   '-y, x, -z'
   '-x, y, -z'
   'x, -y, z'
   'x, -y, -z'
   '-x, y, z'
   'y, x, -z'
   '-y, -x, z'
   '-y, -x, -z'
   'y, x, z'
   'x+1/2, y+1/2, z+1/2'
   '-x+1/2, -y+1/2, -z+1/2'
   '-x+1/2, -y+1/2, z+1/2'
   'x+1/2, y+1/2, -z+1/2'
   '-y+1/2, x+1/2, z+1/2'
   'y+1/2, -x+1/2, -z+1/2'
   'y+1/2, -x+1/2, z+1/2'
   '-y+1/2, x+1/2, -z+1/2'
   '-x+1/2, y+1/2, -z+1/2'
   'x+1/2, -y+1/2, z+1/2'
   'x+1/2, -y+1/2, -z+1/2'
   '-x+1/2, y+1/2, z+1/2'
   'y+1/2, x+1/2, -z+1/2'
   '-y+1/2, -x+1/2, z+1/2'
   '-y+1/2, -x+1/2, -z+1/2'
   'y+1/2, x+1/2, z+1/2'

loop_
   _atom_site_label
   _atom_site_occupancy
   _atom_site_fract_x
   _atom_site_fract_y
```

```
_atom_site_fract_z
_atom_site_adp_type
_atom_site_U_iso_or_equiv
_atom_site_type_symbol
Ti1        0.5000  0.6427(2)    0.6427(2)    0.500000    Uiso  0.020800 Ti
Ca1         0.5000  0.5985(2)    0.5985(2)    0.500000    Uiso  0.029000 Ca
C8         1.0     0.500000     0.7293(2)    0.41922(13) Uiso  0.079000 C
O1         1.0     0.5718(2)    0.7001(2)    0.43134(16) Uiso  0.139000 O
C1         1.0     0.500000     1.000000     0.250000    Uiso  0.027000 C
C2         1.0     0.500000     0.9280(2)    0.29201(14) Uiso  0.064000 C
C7         1.0     0.5755(2)    0.89114(17)  0.31095(12) Uiso  0.075500 C
C6         1.0     0.5751(2)    0.8265(2)    0.35111(12) Uiso  0.119000 C
C5         1.0     0.500000     0.79748(17)  0.37539(11) Uiso  0.093000 C
OWT        0.5000  0.7854(4)    0.7854(4)    0.500000    Uiso  0.179000 O
OWC        0.5000  0.7415(4)    0.7415(4)    0.500000    Uiso  0.179000 O
O2         0.5000  0.5593(7)    0.5593(7)    0.500000    Uiso  0.048000 O
H6         1.0     0.626075     0.802203     0.362005    Uiso  0.143000 H
H7         1.0     0.626776     0.910124     0.296478    Uiso  0.091000 H
```

Chapter 6

3D-Electron Diffraction on a Flexible MOF

6.1 Introduction

Metal-Organic Frameworks (MOFs) are highly valued for their structural versatility and the ease with which their pore environments can be tailored. By carefully selecting metal nodes and organic linkers, or by targeting specific network topologies, we can fine-tune the size and shape of MOF pores to suit a wide range of applications. This adaptability has been a central theme in the previous chapters, where we explored the crystallographic characterization of rigid MOFs with fixed pore structures.

However, not all MOFs are rigid. There is a subset that exhibits flexibility, allowing them to undergo structural changes in response to external stimuli or host–guest interactions. These flexible MOFs, also referred to as breathing MOFs, can adjust their pore sizes and shapes without compromising the overall framework integrity [93, 81]. The structural transformations are commonly associated with interactions between the MOF and guest molecules but can also be triggered by external factors such as light, temperature, or mechanical pressure [93, 10].

Understanding these structural changes at the atomic level is crucial for exploiting the properties and functionalities of these materials. Examples of such MOFs include `PCN-128` [10], `SU-100` [11], and `MIL-53` [12], which exhibit reversible structural transformations that affect their physical and chemical behaviors.

For instance, `PCN-128` can change from a white powder (`PCN-128W`) to a yellow powder (`PCN-128Y`), and vice versa, upon mechanical compression or chemical treatment. This transformation involves a change in the conformation of the organic linker, leading to alterations in its luminescence properties [10]. `SU-100` is a bismuth-based MOF that shows flexible behaviour originating from the Bi–O clusters, leading to changes in bond angles within the clusters upon solvent exchange [11]. `MIL-53`, on the other hand, exhibits a high degree of flexibility upon hydration, with its pore dimensions changing significantly depending on the presence or absence of guest molecules [12].

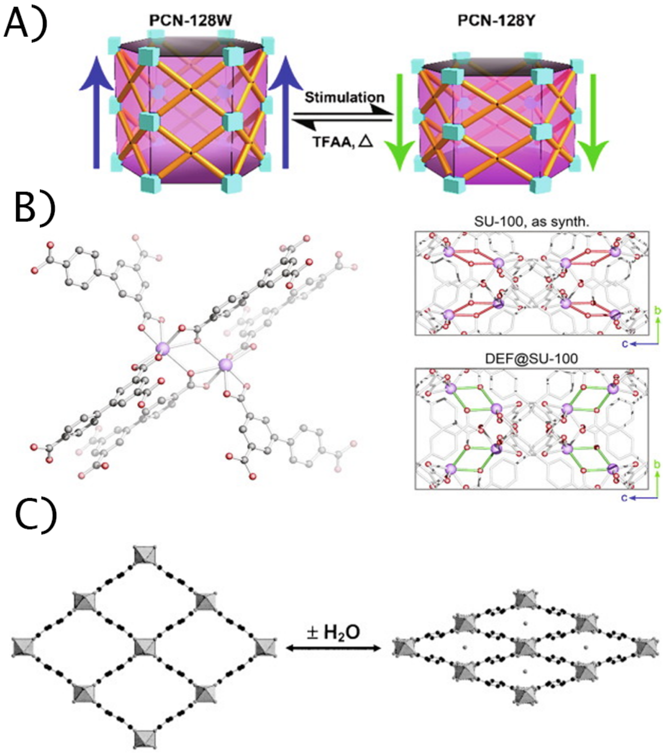

Figure 6.1: Flexible behaviour observed in `PCN-128` upon compression (A) [10], in `SU-100` upon solvent exchange (B) [11] and in `MIL-53` upon hydration (C) [12].

In this chapter, we focus on a zinc-based MOF containing an alanine-derived linker, specifically *(R)-N-(1-((1H-pyrazol-4-yl)amino)-1-oxopropan-2-yl)-1H-pyrazole-4-carboxamide*, abbreviated as Pz-Ala-Pz (see Figure 6.2 A). The MOF, referred to as `MOF-Ala`, was synthesized and provided by Victor Carratalá Muñoz from Carlos Martí-Gastaldo's Functional Inorganic Materials Group at the Institute of Molecular Science of the University of Valencia. The different PXRD patterns observed under wet and dry conditions strongly suggest a flexible behaviour, characterized by open and closed phases (Figure 6.2 B). However, confirming this phenomenon proved challenging due to the sub-micrometer dimensions of the crystals, as revealed by SEM images showing a needle-like morphology ranging from about 100 to 300 nm in thickness (Figure 6.3). Consequently, SCXRD was not feasible, and attempts to solve the structure by PXRD were also unsuccessful. In response, we will discuss different sample preparation strategies to target specific phases of the MOF, enabling 3D-ED experiments that reveal definitive structural models for each phase. Such insights are crucial for elucidating the fundamental mechanism behind the MOF's breathing behaviour and for revealing its potential in diverse applications.

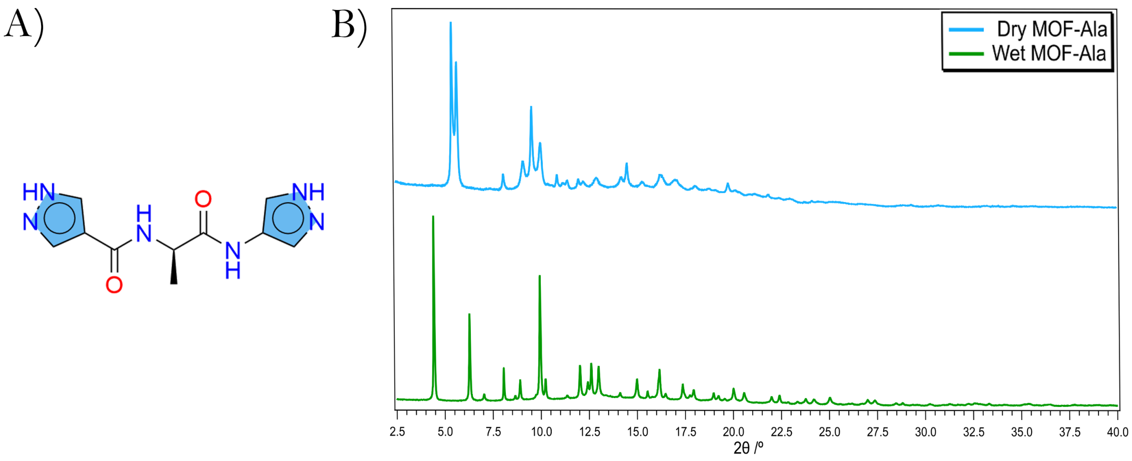

Figure 6.2: (A) Pz-Ala-Pz linker used for the synthesis of `MOF-Ala`. (B) PXRD Profiles of the dry (blue) and wet (green) MOF-Ala.

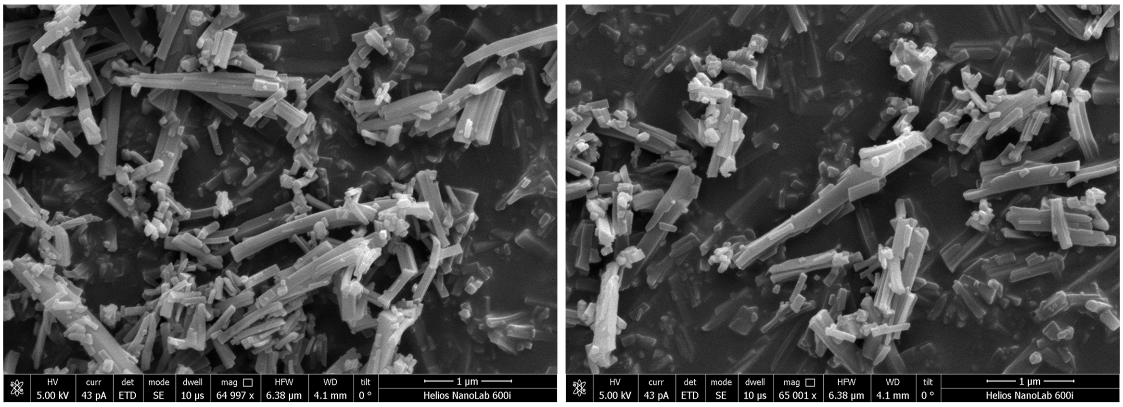

Figure 6.3: SEM Images of `MOF-Ala` showing the needle-like morphologies with thickness ranging between 100 to 300 nm.

6.2 Sample Preparation

Effective sample preparation is essential for accurately studying flexible MOFs using 3D-ED. The process must preserve the desired phase of the MOF (dry or wet) while minimizing beam-induced damage due to the material's sensitivity. In the following subsections, we describe the sample preparation techniques used to target specific MOF phases, all starting from the as synthesized batch, in a DMF (N,N-Dimethylformamide) solution.

6.2.1 Preparation of Dry `MOF-Ala`

To investigate the MOF in its activated, dry state, it was necessary to ensure the complete removal of the solvent molecules from its pores. This activation and drying process was achieved by relying on the high vacuum environment within the TEM. A small drop of DMF solution with the MOF crystals in suspension was carefully placed onto a TEM grid, and excess solvent was removed through bottom blotting. The sample was then inserted into the TEM and cooled down to 100 K ($\approx -170^{\circ}C$), as described in the previous **chapter** **Figure 5.5**.

Images of `MOF-Ala` crystals upon cooling are shown in Figure 6.4.

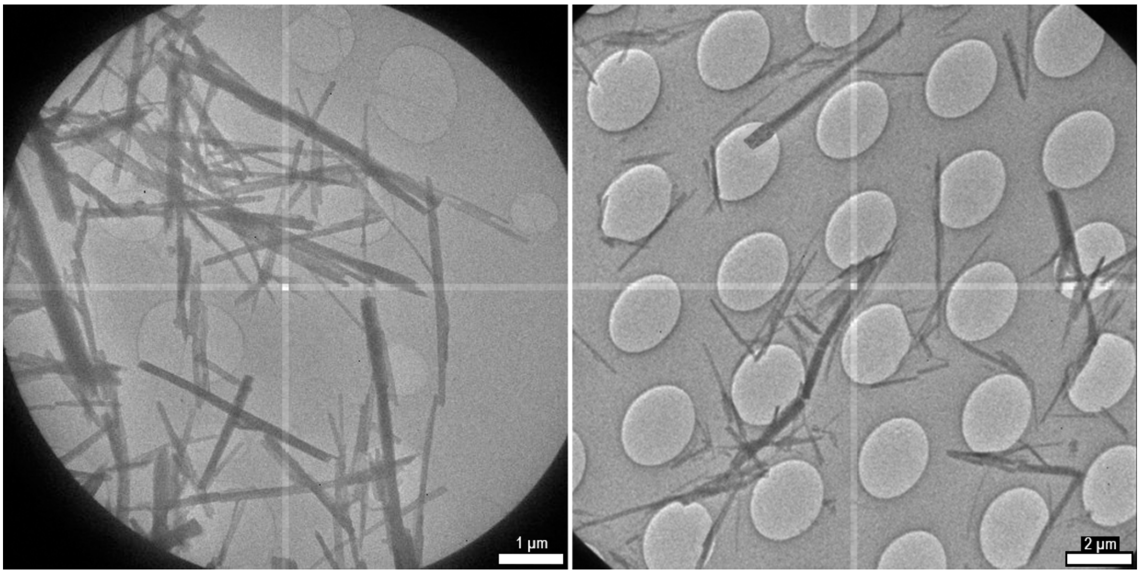

Figure 6.4: `MOF-Ala` Crystals prepared by cooling.

6.2.2 Preparation of Wet `MOF-Ala`

Investigating the MOF in its wet state requires preserving solvent molecules within its pores. To achieve this, two different methods were employed to maintain the guest-filled phase and structural integrity during 3D-ED analysis.

6.2.2.1 Plunge Freezing

Plunge freezing is a widely used approach for preparing solvent-containing samples for cryo-EM analysis, as it rapidly immobilizes the sample in its native state, preserving the structural and chemical integrity of the material. The process begins with glow discharging the TEM grid, which renders its surface hydrophilic. While this step is traditionally employed to promote uniform spreading of aqueous samples, it is equally effective for ensuring the even distribution of organic solvents such as DMF or acetone on the grid surface.

Once the TEM grid is prepared, a small droplet of the MOF suspension is carefully applied to its surface using a micropipette. To ensure the formation of a thin and uniform layer, which is a requirement for TEM analysis, excess solvent is gently removed by bottom blotting with filter paper. This process helps to achieve the optimal sample thickness while retaining sufficient solvent within the MOF pores to simulate its native solvent-containing state.

Finally, the grid is rapidly plunged into a cryogen, typically liquid ethane cooled by liquid nitrogen. This step is essential for vitrifying the organic solvent, such as DMF or acetone, into an amorphous state without crystallization and preserves the native guest-filled structure of the MOF. A schematic representation of the steps involved is illustrated in Figure 6.5.

Images of `MOF-Ala` crystals after plunge freezing are shown in Figure 6.6. The needle-like crystals exhibit a slightly blurry and diffuse appearance, which is a common characteristic of plunge freezing experiments. This effect is attributed to the vitrification of the surrounding solvent, which encapsulates the crystals.

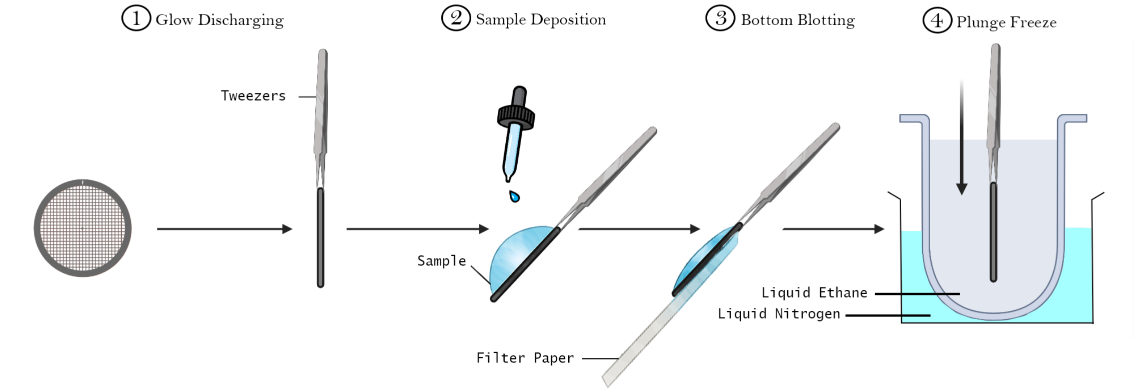

Figure 6.5: Schematic representation of the plunge freezing process used to prepare solvent-containing MOF samples for electron diffraction analysis.

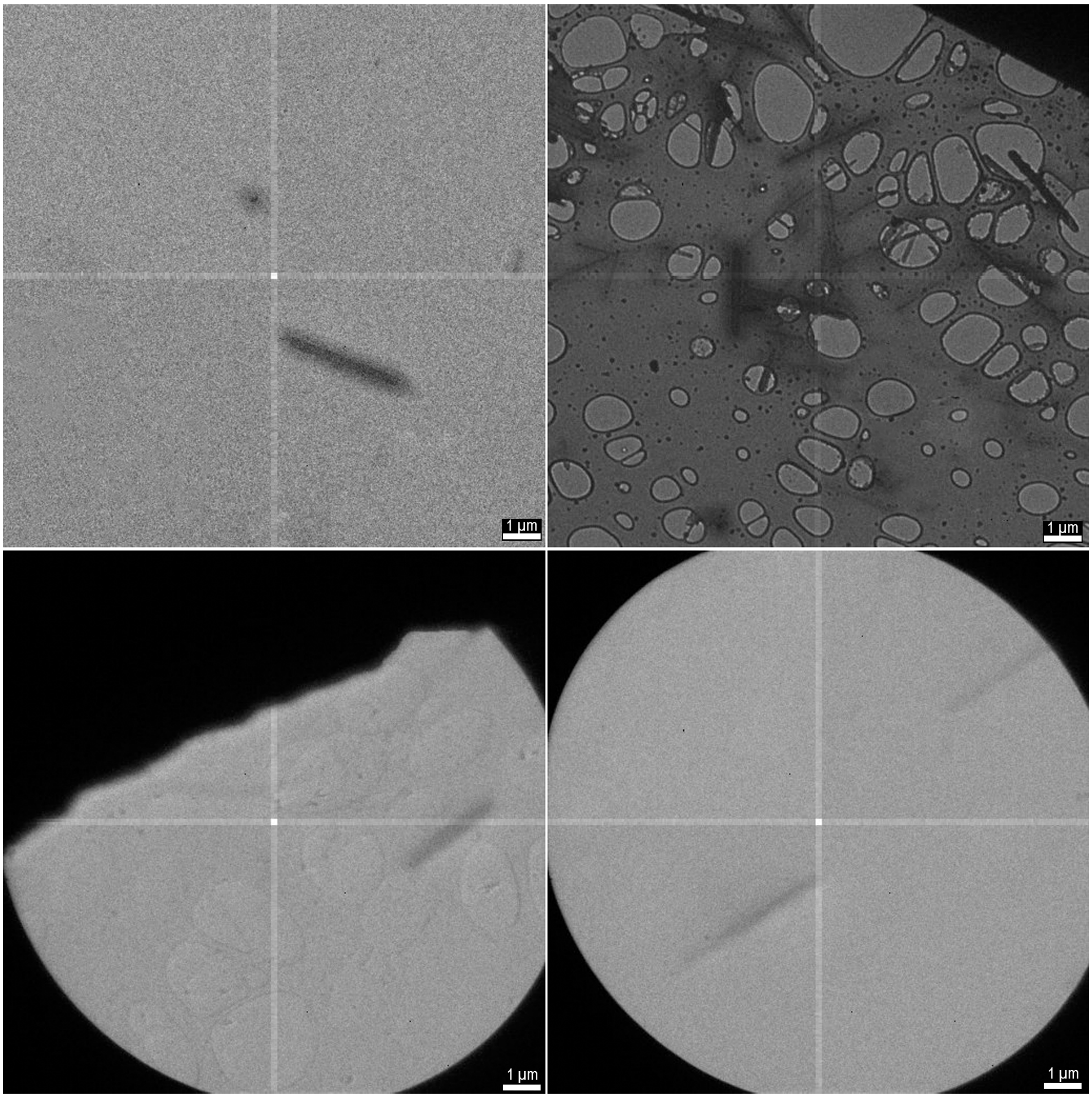

Figure 6.6: `MOF-Ala` crystals prepared by plunge freezing.

6.2.2.2 Grid-Sandwiching

The sandwiching technique is another method employed to prepare solvent-containing MOF samples for 3D-ED analysis. The process begins by placing a continuous carbon copper TEM grid onto a clean glass slide. A small droplet of the MOF suspension is then carefully deposited onto the grid using a micropipette. To create a protective environment and minimize solvent evaporation, a second TEM grid is overlaid and precisely aligned on top of the first grid. For the second grid, different types were tested, including continuous carbon, holey carbon, and Quantifoil grids. This configuration guarantees the formation of liquid pockets between the grids, preserving the guest-filled state of the MOF by preventing the surrounding solvent from evaporation during the TEM analysis. A similar method was recently employed by Sergi Plana-Ruiz et al. to perform electron diffraction on hydrated protein crystals at room temperature using two graphene grids [94]. Here, we adapt the same concept for a different type of material, using readily available TEM grids and an alternative sample preparation approach, illustrated in Figure 6.7.

Images of `MOF-Ala` crystals prepared using the grid sandwiching approach are presented in Figure 6.8. These images clearly illustrate the formation of liquid pockets between the overlaid TEM grids, which encapsulate the crystals. The proper alignment of the two grids creates enclosed areas where the solvent remains trapped, preventing evaporation and preserving the solvent-containing state of the crystals during analysis. We believe that the morphology and, more importantly, the thickness of the crystals are critical for this approach to work effectively. Crystals with appropriate dimensions ensure they can be adequately encapsulated within the liquid pockets.

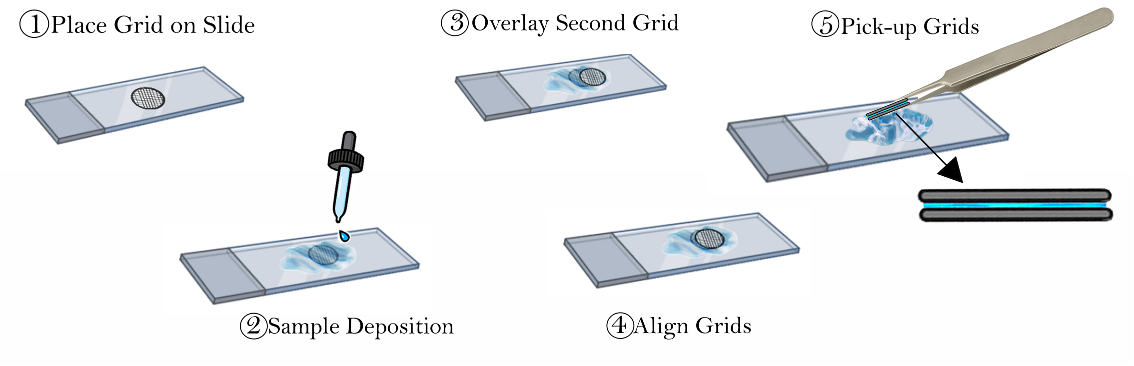

Figure 6.7: Illustration of the sandwiching method employed to prepare solvent-containing MOF samples.

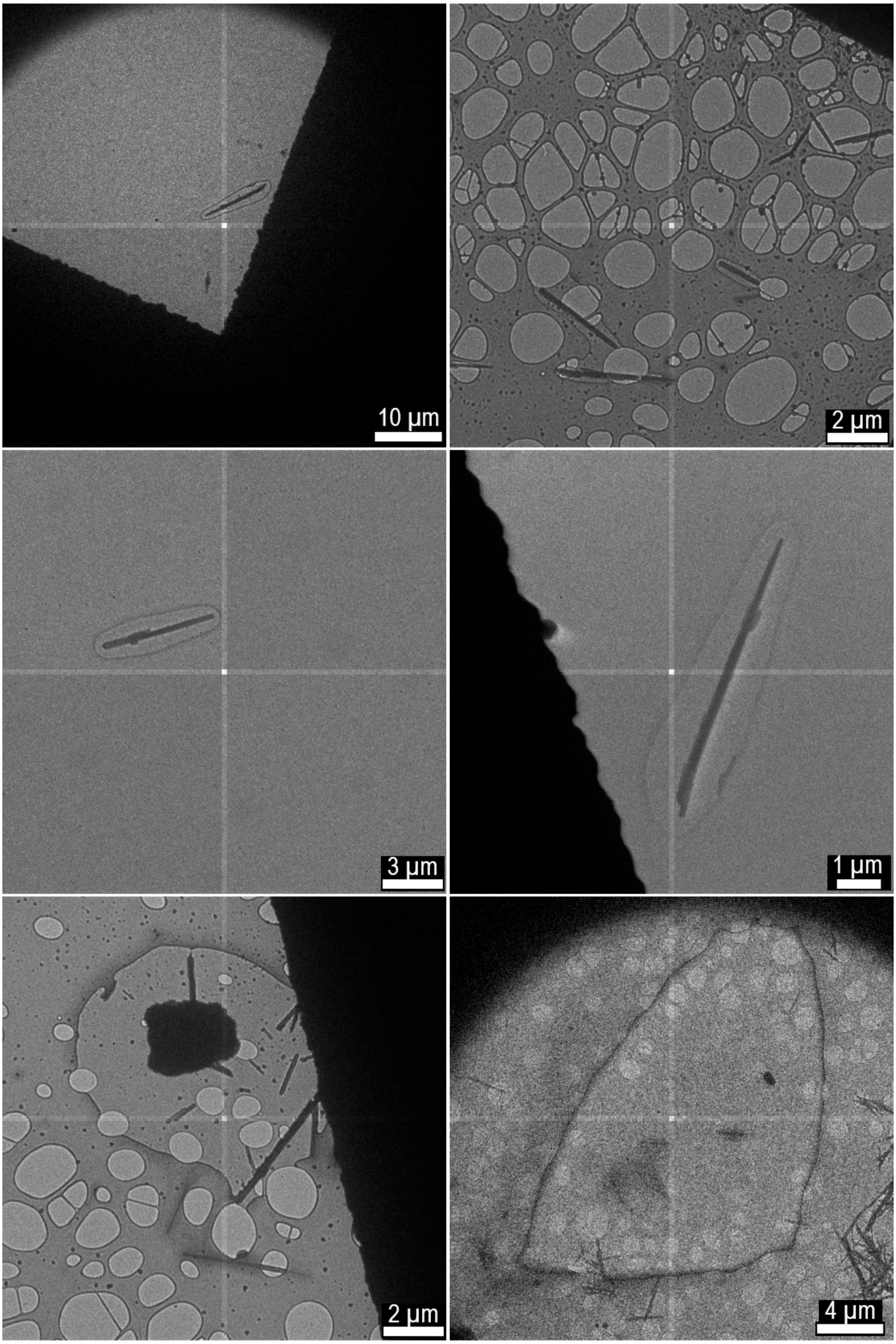

Figure 6.8: `MOF-Ala` crystals prepared by grid-sandwiching.

6.3 3D-ED on `MOF-Ala`

Data acquisition for both wet and dry states of the MOF was performed using the LibraEDT software (**chapter 2**) in cRED. Information regarding two standard data acquisitions on both type of samples, dry and wet are reported in Table 6.1.

Table 6.1: Experimental Parameters for 3D-ED Data Acquisition.

Parameter	**Dry** `MOF-Ala`	**Wet** `MOF-Ala` (1)	**Wet** `MOF-Ala` (2)
Emission Current (μA)	0.40	1.00	0.70
Emission Current (μA)	0.40	1.00	0.70
STEM Mode: Spot Size (nm)	2.00	4.00	2.00
Beam diameter size (nm)	150	150	150
Exposure Time (ms)	700	500	500
Data Collection Duration (s)	72.42	41.23	60.23
Rotation Speed (Deg/s)	1.12	1.95	2.01
Oscillation Range (Deg)	0.81	1.03	1.03
Starting Angle (Deg)	-40.00	-40.00	-60.00
Ending Angle (Deg)	40.50	40.50	60.50

1 - Plunge-Freezing, **2** - Grid-Sandwiching.

6.3.1 Data Processing and Structure Solution

The datasets for both wet and dry `MOF-Ala` were processed using `XDS` [37] for data integration and indexing. Resolution cutoff was determined based on the $CC_{1/2}$ criterion to ensure the reliability of the data. An ab-initio structure solution was obtained using `SHELXT` [46], and subsequent refinements were performed under the kinematical approximation with `SHELXL` [47]. The refinement process was carried out within the `OLEX2` [48] and `ShelXle` [49].

Detailed refinement parameters, including unit cell dimensions, space groups, and

R-factors, are summarized in Table 6.2.

Table 6.2: Refinement details for the dry and wet MOF structures.

Parameter	**Dry MOF**	**Wet MOF**
Empirical formula	$C_{10}H_{10}N_6O_2Zn$	$C_{10}H_{10}N_6O_2Zn$
Formula weight (g/mol)	311.62	311.74
Temperature (K)	100	100
Crystal system	Orthorhombic	Tetragonal
Space group	$P2_12_12$	$P4_2$
a (Å)	10.985(2)	17.373(3)
b (Å)	20.179(4)	17.373(3)
c (Å)	7.2067(14)	7.3526(15)
Volume (Å^3)	1597.5(5)	2219.2(8)
Z	4	4
ρ_{calc} (g/cm^3)	1.253	0.933
Radiation (λ)	0.03350	0.0335
2Θ range (°)	0.2 to 2.08	0.11 to 1.592
Reflections collected	3105	2489
Final R1 indexes [$I \geq 2\sigma(I)$]	0.1676	0.1540

6.3.2 Dry `MOF-Ala`

The structural analysis of dry **`MOF-Ala`** reveals that it crystallizes in orthorhombic symmetry with a space group of $P2_12_12$. Its asymmetric unit comprises the Pz-Ala-Pz linker coordinated to two distinct Zn atoms (Figure 6.9). Each Zn atom exhibits a tetrahedral coordination environment, with four nitrogen atoms from pyrazole groups of different linkers contributing to the connectivity. The framework extends into a one-dimensional zinc tetrahedral chain along the [001] crystallographic direction (Figure 6.10A).

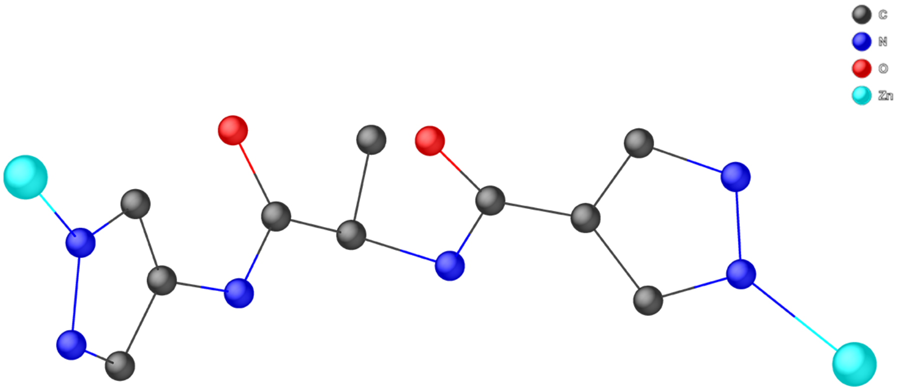

Figure 6.9: Asymmetric unit of dry `MOF-Ala`. Hydrogens are omitted for clarity.

When viewed along the [110] direction (Figure 6.10B), the chain structure features a repeating hexagonal motif, where each hexagon is formed by two Zn atoms and two pyrazole groups from two different linkers. The hexagons alternate in orientation by rotating along the chain direction, as shown in the top-down view along [001] (Figure 6.10C). Extending this view to the full crystal structure (Figure 6.10D), we observe the unit cell of `MOF-Ala` as seen from the c-axis, clearly showing the arrangement of the Zn atoms and the linkers that define the overall framework of the material.

The crystal structure of `MOF-Ala` possesses a unit cell volume of 1597.5 Å^3, with approximately 30% of this volume consisting of voids as estimated by `Mercury` [74]. This compactness reflects the structural contraction of the framework in its dry state, with the absence of solvent molecules reducing the spacing between linkers and Zn atoms, leading to a denser overall arrangement. Further analysis using the Pore Analyzer tool in `Mercury` revealed that the largest pore diameter within the framework is approximately 3.23 Å, with a limiting pore diameter of 2.29 Å. These metrics, summarized in Table S6.1, highlight the reduced porosity of the dry MOF, reason why we refer to it as the closed phase Figure 6.11.

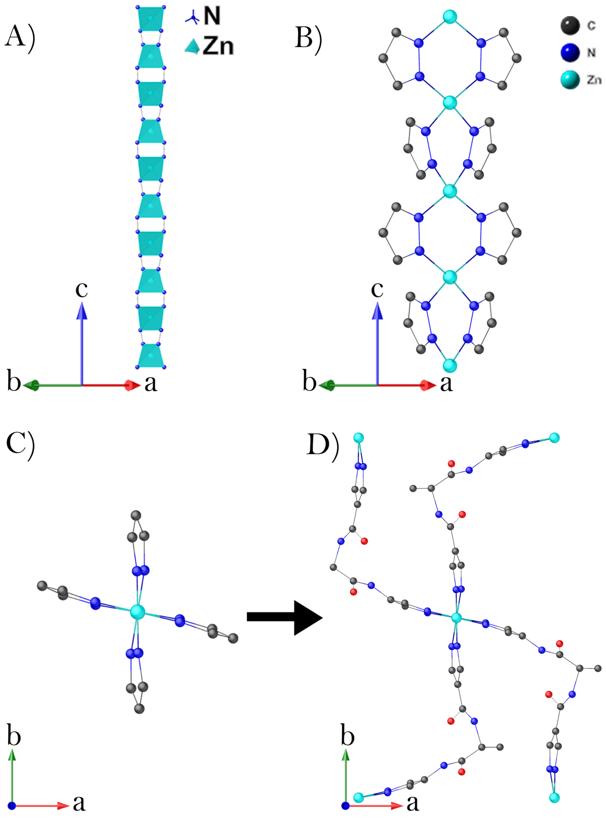

Figure 6.10: (A) Zn chains growing along the [001]. (B) and (C) View of the chain along the [110] and [001] directions. (D) View of a unit cell along [001].

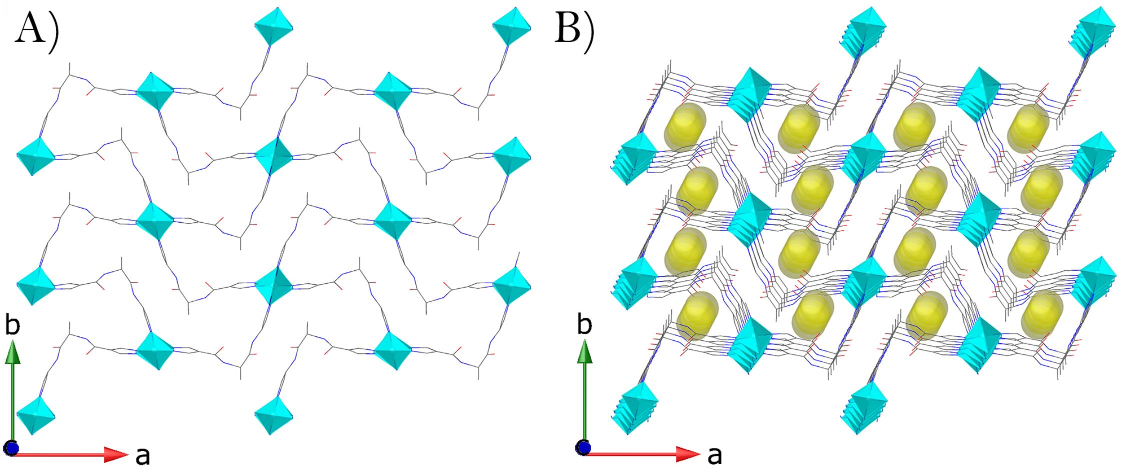

Figure 6.11: (A) Top-down view of the closed `MOF-Ala` structure along the [001] direction. (B) Visualization of the void spaces within the closed `MOF-Ala` framework, with the yellow spheres representing voids.

6.3.3 Wet `MOF-Ala`

The wet `MOF-Ala` crystallizes in a tetragonal system with the space group $P4_2$. The asymmetric unit remains analogous to that of the dry phase, comprising the Pz-Ala-Pz linker coordinated to two distinct Zn atoms (Figure 6.12). Each Zn atom maintains a tetrahedral coordination environment, coordinated by four nitrogen atoms from pyrazole groups of different linkers, thereby preserving the connectivity observed in the dry state. The framework extends into a one-dimensional zinc tetrahedral chain along the [001] crystallographic direction, similar to the dry phase (Figure 6.13A).

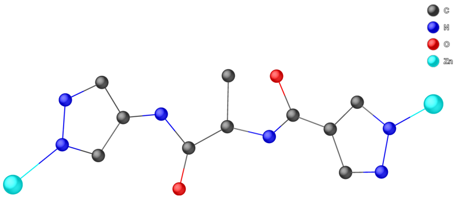

Figure 6.12: Asymmetric unit of wet `MOF-Ala`. Hydrogens are omitted for clarity.

A significant structural difference between the dry and wet phases becomes evident when the framework is viewed along the [001] direction (Figure 6.13C). Specifically, there is a slight variation in the geometry of the Zn coordination environment, which will be examined in detail in the subsequent subsection. Extending this view (Figure 6.13D) reveals a pronounced expansion compared to the dry phase, characterized by larger pore spaces.

The crystal structure of wet `MOF-Ala` exhibits a unit cell volume of approximately 2219.2 Å^3, with 54% of this volume comprising voids, as estimated using `Mercury` [74]. This increase in void space results in a reduced density compared to the dry phase. Further pore analysis using the Pore Analyzer tool in `Mercury` determined that the largest pore diameter within the framework is approximately 6.24 Å, while the limiting pore diameter is 5.24 Å. These parameters, detailed in Table S6.1, highlight the improved porosity of the wet MOF, justifying its designation as the

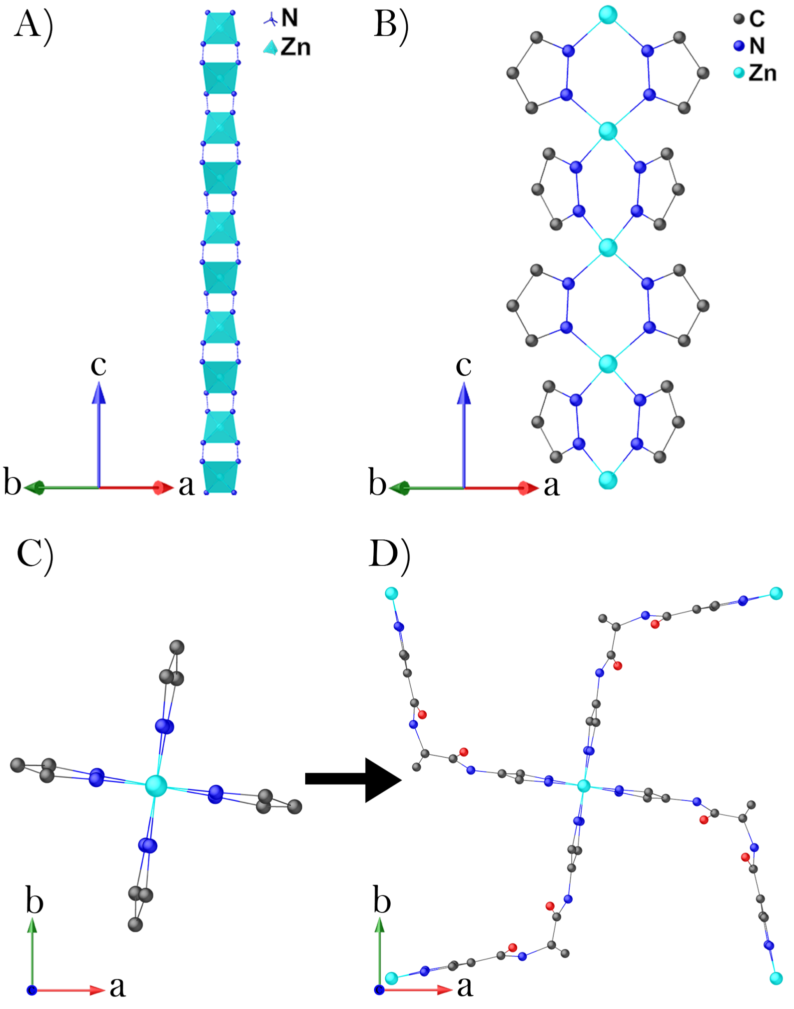

Figure 6.13: (A) Zn chains growing along the [001]. (B) and (C) View of the chain along the [110] and [001] directions. (D) View of a unit cell along [001].

open phase Figure 6.14.

It is worth mentioning that the crystal structure obtained was identical using both sample preparation methods (plunge freezing and grid-sandwiching). This demonstrates that grid-sandwiching can serve as a viable alternative to plunge freezing, particularly in situations where the latter is not feasible due to equipment limitations or the nature of the solvent used in the sample.

Until now, for clarity and simplicity, we have described the wet `MOF-Ala` structure without explicitly considering any guest molecules. However, during the refinement

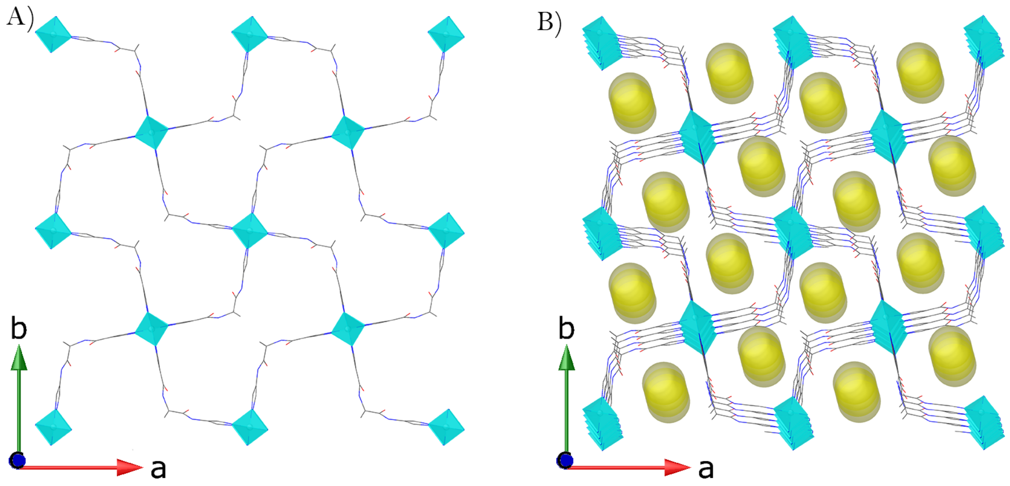

Figure 6.14: Top-down view and void visualization of the open (wet) `MOF-Ala` structure along the [001] direction, highlighting the expanded pore spaces.

of the wet `MOF-Ala` crystal structure, residual electron density was observed within the pores (Figure 6.15A). This residual density was successfully modeled by introducing a DMF molecule split across two positions (Figure 6.15B), which led into an improved crystallographic model, as evidenced by a 6% decrease in the R-factor from the electron diffraction data.

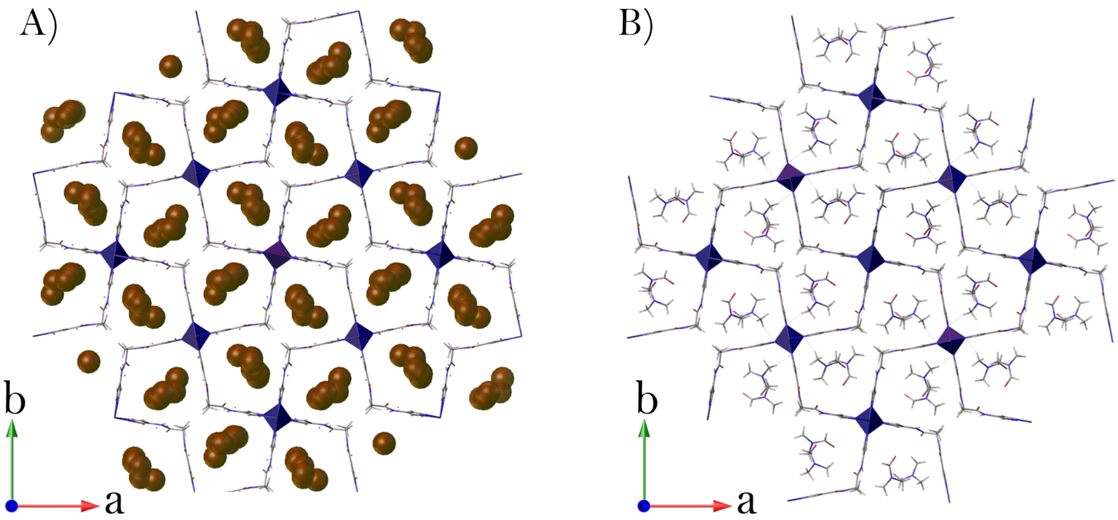

Figure 6.15: Residual electrostatic potential within the pores was modeled as a DMF molecule split across two positions.

6.3.4 Conformational and coordination differences between closed and open `MOF-Ala`

The flexibility inherent in the amino acid-derived linker of `MOF-Ala` induces significant conformational changes between its dry (closed) and wet (open) phases. In the closed phase, the dihedral angle between the planes defined by the central carbon atom of the linker and each attached pyrazole group is approximately 102°, as depicted in Figure 6.16A. Transitioning to the wet phase, this angle expands to 112° (Figure 6.16B), demonstrating the inherent flexibility of the single bonds within the linker.

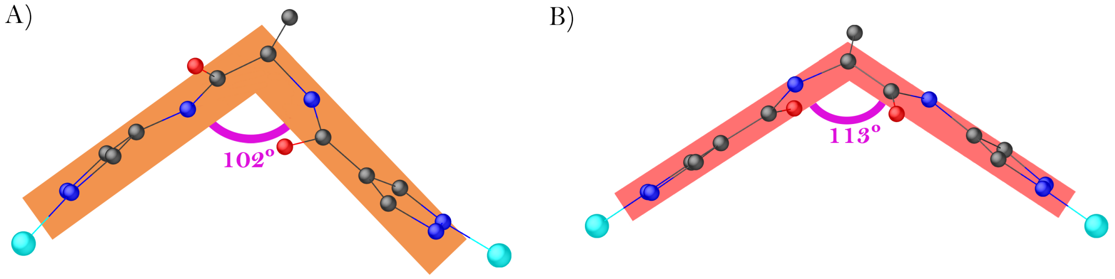

Figure 6.16: Dihedral angle between the planes of the central carbon and pyrazole groups. (A) Closed phase: 102°. (B) Open phase: 112°

In addition to conformational adjustments in the linker, the coordination geometry of the zinc centers undergoes notable alterations. In the closed phase, the angle between the Zn atoms and the coordinating linkers is approximately 72° (Figure 6.17A). Upon transitioning to the open phase, this angle increases to 90° (Figure 6.17B), resulting in a more symmetrical coordination environment.

This angular adjustment of the Zn centers can be compared to a scissor mechanism, where the Zn atoms act as hinges that open and close to accommodate changes in the framework's porosity, much like how the blades of a scissor move to widen or narrow their opening. In the closed phase, the narrower angle restricts the framework, minimizing void spaces, while in the open phase, the widened angle allows the framework to expand, increasing pore volumes and enhancing solvent uptake.

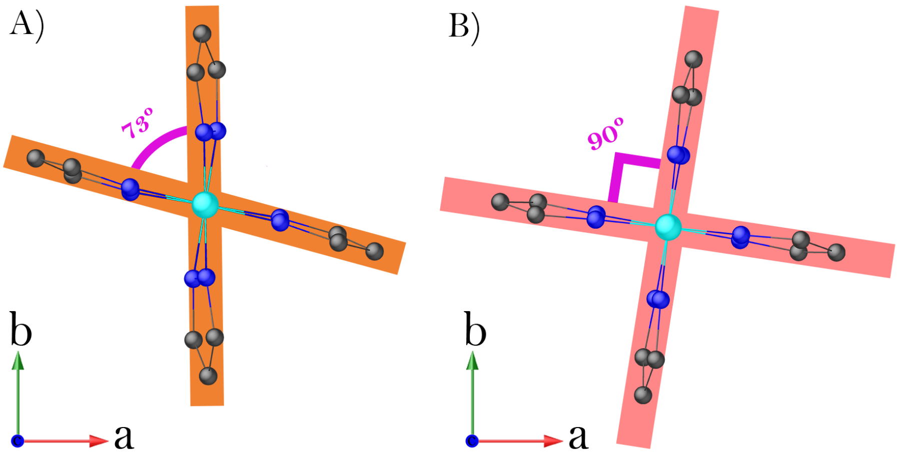

Figure 6.17: Coordination geometry around the Zn center. (A) Closed phase: 72°. (B) Open phase: 90°.

These combined conformational and coordination adjustments drive the structural differences between the closed and open phases of `MOF-Ala`, enabling the framework to adapt its porosity in response to solvent uptake and release with obvious applications in areas such as gas storage, separation, catalysis or drug delivery.

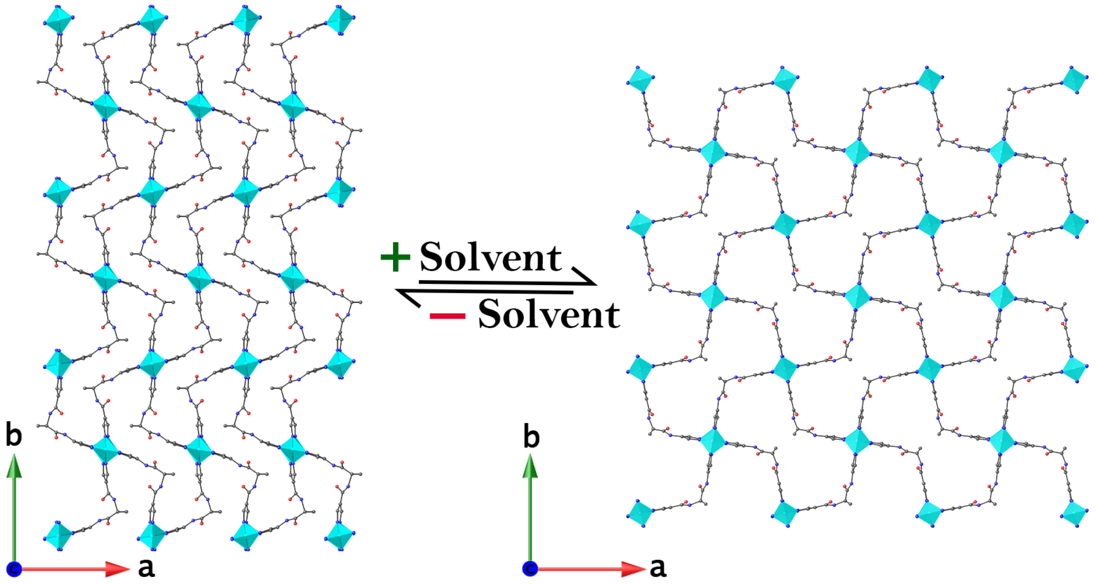

Figure 6.18: Structural transition, driven by solvent uptake (+ Solvent) and solvent release (- Solvent) of `MOF-Ala` between the closed (left) and open (right) phases.

6.3.5 Rietveld Refinement of `MOF-Ala` models

Rietveld refinements of both the dry and wet `MOF-Ala` phases were carried out using `TOPAS Academic` [76]. The refinement of the dry `MOF-Ala` converged smoothly to a weighted profile R-factor (R_{wp}) of **4.883%** without requiring any adjustments to the structural model (Figure 6.19).

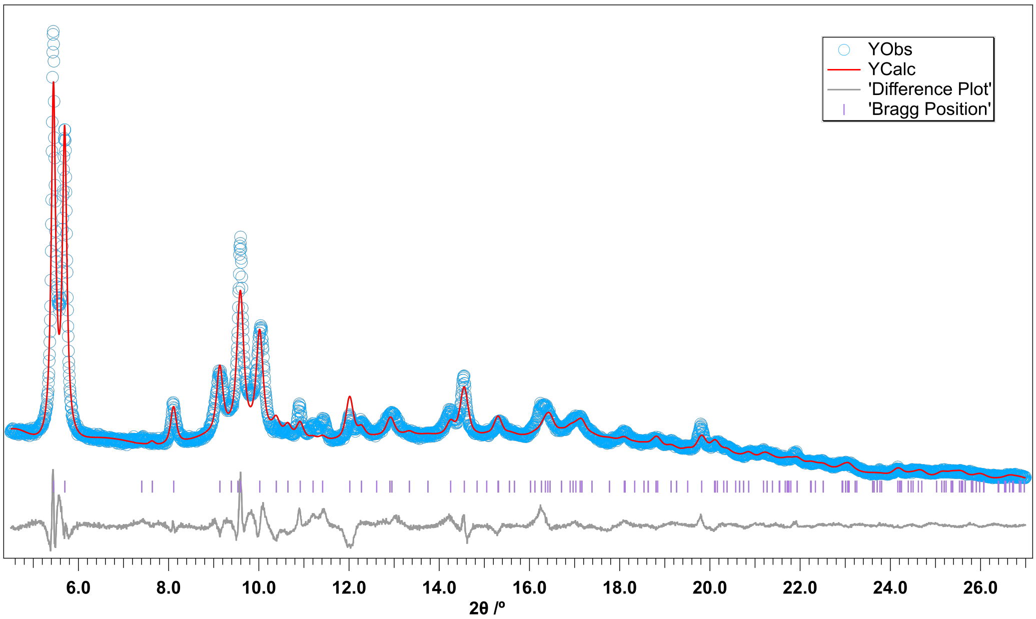

Figure 6.19: PXRD profiles upon Rietveld refinement of the dry `MOF-Ala` that converged to anR_{wp} of **4.883%**.

In contrast, the initial refinement of the wet `MOF-Ala` using a solvent-free model produced a higher R_{wp} of **19%**, suggesting that the absence of guest molecules in the model was significantly affecting the quality of the fit.

Introducing DMF guest molecules as rigid bodies and refining their positions and orientations significantly improved the fit, reducing the R_{wp} to **7.170%** (Figure 6.20). This result mirrors the findings from the electron diffraction refinements, where accounting for disordered DMF also led to a notable improvement in the crystallographic model. The `.INP` file prepared to run Rietveld refinement of the wet `MOF-Ala` in `TOPAS Academic` is listed in Listing S6.1.

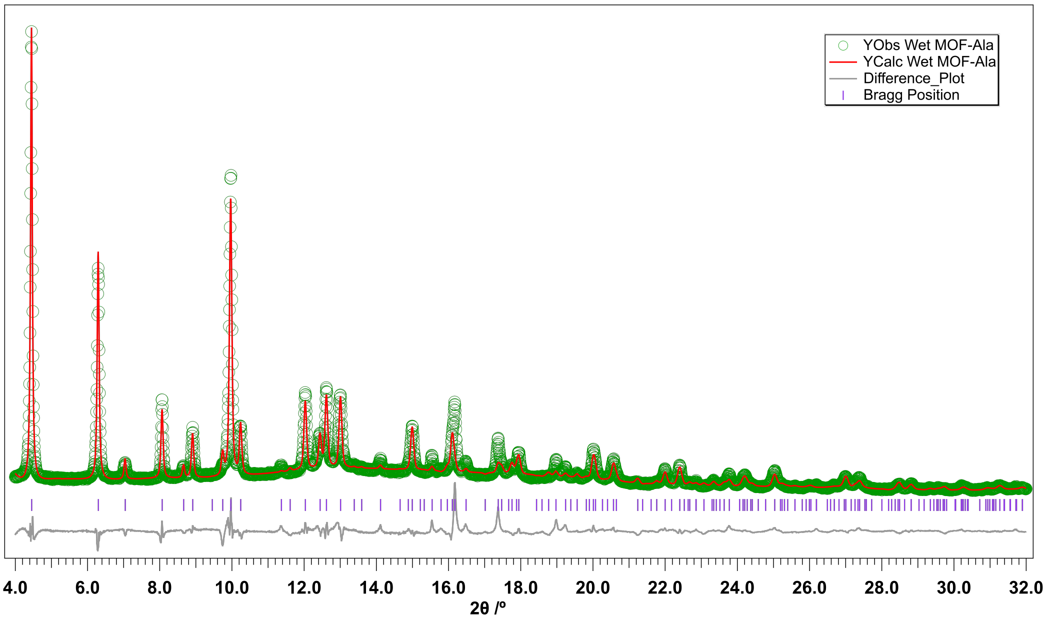

Figure 6.20: PXRD profiles upon Rietveld refinement of the wet `MOF-Ala` that converged to an R_{wp} of **7.170%**.

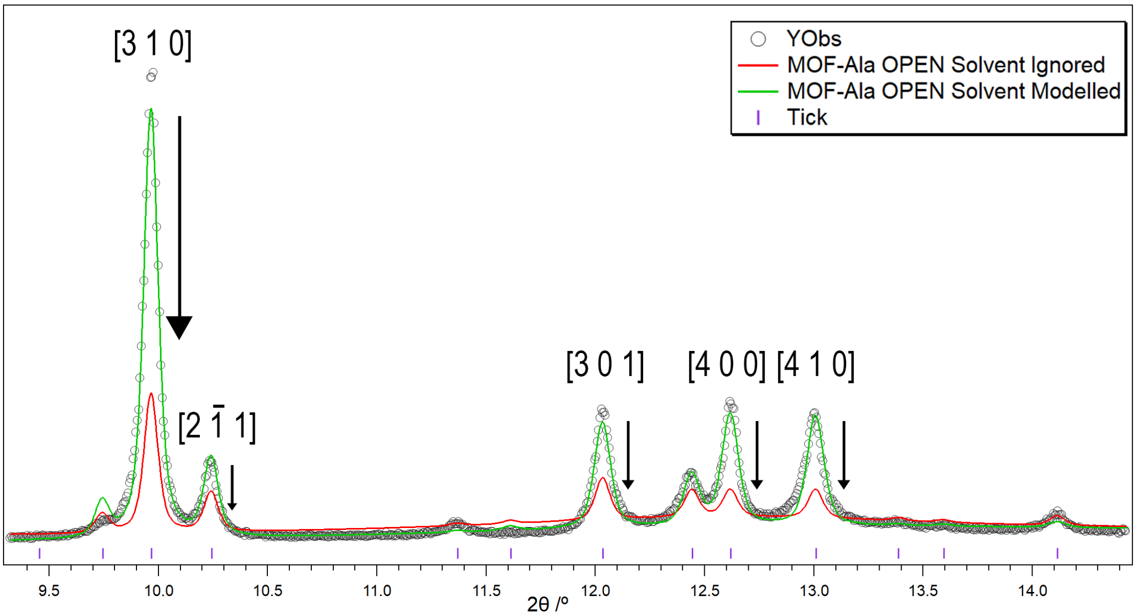

Figure 6.21: Comparison of Rietveld refinements with (green) and without (red) consideration of the solvent in the channels. Neglecting the solvent results in an underestimation of reflection intensities.

Figure 6.21 demonstrates the importance of accurately modeling solvent molecules in the refinement of porous materials like `MOF-Ala`. The solvent-free model (red profile) does not fully reproduce the observed intensities, particularly for reflections such as [310] and $[2\bar{1}1]$, indicating that excluding guest molecules introduces discrepancies. In contrast, incorporating DMF molecules in the pores (green profile) results in a much closer match to the experimental data, particularly for intensity-sensitive reflections.

6.4 Conclusion

In this chapter, we explored the structural flexibility of `MOF-Ala`, a breathing metal-organic framework, using 3D Electron Diffraction. By carefully adapting the sample preparation through cooling, plunge freezing in liquid ethane, or grid-sandwiching (see Figure 6.22), we effectively preserved and analyzed the wet (open) and dry (closed) phases of this framework. These strategies addressed challenges such as crystal sensitivity and phase transitions induced by high vacuum, enabling accurate structural determination. The structural models were further validated by performing Rietveld refinement.

The approaches developed in this work have broader implications for the structural analysis of sensitive crystalline materials. From personal experience working with MOFs, it is frequently observed that PXRD patterns calculated from 3D-ED models diverge from experimental data, often due to phase transitions triggered by high vacuum of the TEM during data collection. The use of plunge freezing or grid-sandwiching provides a practical approach to overcoming this limitation by preserving the native phase of the material. Additionally, grid-sandwiching offers a cost-effective alternative when plunge-freezing equipment is unavailable or when the sample undergoes undesired phase transition at low temperatures.

Future research could further expand the applications of the methodologies presented here. In-situ TEM analysis offers an exciting opportunity to monitor phase transitions in real time across different temperatures. The ability to control the temperature of the sample holder, ranging from liquid nitrogen conditions to temperatures above $100°C$, would enable detailed studies of structural flexibility and phase transformation mechanisms. Moreover, as observed for `MOF-Ala`, which crystallized in the chiral non-centrosymmetric space groups $P2_12_12$ (dry phase) and $P4_2$ (wet phase), determining their absolute structures by applying the methods outlined in **Chapter** 4 could provide a more comprehensive understanding of chirality-related properties and functionalities.

Overall, the techniques developed in this chapter highlight the versatility and importance of 3D-ED as a powerful tool for studying flexible MOFs and other sensitive materials. These methods enable detailed structural analysis that is critical for understanding and optimizing applications extending to gas storage, catalysis, drug delivery, and enantioselective processes.

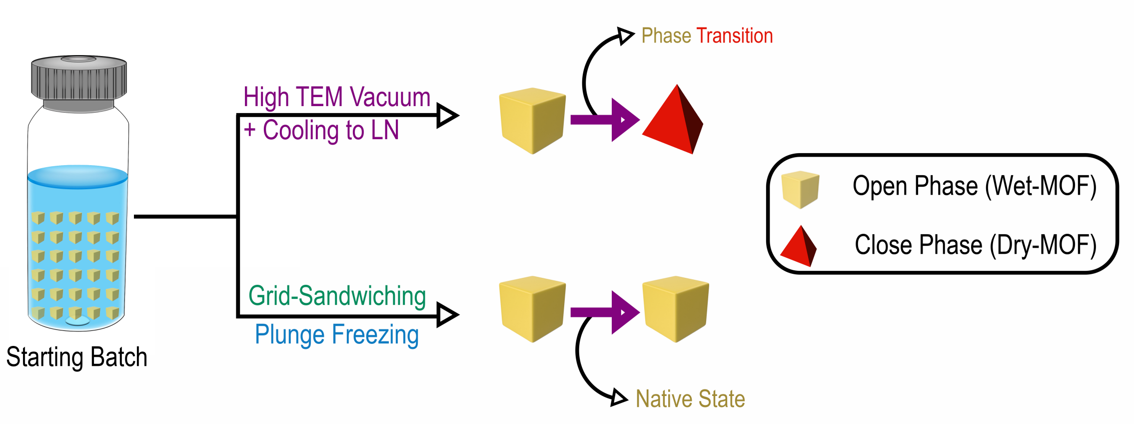

Figure 6.22: Schematic representation of the experimental workflow for studying the structural flexibility of `MOF-Ala`. Starting from a batch of wet crystals, the high vacuum of the TEM combined with cooling to liquid nitrogen temperatures was used to target the dry phase while protecting the crystals from beam sensitivity. To preserve the native open (wet) phase, alternative sample preparation methods such as grid-sandwiching or plunge freezing were employed, preventing phase transitions during analysis.

6.5 Supplementary Information

Table S6.1: Pore Analysis Results for the closed and opened phase of `MOF-Ala`

Parameter	**MOF-Ala Dry**	**MOF-Ala Wet**
System Characteristics		
System Volume (Å^3	1597.483	2219.170
System Mass (g/mol)	1246.536	1246.536
System Density (g/cm^3)	1.296	0.933
Surface Area		
Total Surface Area (Å^2)	85.24	230.42
Total Surface Area per Volume (m^2/cm^3)	533.59	1038.33
Total Surface Area per Mass (m^2/g)	411.81	1113.20
Network-Accessible Surface Area (Å^2)	85.24	230.42
Network-Accessible Surface Area per Volume (m^2/cm^3)	533.59	1038.33
Network-Accessible Surface Area per Mass (m^2/g)	411.81	1113.20
Volume Measurements		
Total Helium Volume (Å^3)	335.935	1257.512
Total Helium Volume (cm^3/g)	0.162	0.608
Total Geometric Volume (Å^3)	730.784	1356.877
Total Geometric Volume (cm^3/g)	0.353	0.656
Network-Accessible Helium Volume (Å^3)	335.935	1257.512
Network-Accessible Helium Volume (cm^3/g)	0.162	0.608
Network-Accessible Geometric Volume (Å^3)	730.784	1356.750
Network-Accessible Geometric Volume (cm^3/g)	0.353	0.655
Pore Dimensions		
Pore Limiting Diameter (Å)	2.29	5.24
Maximum Pore Diameter (Å)	3.23	6.24
Number of Percolated Dimensions	1	1

Listing S6.1: TOPAS Input File for wet MOF-Ala Rietveld Refinement

```
r_exp 0.4253952046 r_exp_dash 1.280281407
r_wp 7.169357125 r_wp_dash 21.57709942
r_p 4.817532343 r_p_dash 22.08637724
weighted_Durbin_Watson 0.1578063988
gof 16.85340372
iters 100000
do_errors
xdd "MOF_Ala_Wet.xy"
    r_exp 0.4253952046 r_exp_dash 1.280281407 r_wp 7.169357125 r_wp_dash 21.57709942 r_p 4.817532343 r_p_dash
     22.08637724 weighted_Durbin_Watson 0.1578063988 gof 16.85340372
    bkg @ 41984.49977 -15055.97481 -4272.21826 8490.059096 -1031.359545 -4893.836871 3184.036584 329.6920487
     -1321.191558 513.3423921 645.1353578 -1486.220947 750.0342027 -1007.300326 1198.944543 86.40647862
     169.9001966 -793.1144284 1509.023628 -607.1110993 378.7892539
    start_X  4
    finish_X  40
    LP_Factor( 90)
    Mixture_LAC_1_on_cm( 24.102428)
    mixture_MAC 22.28778494
    mixture_density_g_on_cm3 1.081418727
    Rp 217.5
    Rs 217.5
    Simple_Axial_Model(@, 2.439791535)
    lam
        ymin_on_ymax  0.001
        la  1 lo  0.9594 lh  0.5
    str
        ' ################################ View Structure   ################################
          view_structure
        ' ################################ View Structure   ################################

        ' ################################ Fourier Map      ################################
          fourier_map 1
          fourier_map_formula = Fobs - Fcalc;
        ' ################################ Fourier Map      ################################

        ' ################################ FRAMEWORK       ################################

        site Zn1    num_posns  2    x  0.5000  y  0.5000 z  -0.011 occ Zn  1 beq  5.44802163
        site Zn2    num_posns  2    x  1.0000  y  0.0000 z  0.5500 occ Zn  1 beq  3.55305758
        site N2     num_posns  4    x  0.5886  y  0.4850 z  0.1500 occ N   1 beq  4.18471227
        site N6     num_posns  4    x  0.9820  y  0.0913 z  0.2070 occ N   1 beq  7.81672669
        site C3     num_posns  4    x  0.6637  y  0.4690 z  0.0950 occ C   1 beq  7.185072
        site N1     num_posns  4    x  0.5885  y  0.4892 z  0.3370 occ N   1 beq  3.00035974
        site C2     num_posns  4    x  0.7101  y  0.4670 z  0.2480 occ C   1 beq  6.47446049
        site C9     num_posns  4    x  0.9650  y  0.1660 z  0.1510 occ C   1 beq  8.2904677
        site N3     num_posns  4    x  0.7886  y  0.4540 z  0.2500 occ N   1 beq  12.5541368
        site C7     num_posns  4    x  0.9560  y  0.2117 z  0.3040 occ C   1 beq  6.47446049
        site C6     num_posns  4    x  0.9410  y  0.2915 z  0.3080 occ C   1 beq  12.5541368
        site C8     num_posns  4    x  0.9680  y  0.1649 z  0.4550 occ C   1 beq  5.84280581
        site C1     num_posns  4    x  0.6639  y  0.4800 z  0.3980 occ C   1 beq  4.89532378
        site C4     num_posns  4    x  0.8360  y  0.4310 z  0.1090 occ C   1 beq  12.5541368
        site N5     num_posns  4    x  0.9820  y  0.0903 z  0.3950 occ N   1 beq  6.23758998
        site O2     num_posns  4    x  0.9350  y  0.3030 z  0.4820 occ O   1 beq  12.5541368
        site C5     num_posns  4    x  0.9160  y  0.4220 z  0.1370 occ C   1 beq  12.5541368
        site O1     num_posns  4    x  0.8230  y  0.4100 z  -0.054 occ O   1 beq  12.5541368
        site N4     num_posns  4    x  0.9350  y  0.3440 z  0.1700 occ N   1 beq  12.5541368
```

```
        site C10   num_posns  4   x  0.9220  y  0.4320 z  0.3420 occ C   1 beq  12.5541368


        ' ################################ SOLVENT MOLECULES (DMF)      ###################

        ' ################################ Parameters      ################################
          prm !bDMF 0.982404842_0.677969044
        ' ################################ Parameters      ################################


        site N8Z   x  0.74080`_0.00142 y  0.21227`_0.00098 z  0.87032`_0.00545 occ N  0.5  beq = bDMF;
        site C14Z  x  0.77315`_0.00203 y  0.20606`_0.00240 z  1.03574`_0.00565 occ C  0.5  beq = bDMF;
        site C15Z  x  0.77643`_0.00210 y  0.19120`_0.00206 z  0.70289`_0.00578 occ C  0.5  beq = bDMF;
        site C16Z  x  0.66350`_0.00180 y  0.23990`_0.00325 z  0.84282`_0.00663 occ C  0.5  beq = bDMF;
        site O4Z   x  0.74161`_0.00295 y  0.22497`_0.00299 z  1.17769`_0.00550 occ O  0.5  beq = bDMF;

        site N7Z   x  0.68197`_0.00093 y  0.19785`_0.00143 z  1.41196`_0.00554 occ N  0.5  beq = bDMF;
        site C11Z  x  0.71206`_0.00224 y  0.20568`_0.00238 z  1.58000`_0.00591 occ C  0.5  beq = bDMF;
        site C12Z  x  0.65152`_0.00227 y  0.12501`_0.00173 z  1.35262`_0.00713 occ C  0.5  beq = bDMF;
        site C13Z  x  0.68160`_0.00214 y  0.26197`_0.00193 z  1.28564`_0.00662 occ C  0.5  beq = bDMF;
        site O3Z   x  0.73981`_0.00361 y  0.26362`_0.00316 z  1.64544`_0.00762 occ O  0.5  beq = bDMF;


        rigid
            z_matrix   N8Z
            z_matrix   C14Z   N8Z     1.3534619
            z_matrix   C15Z   N8Z     1.4352215     C14Z    125.498748
            z_matrix   C16Z   N8Z     1.4476969     C14Z    122.896203    C15Z        178.349038
            z_matrix   O4Z    C14Z    1.2319136     N8Z     124.368519    C15Z        179.530682

        Rotate_about_axies(@  365.59943`_1.38677,@  695.44286`_1.12050,@ -1644.13627`_2.16314)
        Translate(@  0.74080`_0.00142,@  0.21227`_0.00098,@  0.87032`_0.00545)


        rigid
            z_matrix   N7Z
            z_matrix   C11Z   N7Z     1.3578111
            z_matrix   C12Z   N7Z     1.4467787     C11Z    120.606332
            z_matrix   C13Z   N7Z     1.4589772     C11Z    120.813622    C12Z        -178.249888
            z_matrix   O3Z    C11Z    1.2219509     N7Z     126.897552    C12Z          179.530682

        Rotate_about_axies(@  381.01457`_1.64078,@  370.91185`_1.36750,@ -1001.64058`_1.37893)
        Translate(@  0.68197`_0.00093,@  0.19785`_0.00143,@  1.41196`_0.00554)


        Out_X_Yobs_Ycalc_Diff_csv(MOF_Ala_Wet_Rietveld_X_Yobs_Ycalc_Diff.xy)


        LVol_FWHM_CS_G_L( 1, 74.84992166, 0.89, 104.640844,,,, 117.573982)
        TCHZ_Peak_Type(@, 0.2493611846_LIMIT_MAX_0.899361185,@, 0.00965149781,@, -0.0007073625304,, 0,@, 0.03756841809,, 0)
        r_bragg  6.237448328
        phase_MAC 22.28778494
        phase_name "MOF_Ala_Wet"
        MVW( 1470.3728, 2257.787001, 100)
        space_group 77
        scale @ 0.001318844891
```

```
        Phase_LAC_1_on_cm( 24.102428)
        Phase_Density_g_on_cm3( 1.081418727)
        Tetragonal( 17.45980774, 7.406346973)
        PO_Spherical_Harmonics(sh_675888c5_a2, 4 load sh_Cij_prm {
                                                     y00 !sh_675888c5_a2_c00 1
                                                     y20 sh_675888c5_a2_c20 -0.3912989716
                                                     y40 sh_675888c5_a2_c40 -0.4370452503
                                                     y44m sh_675888c5_a2_c44p 4.815944057
                                                     y44p sh_675888c5_a2_c44m 0.2712417837 } )
```

Listing S6.2: Dry MOF-Ala Crystallographic Information Framework file

```

#======================================================================
# CRYSTAL DATA
#----------------------------------------------------------------------
data_DryMOFAla

_chemical_name_common                  'C10 H10 N6 O2 Zn'
_cell_length_a                         10.985(2)
_cell_length_b                         20.179(4)
_cell_length_c                         7.2067(14)
_cell_angle_alpha                      90.000000
_cell_angle_beta                       90.000000
_cell_angle_gamma                      90.000000
_cell_volume                           1597.482616
_space_group_name_H-M_alt              'P 21 21 2'
_space_group_IT_number                 18

loop_
_space_group_symop_operation_xyz
   'x, y, z'
   '-x, -y, z'
   '-x+1/2, y+1/2, -z'
   'x+1/2, -y+1/2, -z'

loop_
   _atom_site_label
   _atom_site_occupancy
   _atom_site_fract_x
   _atom_site_fract_y
   _atom_site_fract_z
   _atom_site_adp_type
   _atom_site_U_iso_or_equiv
   _atom_site_type_symbol
   Zn1        1.0     0.000000     0.500000     0.5637(9)    Uiso  0.054000 Zn
   Zn2        1.0     0.500000     1.000000     0.9438(9)    Uiso  0.048000 Zn
   N2         1.0     0.1480(13)   0.5141(7)    0.9054(14)   Uiso  0.058000 N
   N1         1.0     0.1490(14)   0.5189(7)    0.7140(14)   Uiso  0.058000 N
   N11        1.0     0.4356(16)   0.5899(8)    0.857(2)     Uiso  0.095000 N
   N4         1.0     0.502(2)     0.9217(5)    0.7873(15)   Uiso  0.059000 N
   C2         1.0     0.3359(13)   0.5503(7)    0.8184(18)   Uiso  0.058000 C
   N5         1.0     0.476(2)     0.9201(5)    0.6006(15)   Uiso  0.059000 N
   C9         1.0     0.519(2)     0.8568(5)    0.8493(15)   Uiso  0.059000 C
   C4         1.0     0.531(2)     0.7469(7)    0.681(2)     Uiso  0.095000 C
   C6         1.0     0.2624(14)   0.5325(7)    0.9655(16)   Uiso  0.058000 C
   C7         1.0     0.5060(18)   0.8150(5)    0.6986(15)   Uiso  0.059000 C
   C8         1.0     0.477(2)     0.8540(5)    0.5473(15)   Uiso  0.059000 C
   C3         1.0     0.5268(16)   0.6023(8)    0.731(2)     Uiso  0.095000 C
   C5         1.0     0.6291(15)   0.6403(8)    0.781(2)     Uiso  0.095000 C
   N6         1.0     0.590(2)     0.7126(7)    0.820(2)     Uiso  0.095000 N
   C1         1.0     0.2645(14)   0.5407(7)    0.6622(16)   Uiso  0.058000 C
   C10        1.0     0.722(2)     0.6407(9)    0.622(2)     Uiso  0.095000 C
   O4         1.0     0.526(8)     0.572(7)     0.574(11)    Uiso  0.2230000 O
   O6         1.0     0.471(4)     0.7129(11)   0.562(4)     Uiso  0.213000 O
   H1         1.0     0.2899(14)   0.5478(7)    0.5406(16)   Uiso  0.069000 H
   H5         1.0     0.6666(15)   0.6213(8)    0.892(2)     Uiso  0.114000 H
   H6         1.0     0.2868(14)   0.5329(7)    1.0891(16)   Uiso  0.069000 H
```

```
H8         1.0     0.460(2)     0.8385(5)    0.4286(15)  Uiso  0.071000 H
H9         1.0     0.535(2)     0.8440(5)    0.9706(15)  Uiso  0.071000 H
H11        1.0     0.4408(16)   0.6077(8)    0.965(2)    Uiso  0.114000 H
H10a       1.0     0.704(5)     0.605(3)     0.537(7)    Uiso  0.142000 H
H10b       1.0     0.718(6)     0.682(2)     0.558(8)    Uiso  0.142000 H
H10c       1.0     0.802(2)     0.635(4)     0.672(3)    Uiso  0.142000 H
```

Listing S6.3: Wet MOF-Ala Crystallographic Information Framework file

```

#======================================================================
# CRYSTAL DATA
#----------------------------------------------------------------------
data_WetMOFAlaDMF

_cell_length_a                         17.4597(4)
_cell_length_b                         17.4597(4)
_cell_length_c                         7.4067(4)
_cell_angle_alpha                      90.000000
_cell_angle_beta                       90.000000
_cell_angle_gamma                      90.000000
_cell_volume                           2257.866699
_space_group_name_H-M_alt              'P 42'
_space_group_IT_number                 77

loop_
_space_group_symop_operation_xyz
   'x, y, z'
   '-x, -y, z'
   '-y, x, z+1/2'
   'y, -x, z+1/2'

loop_
   _atom_site_label
   _atom_site_occupancy
   _atom_site_fract_x
   _atom_site_fract_y
   _atom_site_fract_z
   _atom_site_adp_type
   _atom_site_U_iso_or_equiv
   _atom_site_type_symbol
   N8ZA       1.0     0.770(4)     0.2631(17)   0.891(10)   Uiso  0.130500 N
   C14ZA      1.0     0.752(6)     0.226(5)     0.735(11)   Uiso  0.130500 C
   C15ZA      1.0     0.838(5)     0.313(5)     0.892(14)   Uiso  0.130500 C
   C16ZA      1.0     0.723(5)     0.254(4)     1.052(12)   Uiso  0.130500 C
   O4ZA       1.0     0.697(8)     0.184(8)     0.710(16)   Uiso  0.130500 O
   C14ZB      1.0     0.713(3)     0.237(4)     1.135(7)    Uiso  0.130500 C
   C15ZB      1.0     0.642(3)     0.271(3)     1.405(10)   Uiso  0.130500 C
   C16ZB      1.0     0.755(3)     0.179(3)     1.419(10)   Uiso  0.130500 C
   O4ZB       1.0     0.760(5)     0.205(5)     1.039(9)    Uiso  0.130500 O
   Zn1        1.0     0.500000     0.500000     0.132000    Uiso  0.064000 Zn
   Zn2        1.0     1.000000     0.000000     0.694000    Uiso  0.051000 Zn
   N2         1.0     0.588900     0.486000     0.290000    Uiso  0.060000 N
   N6         1.0     0.986000     0.092000     0.354000    Uiso  0.090000 N
   C3         1.0     0.664000     0.471000     0.235000    Uiso  0.090000 C
   N1         1.0     0.587900     0.490000     0.477000    Uiso  0.049000 N
   C2         1.0     0.710200     0.468000     0.390000    Uiso  0.090000 C
   C9         1.0     0.970000     0.167000     0.295000    Uiso  0.090000 C
   N3         1.0     0.787000     0.451000     0.396000    Uiso  0.170000 N
   C7         1.0     0.956000     0.212200     0.447000    Uiso  0.085000 C
   C6         1.0     0.944000     0.293000     0.448000    Uiso  0.170000 C
   C8         1.0     0.963000     0.165000     0.600000    Uiso  0.080000 C
   C1         1.0     0.663000     0.480000     0.540000    Uiso  0.084000 C
   C4         1.0     0.840000     0.431000     0.265000    Uiso  0.170000 C
   N5         1.0     0.980000     0.091000     0.542000    Uiso  0.084000 N
```

```
O2     1.0   0.945000   0.302000   0.622000   Uiso   0.170000 O
C5     1.0   0.920000   0.421000   0.277000   Uiso   0.170000 C
O1     1.0   0.834000   0.411000   0.101000   Uiso   0.170000 O
N4     1.0   0.933000   0.342000   0.304000   Uiso   0.170000 N
C10    1.0   0.919000   0.430000   0.483000   Uiso   0.170000 C
N2     1.0   0.411100   0.514000   0.290000   Uiso   0.060000 N
N6     1.0   0.014000   0.908000   0.354000   Uiso   0.090000 N
C3     1.0   0.336000   0.529000   0.235000   Uiso   0.090000 C
N1     1.0   0.412100   0.510000   0.477000   Uiso   0.049000 N
C2     1.0   0.289800   0.532000   0.390000   Uiso   0.090000 C
C9     1.0   0.030000   0.833000   0.295000   Uiso   0.090000 C
N3     1.0   0.213000   0.549000   0.396000   Uiso   0.170000 N
C7     1.0   0.044000   0.787800   0.447000   Uiso   0.085000 C
C6     1.0   0.056000   0.707000   0.448000   Uiso   0.170000 C
C8     1.0   0.037000   0.835000   0.600000   Uiso   0.080000 C
C1     1.0   0.337000   0.520000   0.540000   Uiso   0.084000 C
C4     1.0   0.160000   0.569000   0.265000   Uiso   0.170000 C
N5     1.0   0.020000   0.909000   0.542000   Uiso   0.084000 N
O2     1.0   0.055000   0.698000   0.622000   Uiso   0.170000 O
C5     1.0   0.080000   0.579000   0.277000   Uiso   0.170000 C
O1     1.0   0.166000   0.589000   0.101000   Uiso   0.170000 O
N4     1.0   0.067000   0.658000   0.304000   Uiso   0.170000 N
C10    1.0   0.081000   0.570000   0.483000   Uiso   0.170000 C
Zn1    1.0   0.500000   0.500000   0.632000   Uiso   0.064000 Zn
Zn2    1.0   0.000000   1.000000   0.694000   Uiso   0.051000 Zn
Zn2    1.0   0.000000   1.000000   0.194000   Uiso   0.051000 Zn
Zn2    1.0   1.000000   0.000000   0.194000   Uiso   0.051000 Zn
N6     1.0   0.908000  -0.014000   0.854000   Uiso   0.090000 N
N6     1.0   1.092000   0.014000   0.854000   Uiso   0.090000 N
N1     1.0   0.510000   0.587900  -0.023000   Uiso   0.049000 N
N1     1.0   0.490000   0.412100  -0.023000   Uiso   0.049000 N
N5     1.0   1.020000  -0.091000   0.542000   Uiso   0.084000 N
N8ZB   1.0   0.7043(17)  0.229(2)   1.316(7)   Uiso   0.130500 N
H1     1.0   0.790462   0.234605   0.621046   Uiso   0.050000 H
H2     1.0   0.864949   0.311896   0.759429   Uiso   0.050000 H
H3     1.0   0.878477   0.292619   0.993020   Uiso   0.050000 H
H4     1.0   0.820859   0.371385   0.924291   Uiso   0.050000 H
H5     1.0   0.675882   0.215005   1.023170   Uiso   0.050000 H
H6     1.0   0.700176   0.309478   1.092250   Uiso   0.050000 H
H7     1.0   0.757795   0.230712   1.160980   Uiso   0.050000 H
H8     1.0   0.683270   0.463046   0.096426   Uiso   0.050000 H
H9     1.0   0.968763   0.186358   0.155262   Uiso   0.050000 H
H10    1.0   0.809505   0.453632   0.522201   Uiso   0.050000 H
H11    1.0   0.956288   0.183162   0.739765   Uiso   0.050000 H
H12    1.0   0.681293   0.481338   0.680528   Uiso   0.050000 H
H13    1.0   0.958731   0.454969   0.194116   Uiso   0.050000 H
H14    1.0   0.934734   0.313372   0.184801   Uiso   0.050000 H
H15    1.0   0.883007   0.385650   0.542068   Uiso   0.050000 H
H16    1.0   0.977068   0.424611   0.535147   Uiso   0.050000 H
H17    1.0   0.896215   0.486128   0.518031   Uiso   0.050000 H
H18    1.0   0.316730   0.536954   0.096426   Uiso   0.050000 H
H19    1.0   0.031237   0.813642   0.155262   Uiso   0.050000 H
H20    1.0   0.190495   0.546368   0.522201   Uiso   0.050000 H
H21    1.0   0.043712   0.816838   0.739765   Uiso   0.050000 H
H22    1.0   0.318707   0.518662   0.680528   Uiso   0.050000 H
H23    1.0   0.041269   0.545031   0.194116   Uiso   0.050000 H
H24    1.0   0.065266   0.686628   0.184801   Uiso   0.050000 H
```

```
   H25        1.0     0.116993     0.614350     0.542068     Uiso    0.050000 H
   H26        1.0     0.022932     0.575389     0.535147     Uiso    0.050000 H
   H27        1.0     0.103785     0.513872     0.518031     Uiso    0.050000 H
   H28        1.0     0.673768     0.276267     1.067940     Uiso    0.050000 H
   H29        1.0     0.611089     0.304818     1.305240     Uiso    0.050000 H
   H30        1.0     0.665807     0.308842     1.507520     Uiso    0.050000 H
   H31        1.0     0.602893     0.230493     1.468260     Uiso    0.050000 H
   H32        1.0     0.797030     0.153396     1.328680     Uiso    0.050000 H
   H33        1.0     0.721454     0.133963     1.482980     Uiso    0.050000 H
   H34        1.0     0.784367     0.212313     1.522240     Uiso    0.050000 H
```

Chapter 7

Serial Electron Diffraction on MOFs

7.1 Introduction

Serial Crystallography (SX), a technique initially developed for X-ray diffraction [95], has transformed the structural analysis of sensitive and complex materials. Central to this approach is the principle of diffraction before destruction [96], which allows data collection from a crystal before it suffers significant damage from the radiation dose. This concept is particularly relevant for biological macromolecules and MOFs, which degrade rapidly under intense radiation exposure.

X-ray serial crystallography uses two main methods for data collection, which are liquid-jet injectors and fixed-target setups (Figure 7.1). Liquid-jet injectors work by suspending crystals in a liquid or viscous medium, delivering them into the X-ray beam path for continuous exposure to fresh crystals during data collection. Alternatively, fixed-target setups immobilize crystals on specialized substrates, such as silicon wafers or microfabricated grids, allowing for systematic scanning of the sample. In both methods, diffraction data are collected from different and randomly oriented crystals in single shots, allowing for the reconstruction of a complete

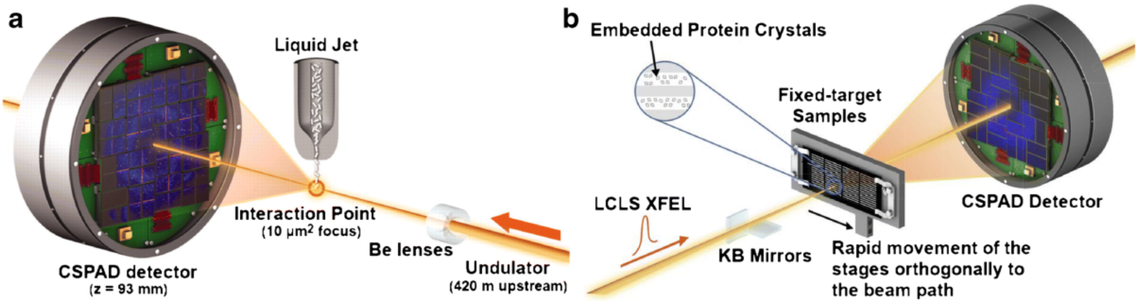

Figure 7.1: Schematic representation of liquid-jet (a) and fixed-target (b) serial crystallography [13]

dataset even when individual crystals are too small or too sensitive for traditional crystallographic techniques. While these techniques have proven to be successful in advancing structural analysis, they rely on highly specialized infrastructure, such as synchrotron radiation facilities or X-ray Free-Electron Lasers (XFELs). These facilities are costly to operate and require careful planning to secure dedicated beam time due to their limited availability.

TEMs naturally provide all the essential tools to perform serial electron crystallography. Widely available in most research laboratories, TEMs are equipped with a controllable electron beam and a movable stage, enabling precise targeting of specific areas of interest. Sample preparation is straightforward and can be adapted to ensure densely packed nanocrystals are distributed across the grid. The strong interaction between electrons and the specimen, along with the ability to adjust the beam size to just a few nanometers, ensures high signal-to-noise ratios. Furthermore, transitioning between imaging and diffraction modes is relatively quick (as discussed in **Chapter** 1.2.4), making data acquisition much easier. For example, a low-magnification image can be taken at a very low dose to identify regions of interest, ensuring that only relevant areas are targeted for diffraction analysis. Although a 3D-ED experiment can be performed on nanocrystals there is a wide spectrum of materials, wider then for x-ray diffraction, that are easily amorphized by the electron beam in a difficult environment of at least 10^{-7} mbar which is the vacuum of the TEM column. In fact not only macromolecular crystals are beam and vacuum sensitive but also organic and hybrid materials like MOFs, therefore a serialED has a wide potential application in different fields. Data acquisition on these regions can be done either by scanning the electron beam across the sample [33] or by moving the stage while keeping the beam fixed, similar to the fixed-target SX. While first approach is faster, it introduces shifts in the central diffraction beam that may require post-corrections, depending on the data processing software being used. Moving the stage on the other hand, is slower but maintains constant beam coordinates in different patterns, which simplifies data processing. Both methods produce a large amount of data, the majority of which is irrelevant and therefore require a robust algorithm to filter out these useless frames (as discussed in **Chapter 2.4.5**).

An alternative approach involves analyzing low-magnification images to identify crystals through contrast thresholding, with their coordinates saved for subsequent diffraction pattern collection [97, 34]. This method can be limited by the type of grid used and does not always guarantee accurate results. A more advanced solution is the use of machine learning algorithms, which are being actively developed to enhance the speed and reliability of crystal recognition. These algorithms can automate the selection of crystals and guide subsequent stage or beam movements for targeted data collection. SerialED can also be conducted without the need for prior illumination, eliminating the requirement for low-magnification imaging and allowing the entire TEM grid to be scanned "blindly" using stage movement or beam shifts.

Despite its numerous advantages, SerialED has been reported in only a few published articles for structure determination [33, 34, 98]. This is largely due to challenges in data processing, which at the time of writing, requires prior knowledge of the unit cell parameters. As discussed in **Chapter 1.2.4**, this is because the flat Ewald sphere in electron diffraction limits the information from a single frame to two unit cell vectors.

This chapter discusses the application of SerialED for solving the structure of a MOF, focusing on both data acquisition and the processing required for this type of analysis.

7.2 Sample Preparation and Data Acquisition

A concentrated solution of the material was deposited onto a holey carbon TEM grid, resulting in a dense distribution of nanocrystals across the grid surface.

Data acquisition was performed using `LibraEDT`, without the need for prior low-magnification imaging. Instead, the integrated *2D Map* feature within the software was used to randomly select regions for scanning.

The acquisition strategy was similar to the fixed-target serial crystallography, employing continuous stage movement as described in **Chapter 2.4.5**. To reduce potential preferred orientations, the stage was randomly rotated every 30 minutes. Overnight, the microscope operated for approximately 10 hours, with the stage moving at a constant speed of 10 μm/s. Diffraction patterns were recorded every 150 ms, resulting in a frame-to-frame displacement of approximately 1.5 μm, which is comparable to the size of the crystals (Figure 7.3).

Over 200000 images were collected. However, rigorous data filtering was implemented to ensure the quality of the dataset. Only frames containing at least five diffraction peaks with an intensity-to-noise ratio (I/σ) exceeding 10 and a resolution for each peak exceeding 0.80 $Å^{-1}$ (1.25 Å) were retained, resulting in a final dataset of 5745 high-quality frames suitable for subsequent structural analysis. It is worth mentioning that all the parameters used for the filtering of the diffraction frames can be changed any time during data acquisition within the `LibraEDT`'s GUI (Figure 7.2). This flexibility provides the ability to apply stricter or more relaxed filtering criteria as needed based on the quality of the crystals. For instance, if a significant number of potentially valuable frames are being excluded, the resolution limit can be adjusted to include lower-resolution reflections, or the thresholds for

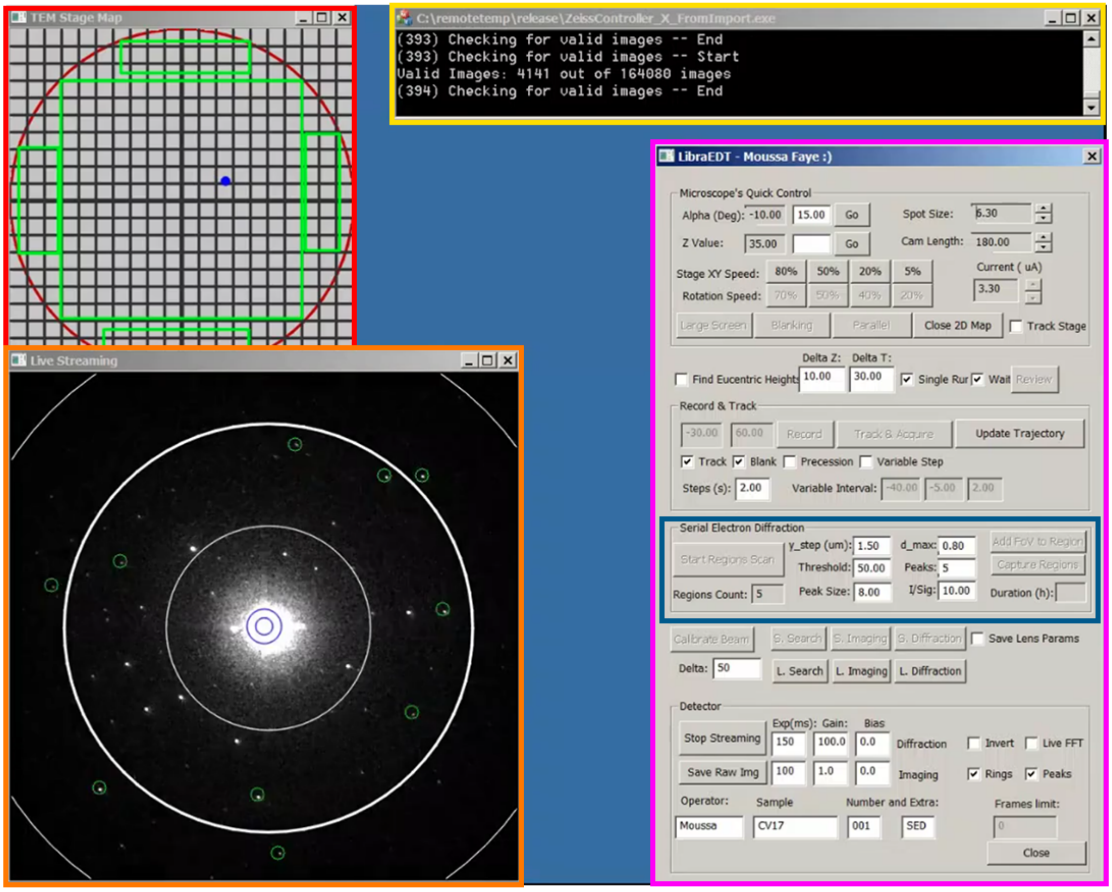

```
(393) Checking for valid images -- End
(393) Checking for valid images -- Start
Valid Images: 4141 out of 164080 images
(394) Checking for valid images -- End
```

Microscope's Quick Control

Alpha (Deg): -10.00 15.00

Z Value: 35.00

Spot Size: 6.30

Cam Length: 180.00

Stage XY Speed: 80% 50% 20% 5%

Rotation Speed: 70% 50% 40% 20%

Current (uA) 3.30

☐ Track Stage

☐ Find Eucentric Heights Delta Z: 10.00 Delta T: 30.00 ☑ Single Run ☑ Wait

Record & Track

-30.00 60.00

☑ Track ☑ Blank ☐ Precession ☐ Variable Step

Steps (s): 2.00 Variable Interval: -40.00 -5.00 2.00

Serial Electron Diffraction

y_step (um): 1.50 d_max: 0.80

Threshold: 50.00 Peaks: 5

Regions Count: 5 Peak Size: 8.00 I/Sig: 10.00 Duration (h):

☐ Save Lens Params

Delta: 50

Detector

	Exp(ms):	Gain:	Bias	
Stop Streaming	150	100.0	0.0	Diffraction
Save Raw Img	100	1.0	0.0	Imaging

☐ Invert ☐ Live FFT ☑ Rings ☑ Peaks

Operator: Moussa

Sample CV17

Number and Extra: 001 SED

Frames limit: 0

Figure 7.2: The **red box** highlights the TEM stage map, showing the grid layout and regions marked for scanning. The **yellow box** displays the log window, tracking the progress of image acquisition and filtering. The **pink box** shows `LibraEDT`'s GUI and data acquisition parameters. The **blue box** focuses on the Serial Electron Diffraction settings, where step size, thresholds, and filtering conditions are configured. Lastly, the **orange box** shows the live feed of diffraction patterns, with resolution rings and detected peaks based on the previously set conditions.

the minimum number of reflections and their intensity-to-noise ratio can be relaxed accordingly.

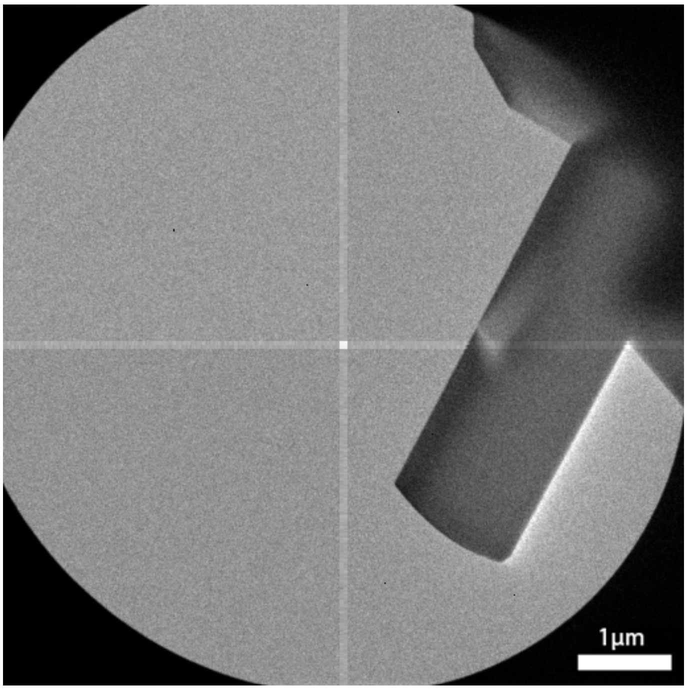

Figure 7.3: TEM image showing the morphology of a single crystal of the material under study. The size of the crystal is on the micrometer scale, as indicated by the 1 μm scale bar.

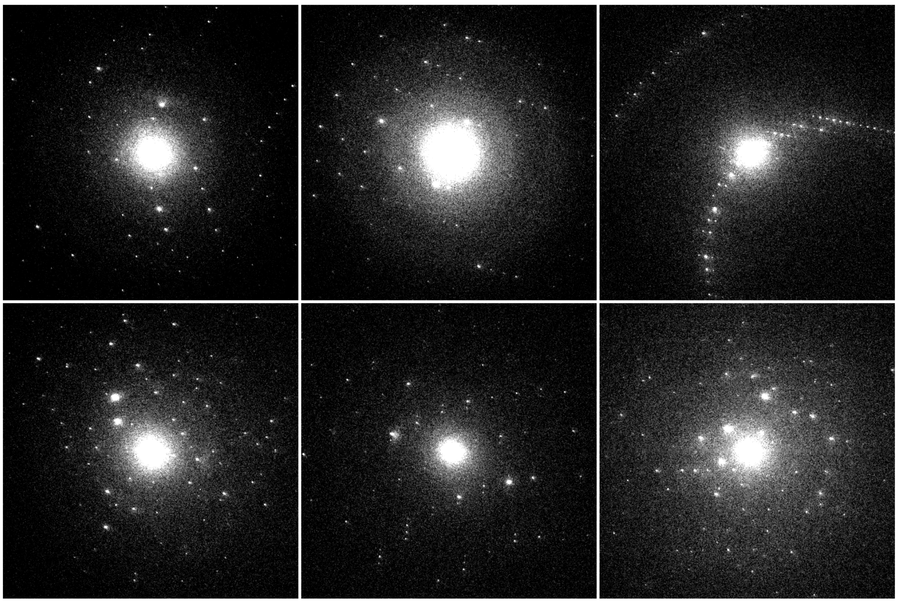

Figure 7.4: Six randomly selected images from the retained dataset of SerialED frames, all of which met the filtering criteria. The selection includes images containing diffraction patterns from multiple crystals.

Table 7.1: Summary of SerialED Data Collection Parameters

Parameter	**Value**
Data Acquisition Software	`LibraEDT`
Data Acquisition Mode	Stage movement
Acquisition Duration	$\approx$ 10 hours
Stage Movement Speed	10 μm/second
Exposure Time	150 ms per frame
Frame Coverage	1.5 μm per frame
Total Images Captured	Over 200000
Retained Frames	5745
Filtering Conditions	At least 5 peaks with I/$\sigma > 10$ AND Resolution better than 1.25 Å

7.3 Data Processing of SerialED Data

The processing of SerialED data can be performed using many of the same software tools developed for Serial X-ray Crystallography, provided that the diffraction geometry is appropriately adjusted. Among the available software packages, `CrystFEL` [61] stands out as the most widely used for processing serial crystallography data. It also includes the `PinkIndexer` module [99], which has been successfully tested on electron diffraction data. A comprehensive guide on data processing of SerialED data using `CrystFEL` has been reported by Robert Bücker et al. using `diffractem` [33].

While the data collected with `LibraEDT` were successfully processed using various software tools, we will primarily focus on the `PETS2` and `nXDS` software packages.

As mentioned earlier, prior knowledge of the unit cell parameters is required for effective data processing. For that purpose, a short angular range of cRED data was collected on the MOF sample and was later indexed in a tetragonal unit cell with the following parameters:

Table 7.2: Tetragonal Unit Cell Parameters Obtained from cRED Data

Parameter	**Value**
a, b (Å)	24.77000
c (Å)	10.29000
α, β, γ (°)	90.0000

7.3.1 Data Processing with PETS2

The data processing procedure using `PETS2` is very similar to the steps described in **Chapter 1.2.7.1.2**, with some variations adapted to SerialED data. Once the diffraction peaks are identified within each frame during the *Peak Search* step, it is necessary to impose the Laue class and define the unit cell parameters. Subsequently, the *Serial ED* task can be executed, which involves generating templates with expected peak positions for a set of discrete orientations based on the provided unit cell information and symmetry constraints. These templates are then compared to the experimental frames to determine their respective orientations.

While this approach proved robust in many cases, visual inspection revealed a significant number of frames where indexing was unsuccessful (Figure 7.5). To the best of our knowledge, `PETS2` lacks an automated mechanism for excluding frames where indexing failed. This manual intervention, while feasible for small datasets, became a very time-consuming process in our analysis, given the size of our dataset containing 5746 frames.

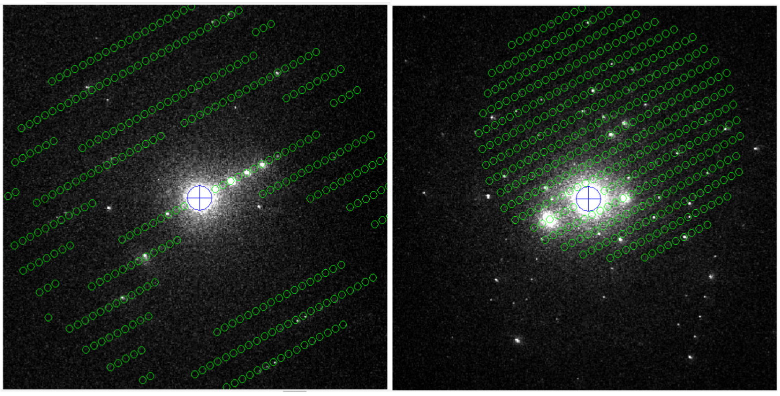

Figure 7.5: Successfully (left) and unsuccessfully (right) indexed frame

To address this, we exploited the detailed information provided by `PETS2` within the `.dyntmp` file. This file, generated during the *Process frames per integration* step, where `PETS2` predicts the positions of reflections based on the determined frame orientation and the associated orientation matrix, contains crucial parameters for each frame, including reflection indices with their corresponding intensities, sigmas, observed positions, predicted positions, and other relevant data. We hypothesized that frames with incorrect indexing would exhibit a significant discrepancy between the predicted and observed reflection positions.

We then developed a Python script to filter the frames. This script selects frames based on the quality of the indexing, retaining only those with a sufficient number of observed peaks exhibiting good agreement with the predicted positions. This filtering process involves:

- Read the `.dyntmp` file and group the data by frame number.
- Discard reflections with a resolution lower than a specified threshold.
- Discard reflections with an intensity-to-sigma ratio (I/σ) lower than a specified threshold.
- Exclude frames with fewer reflections than a specified threshold.

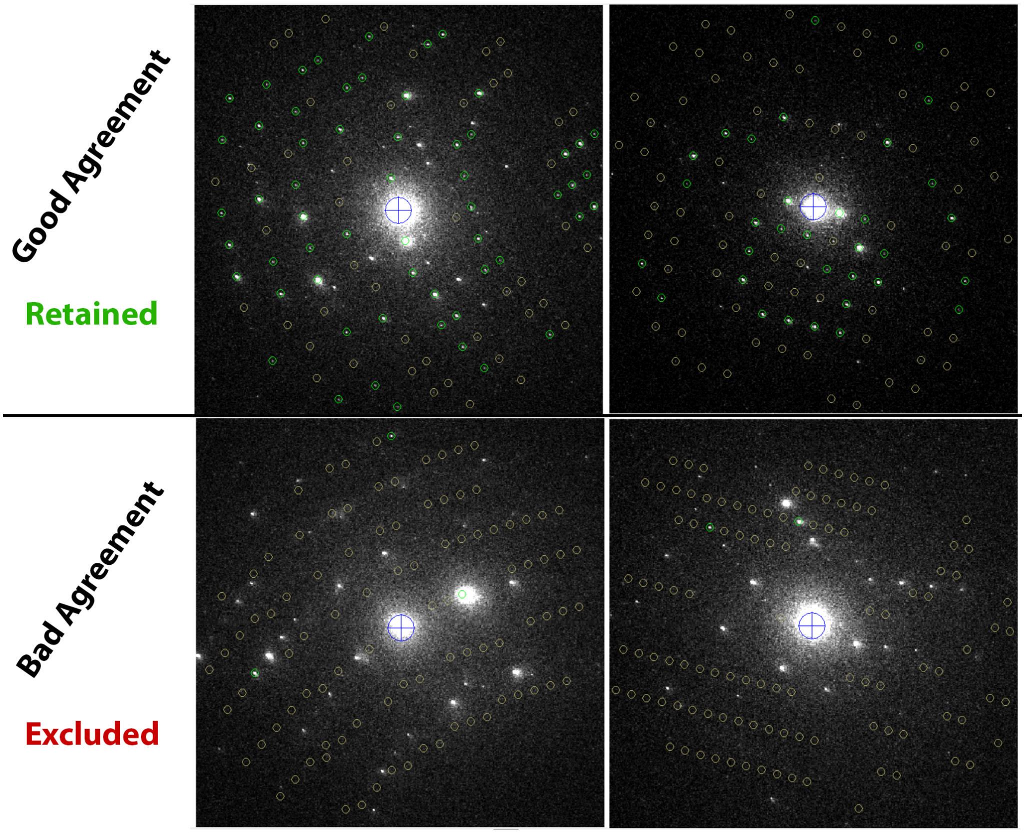

Figure 7.6: Examples of diffraction images retained (top row) and removed (bottom row) by the Python script. Retained frames show good agreement between predicted and observed reflection positions (green markers), while removed frames have misaligned or insufficient reflections.

While more sophisticated approaches for filtering frames may exist, our approach, though potentially susceptible to false negatives (excluding well-indexed frames), effectively removed a large number of unindexed frames that would have significantly degraded the overall quality of the data if not removed. This filtering process resulted in a subset of 1651 frames that met the defined criteria, providing a more reliable foundation for subsequent analysis.

At this point, the data was processed as a normal tilt-series data, with the exception that no smoothing method was used during the geometry optimization steps nor interframe correlation was applied during the scaling step.

The statistics reporting upon running the *Finalize Integration* task are shown in Table 7.3.

Table 7.3: Statistics for Laue class 4/mmm

d^*-range	d-range	Nobs	Nall	Nthr	compl.	rnd. I/σ(cnt)	I/σ(err)	Rint(obs)	Rint(all)	CC1/2
0.00–0.42	Inf–2.40	37	78	92	0.848	3.90	55.05	6.44	15.16	99.82
0.42–0.59	2.40–1.70	40	120	133	0.902	4.33	35.04	9.61	17.88	99.59
0.59–0.72	1.70–1.39	38	160	171	0.936	3.87	18.36	16.50	30.07	92.59
0.72–0.83	1.39–1.20	32	165	194	0.851	4.00	12.96	18.79	37.03	80.26
0.83–0.93	1.20–1.07	23	194	214	0.907	3.59	8.13	20.70	39.88	70.57
0.93–1.02	1.07–0.98	15	217	242	0.897	3.36	6.53	29.56	44.01	31.31
1.02–1.10	0.98–0.91	17	226	256	0.883	3.18	2.25	17.84	52.77	27.93
1.10–1.18	0.91–0.85	7	236	277	0.852	3.05	4.67	7.70	43.85	65.54
1.18–1.25	0.85–0.80	5	218	280	0.779	2.41	3.29	32.78	50.93	55.01
0.00–1.25	**Inf–0.80**	**214**	**1614**	**1859**	**0.868**	**3.40**	**16.22**	**9.82**	**24.39**	**99.69**

7.3.2 Data Processing with nXDS

`nXDS` [100], developed by the same author as `XDS`, is designed for processing X-ray snapshot data. To the best of our knowledge, it has never been used for the processing of electron diffraction data.

Similar to `XDS`, `nXDS` requires an input file, `nXDS.INP`, which defines the experimental geometry and other parameters necessary for running the software. Thanks to our experience with `XDS`, constructing the `nXDS.INP` file for `nXDS` was relatively straightforward and allowed us to adapt it to the specific requirements of electron diffraction data. The `nXDS.INP` file is listed in the Listing S1.

The workflow for data processing with `nXDS` follows the same principles as its predecessor, `XDS`, and has been detailed in **Chapter 1.2.7.1.1**.

During the `COLSPOT` task, which is responsible for identifying the strongest reflections, various peak-finding parameters are defined within the input file. At this stage, `nXDS` also filters out frames that do not contain a minimum number of reflections, as specified by the keyword `MINIMUM_NUMBER_OF_SPOTS`. For this dataset, we set this value to 20. As a result, approximately 600 frames were excluded, leaving us with 5100 frames for subsequent data processing.

The information regarding the remaining frames, specifically the identified spot positions, is then passed to the next task, `IDXREF`. This task is responsible for determining the orientation of the frames based on the provided unit cell parameters and symmetry constraints within the input file. During this step, we allowed the refinement of the crystal orientation and unit cell parameters for each frame, for a more accurate indexing solution. A frame was considered successfully indexed if the proportion of indexed reflections, relative to the total number of expected reflections within that frame, was higher than a user-defined threshold (`MINIMUM_FRACTION_OF_INDEXED_SPOTS = 0.4` in our case). This resulted in 1,357 successfully indexed frames, with all other frames being discarded.

We then proceeded to the `INTEGRATE` task, which calculates the integrated intensities for the indexed reflections. This step refines the reflection profiles and evaluates the quality of the integration process. To ensure accurate measurements, partially integrated reflections are ignored unless at least 75% of their expected intensity has been observed. This threshold is defined in the input file as `MINPK=75`, allowing XDS to estimate the missing intensity by fitting the learned profiles when this condition is met. Finally, the `CORRECT` task was performed to apply corrections to the data, including scaling and error estimation. These steps produced the final dataset statistics summarized in the table below.

Table 7.4: Final Dataset Statistics After `INTEGRATE` and `CORRECT`. In bold is the resolution cut-off.

Resolution Shells	OBSERVED	UNIQUE	POSSIBLE	COMPLETE	I/SIGMA	R_{mrgd}-F	CC(1/2)
4.229	7715	19	19	100.0	7.4	10.2	96.9*
3.135	5701	22	22	100.0	6.7	13.3	92.1*
2.604	5727	23	23	100.0	6.7	10.8	96.0*
2.274	7042	33	33	100.0	6.3	17.4	90.0*
2.045	5961	32	32	100.0	4.6	14.5	96.3*
1.873	6881	38	38	100.0	5.5	13.8	97.0*
1.739	6163	38	38	100.0	5.3	15.6	90.6*
1.630	5255	39	39	100.0	4.6	14.6	96.1*
1.539	6340	41	41	100.0	5.0	17.7	88.9*
1.462	5561	43	43	100.0	4.3	18.9	93.6*
1.395	5132	43	43	100.0	4.5	16.4	96.0*
1.337	6424	50	50	100.0	4.7	17.3	94.3*
1.285	5057	45	45	100.0	4.3	15.8	97.9*
1.239	6340	59	60	98.3	4.2	20.2	91.4*
1.198	5032	48	48	100.0	4.2	21.1	83.7*
1.160	5889	54	54	100.0	3.7	20.9	90.4*
1.126	5067	54	54	100.0	3.5	19.4	91.8*
1.095	5317	58	58	100.0	3.2	24.3	73.5*
1.066	5120	53	53	100.0	3.5	20.7	93.2*
1.039	5443	65	65	100.0	3.3	26.2	84.8*
1.014	4273	57	57	100.0	3.1	26.1	95.9*
0.991	4713	66	66	100.0	3.2	24.1	79.8*
0.970	4497	61	61	100.0	3.2	25.8	81.0*
0.949	4352	64	64	100.0	3.1	26.3	81.3*
0.930	4112	68	68	100.0	2.6	33.2	77.3*
0.913	3491	60	60	100.0	2.9	32.5	72.4*
0.896	4159	77	77	100.0	2.5	33.9	79.2*
0.880	3655	67	67	100.0	2.6	37.4	78.2*
0.864	3281	67	67	100.0	2.3	41.5	67.0*
0.850	**2562**	**72**	**72**	**100.0**	**1.9**	**59.3**	**57.2***

7.4 Structure Solution and Refinement

The obtained `.hkl` files from the data processing software were subsequently used for structure solution. Both `Superflip` [45] and `SHELXT` [46] successfully solved the crystal structure, accurately localizing all non-hydrogen atoms and correctly identifying the space group as $I4_1/amd$ (space group number 141). This successful determination is illustrated in the Fourier map images presented below (Figure 7.7).

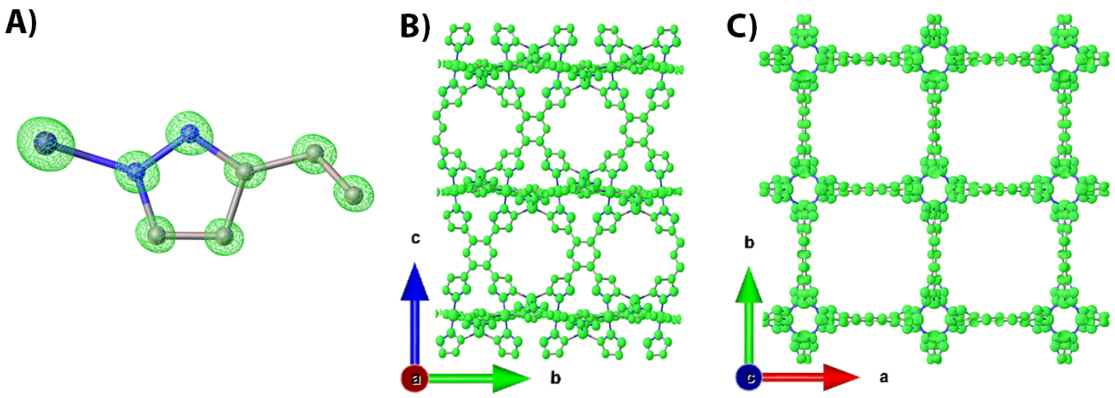

Figure 7.7: Illustration of the structural model obtained from Serial Electron Diffraction data. The green blobs represent the observed electrostatic potential (F_{obs}). (A) The asymmetric unit overlaid with the F_{obs}. (B, C) Structural model with the F_{obs} viewed along different projections.

The structures obtained through different data processing software were refined using `SHELXL` [47] within the `OLEX2` environment [48], and all refined stably. Interestingly, despite the high completeness and high resolution of the data, anisotropic refinement was not possible, as all atoms resulted in non-positive definite ADPs. As a result, ADPs were refined isotropically. A detailed table containing the information regarding the refinement statistics is reported in Table 7.5.

The difference Fourier map revealed the positions of all hydrogen atoms, as highlighted in Figure 7.8. These observations underscore the robustness of the data processing and refinement methods employed while highlighting a limitation in achieving anisotropic refinement for this dataset.

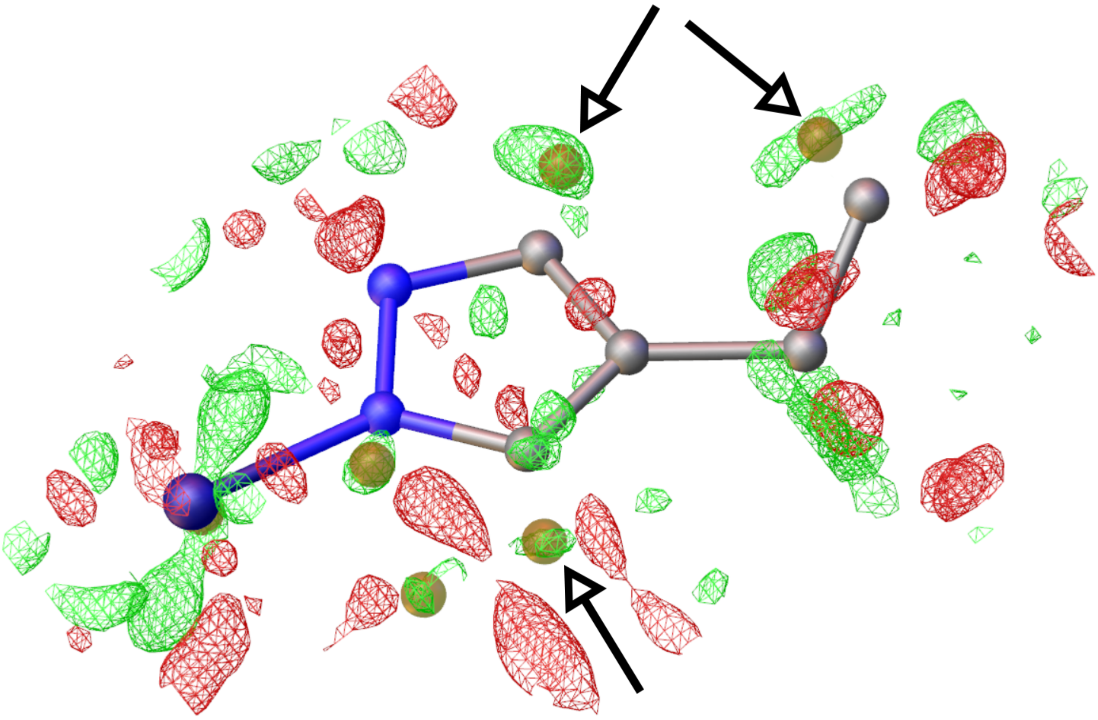

Figure 7.8: Difference Fourier map illustrating the localization of hydrogen atoms (highlighted with arrows). The green mesh represents positive peaks in the difference map, corresponding to the hydrogen atoms, while the red mesh represents negative peaks. The structural model is superimposed for clarity, with bonds shown as sticks and atoms represented as spheres.

Table 7.5: Crystal data and structure refinement for the models obtained after data processing with nXDS and PETS2

Parameter	**nXDS Model**	**PETS2 Model**
Empirical formula	$C_{1.85}H_{1.03}N_{0.82}Zn_{0.2}$	$C_{1.8}H_{1}N_{0.8}Zn_{0.2}$
Formula weight	48.11	46.91
Temperature (K)	293(2)	293(2)
Crystal system	Tetragonal	Tetragonal
Space group	$I4_1/amd$	$I4_1/amd$
a (Å)	24.770(4)	24.800(4)
b (Å)	24.770(4)	24.800(4)
c (Å)	10.290(2)	10.310(2)
α (°)	90	90
β (°)	90	90
γ (°)	90	90
Volume (Å^3)	6313(2)	6341(2)
ρ_{calc} (g/cm^3)	0.987	0.983
$F(000)$	642.0	642.0
Radiation	Electrons ($\lambda = 0.0335$)	Electrons ($\lambda = 0.0335$)
2Θ range for data collection (°)	0.202 to 2.244	0.254 to 2.4
Index ranges	$-28 \leq h \leq 28$, $-19 \leq k \leq 20$, $-11 \leq l \leq 11$	$-30 \leq h \leq 29$, $-30 \leq k \leq 30$, $-12 \leq l \leq 12$
Reflections collected	5020	5246
Independent reflections	1387 [$R_{\text{int}} = 0.2124$, $R_\sigma = 0.1939$]	1512 [$R_{\text{int}} = 0.2924$, $R_\sigma = 0.3002$]
Data/restraints/parameters	1387/24/32	1512/24/32
Goodness-of-fit on F^2	1.797	1.375
Final R_{Obs} [$I \geq 2\sigma(I)$]	$R_1 = 0.2129$, $wR_2 = 0.4923$	$R_1 = 0.1994$, $wR_2 = 0.4616$
Final R_{all} [all data]	$R_1 = 0.2202$, $wR_2 = 0.5039$	$R_1 = 0.2164$, $wR_2 = 0.4821$
Largest diff. peak/hole (e Å^{-3})	0.29/-0.45	0.36/-0.31

7.5 Conclusions

In this chapter, we demonstrated a SerialED approach using continuous stage movement for data acquisition on a novel, beam-sensitive MOF. To minimize preferred orientation effects, the stage was randomly rotated during data acquisitio. Additionally, a strict filtering criteria was applied to retain only high-quality frames with well-defined diffraction peaks.

The dataset, containing about 5700 frames, was independently processed using both `PETS2` [36] and `nXDS` [100]. In `PETS2`, a custom Python script was developed to identify and exclude unindexed frames based on discrepancies between observed and predicted reflection positions. For `nXDS`, an input file was specifically adapted to electron diffraction geometry, ensuring effective data handling of the SerialED dataset. Both software packages ultimately provided accurate integration of diffraction intensities, which led to a successful structure solution and refinement, confirming the robustness of the implemented methods.

While the data presented in this chapter were collected with a static beam, employing precession electron diffraction would be a more advantageous approach for SerialED experiments. Precession results in integrated reflections for each frame, reducing the number of frames required for a complete dataset and improving the accuracy of intensity measurements.

In conclusion, the methods developed and applied in this chapter highlight the versatility of using a TEM for crystallographic analysis and the potential of SerialED as a powerful tool for structural analysis of beam-sensitive nanocrystals.

In conclusion, this work highlights the versatility of the use of TEMs for crystallographic analysis and highlights the potential of SerialED as a powerful tool for the structural investigation of beam-sensitive nanocrystals. Moreover, it represents both the first publicly available demonstration of SerialED data processing using `nXDS` and the first publicly reported SerialED-based structure solution of a novel MOF.

Supplementary Information

Listing S1: nXDS Input File for SerialED Data Processing

```
!*****************************************************************************
! List of the possible input parameters that can be used in file nXDS.INP
! Characters in a line to the right of an exclamation mark are comment.
!*****************************************************************************

!*****************************************************************************
!*****************************************************************************
! Adapted for Serial Electron Diffraction Data by Moussa Faye, December 2024
!*****************************************************************************
!*****************************************************************************

!============= JOB CONTROL
JOB= XYCORR INIT COLSPOT POWDER IDXREF INTEGRATE CORRECT
!JOB= XYCORR INIT COLSPOT
!JOB= POWDER IDXREF
!JOB= INTEGRATE CORRECT


MAXIMUM_NUMBER_OF_PROCESSORS=4
MAXIMUM_NUMBER_OF_JOBS=4             ! # main programs
!CLUSTER_NODES=bragg01 bragg02 bragg03 bragg04 bragg05 bragg06 bragg07 bragg08
!IMAGE_DIRECTORY=../00???.tiff                 ! Contains images
NAME_TEMPLATE_OF_DATA_FRAMES= ../0????.tiff
DATA_RANGE=1 5746
!SECONDS= 0                            ! # seconds to wait for image
!TEST= 1                               ! for testing image reading routine
VERBOSE=0                             ! 0: short listing; 1:long; >1:debug

!============= INIT
BACKGROUND_RANGE= 1 2000
!DARK_CURRENT_IMAGE=
!OFFSET= 0.0
!TRUSTED_REGION=0.0 2.0 !Relative radii limiting trusted detector region
!UNTRUSTED_ELLIPSE=
!UNTRUSTED_RECTANGLE=
!UNTRUSTED_QUADRILATERAL=
!MINIMUM_FRACTION_OF_BACKGROUND_REGION= 0.01
NBX= 4
NBY= 4

!============= COLSPOT
BACKGROUND_PIXEL= 100.0  ! maximum signal/noise (COLSPOT, INTEGRATE)
SIGNAL_PIXEL= 3    ! minimum signal/noise (COLSPOT, INTEGRATE)
MINIMUM_NUMBER_OF_PIXELS_IN_A_SPOT=5
MINIMUM_NUMBER_OF_SPOTS=20     ! per image

!============= POWDER
!POWDER_CENTER_CORRECTION= 0.0 0.0 0.001 ! dx dy (pixel) q (radian)

!============= IDXREF
```

```
REFINE(IDXREF)= BEAM ORIENTATION CELL  ! POSITION
!RGRID=-1.0   ! histogram grid size (rec. A) for locating difference vectors
!SEPMIN=6.0   ! minimum length (pixels) of difference vectors
!CLUSTER_RADIUS=3.0 ! radius of a difference vector cluster (pixels)
!MAXIMUM_NUMBER_OF_DIFFERENCE_VECTOR_CLUSTERS= 30
!MERGE_TREE=0.1
!INTEGER_ERROR=0.1 ! max. allowed deviation of cluster indices from integers
!NUMBER_OF_TESTED_BASIS_ORIENTATIONS=1000000
INDEX_ERROR= 0.05
INDEX_MAGNITUDE=10
INDEX_QUALITY= 0.7
MINIMUM_FRACTION_OF_INDEXED_SPOTS= 0.4 !# Keep the frame only if at least a certain proportion of the reflections were correctly indexed.

!============= INTEGRATE
INCLUDE_RESOLUTION_RANGE= 10.0 0.85       ! INTEGRATE, CORRECT   !# Resolution Range
!BEAM_DIVERGENCE=
!BEAM_DIVERGENCE_E.S.D.=
!REFLECTING_RANGE_E.S.D.=
NUMBER_OF_PROFILE_GRID_POINTS_ALONG_ALPHA/BETA= 13
MINPK= 75.0 ! MINIMUM REQUIRED PERCENTAGE OF RECORDED INTENSITY
!CUT= 2.0    ! CUT-OFF VALUE DEFINING THE INTEGRATION REGION
PROFILE_FITTING= TRUE ! TRUE            !# Profile Fitting or sum counts.
MINIMUM_ZETA= 0.05
MAXIMUM_ERROR_OF_SPOT_POSITION= 3.0      !# Increase this to increase the tolerance between observed and calculated reflections positions, for better indexing.

!============= CORRECT
MINIMUM_EWALD_OFFSET_CORRECTION= 0.1 ! CORRECT
POSTREFINE= SKALA BEAM ORIENTATION CELL POSITION B-FACTOR ! MOSAICITY      !# Refining the mosaicity in this step resulted in a crash
!REFERENCE_DATA_SET=../xds11/XDS_ASCII.HKL
!USE_REFERENCE_IN_POSTREFINEMENT=TRUE ! FALSE is default
FRIEDEL'S_LAW= TRUE ! FALSE
!MERGE=FALSE ! TRUE is default
!MAX_CELL_AXIS_ERROR= 0.03
!MAX_CELL_ANGLE_ERROR= 3.0
!REJECT_ALIEN= 20.0

!============= CRYSTAL
SPACE_GROUP_NUMBER= 97                !# Usually guessing any space group that belongs to the correct laue class is OK
UNIT_CELL_CONSTANTS=24.77 24.77 10.29 90.000 90.000 90.000 !# The lattice parameters of the system

!============= ROTATION PARAMETERS
!ROTATION_AXIS=0.93051 -0.36627 0.00000   !# For Serial Data, this is not needed.
OSCILLATION_RANGE=0.0                     !# For Serial Data with still images, the oscillation range is ZERO

!============= BEAM PARAMETERS
X-RAY_WAVELENGTH=0.03350             !# Electron Wavelenth in Angrstroem
INCIDENT_BEAM_DIRECTION=0 0 1
FRACTION_OF_POLARIZATION=0.5
POLARIZATION_PLANE_NORMAL=0.000000  1.000000  0.000000
!AIR= 0.0                             ! ABSORPTION COEFFICIENT IN AIR

!============= DETECTOR PARAMETERS
DETECTOR=TIMEPIX  ! DETECTOR TYPE
```

```
NX=516            ! NUMBER OF FAST PIXELS ALONG X
NY=516            ! NUMBER OF SLOW PIXELS ALONG Y
QX=0.0550         ! LENGTH OF A PIXEL (mm) ALONG X
QY=0.0550         ! LENGTH OF A PIXEL (mm) ALONG Y
MINIMUM_VALID_PIXEL_VALUE= 1
OVERLOAD=12000    !# Detector Saturation Limit
!SILICON=         ! ABSORPTION COEFFICIENT IN SILICON
SENSOR_THICKNESS=0.30
DIRECTION_OF_DETECTOR_X-AXIS= 1 0 0
DIRECTION_OF_DETECTOR_Y-AXIS= 0 1 0
ORGX= 259.438 ! DETECTOR ORIGIN in X    !# Central beam X Coordinates
ORGY= 256.271! DETECTOR ORIGIN in Y     !# Central beam Y Coordinates
DETECTOR_DISTANCE=340.9742              !# DETECTOR DISTANCE, Can be calculated from the pixel size
```

Closing Remarks

This thesis has demonstrated the potential of 3D-ED as a powerful tool for the structural characterization of nanomaterials, particularly for cases where traditional methods face limitations due to sample size constraints. 3D-ED therefore bridges the gap imposed by crystal size limitations as a complementary technique to XRD, enabling the use of different diffraction methods adapted to the specific dimensions of the sample. While the technique has been applied to MOFs in this thesis, the same methods discussed here can be, and have been, applied to a variety of materials such as pharmaceutical compounds, organics, co-crystals, perovskites, proteins, and more.

Electron diffraction has come a long way, evolving from solving structures by collecting patterns oriented along a zone axis to the modern advancements of 3D-ED, which comprehensively sample the reciprocal space and made the presented results possible. Future developments could focus on exploiting its ability to operate in both real space and reciprocal space. In combination with recent advancements in Artificial Intelligence (AI), computer vision models capable of identifying and localizing crystal positions may facilitate fully automated data acquisition workflows for methods such as PEDT, cRED, and SerialED, significantly enhancing the efficiency and accessibility of structural characterization. Another promising application of AI in 3D-ED is in solving the phase problem, where machine learning algorithms can enable ab-initio structure solutions even for low-resolution crystals.

In conclusion, the future of 3D-ED appears exceptionally bright, with ongoing advancements expected to further expand its capabilities and applications.

Acknowledgments

The journey of a PhD away from home is both challenging and life-changing. This journey would not have been possible without the contributions of the many people I have had the privilege to encounter along the way, each of whom has, in one way or another, helped shape the person I am today. While it is impossible to name everyone, I would like to take a moment to express my gratitude to some of the people who have been especially impactful throughout this journey.

First and foremost, my supervisor, *Mauro Gemmi*. I want to express my deepest gratitude to you for your guidance and support throughout my PhD journey. Your expertise in electron microscopy and crystallography has been an invaluable resource, and your passion for science, research, and teaching has been a constant source of inspiration. Thank you for always being available to discuss ideas, offer assistance, and guide my progress. I am particularly grateful for your trust in allowing me to manipulate the microscope in unconventional ways, even when risks were involved and for ensuring I never missed opportunities to learn new topics by encouraging my participation in conferences and workshops. Your belief in my abilities and commitment to my development have profoundly shaped both my research and my growth as a scientist.

I would also like to thank the rest of the members of the Electron Crystallography Group: *Vincentia Agbemeh*, *Paola Parlanti*, *Danilo Marchetti*, *Andrea Sala*, *Elena Husanu*, *Goulielmina Anyfanti*, *Iryna Andrusenko* and *Valentina Capello*, for their support and the welcoming environment they created. I am especially grateful to *Paola Parlanti* for her patience and dedication in teaching me to use the TEM. A special thank you also goes to *Vincentia Agbemeh*, my office mate for the last three years, for her friendship and support.

Next, I would like to express my gratitude to the people who hosted me during my secondments. In Prague, I had the privilege of working with the Electron Crystallography group. My deepest thanks go to *Lukáš Palatinus*, *Petr Brázda*, *Ashwin Suresh*, and *Hrushikesh Chintakindi* for sharing their expertise in PETS2 and Dynamical Refinement. Beyond the lab, I am incredibly grateful for their warm hospitality, engaging city tours, and the introduction to delicious Czech and Indian food.

In Brussels, I am deeply thankful to the NanoMEGAS team, especially *Alejandro Perez*, for the interesting discussions about the applications of precession electron diffraction as well as the memorable moments we shared outside work during my time there.

In Eindhoven, I had the pleasure of being hosted by ThermoFisher Scientific. I am sincerely grateful to *Lingbo Yu*, *Oliver Raschdorf*, *Bart Buijsse*, *Nadishka Jayawardena*, and *Adrian Koh* for their warm welcome, granting me access to the Nanoport facilities, and allowing me to explore the clean room where high-end TEMs are manufactured. That was an incredible experience.

At the University of Antwerp, I want to thank *Joke Hadermann*, *Matthias Quintelier*, *Sepideh Rahimisheikh*, *Amirhossein Hajizadeh*, and *Saleh Gholam* for teaching me about in-situ electron microscopy, and I deeply appreciate their kindness and hospitality during my stay.

I would also like to express my sincere thanks to all the supervisors who have built and supported the NanED community. Their dedication and efforts have created an exceptional network of collaboration and learning. I am equally grateful to my fellow NanED PhD students, whose support, teamwork, and shared experiences have made this journey unforgettable.

I would like to extend my gratitude to all my collaborators, whose help, contributions, and encouragement have truly enriched my research. A special mention goes

to *Carlos Martí-Gastaldo*, who has supported me even before I began this journey, and to *Santiago Sarasa San José*, without whom I would not have been able to start this journey. I wish you all the best for the remainder of your PhD.

Last but not least, I want to thank *my family* for always trusting and believing in me. A special thanks to *Sofia Fusco* for her patience, collaboration, and constant support during this journey. To the rest of the *Fusco family*, thank you for welcoming me, supporting me since I moved to Italy, and taking care of me like family, making my stay here truly feel like home.

Contact Information

Should you wish to reach out, please feel free to contact me through the following platforms:

✉ **Email:**

moussa.faye.chem@gmail.com

in LinkedIn:

linkedin.com/in/moussa-faye-diouf

GitHub:

github.com/Thioo

Bibliography

[1] Mauro Gemmi, Enrico Mugnaioli, Tatiana E Gorelik, Ute Kolb, Lukas Palatinus, Philippe Boullay, Sven Hovmöller, and Jan Pieter Abrahams. 3D Electron Diffraction: The Nanocrystallography Revolution. *ACS central science*, 5(8):1315–1329, 2019.

[2] U. Kolb, T. Gorelik, C. Kübel, M.T. Otten, and D. Hubert. Towards automated diffraction tomography: Part I—Data acquisition. *Ultramicroscopy*, 107(6-7):507–513, 2007.

[3] U. Kolb, T. Gorelik, and M.T. Otten. Towards automated diffraction tomography. Part II—Cell parameter determination. *Ultramicroscopy*, 108(8):763–772, 2008.

[4] Devrim Acehan, Katherine A. Spoth, Gabrielle R. Budziszewski, M. Elizabeth Snell, Christopher S. Campomizzi, Miranda L. Lynch, and Sarah E.J. Bowman. Reaching the potential of electron diffraction. *Cell Reports Physical Science*, 5(6):102007, 2024.

[5] Wolfgang Brehm, Josep Triviño, Juno M. Krahn, Isabel Usón, and Kay Diederichs. XDSGUI: a graphical user interface for XDS, SHELX and ARCIMBOLDO. *Journal of Applied Crystallography*, 56(Pt 5):1585–1594, 9 2023.

[6] Paul B. Klar, Yaşar Krysiak, Hongyi Xu, Gwladys Steciuk, Jung Cho, Xiaodong Zou, and Lukas Palatinus. Accurate structure models and absolute

configuration determination using dynamical effects in continuous-rotation 3D electron diffraction data. *Nature Chemistry*, 15(6):848–855, 2023.

[7] Mark S. Hunter, Brent Segelke, Marc Messerschmidt, Garth J. Williams, Nadia A. Zatsepin, Anton Barty, W. Henry Benner, David B. Carlson, Matthew Coleman, Alexander Graf, Stefan P. Hau-Riege, Tommaso Pardini, M. Marvin Seibert, James Evans, Sébastien Boutet, and Matthias Frank. Fixed-target protein serial microcrystallography with an x-ray free electron laser. *Scientific Reports*, 4(1):6026, 8 2014.

[8] Elena López-Maya, Natalia M. Padial, Javier Castells-Gil, Carolina R. Ganivet, Ana Rubio-Gaspar, Francisco G. Cirujano, Neyvis Almora-Barrios, Sergio Tatay, Sergio Navalón, and Carlos Martí-Gastaldo. Selective Implantation of Diamines for Cooperative Catalysis in Isoreticular Heterometallic Titanium–Organic Frameworks. *Angewandte Chemie International Edition*, 60(21):11868–11873, 2021.

[9] Markus J. Kalmutzki, Nikita Hanikel, and Omar M. Yaghi. Secondary building units as the turning point in the development of the reticular chemistry of MOFs. *Science Advances*, 4(10):eaat9180, 10 2018.

[10] Qiang Zhang, Jie Su, Dawei Feng, Zhangwen Wei, Xiaodong Zou, and Hong-Cai Zhou. Piezofluorochromic Metal–Organic Framework: A Microscissor Lift. *Journal of the American Chemical Society*, 137(32):10064–10067, 8 2015.

[11] Erik Svensson Grape, Hongyi Xu, Ocean Cheung, Marion Calmels, Jingjing Zhao, Catherine Dejoie, Davide M. Proserpio, Xiaodong Zou, and A. Ken Inge. Breathing Metal–Organic Framework Based on Flexible Inorganic Building Units. *Crystal Growth & Design*, 20(1):320–329, 2020.

[12] Thierry Loiseau, Christian Serre, Clarisse Huguenard, Gerhard Fink, Francis Taulelle, Marc Henry, Thierry Bataille, and Gérard Férey. A Rationale for

the Large Breathing of the Porous Aluminum Terephthalate (MIL-53) Upon Hydration. *Chemistry – A European Journal*, 10(6):1373–1382, 3 2004.

[13] Austin Echelmeier, Mukul Sonker, and Alexandra Ros. Microfluidic sample delivery for serial crystallography using XFELs. *Analytical and Bioanalytical Chemistry*, 411(25):6535–6547, 2019.

[14] G.E. BACON. Hydrogen Bonding: The study of hydrogen bonds by Neutron Diffraction . pages 23–32, 1959.

[15] V. Ovidiu Garlea and Bryan C. Chakoumakos. Chapter 4 Magnetic Structures. *Experimental Methods in the Physical Sciences*, 48:203–290, 2015.

[16] Richard Dronskowski, Thomas Brückel, Holger Kohlmann, Maxim Avdeev, Andreas Houben, Martin Meven, Michael Hofmann, Takashi Kamiyama, Mirijam Zobel, Werner Schweika, Raphaël P Hermann, and Asami Sano-Furukawa. Neutron diffraction: a primer. *Zeitschrift für Kristallographie - Crystalline Materials*, 239(5-6):139–166, 3 2024.

[17] Justin A. Newman, Luca Iuzzolino, Melissa Tan, Peter Orth, Jessica Bruhn, and Alfred Y. Lee. From Powders to Single Crystals: A Crystallographer's Toolbox for Small-Molecule Structure Determination. *Molecular Pharmaceutics*, 19(7):2133–2141, 2022.

[18] R E Dinnebier and S J L Billinge. *Powder Diffraction: Theory and Practice.* The Royal Society of Chemistry, 03 2008.

[19] Herbert Hauptman. The Direct Methods of X-ray Crystallography. *Science*, 233(4760):178–183, 1986.

[20] Robert E. Dinnebier, Andreas Leineweber, and John S.O. Evans. *Rietveld Refinement.* De Gruyter, Berlin, Boston, 2019.

[21] Axel T. Brünger, John Kuriyan, and Martin Karplus. Crystallographic R Factor Refinement by Molecular Dynamics. *Science*, 235(4787):458–460, 1987.

[22] Athanassios D. Katsenis, Andreas Puškarić, Vjekoslav Štrukil, Cristina Mottillo, Patrick A. Julien, Krunoslav Užarević, Minh-Hao Pham, Trong-On Do, Simon A. J. Kimber, Predrag Lazić, Oxana Magdysyuk, Robert E. Dinnebier, Ivan Halasz, and Tomislav Friscic. In situ X-ray diffraction monitoring of a mechanochemical reaction reveals a unique topology metal-organic framework. *Nature Communications*, 6(1):6662, 2015.

[23] G. Oszlányi and A. Sütő. The charge flipping algorithm. *Acta Crystallographica Section A: Foundations of Crystallography*, 64(1):123–134, 2008.

[24] Danilo Marchetti, Alessandro Pedrini, Chiara Massera, Moussa Diame Faye Diouf, Christian Jandl, Gunther Steinfeld, and Mauro Gemmi. 3D electron diffraction analysis of a novel, mechanochemically synthesized supramolecular organic framework based on tetrakis-4-(4-pyridyl)phenylmethane. *Acta Crystallographica Section B*, 79(Pt 6):432–436, 2023.

[25] Lynne McCusker and Christian Baerlocher. Electron crystallography as a complement to X-ray powder diffraction techniques. *Zeitschrift für Kristallographie - Crystalline Materials*, 228(1):1–10, 1 2013.

[26] Da Neng Wang and Werner Kühlbrandt. Three-dimensional electron diffraction of plant light-harvesting complex. *Biophysical Journal*, 61(2):287–297, 2 1992.

[27] Petr Brázda, Lukáš Palatinus, and Martin Babor. Electron diffraction determines molecular absolute configuration in a pharmaceutical nanocrystal. *Science*, 364(6441):667–669, 2019.

[28] R. Vincent and P.A. Midgley. Double conical beam-rocking system for measurement of integrated electron diffraction intensities. *Ultramicroscopy*, 53(3):271–282, 1994.

[29] E. Mugnaioli, T. Gorelik, and U. Kolb. “Ab initio” structure solution from electron diffraction data obtained by a combination of automated diffraction tomography and precession technique. *Ultramicroscopy*, 109(6):758–765, 2009.

[30] Daliang Zhang, Peter Oleynikov, Sven Hovmöller, and Xiaodong Zou. Collecting 3D electron diffraction data by the rotation method. *Zeitschrift für Kristallographie*, 225(2-3):94–102, 2010.

[31] Mauro Gemmi, Maria G. I. La Placa, Athanassios S. Galanis, Edgar F. Rauch, and Stavros Nicolopoulos. Fast electron diffraction tomography. *Journal of Applied Crystallography*, 48(3):718–727, 2015.

[32] Brent L Nannenga, Dan Shi, Andrew G W Leslie, and Tamir Gonen. High-resolution structure determination by continuous-rotation data collection in MicroED. *Nature Methods*, 11(9):927–930, 2014.

[33] Robert Bücker, Pascal Hogan-Lamarre, and R. J. Dwayne Miller. Serial Electron Diffraction Data Processing With diffractem and CrystFEL. *Frontiers in Molecular Biosciences*, 8:624264, 2021.

[34] Pascal Hogan-Lamarre, Yi Luo, Robert Bücker, R. J. Dwayne Miller, and Xiaodong Zou. STEM SerialED: achieving high-resolution data for ab initio structure determination of beam-sensitive nanocrystalline materials. *IUCrJ*, 11(Pt 1):62–72, 2024.

[35] Yi Luo, Bin Wang, Stef Smeets, Junliang Sun, Weimin Yang, and Xiaodong Zou. High-throughput phase elucidation of polycrystalline materials using serial rotation electron diffraction. *Nature Chemistry*, 15(4):483–490, 2023.

[36] Lukáš Palatinus, Petr Brázda, Martin Jelínek, Jaromíra Hrdá, Gwladys Steciuk, and Mariana Klementová. Specifics of the data processing of precession electron diffraction tomography data and their implementation in the program PETS2.0. *Acta Crystallographica Section B*, 75(4):512–522, 2019.

[37] W. Kabsch. XDS. *Acta Crystallographica Section D: Biological Crystallography*, 66(2):125–132, 2010.

[38] G. Winter, D.G. Waterman, J.M. Parkhurst, A.S. Brewster, R.J. Gildea, M. Gerstel, L. Fuentes-Montero, M. Vollmar, T. Michels-Clark, I.D. Young, N.K. Sauter, and G. Evans. DIALS: implementation and evaluation of a new integration package. *Acta Crystallographica Section D: Structural Biology*, 74(2):85–97, 2 2018.

[39] Max T. B. Clabbers, Tim Gruene, James M. Parkhurst, Jan Pieter Abrahams, and David G. Waterman. Electron diffraction data processing with DIALS. *Acta Crystallographica Section D*, 74(6):506–518, 2018.

[40] Angelina Vypritskaia, Xiaodong Zou, Taimin Yang, and David Geoffrey Waterman. How to use DIALS to process chemical crystallography 3D ED rotation data from pixel array detectors. *Acta crystallographica. Section C, Structural chemistry*, 81(1):1–13, 1 2025.

[41] P Andrew Karplus and Kay Diederichs. Linking crystallographic model and data quality. *Science (New York, N.Y.)*, 336(6084):1030–3, 5 2012.

[42] Jimin Wang, Gary W. Brudvig, Victor S. Batista, and Peter B. Moore. On the relationship between cumulative correlation coefficients and the quality of crystallographic data sets. *Protein Science*, 26(12):2410–2416, 12 2017.

[43] Petr Brázda, Mariana Klementová, Yaşar Krysiak, and Lukáš Palatinus. Accurate lattice parameters from 3D electron diffraction data. I. Optical distortions. *IUCrJ*, 9(Pt 6):735–755, 2022.

[44] Malak Khouchen, Paul Benjamin Klar, Hrushikesh Chintakindi, Ashwin Suresh, and Lukas Palatinus. Optimal estimated standard uncertainties of reflection intensities for kinematical refinement from 3D electron diffraction data. *Acta Crystallographica Section A*, 79(5):427–439, 2023.

[45] Lukáš Palatinus and Gervais Chapuis. SUPERFLIP– a computer program for the solution of crystal structures by charge flipping in arbitrary dimensions. *Journal of Applied Crystallography*, 40(4):786–790, 8 2007.

[46] George M. Sheldrick. SHELXT– Integrated space-group and crystal-structure determination. *Acta Crystallographica Section A*, 71(1):3–8, 2015.

[47] George M. Sheldrick. Crystal structure refinement with SHELXL. *Acta Crystallographica Section C*, 71(1):3–8, 2015.

[48] Oleg V. Dolomanov, Luc J. Bourhis, Richard J. Gildea, Judith A. K. Howard, and Horst Puschmann. OLEX2: a complete structure solution, refinement and analysis program. *Journal of Applied Crystallography*, 42(2):339–341, 2009.

[49] Christian B. Hübschle, George M. Sheldrick, and Birger Dittrich. *ShelXle*: a Qt graphical user interface for *SHELXL*. *Journal of Applied Crystallography*, 44(6):1281–1284, Dec 2011.

[50] Kunio Fujiwara. Relativistic dynamical theory of electron diffraction. *Journal of the Physical Society of Japan*, 16(11):2226–2238, 1961.

[51] Václav Petříček, Michal Dušek, and Lukáš Palatinus. Crystallographic Computing System JANA2006: General features. *Zeitschrift für Kristallographie - Crystalline Materials*, 229(5):345–352, 2014.

[52] Václav Petříček, Lukáš Palatinus, Jakub Plášil, and Michal Dušek. Jana2020 – a new version of the crystallographic computing system Jana. *Zeitschrift für Kristallographie - Crystalline Materials*, 238(7-8):271–282, 2023.

[53] H D Flack. On enantiomorph-polarity estimation. *Acta Crystallographica Section A Foundations of Crystallography*, 39(6):876–881, 11 1983.

[54] S. Parsons, H.D. Flack, and T. Wagner. Use of intensity quotients and differences in absolute structure refinement. *Acta Crystallographica Section B: Structural Science, Crystal Engineering and Materials*, 69(3):249–259, 6 2013.

[55] A.J. Koster, H. Chen, J.W. Sedat, and D.A. Agard. Automated microscopy for electron tomography. *Ultramicroscopy*, 46(1-4):207–227, 1992.

[56] U. Ziese, A. H. Janssen, J.-L. Murk, W. J. C. Geerts, T. Van der Krift, A.J. Verkleij, and A.J. Koster. Automated high-throughput electron tomography by pre-calibration of image shifts. *Journal of Microscopy*, 205(2):187–200, 2002.

[57] S Plana-Ruiz, Y Krysiak, J Portillo, E Alig, S Estradé, F Peiró, and U Kolb. Fast-ADT: A fast and automated electron diffraction tomography setup for structure determination and refinement. *Ultramicroscopy*, 211:112951, 2020.

[58] Jaedong Kang, Yunbeom Lee, Seonggon Lee, Hosung Ki, Jungmin Kim, Jain Gu, Yongjun Cha, Jun Heo, Kyung Won Lee, Seong Ok Kim, Jaehyun Park, Sang-Youn Park, Sangsoo Kim, Rory Ma, Intae Eom, Minseok Kim, Jeongho Kim, Jae Hyuk Lee, and Hyotcherl Ihee. Dynamic three-dimensional structures of a metal–organic framework captured with femtosecond serial crystallography. *Nature Chemistry*, 16(5):693–699, 5 2024.

[59] Sofia Jaho, Danny Axford, Do-Heon Gu, Michael A. Hough, and Robin L. Owen. Use of fixed targets for serial crystallography. *Methods in Enzymology*, 709:29–55, 10 2024.

[60] Anton Barty, Richard A. Kirian, Filipe R. N. C. Maia, Max Hantke, Chun Hong Yoon, Thomas A. White, and Henry Chapman. Cheetah: software for high-throughput reduction and analysis of serial femtosecond X-ray diffraction data. *Journal of Applied Crystallography*, 47(3):1118–1131, 6 2014.

[61] Thomas A. White, Richard A. Kirian, Andrew V. Martin, Andrew Aquila, Karol Nass, Anton Barty, and Henry N. Chapman. CrystFEL: a software suite for snapshot serial crystallography. *Journal of Applied Crystallography*, 45(2):335–341, 4 2012.

[62] G. Bradski. The OpenCV Library. *Dr. Dobb's Journal of Software Tools*, 2000.

[63] Laszlo Takacs. The historical development of mechanochemistry. *Chemical Society Reviews*, 42(18):7649–7659, 2013.

[64] Jean-Louis Do and Tomislav Friscic. Mechanochemistry: A Force of Synthesis. *ACS Central Science*, 3(1):13–19, 2017.

[65] R. B. Nasir Baig and Rajender S. Varma. Alternative energy input: mechanochemical, microwave and ultrasound-assisted organic synthesis. *Chemical Society Reviews*, 41(4):1559–1584, 2011.

[66] Stuart L. James, Christopher J. Adams, Carsten Bolm, Dario Braga, Paul Collier, Tomislav Friscic, Fabrizia Grepioni, Kenneth D. M. Harris, Geoff Hyett, William Jones, Anke Krebs, James Mack, Lucia Maini, A. Guy Orpen, Ivan P. Parkin, William C. Shearouse, Jonathan W. Steed, and Daniel C. Waddell. Mechanochemistry: opportunities for new and cleaner synthesis. *Chemical Society Reviews*, 41(1):413–447, 2011.

[67] Concepción Jiménez-González, David J. C. Constable, and Celia S. Ponder. Evaluating the "Greenness" of chemical processes and products in the pharmaceutical industry—a green metrics primer. *Chemical Society Reviews*, 41(4):1485–1498, 2011.

[68] Tomislav Friscic and László Fábián. Mechanochemical conversion of a metal oxide into coordination polymers and porous frameworks using liquid-assisted grinding (LAG). *CrystEngComm*, 11(5):743–745, 2009.

[69] Christopher J. Adams, Mukhtar A. Kurawa, Matteo Lusi, and A. Guy Orpen. Solid state synthesis of coordination compounds from basic metal salts. *CrystEngComm*, 10(12):1790–1795, 2008.

[70] Alexander Czaja, Emi Leung, Natalia Trukhan, and Ulrich Müller. Metal-Organic Frameworks: Industrial MOF Synthesis. pages 337–352, 2011.

[71] Andrea Sala, Moussa D Faye Diouf, Danilo Marchetti, Lea Pasquale, and Mauro Gemmi. Mechanochemical Synthesis and Three-Dimensional Electron Diffraction Structure Solution of a Novel Cu-Based Protocatechuate Metal–Organic Framework. *Crystal Growth & Design*, 2024.

[72] Danilo Marchetti, Francesca Guagnini, Arianna E. Lanza, Alessandro Pedrini, Lara Righi, Enrico Dalcanale, Mauro Gemmi, and Chiara Massera. Combined Approach of Mechanochemistry and Electron Crystallography for the Discovery of 1D and 2D Coordination Polymers. *Crystal Growth & Design*, 21(12):6660–6664, 2021.

[73] Estitxu Echenique-Errandonea, Sara Rojas, Víctor Karim Abdelkader-Fernández, Manuel Pérez-Mendoza, Ricardo F. Mendes, Paula Barbosa, Filipe Figueiredo, Flávio Figueira, Filipe A. Almeida Paz, José Manuel Delgado-López, Antonio Rodríguez-Diéguez, and José Manuel Seco. Adsorptive Capacity, Inhibitory Activity and Processing Techniques for a Copper-MOF Based on the 3,4-Dihydroxybenzoate Ligand. *Molecules*, 27(22):8073, 2022.

[74] Clare F. Macrae, Ioana Sovago, Simon J. Cottrell, Peter T. A. Galek, Patrick McCabe, Elna Pidcock, Michael Platings, Greg P. Shields, Joanna S. Stevens, Matthew Towler, and Peter A. Wood. Mercury 4.0: from visualization to analysis, design and prediction. *Journal of Applied Crystallography*, 53(Pt 1):226–235, 2 2020.

[75] H. M. Rietveld. A profile refinement method for nuclear and magnetic structures. *Journal of Applied Crystallography*, 2(2):65–71, Jun 1969.

[76] A.A. Coelho. TOPAS and TOPAS-Academic: an optimization program integrating computer algebra and crystallographic objects written in C++. *Journal of Applied Crystallography*, 51(1):210–218, 2018.

[77] Jung Soo Seo, Dongmok Whang, Hyoyoung Lee, Sung Im Jun, Jinho Oh, Young Jin Jeon, and Kimoon Kim. A homochiral metal–organic porous material for enantioselective separation and catalysis. *Nature*, 404(6781):982–986, 4 2000.

[78] Joseé Navarro-Saénchez, Ana I. Argente-Garciéa, Yolanda Moliner-Martiénez, Daniel Roca-Sanjuaén, Dmytro Antypov, Pilar Campiéns-Falcoé, Matthew J. Rosseinsky, and Carlos Martié-Gastaldo. Peptide Metal–Organic Frameworks for Enantioselective Separation of Chiral Drugs. *Journal of the American Chemical Society*, 139(12):4294–4297, 3 2017.

[79] Zongsu Han, Tiankai Sun, Rong-Ran Liang, Yifan Guo, Yihao Yang, Mengmeng Wang, Yue Mao, Peter R. Taylor, Wei Shi, Kun-Yu Wang, and Hong-Cai Zhou. Chiral Linker Installation in a Metal–Organic Framework for Enantioselective Luminescent Sensing. *Journal of the American Chemical Society*, 146(22):15446–15452, 5 2024.

[80] Qun Liu and Wayne A Hendrickson. Crystallographic phasing from weak anomalous signals. *Current Opinion in Structural Biology*, 34:99–107, 2015.

[81] Zhehao Huang, Erik Svensson Grape, Jian Li, A. Ken Inge, and Xiaodong Zou. 3D electron diffraction as an important technique for structure elucidation of metal-organic frameworks and covalent organic frameworks. *Coordination Chemistry Reviews*, 427:213583, 2021.

[82] Y. Le Page, E. J. Gabe, and G. J. Gainsford. A robust alternative to η refinement for assessing the hand of chiral compounds. *Journal of Applied Crystallography*, 23(5):406–411, Oct 1990.

[83] Omar M. Yaghi. Reticular Chemistry in All Dimensions. *ACS Central Science*, 5(8):1295–1300, 8 2019.

[84] Michael O'Keeffe, Maxim A. Peskov, Stuart J. Ramsden, and Omar M. Yaghi. The Reticular Chemistry Structure Resource (RCSR) Database of, and Symbols for, Crystal Nets. *Accounts of Chemical Research*, 41(12):1782–1789, 12 2008.

[85] Lawson T. Glasby, Joan L. Cordiner, Jason C. Cole, and Peyman Z. Moghadam. Topological Characterization of Metal–Organic Frameworks: A Perspective. *Chemistry of Materials*, 2024.

[86] Dawei Feng, Zhi-Yuan Gu, Jian-Rong Li, Hai-Long Jiang, Zhangwen Wei, and Hong-Cai Zhou. Titelbild: Zirconium-Metalloporphyrin PCN-222: Mesoporous Metal–Organic Frameworks with Ultrahigh Stability as Biomimetic Catalysts (Angew. Chem. 41/2012). *Angewandte Chemie*, 124(41):10343–10343, 10 2012.

[87] Dawei Feng, Wan-Chun Chung, Zhangwen Wei, Zhi-Yuan Gu, Hai-Long Jiang, Ying-Pin Chen, Donald J. Darensbourg, and Hong-Cai Zhou. Construction of Ultrastable Porphyrin Zr Metal–Organic Frameworks through Linker Elimination. *Journal of the American Chemical Society*, 135(45):17105–17110, 11 2013.

[88] Hao Wang, Xinglong Dong, Junzhong Lin, Simon J. Teat, Stephanie Jensen, Jeremy Cure, Eugeny V. Alexandrov, Qibin Xia, Kui Tan, Qining Wang, David H. Olson, Davide M. Proserpio, Yves J. Chabal, Timo Thonhauser, Junliang Sun, Yu Han, and Jing Li. Topologically guided tuning of Zr-MOF pore structures for highly selective separation of C6 alkane isomers. *Nature Communications*, 9(1):1745, 5 2018.

[89] Kang Sun, Yunyang Qian, and Hai-Long Jiang. Metal-Organic Frameworks for Photocatalytic Water Splitting and CO2 Reduction. *Angewandte Chemie*, 135(15), 4 2023.

[90] Javier Castells-Gil, Natalia M. Padial, Neyvis Almora-Barrios, Josep Albero, A. Rabdel Ruiz-Salvador, Javier González-Platas, Hermenegildo García, and Carlos Martí-Gastaldo. Chemical Engineering of Photoactivity in Heterometallic Titanium–Organic Frameworks by Metal Doping. *Angewandte Chemie*, 130(28):8589–8593, 2018.

[91] TopCryst. www.topcryst.com.

[92] Benjamin J. Bucior, Andrew S. Rosen, Maciej Haranczyk, Zhenpeng Yao, Michael E. Ziebel, Omar K. Farha, Joseph T. Hupp, J. Ilja Siepmann, Alaén Aspuru-Guzik, and Randall Q. Snurr. Identification Schemes for Metal–Organic Frameworks To Enable Rapid Search and Cheminformatics Analysis. *Crystal Growth & Design*, 19(11):6682–6697, 2019.

[93] Mays Alhamami, Huu Doan, and Chil-Hung Cheng. A Review on Breathing Behaviors of Metal-Organic-Frameworks (MOFs) for Gas Adsorption. *Materials*, 7(4):3198–3250, 4 2014.

[94] Sergi Plana-Ruiz, Alejandro Goémez-Peérez, Monika Budayova-Spano, Daniel L. Foley, Joaquim Portillo-Serra, Edgar Rauch, Evangelos Grivas, Dominique Housset, Partha Pratim Das, Mitra L. Taheri, Stavros Nicolopoulos, and Wai Li Ling. High-Resolution Electron Diffraction of Hydrated Protein Crystals at Room Temperature. *ACS Nano*, 17(24):24802–24813, 12 2023.

[95] Henry N. Chapman, Petra Fromme, Anton Barty, Thomas A. White, Richard A. Kirian, Andrew Aquila, Mark S. Hunter, Joachim Schulz, Daniel P. DePonte, Uwe Weierstall, R. Bruce Doak, Filipe R. N. C. Maia, Andrew V. Martin, Ilme Schlichting, Lukas Lomb, Nicola Coppola, Robert L. Shoeman, Sascha W. Epp, Robert Hartmann, Daniel Rolles, Artem Rudenko, Lutz Foucar, Nils Kimmel, Georg Weidenspointner, Peter Holl, Mengning Liang, Miriam Barthelmess, Carl Caleman, Sébastien Boutet, Michael J. Bogan, Jacek Krzywinski, Christoph Bostedt, Saša Bajt, Lars Gumprecht, Benedikt

Rudek, Benjamin Erk, Carlo Schmidt, André Hömke, Christian Reich, Daniel Pietschner, Lothar Strüder, Günter Hauser, Hubert Gorke, Joachim Ullrich, Sven Herrmann, Gerhard Schaller, Florian Schopper, Heike Soltau, Kai-Uwe Kühnel, Marc Messerschmidt, John D. Bozek, Stefan P. Hau-Riege, Matthias Frank, Christina Y. Hampton, Raymond G. Sierra, Dmitri Starodub, Garth J. Williams, Janos Hajdu, Nicusor Timneanu, M. Marvin Seibert, Jakob Andreasson, Andrea Rocker, Olof Jönsson, Martin Svenda, Stephan Stern, Karol Nass, Robert Andritschke, Claus-Dieter Schröter, Faton Krasniqi, Mario Bott, Kevin E. Schmidt, Xiaoyu Wang, Ingo Grotjohann, James M. Holton, Thomas R. M. Barends, Richard Neutze, Stefano Marchesini, Raimund Fromme, Sebastian Schorb, Daniela Rupp, Marcus Adolph, Tais Gorkhover, Inger Andersson, Helmut Hirsemann, Guillaume Potdevin, Heinz Graafsma, Björn Nilsson, and John C. H. Spence. Femtosecond X-ray protein nanocrystallography. *Nature*, 470(7332):73–77, 2011.

[96] Henry N. Chapman, Carl Caleman, and Nicusor Timneanu. Diffraction before destruction. *Philosophical Transactions of the Royal Society B: Biological Sciences*, 369(1647):20130313, 2014.

[97] Magdalena Ola Cichocka, Jonas Ångström, Bin Wang, Xiaodong Zou, and Stef Smeets. High-throughput continuous rotation electron diffraction data acquisition via software automation. *Journal of Applied Crystallography*, 51(6):1652–1661, 2018.

[98] Stef Smeets, Xiaodong Zou, and Wei Wan. Serial electron crystallography for structure determination and phase analysis of nanocrystalline materials. *Journal of Applied Crystallography*, 51(5):1262–1273, 10 2018.

[99] Yaroslav Gevorkov, Anton Barty, Wolfgang Brehm, Thomas A. White, Aleksandra Tolstikova, Max O. Wiedorn, Alke Meents, Rolf-Rainer Grigat, Henry N. Chapman, and Oleksandr Yefanov. pinkIndexer – a universal indexer

for pink-beam X-ray and electron diffraction snapshots. *Acta Crystallographica Section A*, 76(2):121–131, 2020.

[100] Wolfgang Kabsch. Processing of X-ray snapshots from crystals in random orientations. *Acta Crystallographica Section D*, 70(8):2204–2216, 2014.